UNIVERSITAT DE BARCELONA

BasC K154 role on cytosolic gate closing

The bacterial alanine-serine-cysteine transporter as a model

Adrià Nicolàs i Aragó

Universitat de Barcelona
Facultat de Farmàcia i Ciències de l'Alimentació

Doctoral Thesis

BasC K154 role on cytoplasmic gate closing

The Bacterial Alanine-Serine-Cisteine transporter as a model

Adrià Nicolàs i Aragó

2022

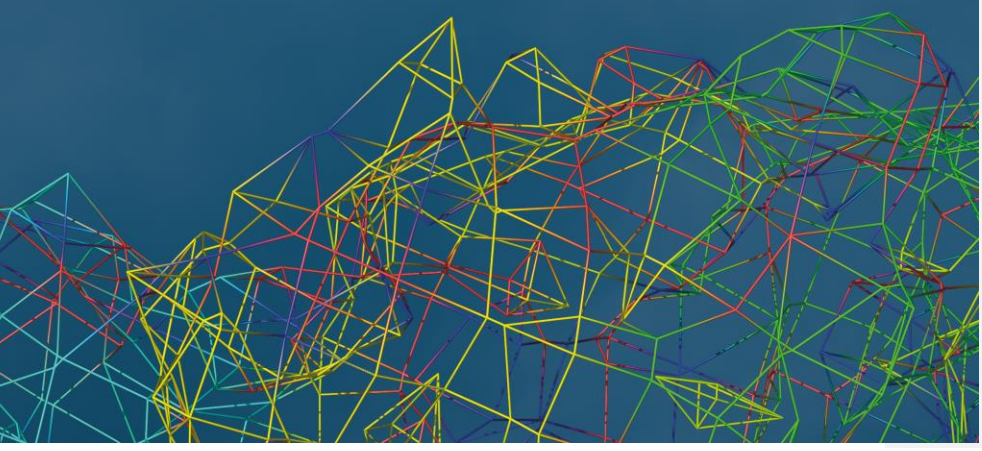

Universitat de Barcelona
Facultat de farmàcia i ciències de l'alimentació

BasC K154 key role on cytosolic gate closing

The bacterial alanine-serine-cysteine transporter as a model

El rol de la K154 de BasC en el tancament de la porta citosòlica
El transportador bacterià d'alanina-serina-cisteïna com a model

Adrià Nicolàs i Aragó
September 2022

Universitat de Barcelona
Facultat de farmàcia i ciències de l'alimentació
Programa de doctorat en **Biotecnologia**

BasC K154 key role on cytosolic gate closing

The bacterial alanine-serine-cysteine transporter as a model

El rol de la K154 de BasC en el tancament de la porta citosòlica
El transportador bacterià d'alanina-serina-cisteïna com a model

Tesi realitzada a l'**Institut de Recerca Biomèdica** (IRB) de Barcelona
Grup d'investigació Transportadors d'Aminoàcids i Malaltia.

Supervisada per:

Prof. Dr. Manuel Palacín Prieto
codirector i tutor

Dr. Joana Fort i Baixeras
codirectora

A les dones de la meva vida

àvies
mare
amigues
i companyes de feina

Moltes gràcies
Thank you
Vielen danke
Muchas gracias
Grazie mille

Aknowledgements / Agraïments

Mai negaré que han estat uns anys molt intensos. Des que vaig començar amb el projecte el 2016 quan somiava fent el TFG, la proteïna d'estudi s'ha acabat convertint en el pilar de la meva tesi, la meva amiga BasC. Ara amb perspectiva, mirant enrere en el temps, no oblido tampoc dels dos anys de TFG i TFM, els quals van començar a encaminar-me cap a aquesta aventura que ha esdevingut el doctorat.

Com en tota aventura, hi ha alts i baixos. I és que sempre ens en recordem de les experiències negatives més que de les positives, malauradament, com a la resta de facetes de les nostres vides. Però jo no vull que acabi així, amb aquest regust. És obvi que no tot ha estat flors i violes, tots els que hi heu sigut ho sabeu prou bé. M'atreviria a dir que ha estat dur en moltes ocasions. Més si li sumem la pandèmia que hem passat i els diversos entrebancs personals pels quals m'he topat. Malgrat tot, quan mires enrere, la presa de distància t'aporta una nova perspectiva. Valorar tot el que has après, tot el que has viscut i tot el suport que has rebut. I aquest apartat, el d'agraïments, *aknowledgements*, és per posar en valor tota aquella gent que m'heu ofert el vostre suport al llarg d'aquests llargs anys.

Gràcies a tots i totes.

Primer de tot, vull parlar de les dues persones que em van portar al món, la meva **mare**, Montse, i el meu **pare**, Carles. Elles son les dues persones més preuades de la faç de la Terra. Perquè sense elles no seria res del que em considero que soc avui. I mai tinc les paraules escaients ni suficients per agrair-vos tot el que m'heu donat: com m'heu educat, com m'heu empès i encoratjat en totes les decisions que he anat prenent al llarg de la meva vida i com, sempre, m'heu donat el vostre suport incondicional, més tenint en compte que moltes vegades no enteníeu res del que feia. Tant en la vessant més acadèmica com en la personal. Moltes gràcies per haver-me acompanyat durant tots aquests anys, per ser-hi, sempre. Perquè m'ho heu donat tot i més. Pensant en vosaltres no puc evitar donar les gràcies a les dues dones més fortes que mai coneixeré: l'**àvia Mercè** i l'**àvia Teresa**. Les dues dones que van mantenir dins aquest món tan contaminat dues famílies impressionantment boniques. I no menteixo, crec, si digués que n'esteu molt orgulloses de mi, tan com jo de vosaltres, us estimaré sempre. Allà on sigueu, us porto al cor.

Tampoc em puc oblidar de vosaltres, **Marc** i **Raquel**, per haver-hi estat, ajudant en tot el que ha calgut. I, òbviament, als dos petits de la casa, **Isaac** i **Isona**, l'energia dels quals sempre m'ha ajudat a seguir endavant. Encara que no en sigueu conscients. Al laboratori, un ha de tenir la curiositat que vosaltres sempre porteu a sobre, les ganes de descobrir, la set de saber. Això també va per vosaltres. I, tampoc puc deixar-me de citar-te a tu, **Carme**, perquè sempre hi has estat, sempre. Interessant-te per la tasca que tant valores, la recerca. Gràcies per interessar-te'n sempre. Gràcies.

I és que quan passem pels moments difícils, el més important és envoltar-te d'aquells que t'estimen i estimes, aquelles persones que saps que sempre hi seran, t'escoltaran i t'abraçaran. Són aquella mena de para-xocs o salvavides que t'esmorteeixen tots els cops, que t'aplanen els alts i baixos... en definitiva, les que m'han ajudat més sobreviure durant el doctorat. Em refereixo a vosaltres amigues, sí. Totes les que heu compartit algun dels moments que m'he anat trobant, els dolents però també els bons. Sobretot les que heu conviscut amb mi, dia a dia, durant els mesos més difícils: sí, sobretot la **Clara** i també la **Laia**, sabeu en escreix que mai oblidaré tot el suport incondicional que m'heu donat. Les llàgrimes eixugades, de riure i de tristor; les abraçades asfixiants que ens hem brindat les unes a les altres; les llargues xerrameques que han farcit tants moments. També vull esmentar a tota la resta de **Perris** que hi heu estat en la vostra mesura: **Eloi**, **Marina**, **Alba**, **Júlia**, **Joana**, **Jowa** i **Rocío**. Sense vosaltres no ho hagués viscut igual. Perquè els missatges de suport i d'ànims han estat imprescindibles. Així com tots els dinars i sortides que sempre anem fent i ajuden a desconnectar, a alliberar tensió i pressió. I a tu també, **Gil**, perquè ens hem descobert quan menys ens ho esperàvem i ha set preciós. Seguim domesticant-nos fins cansar-nos.

També vull agrair a la resta d'amistats que, d'alguna manera o altra, hi heu sigut sempre. Als còmplices del cinema més terrorífic, **Pere** i **Laia**. Perquè els festivals i films en són l'excusa que aprofitem per gaudir d'una amistat que sabem que va més enllà de tot el que hem arribat a compartir des que ens vam descobrir a el **Ball Pla de Vilafranca**. Danses que m'han dut a acabar endinsant-me a l'**Esbart Rocasagna de Gelida**. És a través de la dansa que m'agradaria donar-vos les gràcies amb el millor Ball d'Homenatge. Gràcies per haver-me acompanyat durant el dia a dia més dur, sent-hi durant els assajos que m'han permès, i molt, desconnectar. Especialment a vosaltres, gràcies **Clàudia** i **Carles**. I també un esment a totes les companyes del **Ball dels Malcasats** de Vilafranca, que estiu rere estiu hem versat i, entre grolleries, ens hem estimat.

Alguns es preguntaran perquè vaig acceptar endinsar-me en aquesta llarga aventura. Doncs la vaig acceptar en el moment que la meva mentora científica em va il·luminar amb la idea de seguir després del màster. **Joana**, no saps com t'odio i t'estimo a la vegada, més la última, és clar. Perquè a part de tot el que podria afalagar-te de la teva vessant més professional i acadèmica, el que penso deixar per escrit és l'admiració que professo a la teva persona. No hagués estat tant còmode enlloc, no hagués fet mai tant bon tàndem com amb tu amb ningú d'aquest sistema acadèmic. No hagués gaudit mai tant de les hores pescant, escrivint, experimentant, xerrant, fent cafès, provant noves tècniques... M'has sabut transmetre una estima cap a la ciència i cap a la vida immensos. Mestra de mestres, GRÀCIES. Si tot el que està escrit en aquestes pàgines és responsabilitat última d'alguna persona, aquesta ets tu.

Y no lo hubiese podido hacer sin estar protegido bajo un paraguas tan noble como el tuyo, **Manuel**. Porque aprendí tanto a tu lado que ni te lo imaginas. Sabiendo que tu curiosidad e interés por lo más profundo de la ciencia son insaciables. Porque tu cerebro es como un rompecabezas que necesita que entenderlo todo y ordenarse. Y es ésta pasión por la ciencia la que me ha permitido alimentarme a lo

largo de estos años. Siempre sabiendo que en el momento que entraba en tu despacho ya no había forma de salir de él, rezando para terminar pronto para fumar un piti enfriando mi cerebro, rezando para que quedasen buses hacía Vilafranca. Gracias a ti, i a l'**IRB Barcelona**, per haver-me brindat aquesta oportunitat en aquesta gran casa.

Vull agrair també a totes les persones que de manera més o menys continuada heu format part de la meva família laboratorienca. **Paola**, ets un amor de persona i no m'imagino un laboratori sense el teu somriure i les teves paraules d'amor. **Susanna**, compartir passadís amb tu, així com tantes i tantes bromes, no hauria pogut ser millor. **Ekaitz**, sense el teu petit "*pequeño saltamontes*" cada vegada que ens vèiem, no hagués estat el mateix. **Judith** i **Josep**, els que colze a colze hem compartit moments en hores intempestives fent poyata i suant de valent. Especialmente también quiero agradecerte a ti, **Paloma**. Porqué los buenos momentos que pasamos al laboratorio fueron tan importantes para mí como el allanamiento de terreno que siempre hiciste precediéndome en el transcurso de nuestros caminos académicos. Nos seguimos viendo allí donde estemos. Gracias. Menció especial també pels dos estudiants que han passat per la poyata, la **Laia** i en **Javi**. Perquè, com a més petits de la casa heu demostrat una vegada més la importància de voler saber més, les ganes d'aprendre'n. I és gràcies a vosaltres que reactiveu als que som de la casa, aportant aire fresc i noves ganes de seguir endavant. Gràcies als dos.

I el laboratori no hauria estat el mateix sense la gran família que formem entre totes. **Sara**, gracias por ser mi hermana mayor, aun siendo una *former member*, sempre seràs la crack de les més cracks. **Andrea**, nire bihotzeko azukre kozkorra, eskerrik asko per tots aquests moments de suport moral. Encara ens queden molts vins per prendre, al Penedès, Dinamarca o qui sap on. Les portes de casa meva les tens obertes de bat a bat. **Isa**, compañera de despacho, tus bromas y tu perspicacia han sido inspiración para mí. **Alba**, gràcies per compartir tant amb mi, per tots els cafès i cigarrets compartits tot intentant alliberar-nos de tanta pressió. Estic molt orgullós que els nostres camins s'hagin alineat! **Katerina**, ευχαριστώ, thanks a lot for so much that we have shared. For all those gossips, academic and personal, that we have. Y cómo no, gràcies **David**, compañero infalible de bus (cuando estabas en Reus molabas más) y desayuno. I no em vull deixar la **Maribel**, que has volat com et mereixies i t'he trobat a faltar al nostre passadís. I també a tota la resta de persones del laboratori que hi heu sigut sempre: **Jordi** amb tota la feinada que fas per nosaltres entre xiulets; **Olga** envoltada del teu teu patchwork; **Natàlia** amb la gran feinada que fas (t'he trobat a faltar aquest últim mes); **Jia**, **Paula** i **Petra**, thanks for this pretty PhD student familly we have breeded; i **Manu**, per les hores de bus de Vilafranca a Barcelona compartides. Gràcies a vosaltres i a tota la resta per fer del laboratori un espai més amable.

I no hi ha ningú amb els que puguis compartir més la teva desesperació que els teus iguals dels altres laboratoris. Gràcies per les sortides, barbacoes i dies de bar que hem compartit. **Marina**, **Elena**, **Paula**, **Adrià**, **Clara**, **Hania**, **Pep** i **Marina**. I agrair la tasca dels companys que tant m'han acompanyat durant aquest viatge. I també els històrics que ja fa anys que ens compartim, **Núria** i **Laura**, les meves

caris enamorades de la GFP. I també vosaltres, **Marcos**, **María** i **Mireia**, les patidores paral·leles de l'edifici de davant.

No m'oblido del **comitè d'empresa**, ple de persones que vam lluitar per la creació d'aquest el setembre de 2018 (quina experiència) per defensar que la plantilla de l'IRB tingui unes condicions més dignes dins de tota aquesta merda de societat i sistema. Gràcies **Marina**, **David**, **Natàlia**, **Jomi**, **Lídia**, **Anna**, **Rodolfo**, **Marc**, **Laura**, **Guio**, **Andrés**, **Natàlia**, **Sara** i **Mar**.

I també a tota la gent del **comitè d'igualtat i diversitat**, per vetllar, donar recursos i eines per tal de fer dels centres de recerca espais més amables per a totes les persones. Lluitant contra la realitat d'un entorn abusiu, excloent i assassí. Ens queda molta feina per fer. Per un futur millor, gràcies **Sònia**, **Marta**, **Martina**, **Guio**, **Susanna**, **Maria**, **Neus**, **Maribel**, **Marcelo** i **Antoni**.

In addition, I have still to thank all my **Münchner Familie**, Vielen Dank an alle. All of you made me feel like home. First of all, **Thorben**, because I know that you made a big effort permitting a biochemist assault your physicist home. Yet, we made understand each other and I learned infinite. I want to thank also my scientific guides in the north, **Niels**, **Gabriel** and **Despoina**. You helped me a lot not to fall into desperate. Y, además, pasamos también muy buenos momentos con las buenas cervezas que tenéis. I do not want to forget about the amazing office friend I met, **Zongying**, 谢谢, it was a pleasure to meet you and you become one of my best friends there too, just say that we will see each other again in China for sure. Moreover, all the amazing fellows that accompanied me so nicely during some of the toughest months of my life. Thanks **Alessandra**, **Douglas**, **Christian**, **Oliver**, **Marija**, **Lei**, **Yuan**, **Michael** and **Rebecca**.

Gràcies també, a la **Montse** i l'**Ulli**, per ser la meva família d'acollida. No em vull imaginar com hagués sigut la meva estada si no hagués estat a casa vostra. Gràcies, Danke! Grazie mille anche a te **Matteo**, per essere la persona piú iperattiva e desiderosa di vivere che io conosco. Even more knowing that we, Mediterranean people, have to struggle not to forget our southern roots in a northern country as Germany. Also thanks to you, **Lou**, for not letting your lab brothers fall apart, I am glad we met and hope we will continue seeing each other. I com no, a tu **Sergi**. Per ser la meva segona ànima, per tot el que m'has aguantat, per ser el meu oasi dins el desert de desesperació alemano-desamor-covidí. T'has convertit ràpidament, després de l'ajuda de la Tinderel·la, en una de les persones més importants de la meva vida, amb qui no tindria por de compartir-ho absolutament tot. Un nou millor amic que espero no perdre mai. Gràcies per tot, mai n'estaré prou agraït. Gràcies també a totes les altres persones que en un moment o altre vau fer que alemanya no fos tan freda i em sentís un xic més com a casa.

GRÀCIES, THANKS, VIELEN DANKE, GRACIAS

aquesta tesi també és vostra

Abstract

L-type amino acid transporters play key roles in human physiology and are involved in several human pathologies such as primary inherited aminoacidurias (Feliubadaló et al., 1999; Torrents et al., 1999), autism spectrum disease (Tărlungeanu et al., 2016) and age-related hearing loss (Espino Guarch et al., 2018) among others. However, their complete and detailed transport mechanism is still unknown as the structures solved until now are most of them in the same conformational state, open-to-in, with an exception of LAT1 bound to inhibitors that showed for the first time an inward occluded conformation (Yan et al., 2021). To decipher LATs transport mechanism we study the bacterial LAT alanine-serine-cysteine exchanger BasC as a LAT model. BasC has been already characterized (Bartoccioni et al., 2019) and 3D structurally solved in complex with the specific nanobody 74 (Errasti-Murugarren et al., 2019). The 29 nanobodies were characterised for their binding parameters, sidedness and possible conformational effect on BasC through single-molecule Fluorescence Resonance Energy Transfer (smFRET) measurements on TM1a on the cytoplasmic gate. Dynamics of this cytoplasmic gate were studied upon substrate addition. These, L-Ala and L-Ser, induced a closing of the TM1a. Moreover, nanobodies offer a powerful tool to block the substrate induced effect of closing the cytosolic gate and eventually force BasC to adopt new conformational states unsolved until now, to select this nanobodies to use in complex with BasC to solve its structure through structural techniques such as X-ray crystallography and cryogenic electro-microscopy. Finally, substrate induced closing effect was studied on lysinuric protein intolerance related variant (K154A) to study its molecular mechanism deficiency. The lack of this residue made the transporter unable to close the cytosolic gate, building the first experimental evidence of the key role of K154. Overall, we present a useful approach that can be used to study the transport mechanism of membrane proteins and the miss functions of disease related variants

Extracte

Els transportadors d'L-aminoàcids (LATs) tenen un paper important en la fisiologia humana i estan involucrats en diverses patologies com aminoacidúries primàries heretades (Feliubadaló et al., 1999; Torrents et al., 1999), l'espectre autista (Tărlungeanu et al., 2016) o la pèrdua d'oïda relacionada amb l'edat (Espino Guarch et al., 2018). Així i tot, el seu mecanisme de transport complet i en detall encara es desconeix, atès que la gran majoria d'estructures resoltes fins a l'actualitat es troben en el mateix estat obert cap a dins, amb l'única excepció de LAT1 unit a inhibidors resolt tancat per dins (Yan et al., 2021). Amb la finalitat de revelar el mecanisme de transport dels LATs ens proposem emprar com a model l'intercanviador obligat bacterià d'alanina-serina-cisteïna (BasC). Aquest intercanviador ja ha estat prèviament caracteritzat funcionalment (Bartoccioni et al., 2019) i la seva estructura es va resoldre en complex amb el nanocòs específic 74 (Errasti-Murugarren et al., 2019). Els 29 nanocossos han sigut caracteritzats pels seus paràmetres d'unió, el seu costat d'interacció amb BasC i l'efecte conformacional que efectuen sobre BasC per assajos de transferència d'energia de ressonància fluorescent per molècules individuals (smFRET) sobre el TM1a de la porta citosòlica de BasC. Els estudis de smFRET ens han permès estudiar la dinàmica de tancament de la porta citosòlica induïda per l'adició de substrats, L-Ala i L-Ser. A més, s'ha comprovat que els nanocossos poden esdevenir una eina molt útil a l'hora de bloquejar certs moviments de la proteïna i, eventualment, bloquejar el transportador en un estat conformacional diferent del ja resolt, seleccionant els nanocossos prometedors per resoldre l'estructura de BasC en complex amb ells per tècniques estructurals com la cristal·lografia de raigs X o la crio-microscòpia electrònica. Finalment, aquests efectes de tancament de la porta citosòlica induïts pels substrats van ser assajats sobre la variant relacionada amb la malaltia d'intolerància lisinúrica proteica de BasC (K154A). Aquesta variant ha resultat ser incapaç de tancar la porta citosòlica, esdevenint la primera evidència experimental sobre el rol clau d'aquest residu, K154, en el mecanisme de transport dels LATs, més concretament el tancament de la porta citosòlica. Al cap i a la fi, aquest projecte pretén presentar i posar a punt una tècnica que pot ser d'alta utilitat per estudiar el mecanisme de transport de proteïnes de membranes, així com els funcionament aberrants de les variants relacionades amb les malalties.

Contents

List of figures

Introduction

Results

Discussion

Experimental procedures

Annexes

Resum en català

List of tables

Introduction

Results

Appendix

Resum en català

Abbreviations

#

2-AIB 2-aminoisobutyric acid
2D two-dimensional
3D three-dimensional

A

A acceptor
AA amino acid
AA^+ cationic amino acid
AA^0 neutral amino acid
AAT amino acid transporter
Ab antibody
AdiC arginine:agmatine antiporter
ALEX Alternating Laser Excitation
APBS all-photon-bursts-search
APC amino acid, polyamine-organocation
Asc-1 alanine-serine-cysteine transporter 1
AU absorbance units
AV accessible volumes

B

system $b^{0,+}$ branched chain and benzenoid AAs transport system
$b^{0,+}$AT $b^{0,+}$-like amino acid transporter
BasC bacterial alanine-serine-cysteine transporter

C

C-ter C-terminal
CAT cationic amino acid transporter
CDR complementary determining regions
CHS cholesteryl hemisuccinate
Ctrl control
CMC critical micelle concentration
Cryo-EM cryogenic electron microscopy

D

D donor
DCBS dual-photon-burst-search
DDM n-Dodecyl-β-Maltoside
DG digitonin
DNA deoxyribonucleic acid
DM n-Decyl-β-D-Maltopyranoside
DMSO dimethyl sulfoxide

DTT dithiothreitol

E

E* apparent FRET efficiency
ED ectodomain
EDTA ethylthyimidine diphosphate
EL extracellular loop

F

Fab fragment antigen-binding
FRET Fluorescence resonance energy transfer
FP forward primer

G

g relative centrifuge force (RCF)
GDN glycol-diosgenin
GFP green fluorescent protein

H

HAT heterodimeric amino acid transporter
His-tag histidine tag
HS-HAT heacy subunit of HATs

I

Ig immunoglobulin
IL intracellular loop
IPTG isopropyl β-D-1-thiogalactopyranoside

K

k_a association rate
k_d dissociation rate
K_D equilibrium constant
K_m Michaelis-Menten constant

L

LAT L-type amino acid transporter
LAT1 L-type amino acid transporter 1
LAT2 L-type amino acid transporter 2
LB Luria Broth medium
LMNG lauryl maltose neopentyl glycol
LN liquid nitrogen
LPI lysinuric protein intolerance
LS-HAT light subunit of HATs

M

mAU mili-absorbance units
MD molecular dynamics
MST micro scale thermophoresis
MSP membrane scaffold protein

N

nanoDSF	nano differential scanning fluorimetry
Nb	nanobody
ND	nanodisc
NT	non-treated
Nt	nucleotide
NMR	Nuclear Magnetic Resonance

O

OD	opical density
ON	over night

P

PAGE	polyacrylamide gel electrophoresis
PBS	phosphate-buffered saline
PEG	polyethylene glycol
PCR	polymerase chain reaction
POPC	1-palmitoyl-2-oleoyl-sn-glycero-3-phosphocholine

R

R_0	Förster Radius
RCSB	Research Collaboratory for Structural Bioinformatics
RP	reverse primer
RT	room temperature

S

S*	apparent FRET stoichiometry
scFv	single-chain variable fragment
sCy3	sulfo-cyanine 3 dye
sCy5	sulfo-cyanine 5 dye
SDS	sodium dodecyl sulphate
SEC	size exclusion chromatography
SI	sequence identity
SLC	solute carrier
smFRET	single molecule FRET
SN	supernatant

T

TC transporter classification
TCDB transporter classification database
TM transmembrane segment
T_m melting temperature
TIRF total internal reflection fluorescence

V

V_{max} maximum velocity of transport

X

X-ray energetic high-frequency electromagnetic radiation
XRC x-ray crystallography

Y

y^+ system system of transport of AA^+
y^+LAT1 y^+L amino acid transporter 1
y^+LAT2 y^+L amino acid transporter 2

W

WT wild-type

Amino Acid Abbreviations

A	**Ala**	alanine
C	**Cys**	cysteine
D	**Asp**	aspartic acid
E	**Glu**	glutamic acid
F	**Phe**	phenylalanine
G	**Gly**	glycine
H	**His**	histidine
I	**Ile**	Isoleucine
K	**Lys**	lysine
L	**Leu**	leucine
M	**Met**	methionine
N	**Asn**	asparagine
P	**Pro**	proline
Q	**Gln**	glutamine
R	**Arg**	arginine
S	**Ser**	serine
T	**Thr**	threonine
V	**Val**	valine
W	**Trp**	tryptophan
Y	**Tyr**	tyrosine

Introduction

1. Evolution of life

1.1. Membranes and proteins

During the evolution of life, one of the most crucial steps was the finite compartmentalisation of the prebiotic soup. This enclosure of substrates and substances brought about a highly favourable environment for this process.

The need for communication and exchange between the inside and outside of these new prototyped cells then emerged as an intrinsic need of this fortuitous appearance of compartments. Without such communication through the barrier, then the benefits of the compartmentalisation would have been lost. Moreover, the traffic between the two sides of the membrane of these new prototyped cells had to be strictly regulated otherwise free diffusion would have rendered the compartmentalisation useless.

Later, nature came up with proteins embedded in the membranes, widely known as membrane proteins (MPs), which serve as precisely controlled valves directly at the interface, where they mediate the transport of substances through the membrane, providing this barrier with what is called selective permeability. In fact, these proteins are designed to act either passively as filters and channels, or actively as transporters.

Coming with the current concept of cells, MPs not only act as transporters or selectors of what comes in and out of a cell but they also have an additional wide range of functions (Almén et al., 2009), all of which relate to the interaction between the cell and its surroundings. This concept can be extrapolated to any compartment in a living organism. Thus, MPs can act as receptors to induce intracellular signals, enzymes that can catalyse chemical reactions from membranes, ligands for other MPs, adhesion proteins, structural proteins and transporters. In this context, this thesis focuses on the latter.

The huge diversity of MPs involved in the transport of diverse molecules into and out of the compartments and cells exert their action via the following (Lodish et al., 2000):

- **Passive diffusion**. The simplest way small substrates and molecules can cross the membrane in a concentration gradient without participation of MPs.
- **Facilitated substrate passage**. The other types of transport systems that need of MPs:
    - **Facilitated diffusion**: this transport is coupled to channels and transporters, and it works following a concentration gradient without any energy dependence.
    - **Active transport**: this transport is coupled directly to a form of energy. Transporters involved in this mode of transport can be classified as:

- **Uniporters**: a single species is transported.
- **Symporters**: two or more species are transported together in the same direction.
- **Antiporters**: two or more species are transported in opposite directions.

The proportion of MPs among the total number of proteins can be predicted using different methods, and the result varies between 15 and 39 % depending on the species analysed (Almén et al., 2009). This wide range illustrates the difficulty encountered when attempting to estimate numbers with automatic approaches and the diversity between species. In the genomes of bacteria, archaea and eukaryotic organisms, MPs account for between 20 and 30 % (Wallin and Heijne, 1998), and in the human genome around 23 % (Figure 1 A) (Uhlén et al., 2015). The importance of MPs gains relevance given that these proteins account for more than 60% of current drug targets (Figure 1 B) (Overington et al., 2006).

Over the past decades, amino acid (AA) transport functions have been studied using newly available techniques. In this regard, novel insights into AA transporters (AATs) were gained at the beginning of the XXI century with the atomic-resolution structures of some prokaryotic models of several transporters involved in the renal reabsorption of AAs. However, despite the above considerations, only a tiny fraction of the structures available in the Protein Data Bank (PDB) from the Research Collaboratory for Structural Bioinformatics (RCSB) are MPs (Almeida et al., 2017).

The first structure of a MP was solved by X-ray crystallography (XRC) in 1985, revealing the architecture of the reaction centre of purple bacterial *Rhodopseudomonas viridis* (Deisenhofer et al., 1985). Since then, the three-dimensional (3D) structures of various MPs have been characterised using several experimental methods, including Nuclear Magnetic Resonance (NMR), XRC, and cryogenic electron microscopy (Cryo-EM). A total of 193,455 protein structures are deposited in the RCSB-PDB but only 1,471 correspond to MPs (Figure 1 C), accounting for 0.75% (data retrieved from RCSB-PDB (rcsb.org) and mpstruc (blanco.biomol.uci.edu/mpstruc/) on 28 July of 2022). Over recent years, increasing research efforts have been devoted to the structures of MPs. This increased attention has been driven by the pharmacological need to find treatments for diseases directly linked to the dysfunction of a certain receptor or transporter.

The striking discrepancy between the availability of MP structures and the need for more (Figure 1) is due to the peculiarities of this class of proteins (mainly its hydrophobicity), which hinder efforts to solve their structures.

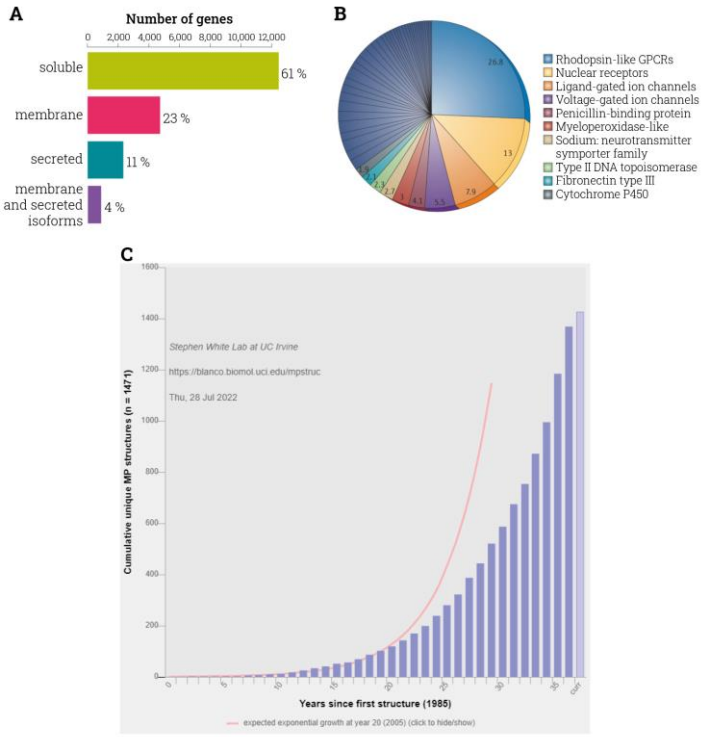

Figure 1. The discrepancy between the relevance of membrane protein and the number of their structures. A. Number and fraction of all human genes classified in the categories of soluble, membrane-spanning, and secreted, as well as genes with isoforms belonging to two or all three categories (Uhlén et al., 2015). **B.** Gene-family percentage distribution of FDA-approved drug targets (Overington et al., 2006) **C.** Progress of MP structure determination per year (blue bars) and its original expected growth (red line). Data obtained from the RCSB-PDB (rcsb.org) and mpstruc (blanco.biomol.uci.edu/mpstruc/) on 28 July 2022.

The discrepancy between the relevance of MPs and the low number of structures found in the literature can be explained by two major factors (Almeida et al., 2017):

Complications in both expression and purification processes.
Challenges associated with the current determination of the 3D structure of purified MPs.

The first MP structures were recovered from their natural source, namely bacteria, which offer a high natural yield (Vinothkumar and Henderson, 2010). Another major group of structures come from recombinant bacterial expression (proteins overexpressed in other host cells). However, the current challenges focus on the overproduction of mammalian and human proteins, which are much more intricate to express and purify since, for example, large-scale culture of mammalian cells is not as straightforward as for bacterial cells, and post-transcriptional and post-translational modifications make the process very delicate (Almeida et al., 2017). Thus, the study of bacterial homologues is a widely used approach when studying structures and transport mechanisms of eukaryotic MPs.

1.2. The importance of amino acids

Another crucial step in evolution was the synthesis of the enclosed substrates, metabolic substances, and the corresponding transporters. Amino acids (AAs) are their basis. In this regard, AAs are critical to life and have a variety of roles in metabolism. A particularly important function is that they serve as the building blocks of proteins, which are formed by linear chains of AAs. Furthermore, AAs are also important in many other biological molecules, forming form part of coenzymes and serving as precursors for the biosynthesis of many relevant molecules.

In the metabolism of all types of organisms, AAs play central roles and are essential for the regulation of homeostasis (Bröer and Bröer, 2017). It has been described that, for mammals, approximately half the proteogenic AAs are essential. Thus, this means that we need take them up from the diet, since we cannot synthesise them ourselves.

Furthermore, protein accounts for up to 30% of the typical western diet (Bröer, 2008). During digestion, protein is broken down into peptides, and individual AAs are then efficiently absorbed by the enterocytes of the small intestine (Adibi et al., 1967). These molecules are then transported through the blood to all tissues, and, consequently, to all cells. Moreover, in the kidney, plasma AAs are filtered and subsequently reabsorbed to avoid wastage.

Studies performed in the '50s and '60s revealed that peptides and AAs are actively absorbed in the intestine. The proximal jejunum is the major site of absorption of these valuable metabolites, but other parts of the small intestine also have significant transport capacity (Silk et al., 1985; Mariotti et al., 2000). In the kidney nephron, the proximal tubule is the major site of nutrient reabsorption. About 95–99% of all AAs are reabsorbed in the proximal convoluted tubule and to a lesser extent in the proximal straight tubule (Young and Freedman, 1971; Silbernagl et al., 1975; Silbernagl, 1979, 1988).

Based on multiple functional studies in kidney and intestine and the AA profile of the urine of individuals with distinct types of aminoaciduria, five

transport activities were proposed (Milne, 1964; Young and Freedman, 1971; Bröer, 2008):

i. **The "neutral system", "methionine preferring system" or "monoamino-monocarboxylic system"**, which transports all neutral AAs (AA^0); Ala, Ser, Thr, Val, Leu, Ile, Phe, Tyr, Trp, Asp, Glu, His, Cys, Met and citrulline.
ii. **The "basic system"**, which transports cationic AAs (AA^+); Lys, Arg and ornithine) plus cystine.
iii. **The "acidic system"**, which transports Glu and Asp.
iv. **The "iminoglycine system"**, which transports Pro, hydroxyproline, and Gly.
v. **The "β-amino acid system"**, which transports β-AA plus taurine.

AA transport activities are frequently referred to as systems; the term indicates a functionally identified transport activity that appears to be similar in a variety of cell types. Thus, it is a way to classify the transporters based on their specificity and thermodynamic properties. After pioneering studies by Halvor Christensen in non-epithelial cells (Christensen, 1984, 1990), it was recognised that AA transport systems accept groups of AA rather than individual molecules. Christensen's work (Oxender and Christensen, 1963) established the presence of AA^0 transporters that have a preference for the following: Leu and other large hydrophobic AA^0 (system L); Ala and other small and polar AA^0 (system A); and Ala, Ser, and Cys (system ASC). A separate nomenclature (x for anionic, y for cationic) has been applied to systems mediating the transport of AA^+ (system y^+) and anionic AAs (system X^-_{AG}). System $b^{0,+}$ is used to transporter with specificities to branched chain and benzenoid AAs. These AA transport systems have subsequently been identified in many cell types and confirmed by molecular cloning of the mediators of these transport activities (Palacín et al., 1998a).

Our laboratory has devoted more than 30 years to research into amino acid transport, specifically into the members of the L-type amino acid transporter (LATs) subfamily. Our studies have addressed the molecular cloning, physiological and pathological aspects of this transport of AAs (Palacín et al., 1998b; Palacín and Kanai, 2004; Palacín et al., 2005; Bröer and Palacín, 2011; Fotiadis et al., 2013; Bartoccioni et al., 2019), as well as the structure of the LATs (Fort et al., 2007; Ilgü et al., 2016; Errasti-Murugarren et al., 2019; Rodriguez et al., 2021).

1.3. Transporters classification

As mentioned at the start of this section, the primordial prokaryotic cell probably had few transporters, and these served for the essential functions without which cells could not survive. Due to gene duplication and divergence, as well as speciation, these early transporters developed into our current, large, ubiquitous superfamilies of transporters.

The importance of identifying and classifying protein families is emphasised by the fact that structural, functional and mechanistic data for transporters

can be extrapolated from one protein to another when—and only when—they have been shown to be related to a common descendent (Lam et al., 2011).

There are different ways to classify proteins. For transporters, there are different classification systems that facilitate the communication between researchers. We will be referring along this thesis to the Transporter Classification (TC) and the solute carrier (SLC) systems.

The solute carrier system was originally developed as a collaboration between the HUGO Gene Nomenclature Committee (http://www.genenames. .org/) and the SLC tables (https://www.bioparadigms.org/slc/intro.htm). Currently, there are more than 450 SLC members (genes and pseudogenes) divided into 71 SLC families (Dvorak et al., 2021). We must consider that of all the identified genes in humans, it is estimated that a 10-30 % are still orphans, genes lacking characterised function or detectable similarity to other genes (Wissler et al., 2013). SLC system classifies transporters by their similarity of sequence.

In this regard, has provided a huge amount of information about the evolutionary history of numerous permease families (Saier et al., 1994; Saier, 2000). This is how the Transporter Classification system was born from a multi-organism perspective, analogous to the Enzyme Commission system. TC classifies transporters not only by their functional role, but also by their phylogeny information, and it can be accessed in the Transporter Classification Data Base (TCDB) (www.tcdb.org). This system considers five criteria:

vi. Transporter class (i.e., channel, transporter, primary active transporter or group translocator)
vii. Transporter subclass (in the case of primary active transporters refer to the energy source used to drive transport)
viii. Family or superfamily
ix. Subfamily
x. Substrate or range of substrates recognised and transported.

Sequenced homologues of unknown function can be present in the TC system unless they are unique or from an unrepresented organismal kingdom. Moreover, TC has been adopted by the International Union of Biochemistry and Molecular Biology (IUBMB) (Saier et al., 2016).

It is important to bear in mind that these two classification systems are independent one from the other as they take into account different classification criteria of different transporters throughout organisms. Nevertheless, their classifications are very similar and it might be confusing.

1.3.1. Amino acid / polyamine / organocation superfamily

Initially described by Jack and co-workers in 2000, the APC superfamily is one of the largest superfamilies in the TCDB (Jack et al., 2000). Initially three families appeared to be related to each other constituting this superfamily, they were the amino acid, polyamine-organocation (APC), amino acid/auxin permease (AAAP) and hydroxyl/aromatic amino acid permease (HAAAP) families (Saier, 2000). Currently, the APC superfamily englobes 18 families (Table 1) found in bacteria, archaea, yeast, fungi, unicellular eukaryotic protists, slime moulds, plants and animals. Sequence analyses revealed that most of the members of the APC superfamily had 12 transmembrane spanners (TMs). Nevertheless, some members deviate from this pattern, presenting either 10, 11 or 14 TMs (Jack et al., 2000).

Although it was believed that all APC superfamily members transported AAs and their derivatives, the extent of this transport was later revealed to be much greater than expected. Of the five original families (APC, AAAP, Ala or Glycine:Cation Symporter (AGCS), Cation-Chloride Cotransporter (CCC) and HAAAP families), four are specific for AAs and their derivatives, while the rest transport a wide range of solutes and exhibit sufficiently similar folds to suggest a common evolutionary origin.

Presently, the TC encloses 18 families of the APC superfamily (Table 1). New families are continually being added to this already populated superfamily. Regarding the SLC system, the APC superfamily comprises SLC6, SLC7, SLC32, SLC36 and SLC38 families (Kandasamy et al., 2018).

The size of the APC superfamily is surpassed only by the Major Facilitator Superfamily (MFS) (Reddy et al., 2012; Wong et al., 2012). Both superfamilies appear to have arisen from a common ancestor of two TMs hairpin structure (i.e., alpha helical hairpin) (Figure 2. A). Wong and co-work proposed two pathways for the origin of the APC superfamily members from this common ancestor (Figure 2. B). Reddy and co-work coincide with their proposal as to how this double hairpin underwent intragenic triplication, followed by the loss of a TM in the APC superfamily ending up with a common five TMs repeat unit. A characteristic fold of these families, including LAT subfamily, widely known as the LeuT fold or APC fold, which is further, explained in detail in Introduction 2.2. Structural Studies of LATs.

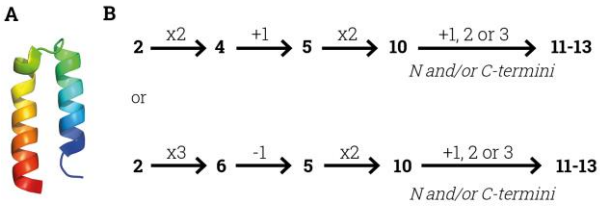

Figure 2. The origin of the APC superfamily. A. Schematic representation of a 2-TMs harping structure as the thought common ancestor of the APC and MSF superfamilies (PDB ID 1EI0, alpha helical hairpin of P8MTCP1). **B.** Sequentially modifications of the TMs of the common ancestor during evolution to become finally the currently known APC transporters. The numbers indicate the TMs (Adapted from Wong et al., 2012).

The APC Superfamily	
TC No.	**Family**
2.A.3	**Amino Acid-Polyamine-Organocation (APC)**
2.A.15	Betaine/Carnitine/Choline Transporter (**BCCT**)
2.A.18	**Amino Acid/Auxin Permease (AAAP)**
2.A.21	Solute:Sodium Symporter (**SSS**)
2.A.22	Neurotransmitter:Sodium Symporter (**NSS**)
2.A.25	**Alanine or Glycine:Cation Symporter (AGCS)**
2.A.26	Branched Chain Amino Acid:Cation Symporter (**LIVCS**)
2.A.30	**Cation-Chloride Cotransporter (CCC)**
2.A.31	Anion Exchanger (**AE**)
2.A.39	Nucleobase:Cation Symporter-1 (**NCS1**)
2.A.40	Nucleobase/Ascorbate Transporter (**NAT**) or Nucleobase:Cation Symporter-2 (**NCS2**)
2.A.42	**Hydroxy/Aromatic Amino Acid Permease (HAAAP)**
2.A.46	Benzoate:H+ Symporter (**BenE**)
2.A.53	Sulfate Permease (**SulP**)
2.A.55	Metal Ion (Mn^{2+}-iron) Transporter (**Nramp**)
2.A.72	K^+ Uptake Permease (**KUP**)
2.A.114	Putative Peptide Transporter Carbon Starvation CstA (**CstA**)
2.A.120	Putative Amino Acid Permease (**PAAP**)

Table 1. The APC superfamily. List of all families comprising the APC superfamily (data retrieved from the TCDB (www.tcdb.org) on 28 July 2022). The five original families that form the APC superfamily have their TC No. highlighted in purple.

1.3.2. The Amino acid-Polyamine-Organocation (APC) family

The APC family is comprised by transporters that function as solute:cation symporters and solute:solute antiporters (Jack et al., 2000), and their substrate specificities range from exceptionally broad to just one or a few AAs or related compounds (Brechtel and King, 1998; Hu and King, 1998; Sato et al., 1999).

The APC family		
TCDB id	**Subfamily**	**Members**
2.A.3.1	Amino Acid Transporter (**AAT**)	24
2.A.3.2	Basic Amino Acid/Polyamine Antiporter (**APA**)	11
2.A.3.3	**Cationic Amino Acid Transporter (CAT)**	24
2.A.3.4	Amino Acid/Choline Transporter (**ACT**)	7
2.A.3.5	Ethanolamine Transporter (**EAT**)	2
2.A.3.6	Archaeal/Bacterial Transporter (**ABT**)	5
2.A.3.7	Glutamate:GABA Antiporter (**GGA**)	7
2.A.3.8	**The L-type Amino Acid Transporter (LAT)**	32
2.A.3.9	Spore Germination Protein (**SGP**)	5
2.A.3.10	Yeast Amino Acid Transporter (**YAT**)	28
2.A.3.11	Aspartate/Glutamate Transporter (**AGT**)	1
2.A.3.12	Polyamine:H^+ Symporter (**PHS**)	5
2.A.3.13	Amino Acid Efflux (**AAE**)	3
2.A.3.14	Unknown APC-1 (**U-APC1**)	3
2.A.3.15	Unknown APC-2 (**U-APC2**)	5

Table 2. The APC family. Complete list of current transporters subfamilies in the APC family (data retrieved from the TCDB (www.tcdb.org) on 28 July 2022). CAT and LAT subfamilies have their TC No. highlighted in purple.

The APC family from the TC system comprises the SLC7 family (also known as cationic amino acid transporter/glycoprotein-associated family), that at his side comprises two of the APC subfamilies, namely the L-type amino acid transporter (LAT) and cationic amino acid transporter (CAT) subfamilies from the TC system, very tight related between them (Figure 3). On the one hand, ten members of the SLC7 belong to the LAT subfamily (from SLC7A5 to SLC7A13 and SLCA15). On the other hand, five other members belong to the CAT subfamily (SLC7A1 to SLC7A4 and SLC7A14). CATs transport essentially AA^+ by facilitated diffusion with differential trans-stimulation by intracellular substrates (system y^+). However, SLC7A4 and SLC7A14 are not fully characterized. CATs show on average < 25 % sequence identity (SI) to the LATs, they present 14 putative TMs, and they are glycosylated. In contrast, LATs present

12 TMs, they are not glycosylated, and they need to associate with a glycoprotein of the SLC3 family for cell surface expression (Feliubadaló et al., 1999; Verrey et al., 2004; Fotiadis et al., 2013). CATs are found in bacteria and eukarya kingdoms, but not in archaea, while LATs are present in eukarya, in both fungi and animals, but not in plants (Jack et al., 2000).

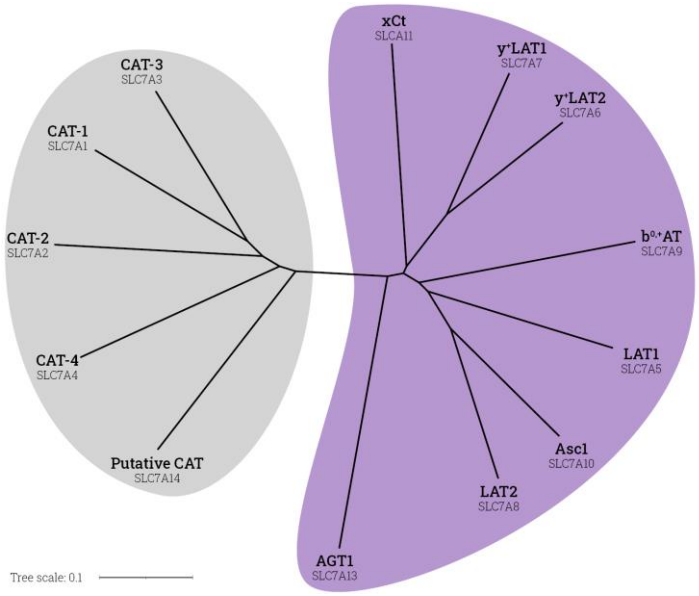

Figure 3. Phylogenetic relationships within the SLC7 family. Human members of the SLC7 family. CATs and LATs are shown in grey and purple, respectively. SLC7A4 and SLC7A14 are orphan transporters, their function are not fully characterised yet. Tree build using SLC gene mRNA sequences alignment. SLC7A12 and SLC7A15P are pseudogenes not expressed in humans, and both have been excluded from this phylogenetic representation.

1.3.3. The L-type amino acid transporter (LAT) subfamily

Members of the LAT subfamily from the TC are detailed in Table 3, where hLATs are also listed. LAT subfamily members are found in all domains as exposed below.

TCDB id	Member	Domain	Kingdom/Phylum	Specie
2.A.3.8.1	**LAT1** L-type AA^0 transporter	Euk.	Metazoan	*R.norvegicus*
2.A.3.8.2	**ASUR4** L-type AA^0 transporter			*X.laevis*
2.A.3.8.3	**SPRM1lc** schistosome AA^0 + AA^+ transporter			*S.mansoni*
2.A.3.8.4	**MUP1** L-methionine transporter		Fungi	*S.cerevisiae*
2.A.3.8.5	**xCT** Cystine/Glu antiporter		Metazoan	*M.musculus*
2.A.3.8.6	**LAT2** L-type AA^0 transporter			*R.norvegicus*
2.A.3.8.7	**y⁺LAT1** y^+L AAT 1			
2.A.3.8.8	**AGT1** Asp/Glu Na^+-independent transporter			*M.musculus*
2.A.3.8.9	**AAT1** Heteromeric AAT 1			*C.elegans*
2.A.3.8.10	**AAT-9** Aromatic AA exchanger			
2.A.3.8.11	**ArpAT** The aromatic-preferring AAT			*M.musculus*
2.A.3.8.12	**SteT** The Ser/Thr exchange transporter	Bac.	Firmicutes	*B.subtilis*
2.A.3.8.13	**Asc-1** The -type small neutral D- and L-$AA:H^+$ symport transporter-1	Euk.	Metazoan	*M.musculus*
2.A.3.8.14	**Asc-2** The Asc-type small neutral L-$AA:H^+$ symport transporter-2			
2.A.3.8.15	**$b^{0,+}$** The $b^{0,+}$ AA (cystine) transporter			*R.norvegicus*
2.A.3.8.16	**MUP3** Low-affinity methionine permease, MUP3		Fungi	*S.cerevisiae*
2.A.3.8.17	**FrlA** Putative fructoselysine transporter	Bac.	Proteobacteria	*E.coli*
2.A.3.8.18	**xCT** (SLC7A11) Cystine/Glu antiporter	Euk.	Metazoan	*H.sapiens*
2.A.3.8.19	**$b^{0,+}$AT** (SLC7A9) $b^{0,+}$-type AAT 1			
2.A.3.8.20	**LAT2** (SLC7A8) Large AA^0 transporter small subunit 2			
2.A.3.8.21	**Asc-1** / SLC7A10 Asc-type AAT 1			
2.A.3.8.22	**y⁺LAT1** (SLC7A7) y^+L AAT 1 (Monocyte AA permease 2)			
2.A.3.8.23	**y⁺LAT2** (SLC7A6) y^+L type AAT 2			
2.A.3.8.24	**AGT-1** (SLC7A13) Sodium-independent Asp/Glu transporter 1 (X-AAT 2)			
2.A.3.8.25	**LAT1** (SLC7A5) Large AA^0 transporter small subunit 1			
2.A.3.8.26	Uncharacterised transporter	Bac.	Actinobacteria	*S.coelicolor*
2.A.3.8.27	**AAT-6** amino acid transporter 6	Euk.	Metazoan	*C.elegans*
2.A.3.8.28	**SteT** Ser/Thr exchanger	Bac.	Bacteriodetes/Chlorobi group	*C.lonarensis*
2.A.3.8.29	**y⁺LAT1** AA^+ transporter	Euk.	Metazoan	*D.rerio*
2.A.3.8.30	Putative AAT	Arch.	Crenarchaeota	*S.islandica*
2.A.3.8.31	Putative polyamine transporter	Bac.	Tenericutes	*M.florum*
2.A.3.8.32	Large AA^0 transporter, CD98lc (LAT), of 442 AAs.	Euk.	Metazoan	*D.melanogaster*

Table 3. The LAT subfamily. Domains abbreviations Euk., Bac. and Arch. refer to Eukarya, Bacteria and Archean, respectively. Human LATs are referred also by their SLC (between

brackets) and their TCDBid is highlighted in bold purple. Data retrieved from the Transporters Classification Database (www.tcdb.org) on 25 May 2021.

The Bacterial alanine-serine-cysteine exchanger (BasC) is expressed in *Carnobacterium sp. AT7*. It was identified as the best suitable prokaryotic candidate for structure-function analysis of LATs transporters after BLAST analysis on the hLAT1 sequence (default settings (AltschuP et al., 1990)). BasC shows between 25 to 30 % sequence identity (SI) with the human LATs (Bartoccioni et al., 2019). Moreover, it allows a high yield of purified protein and shows high stability and a monodisperse behaviour in detergents (DDM and DM).

A wider phylogenetic study of the APC family of transporters, sequence comparisons, and the constructed phylogenetic tree indicates that BasC is clustered with all the members of the LAT subfamily (Figure 4). Furthermore, BasC also shows extremely similar functional features to those of LAT subfamily members. Thus, BasC is a suitable model with which to study the structure and mechanisms of transport of LATs.

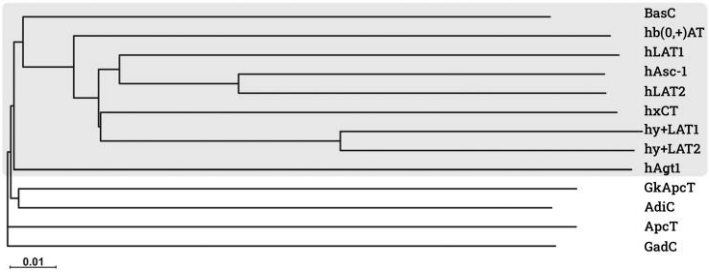

Figure 4. Phylogenetic relationships of BasC with other members of the APC family. The neighbour-joining tree shows the phylogenetic relationships of BasC with members of the human LAT subfamily and the most relevant prokaryotic homologues. The tree was build using the sequences available in the TCDB (www.tcdb.org) (Bartoccioni et al., 2019).

2. Heteromeric amino acid transporters

Heteromeric amino acid transporters (HATs) belong to the collectively known Heteromeric Solute Carrier Superfamily (Saier et al., 2016). The general features of HATs are described below (Verrey et al., 1999; Jack et al., 2000; Verrey et al., 2000, 2004; Palacín and Kanai, 2004; Fotiadis et al., 2013; Scalise et al., 2018; Fairweather et al., 2020; Nicolàs-Aragó et al., 2021; Fort et al., 2021; Rullo-Tubau et al., 2022).

HATs are heteromeric transporters formed by two independently encoded cistrons, which are two subunits bound by a disulphide bridge (Figure 5) (Palacín et al., 2005; Fort et al., 2007). These two subunits are:

- **Light subunit (LS-HAT)**: MPs of 12 TMs that actually have the solute exchange activity of the HATs. LS-HAT are the human LATs (hLATs) belonging to the SLC7 family, from here on LS-HATS will be referred as hLATs.
- **Heavy subunit (HS-HAT)**: a membrane single-pass protein, which interaction with its hLAT permits the localisation the whole HAT into the cell surface (Bartoccioni et al., 2008; Feliubadaló et al., 1999; Mastroberardino et al., 1998; Verrey et al., 2000). HS-HAT members belong to the SLC3 family.

HS-HATs consist of two members of the SLC3 family, namely rBAT (SLC3A1) and 4F2hc (SLC3A2, CD98 or FRP1) (Ohgimoto et al., 1995; Fort et al., 2007). They were described as SLC transporter genes as these HS-HAT were initially thought to have the AA transport activity (Wells et al., 1992). However, the unlikelihood of a single TM-containing protein having this sort of activity was recognised immediately (Palacín, 1994). rBAT and 4F2hc share ~30 % SI and have a molecular mass of ~90 and ~80 kDa, respectively. They are type II membrane N-glycoproteins with a single TM (TM domain), an intracellular N-terminal (N-ter) domain, and an extracellular C-terminal (C-ter) region, the ectodomain (ED) that is homologous to insect and bacterial α-amylases (Figure 5) (Fort et al., 2021). This ED is composed of a $(\beta\alpha)_8$ barrel and an antiparallel β_8 sandwich. The first structure of an SLC3 family member was obtained by XRC in 2007 (Fort et al., 2007). In this regard, this molecule did not show any key catalytic residues and, therefore, no catalytic activity. The conserved Cys residue responsible for the intersubunit disulphide bridge is located between the TM and ED (Figure 5). Members of the SLC3 family appear to be present throughout the animal kingdom (e.g., Metazoan). For example, mammalian rBAT (human, rat, mouse, rabbit, dog, and American opossum) share 69–80 % SI, and vertebrate's 4F2hc (human, rat, mouse, Chinese hamster, zebrafish, and sea lamprey) share 31–77 % SI. Moreover, three hypothetical proteins from *Caenorhabditis elegans* and *Drosophila melanogaster* show homology with vertebrate SLC3 members (~25 % SI).

Ten hLATs are currently known (from SLC7A5 to SLC7A15). Of these ten hLATs, six are partnered with 4F2hc (LAT1, LAT2, y$^+$LAT1, y$^+$LAT2, Asc-1, and xCT); two form the heterodimer with rBAT ($b^{0,+}$AT and AGT-1); and the last two (Asc-2 and

arpAT) interact with as yet unknown heavy subunits (Fernández et al., 2005) (Table 4). The elimination of the disulphide bridge reduces but does not abolish the expression of the heterodimer in the cell plasma membrane. This observation thus points to other non-covalent interactions between the two (Estévez et al., 1998; Pfeiffer et al., 1998).

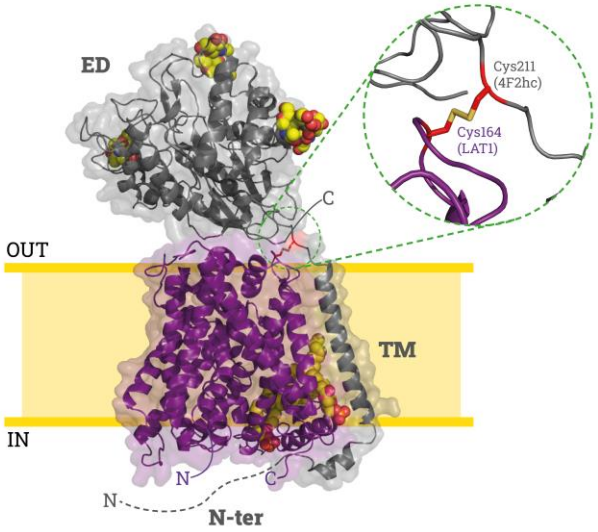

Figure 5. HAT structure and domains. LAT1-4F2hc (PDB ID: 6IRS) structure embedded schematically into a lipid bilayer. LS-HAT (LAT) is shown in purple and HS-HAT in grey and its N-ter domain, transmembrane domain (TM) and ectodomain (ED) are labelled. Glycosylation positions in HS-HAT and lipids in LS-HAT are shown in spheres. Zoom in shows in detail the disulphide bridge between HAT subunits. Adapted from (Fort et al., 2021), created with Open-Source PyMol (The PyMOL Molecular Graphics System, Version 2.0 Schrödinger, LLC.).

HATs activities are tightly coupled with AA exchange, with the exception of 4F2hc-Asc-1, which can function as an uniporter, although its preferred transport mode is as an AA exchange (Fukasawa et al., 2000; Pineda et al., 2004) (Table 4). Some of these transporters show asymmetric ion dependence and vary in their relative affinity for distinct types of AAs at extracellular and intracellular sides (Napolitano et al., 2017; Scalise et al., 2018; Rodriguez et al., 2021). As an example, LAT1 and LAT2 display much lower intracellular apparent affinities (milimolar range) than the extracellular ones (micromolar range). This sidedness would suggest and highlight a main role involved in the AA uptake (Meier et al., 2002).

The substrate selectivity of HATs ranges from large AA^0 (system L) to small AA^0 (Ala, Ser, Cys-preferring, system Asc), negatively charged AAs (system x_c^-) and AA^+ plus AA^0 (system y^+L and $b^{0,+}$-like) (Nicolàs-Aragó et al., 2021; Rullo-Tubau et al., 2022).

SLC name	Translocator protein	Ancillary gene	Ancillary protein	Substrate stoichiometry	Transport mode
SLC7A9	$b^{0,+}AT$	SLC3A1	rBAT	Cystine, L-AA^+ (EC):L-AA^0(IC)	E, 1:1
SLC7A13	AGT1			Cystine, L-Asp, L-Glu	E, 1:1
SLC7A5	LAT1	SLC3A2	4F2hc, CD98	Large L-AA^0, L-DOPA, BCH, T_3, T_4, gabapentin, diverse AA analogues	E, 1:1
SLC7A8	LAT2			L-AA^0, L-DOPA, BCH, T_3, T_4	E, 1:1
SLC7A7	y^+LAT1			L-AA^0/Na^+ (EC):LAA^+ (IC)	E, 1:1
SLC7A6	y^+LAT2			L-AA^0/Na^+ (EC):LAA^+ (IC)	E, 1:1
SLC7A10	Asc-1			Small L- and D-AA^0, β-Ala, α-aminobutirate	E, 1:1, U
SLC7A11	xCT			Anionic Cystine (EC):L.Glu (IC)	E, 1:1
SLC7A12	(pseudogene) Asc-2	unknown	unknown	Small L-AA^0	Unknown
SLC7A15P	(pseudogene) ArpAT	unknown	unknown	L-Tyr, L-DOPA, AA^0, L-Arg, Cystine	E, 1:1

Table 4. Overview of HATs: classification, physiology and expression. Each subunit is defined by its SLC gene name and protein name. Substrate stoichiometry expressed for the extracellular (EC) and intracellular (IC) sides. Mode of transport as exchanger (E) or uniporter (U). SLC7A12, SLC7A14 and SLC7A15P are yet infrastudied, silenced genes or non-functional protein. Adapted from (Fairweather et al., 2020) and SLC tables (www-slc.bio-paradigms.org).

2.1. HATs and human pathologies

Several human pathologies highlight the physiological roles of HATs. Two transporters of this family are responsible for inherited aminoacidurias. Mutations in either of the two genes coding for the subunits of system $b^{(0,+)}$ (rBAT and $b^{(0,+)}$AT) lead to cystinuria (MIM 220100) (Calonge et al., 1994; Feliubadaló et al., 1999), while mutations in y^+LAT1 (a 4F2hc associated system y^+L) result in lysinuric protein intolerance (LPI, MIM 222700) (Borsani et al., 1999; Torrents et al., 1999).

In addition, mutations in LAT1 are associated with autism spectrum disorder and motor delay in humans (Tărlungeanu et al., 2016), while low levels of this protein in brain capillaries is linked to the development of Parkinson's disease (Ohtsuki et al., 2010). Mutations in LAT2 are associated with age-related hearing loss (Espino Guarch et al., 2018) and cataracts (Knöpfel et al., 2019).

Asc-1/4F2hc is a druggable target in schizophrenia as it is the major D-Ser transporter in brain, where it acts as a co-agonist of N-methyl-D-aspartate and Glu receptors (Sakimura et al., 2016).

Moreover, xCT and LAT1 are overexpressed in many human tumours, as the 4F2hc; thereby suggesting that these transporters are essential or give metabolic advantage for tumour cell survival and progression (del Amo et al., 2008;

Lo et al., 2008; Savaskan and Eyüpoglu, 2010). In this regard, two anticancer therapies involving both xCT and LAT1 have been proposed. On the one hand, these transporters mediate the uptake of several AA-derived anticancer drugs. This observation thus suggests that these proteins are involved in the cellular uptake of these antineoplastic pharmaceuticals. On the other hand, a new strategy based on the inhibition of xCT and LAT1 activities has been described (Chung et al., 2005; del Amo et al., 2008; Lo et al., 2008; Savaskan and Eyüpoglu, 2010), thus reducing tumour proliferation and progression. Targeting AAT in cancer is conceptually new since specific inhibitors are scarce. In parallel, 4F2hc has also been seen to overexpress in tumours, suggesting an independent role from the hLATs; silencers of this HS-HAT were found to suppress cellular growth (Maimaiti et al., 2021). In this regard, the development of drugs with greater activity against these MPs is expected to challenge the current scenario.

Ongoing research is starting to reveal that LATs are involved in several other diseases. In this regard, LAT1 participates in rheumatoid arthritis (Owada et al., 2022) and lupus erythematosus (Tian et al., 2022), and xCT and Asc-1 in diabetes (Jersin et al., 2021; Maschalidi et al., 2022).

The involvement of LATs in diverse diseases highlights the importance of studying these transporters and their structure-function relation in order to understand better their function in humans and the diseases associated with them.

2.1.1. Lysinuric Protein Intolerance

Lysinuric protein intolerance (LPI) was first diagnosed in 1965 in Finnish patients under the name of "protein intolerance with deficient transport of basic AAs" (Perheentupa and Visakorpi, 1965). The inherited loss-of-function in y^+LAT1 (SLC7A7) causes this very rare, autosomal-recessive disorder (Borsani et al., 1999; Torrents et al., 1999). To date, no mutations have been described in 4F2hc (SLC3A2) (Mauhin et al., 2017), suggesting embryonic lethality as in the constitutional knockout mouse (Tsumura et al., 2003). The ancillary role of 4F2hc for six SLC7 transporters (LAT1, XCT, LAT2, Asc-1, y^+LAT2 and y^+LAT1) it is thought to be at the basis of this lethality (Fotiadis et al., 2013).

Defective AA^+ transport (Lys, Arg and ornithine) through y^+LAT1 in the epithelial cells of the renal tubules and small intestine results in a decreased concentration of circulating cationic AAs (CAAs). This deficiency in urea cycle intermediates causes hyperammonemia, the main metabolic alteration in LPI, which results in encephalopathy, among many other complications of this disease (Mykkänen et al., 2000; Zhang and Cao, 2017). The haematological and immune-related complications of LPI opens the question of whether defective y^+LAT1 activity in immune cells underlie these complications (Bodoy et al., 2019; Giroud-Gerbetant et al., 2021).

Currently, 59 different mutations in the SLC7A7 gene have been identified to cause LPI in more than 181 individuals from 120 independent families (Fairweather et al., 2020) documented in Finland, Japan, Turkey, Italy, Spain and Maghreb (Mauhin et al., 2017). In y+LAT1, K191E is a mutation reported to cause LPI (Sperandeo et al., 2008). This Lys residue is fully conserved in LATs' TM5 and is relevant regarding its key location on the reminiscences of the sodium-binding site 2 (Na2) of the sodium symporters of the APC superfamily (detailed explained further in this introduction, Introduction 2.4. Mechanism of transport). This thesis is focused on the cytosolic dynamics of BasC studying the relevance of the homologous Lys K154 through the LPI-related BasC variant K154A. Our research group has channelled huge effort into structural and functional studies of HATs and mouse models of LPI in order to unravel the mechanisms of this pathology (Bodoy et al., 2019; Giroud-Gerbetant et al., 2021).

2.2. Structures of APC fold transporters

As explained above, multiple human diseases are related to HATs, where LATs play key roles in these conditions. Thus, the atomic structures of plasma membrane transporter proteins emerge as one of the most powerful tools through which to study substrate binding and translocation mechanisms, and to design more specific and active therapeutic molecules (Morth et al., 2009).

Before the first LATs structures were solved in 2019, the only known structures were from some bacterial LAT homologues from other members of the APC superfamily. Indeed, the structure of LeuT was the first to be solved (Yamashita et al., 2005). This Leu transporter belongs to the NSS family (Table 1), and has an average of ~9 % SI with LATs. Nevertheless, LeuT has received considerable attention because the two subfamilies share the same folding of 12 TMs.

This shared tertiary structure between the SLC7 members was initially named LeuT fold, as it was described for the first time in LeuT. This common structural composition is based on an inverted repeat fold of five TMs (5+5 inverted repeat fold). Of note, this 5+5 repetition is characteristic of all transporters of the APC superfamily, being currently known as APC fold. Therefore, each repetition fold can be superimposed by inverting and overlaying them by rotation of a pseudo two-fold axis of symmetry within the plane of the membrane (Figure 6 A-B) (Bai et al., 2017; Navratna and Gouaux, 2019). This repetition, or rather pseudo-symmetry, is based on repetitions from TM1 to 5 and from TM6 to 10, and there are two TMs, helices 11 and 12, not included in the repetition core.

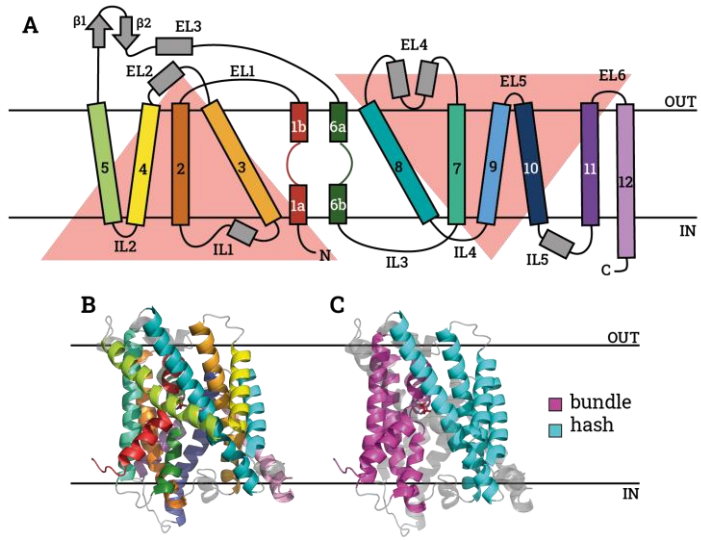

Figure 6. APC fold. Black horizontal lines symbolise the lipid bilayer. **A.** APC fold scheme. Red triangles show the two halves of the pseudo-symmetry of TMs. The first repetition comprises from TM1 to 5, and the second, from TM6 to 10. TM11 and 12 are not involved in this symmetry. Note how the truncated helices TM1 and TM6 build an unwound region. Internal and external loops are named and numbered as IL and EL, respectively. Two β-sheets were described between TM5 and TM6 (EL3) in LeuT (adapted from Yamashita et al., 2005). **B-C.** BasC structure (PDB ID: 6F2W) in B coloured in chainbow as in A with grey loops, and in C coloured by bundle and hash subdomains in pink and cyan, respectively. Not involved TMs in the subdomains are shown in transparent grey in C. Structures drawn with Open-Source PyMol (The PyMOL Molecular Graphics System, Version 2.0 Schrödinger, LLC), following same TM colouring as in (A) from Yamashita et al., 2005.

Also two common subdomains were described for the APC fold (Shi et al., 2008; Fairweather et al., 2020), namely the bundle, made up of the first two helices of each repeat motif (TM1, 2, 6 and 7) and the hash, formed by the third and fourth helices in each inverted repeat (TM3, 4, 8 and 9) (Figure 6. C). Moreover, TMs 1 and 6 present a non α-helix structured segment, the unwound region that divides each TM into two, TM1 into TM1a and TM1b, and TM6 into TM6a and TM6b. The unwound region permits the bundle subdomain to bends through it, and creates the cavity that is key for the binding of solutes to be transported and competitive inhibitors too through their α-amino carboxyl moiety. The hash domain would work more as scaffold, as described by Pentmatsa and Goaux in 2014, while the bundle domain would be the one that would alternate the access to the substrate cavity by tilting around the hash. Helices 5 and 10 are considered apart of these conserved sub-domains and are

referred to as the 'arms' (Shimamura et al., 2010; Krishnamurthy and Gouaux, 2012; Penmatsa and Gouaux, 2014).

Another structure insight shared with all APC transporters is their substrate vestibules also described with the first LeuT structure (Yamashita et al., 2005), namely the substrate-binding site 1 (S1) and 2 (S2). The former and previously described is located in the unwound region. The latter, was firstly described for ion symporters when they were solved bound to different inhibitors found in this S2 (Singh et al., 2008, 2007; Quick et al., 2009; Coleman and Gouaux, 2018; Coleman et al., 2019). In these symporters (e.g., LeuT, MhsT, SERT…), the S2 is located halfway between the extracellular gate and the S1. Other shared binding sites are the sodium-binding sites for the sodium symporters, namely Na1 and Na2. Na2 is highly conserved among APC fold transporters. Both sodium-binding sites play a key role in the transport mechanism, detailed below (Introduction 2.4. Mechanism of Transport), where the involved TMs, substrate-binding sites and ion-binding sites are described.

APC fold structures conformational states in this thesis will be referred as inward or outward facing indicating to which side the transporter is facing for a unique purpose to define the state of the cytosolic gate. When the cytoplasmic gate is open the state will be named inward facing, and if it is closed, outward facing. The cytoplasmic gate is also closed for the states designated as fully occluded, where both the extracellular and the cytosolic gates are occluded.

The structures of relevant APC superfamily transporters are listed in Table 5 reviewing them from the APC superfamily level, through the APC family and finally the LAT subfamily (Table 6) (as of 13 June 2022).

Table 5. APC superfamily structures. (*Following page*) Summary list of available APC family members solved structures. Substrates, inhibitors and chaperones (e.g., fragment antigen-binding (Fab)) are indicated in substrates column in black, italic and purple, respectively. Absence of any binder correlates to apo conditions. All of them were solved through XRC with the only three exceptions in hSERT. APC family members are coloured in purple background. BetP trimers are listed as monomers indicating how many out of the three where found in the specific state.

Transporter & classification	**State**	**Substrates** & other binders	**PDB ID**	**Reference**
BetP BCCT family	Outward facing		(2 of 3) 4DOJ	(Perez et al., 2012)
		Arseno-choline	(2 of 3) 4LLH	(Perez et al., 2014)
	Fully occluded	Betaine	(1 of 3) 4AIN	(Perez et al., 2012)
			(1 of 3) 4AIN	(Perez et al., 2012)
	Outward facing *Intermediate*	Betaine	2WIT	(Ressl et al., 2009)
	Inward facing	Choline	(1 of 3) 3P03	(Perez et al., 2011)
		Arseno-choline	(1 of 3) 4LLH	(Perez et al., 2014)
		Choline	(1 of 3) 4DOJ	(Perez et al., 2012)
		Betaine	(1 of 3) 4AIN	(Koshy et al., 2013)
			4C7R	
			(2 of 3) 3P03	(Perez et al., 2011)
LeuT NSS family	Outward facing		5JAE	(Malinauskaite et al., 2016)
			5JAF	
			5JAG	
			3TT1	(Krishnamurthy and Gouaux, 2012)
		L-Trp / SeMet	3F3A / 3F4I	(Singh et al., 2008)
	Fully occluded	L-Leu	2A65	(Yamashita et al., 2005)
		L-Ala / L-Met ...	3F48 / 3F3D...	(Singh et al., 2008)
		L-Leu + CXX ...	2Q6H ...	(Singh et al., 2007)
		L-Leu + DSM	2QJU	(Zhou et al., 2007)
	Inward facing		3TT3	(Krishnamurthy and Gouaux, 2012)
Mhp1 NCS1 family	Outward facing		2JLN	(Weyand et al., 2008)
	Fully occluded	IMH / *NMH...*	4D1A, 4D1D...	(Simmons et al., 2014)
	Inward facing		2X79	(Shimamura et al., 2010)
SglS / SglT SSS family	Inward facing	Galactose	3DH4	(Faham et al., 2008)
			2XQ2	(Watanabe et al., 2010)
CaiT BCCT family	Inward facing	γ-Butyrobetaine	2WSX	(Schulze et al., 2010)
		L-carnitine	3HFX	(Tang et al., 2010)
		γ-Butyrobetaine	4M8J	(Kalayil et al., 2013)
			2WSW	(Schulze et al., 2010)
MhsT	Inward occluded	L-Trp	4US3	(Malinauskaite et al., 2014)
		L-Trp	4US4	
dDAT	Outward facing	*Nortriptyline*	4M48	(Penmatsa et al., 2013)
		Cocaine	4XP4, 4XPB...	(Wang et al., 2015)
hSERT	Outward facing	*Antidepressants* + Fab	5I6Z, 5I74...	(Coleman et al., 2016)
			6AWO, 6AWN...	(Coleman and Gouaux, 2018)
		Fab	6W2B, 6W2C...	(Coleman et al., 2020)
		Fab (by Cryo-EM)	6DZW 6DZY	(Coleman et al., 2019)
	Fully occluded	Fab (by Cryo-EM)	6DZV	
	Inward facing	Fab (by Cryo-EM)	6DZZ	
AdiC APA subfamily	Outward facing	Fab	3LRB, 3LRC	(Gao et al., 2009)
			3NCY	(Fang et al., 2009)
			5J4I	(Ilgü et al., 2016)
		L-Arg	3OB6	(Kowalczyk et al., 2011)
		Agmatine	5J4N	(Ilgü et al., 2016)
	Fully occluded	L-Arg	3L1L	(Gao et al., 2010)
GadC	Inward facing		4DJK	(Ma et al., 2012)
ApcT	Fully occluded		3GIA	(Shaffer et al., 2009)
		Fab	3GI8, 3GI9	
GkApcT	Inward facing intermediate	L-Arg + MgtS	6F34, 5OQT	(Jungnickel et al., 2018)

Regarding the structures of the members of the LAT subfamily, until the beginnings of 2019, the only known structures were from the above-indicated remote bacterial homologues, which show 17-22 % of SI (AdiC, GadC, ApcT and GkApcT). All of these transporters belong to the APC family (Fang et al., 2009; Gao et al., 2009, 2010; Shaffer et al., 2009; Kowalczyk et al., 2011; Ma et al., 2012; Ilgü et al., 2016; Jungnickel et al., 2018). Nevertheless, several structures for LATs and HATs have been solved in the past three years (Table 6). All these authors ascertained the predicted similarity of them and their previously solved homologues. The known structures for LATs are as follows:

- **BasC** (Bacterial Asc-type like transporter) was first solved by XRC in an inward facing conformation with and without 2-aminoisobutyric acid (2-AIB), a poor substrate (PDB ID: 6F2W and 6F2G, respectively) (Errasti-Murugarren et al., 2019). It is the only LAT structure solved by XRC (all the others have been solved through Cryo-EM).
- **LAT1** (L-type neutral AAT 1) is the most prolific LAT in terms of structures available. Actually, LAT1 was the first LAT to be solved (2019) with and without BCH, a poor substrate (PDB ID: 6IRT and 6IRS, respectively). LAT1 is the only LAT solved in an outward facing / fully occluded conformation with several inhibitors, which might represent an intermediate state between occluded and open conformations (PDB ID: 7DSK, 7DSL, 7DSN and 7DSQ) (Yan et al., 2021). Like all other subfamily transporters, all other LAT1 structures solved show an inward facing conformations (Yan et al., 2019; Lee et al., 2019).
- **$b^{0,+}$AT** ($b^{0,+}$-type AAT 1): for all cases, this transporter has been solved in an inward facing state forming super-dimers of heterodimers. One of them (PDB ID 6LI9) bound to its substrate L-Arg. Moreover, this LAT member was solved being reconstituted into membrane scaffold protein (MSP) 1E3D1 nanodiscs (ND) (MSP1E3D1-ND) containing diverse lipids and phospholipids (phosphatidylcholine, phosphatidylglycerol, and cholesterol) (PDB ID: 7NF8). This first LAT reconstituted in a lipid environment has allowed to see its structure in a native-like environment, in contrast to all the other cases, which involved the use of detergents (Lee et al., 2022; Wu et al., 2020; Yan et al., 2020a).
- **LAT2** (L-type neutral AAT 2): LAT2 has been solved twice bound to AA substrates, L-Trp and L-Leu (PDB ID: 7CMH and 7CMI, respectively). LAT2 structures revealed the substrates position on the substrate-binding sites and the study of its substrate selectivity regarding the residues in this binding sites (PDB ID: 7B00) (Yan et al., 2020b; Rodriguez et al., 2021).
- **xCT** (cystine/Glu antiporter): in 2020 xCT was solved at low resolution due to its low stability (PDB ID 7CCS). This was achieved thanks to consensus-mutated version to increase protein stability. xCT structure was obtained in an inward facing state. Later on, more structures have been solved, one of them bound to erastine, an inhibitor (PDB ID 7EPZ),

and another bound to L-Glu, a substrate (PDB ID 7P9U) (Oda et al., 2020; Parker et al., 2021a; Yan et al., 2022).

Transporter & classification	State	Substrates *& other binders*	Amphipathic environment	Method	PDBs	Reference
BasC	Inward Facing	Nb74	DM	XRC	6F2G	(Errasti-Murugarren et al., 2019)
		2-AIB + Nb74	DM	XRC	6F2W	
LAT1 SLC7A5	Inward facing	*BCH*	DG	Cryo-EM	6IRT	(Yan et al., 2019)
			GDN	Cryo-EM	6IRS	
			DG	Cryo-EM	6JMQ	(Lee et al., 2019)
	Outward facing	*JX-075*	GDN	Cryo-EM	7DSK	(Yan et al., 2021)
		JX-078	GDN	Cryo-EM	7DSL	
		JX-119	GDN	Cryo-EM	7DSN	
		Diiodo-Tyr	GDN	Cryo-EM	7DSQ	
$b^{0,+}$AT SLC7A9	Inward facing	L-Arg	GDN	Cryo-EM	6LI9	(Yan et al., 2020a)
			GDN	Cryo-EM	6LID	
			DG	Cryo-EM	6YUP	(Wu et al., 2020)
			DG	Cryo-EM	6YV1	
			ND	Cryo-EM	7NF8	(Lee et al., 2022)
LAT2 SLC7A8	Inward facing	L-Trp	GDN	Cryo-EM	7CMH	(Yan et al., 2020b)
		L-Leu	GDN	Cryo-EM	7CMI	
			DG	Cryo-EM	7B00	(Rodriguez et al., 2021)
xCT SLC7A11	Inward facing		DG	Cryo-EM	7CCS	(Oda et al., 2020)
		Erastine	GDN	Cryo-EM	7EPZ	(Yan et al., 2022)
		L-Glu	LMNG + CHS	Cryo-EM	79PU	(Parker et al., 2021a)
				Cryo-EM	79PV	

Table 6. LAT subfamily structures. Listed table of all available LAT subfamily members solved structures. Amphipathic compounds (e.g., detergents, lipids…) listed are DM, digitonin (DG), glycol-diosgenin (GDN), lauryl maltose neopentyl glycol (LMNG), cholesteryl hemisuccinate (CHS) and nanodiscs (ND). Substrates, inhibitors and chaperones (e.g., Fab) are indicated in substrates column in black, italic and purple, respectively

All the above-cited structures of LATs showed the same inward facing conformation (Nicolàs-Aragó et al., 2021) with only a single exception: LAT1 (Yan et al., 2021), which structures of LAT1 bound to inhibitors correspond to variants of fully-occluded / outward facing conformations.

2.3. Functional and structural characterisation of BasC

A detailed functional characterisation of BasC was first provided by our group in 2019 (Bartoccioni et al., 2019), the same year as studies on the structure of BasC-Nb74 and K154A function were published (Errasti-Murugarren et al., 2019). Thus, all BasC data cited in this section are taken from these two articles. The figures shown in this subsection have been adapted to the need of this thesis to make them easily understandable.

BasC show an obligate AA exchange activity when reconstituted in proteoliposomes (PLs), which is characteristic of the catalytic subunits of HATs (Fotiadis et al., 2013). Thus, BasC needs the presence of AA substrates in both sides

of the PLs to show transport activity, which can be measured bidirectional (Figure 7. A).

BasC has substrate selectivity for small AA^0 (Gly, L-Ala, D-Ala, L-Ser, D-Ser L-Thr, and L-Cys) and L-asparagine, excluding other AA^0 and acidic and AA^+ (Figure 7. C). Actually, BasC name was chosen regarding the highly similar substrate selectivity with human and mouse Asc-1 (alanine-serine-cysteine exchanger) (Fukasawa et al., 2000; Brown et al., 2014).

BasC transport occurs similarly in a pH range from 7.0 to 9.4, and its exchange activity is independent of ions, as transport is not affected by the presence of Na^+, K^+ or Cl^- in the PLs external medium (Bartoccioni et al., 2019).

Functional transport assays for BasC reconstituted in PLs revealed a random incorporation of BasC-GFP molecules (i.e., right side out and inside out). BasC was GFP-tagged at C-ter, in the cytosol. As the protease site between BasC and GFP is accessible only from the outside of the PLs, the resulting GFP cleavage for PLs containing BasC-GFP is partial. HRV 3C protease cleaves only inside-out molecules exposing their cytoplasmic side to the medium. Similarly, vectorial inactivation of BasC in PLs demonstrated the random incorporation of the transporter (Bartoccioni et al., 2019).

BasC presents substrate affinity sidedness, meaning that it has distinct affinity for the cytoplasmic and extracellular sides. When performing BasC kinetics a complex profile was found suggesting two distinct components, one at low concentrations (µM range) and the another at higher ones (mM range) (Figure 7. B). To elucidate the Michealis-Menten constant (K_M) for each side, right side-out and inside-out BasC molecules needed to be inhibited specifically and individually. This specific inhibition was performed using MTSES (non-permeable) and MTSEA (permeable) reagents, which are Cys-modifying reagents. To this end, several Cys variants of BasC were used, one exposing C427 (i.e., the WT and unique Cys in the BasC sequence) on the cytosolic side, and A20C-C427A, exposing A20C on the extracellular side. Finally, the extracellular side was found to be the one with high affinity (K_M = 45 ± 5 µM), and the cytoplasmic one the lower affinity (K_M = 2.5 ± 0.4 mM). BasC presents a V_{max} value of 6.0 ± 0.2 pmol [^{3}H]L-Ser/$\mu g_{protein}$/s) when assayed in BasC-GFP-PLs containing 4 mM L-Ala, varying extracellular L-Ser concentrations (Bartoccioni et al., 2019).

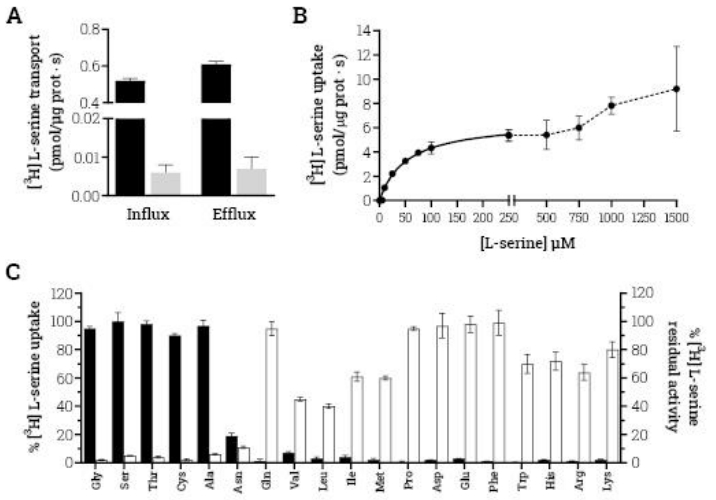

Figure 7. Functional characterisation of BasC. A. Comparison of 10 µM [3H]L-Ser (1 µCi/data point) influx and 10 µM [3H]L-Ser (1 µCi/data point) efflux in BasC-GFP-PLs, expressed in pmol/µgprotein/s. **B.** Determination of extraliposomal kinetic parameters. Michaelis–Menten plot of the transporter-mediated uptake of [3H]L-Ser (1 µCi/µl, 4 s pmol/µgprotein/s) in BasC-GFP-PLs containing 4 mM L-Ala, varying extracellular L-Ser concentrations (0–1,500 µM). KM and Vmax values were 45 ± 5 µM and 6.0 ± 0.2 pmol [3H]L-Ser/µgprotein/s, respectively. **C.** 10 µM [3H]L-Ser (1 µCi/µl) influx into BasC-GFP-PLs containing 4 mM of the indicated AAs (black bars). Transport is expressed as the percentage of the transport in BasC-PLs containing 4 mM L-Ala. 10 µM [3H]L-Ser (1 µCi/µl) influx into BasC-GFP-PLs measured in the presence of 5 mM of the indicated AAs in the external medium (white bars). Inhibition is expressed as the percentage of transport in BasC-GFP-PLs containing 4 mM L-Ala with no cis-inhibitors. Data are from three experiments, with three replicates per condition. (Adapted from Bartoccioni et al., 2019).

As mentioned previously, BasC structure was published in 2019 in an inward facing conformation in apo (i.e., substrate-free) and holo (i.e., substrate-bound), in complex with the poor substrate 2-AIB. Both structures were solved in complex with the nanobody (Nb) 74 (Nb74) (Errasti-Murugarren et al., 2019). This Nb was selected due to its highest affinity for BasC and the blocking effect it had on BasC efflux transport activity (Figure 8. A). Nb74 binds to the cytosolic side of BasC, and accordingly blocks the cytosolic kinetic component of the transporter (i.e., the low-affinity one) (Figure 8. B) (Bartoccioni et al., 2019).

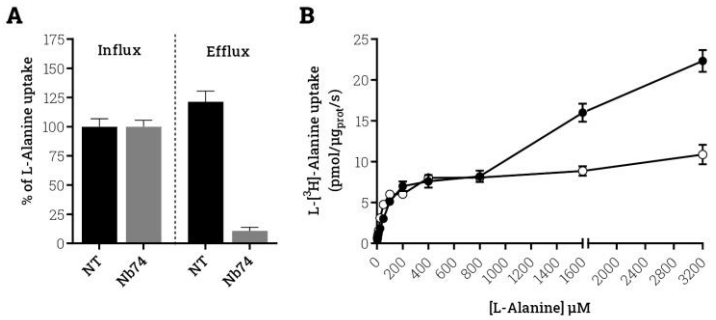

Figure 8. Nb74 functional characterisation. A. Effect of influx and efflux transport activity inhibition normalised against the influx non-treated (NT). **B.** Effect of Nb74 on the transport kinetics, depleting the low affinity component but not the high affinity one.

Using this Nb, it was possible to structurally solve BasC at (2.9-3.4 Å), as previous attempts reached only low resolutions of ~7 Å. Finally, the crystallographic apo and holo structures solved in complex with Nb74 reached 2.9 and 3.4 Å, respectively. BasC shares the APC fold with 12 TMs organised like all the other LATs, in an inward facing state and thus as the vast majority of the solved structures of the APC family (Figure. 9).

Differences seen between BasC and the original APC fold defined by LeuT structure in 2005 are present in the internal loop 4 (IL4, between TM8 and 9), where BasC presents an extra helix. Oppositely, BasC does not show the two β-sheets between TM5 and 6 and neither the helix in the EL2 that LeuT had.

The BasC-Nb74 structure confirmed that Nb74 interacts through the cytoplasmic side of BasC (Figure 9 A-B), and provided details of this interaction (Figure 9. C). Nb74 interacts mainly through its complementary determining region (CDR) 3 to BasC TM2, 6b, 8 and IL4. Nb74 interacts with both the bundle (TM2 and 6b) and hash (TM8, 9 and IL4) domains of BasC. These observations suggest that binding to both domains is the main cause of the inhibition of BasC' transport activity.

Furthermore, regarding the involvement of LATs in human diseases, specifically with LPI, mutations K154A and K154E in BasC were studied, corresponding to residue K191 in y+LAT1 mutated in a patient with LPI (K191E) (Errasti-Murugarren et al., 2019). These two mutations almost completely abolished L-Ala uptake. The kinetic analysis of this uptake in the BasC K154A variant revealed a dramatic 10-fold reduction of the external affinity for the uptake of L-Ala versus L-Ala. K154A variant presents and increased K_M of 474 ± 42 µM. Surprisingly, the internal side K_M did not show significant changes (K_M = 2.04 ± 0.4 mM). Thus, K154A turned BasC into a more symmetric transporter with more similar K_M at each side. In addition, K154A caused a 20-fold reduction of

the V_{max} until 0.32 ± 0.04 $pmol_{L\text{-}Ala}/\mu g_{prot}/s$. This observation points to a key role of this residue in the transport cycle. Detailed involvement of this conserved Lys (K154 in BasC) in transport mechanism is further described below in Introduction 2.4 Mechanism of transport.

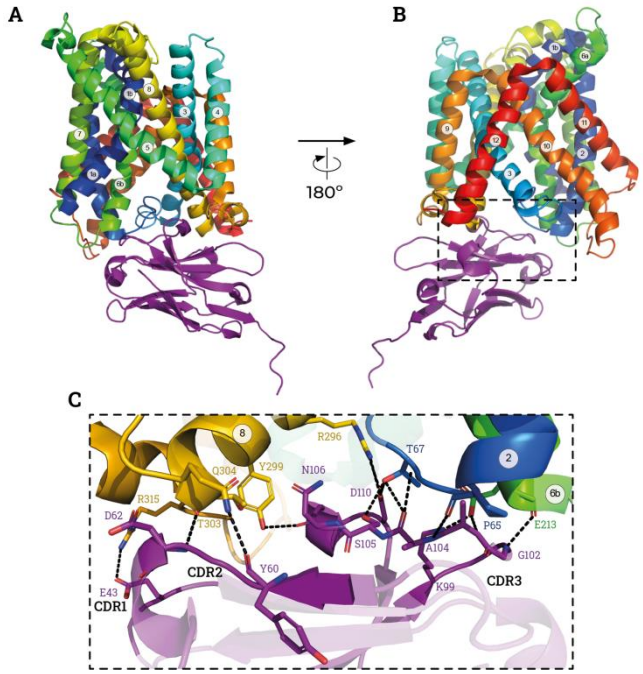

Figure 9. BasC-Nb74 complex structure. TMs are coloured from blue to red from the N-ter (rainbow, from here on, rainbow will designate this scale of colours, from blue to red, unless the contrary is indicated.) and Nb74 is shown in purple. **A-B.** Wide view of the inward facing structure of BasC in complex with Nb74 at 2.9 Å (PDB ID 6F2G). **C.** Detailed view of the cytoplasmic interaction between Nb74 and BasC zoomed from dashed rectangle in B. Complementarity-Determining Region (CDR) 3 is the most involved CDR on complex interaction of all CDRs to TM2, 6b, 8 and IL4 (between TM8 and 9). Figure adapted from Errasti-Murugarren et al., 2019 with Open-Source PyMol (The PyMOL Molecular Graphics System, Version 2.0 Schrödinger, LLC).

2.4. Mechanism of transport

The main objective of this project is to decipher and describe the dynamics and the occlusion of the cytosolic gate of BasC as the related role of K154 in this dynamics to bring new insights into the transport mechanism of LATs through our bacterial model, BasC. With this purpose, the hypothesis is based in previous studies and structures of other transporters from the APC superfamily. Although the sequence similarity among the APC superfamily members is low, their common fold (APC fold) with several structural motifs at sequence level is what actually allows their comparison. One of these motifs is the GX_nP in TM5 for APC fold transporters. This motif has been deeply studied throughout the bacterial members of the NSS family. These members share a conserved GX9P motif (e.g., G171-X_9-P181 for MhsT, G190-X_9-P200 for LeuT) (Malinauskaite et al., 2014). It has been described how this motif is of paramount importance for the unwinding of TM5, a crucial step during the transport cycle, which triggers the switch from outward- to inward facing states (del Alamo et al., 2022).

Considering the first structures solved for LeuT transporter in 2005, two sodium-binding sites (Na1 and Na2) were described at only 6 Å distance from the α-carbon of the bound substrate, L-Leu molecule (Figure 10. A) (Loo et al., 2013). In the one hand, Na1 involves the TM1 (A22 and N27 in LeuT), TM6 (T254 in LeuT) and TM7 (N286 in LeuT). In the other hand, Na2 involves the TM1 (G20 and V23 in LeuT) and TM8 (A351, T354 and S355 in LeuT) (Figure 10. B) (Yamashita et al., 2005). The latter, is the most conserved ligand-binding site among all the APC fold transporters (del Alamo et al., 2022). Indeed, no ion-coupled transporters, such as members of the APC family, present Na2 reminiscences, where the site is characterised by the location of positively charged residues (Shaffer et al., 2009; Tang et al., 2010; Jungnickel et al., 2018; Errasti-Murugarren et al., 2019). When the two Na^+ are bound, they have key roles in stabilizing the transporter. Even existing these two sodium-binding sites, there are exceptions among ion-coupled transporters such as AgcS, which only uses the Na1 in its transport cycle (Ma et al., 2019). The use of only the Na1 contrasts with the fact that Na2 is the most conserved one.

Lys K154 in BasC is located in an equivalent position to the, while Tyr236 (Y236) is in the Na1 (Errasti-Murugarren et al., 2019) both residues are conserved among all hLATs in TM5 and 7 respectively (Bartoccioni et al., 2019). K154 substitutes the Na2 role permitting TM1a and 8 to stablish the interaction through itself in the TM5 (Figure 11) stablishing a similar mechanism of transport as previously described for LeuT (Loo et al., 2013; Yamashita et al., 2005).

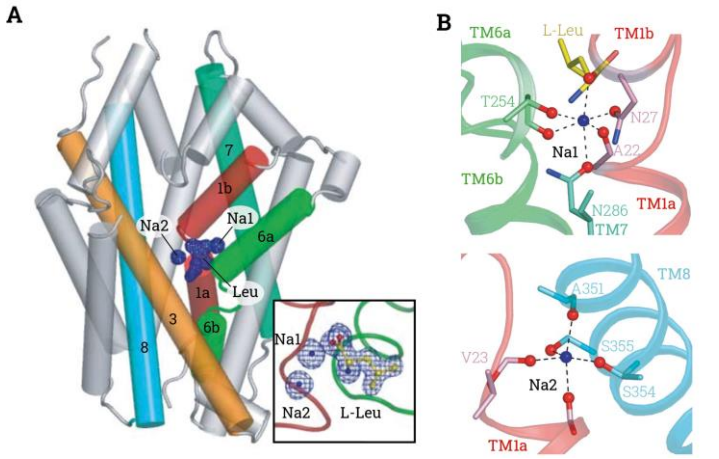

Figure 10. Na+ binding sites in LeuT. A. General view of LeuT transporter showing Leu and Na^+ densities (blue). Na1 and Na2 sites are positioned next to the substrate-binding site. **B.** Sodium binding sites Na1 (top) and Na2 (bottom) detail. Sodium ions are shown in blue spheres, Leu in yellow, TMs and residues involved are labelled and hydrogen bonds shown (dashed lines) (Yamashita et al., 2005). *Note TMs in (B) are coloured in rainbow from the red to purple.*

Structural analysis between BasC and GkApcT structures (Figure 11), in inward facing open and occluded, respectively, shows how this Lys (K154 in BasC and K191 in GkApcT) interacts with previous described involved TMs on the alternating access to the binding site. In an inward open state, K154 in BasC interacts with G15 (G38 on GkApcT) on TM1a while K191 in the occluded structure of GkApcT interacts not only with TM1a (G38 and I41) but also with the backbone atoms of G313 (S282 in BasC) and the lateral chain of T316 in TM8 (Figure 11). This structural evidence reinforces the importance of the coordination between TM1a-5-8 for the availability of the transport cycle, and the conserved Lys in TM5 that coordinates these TMs.

Moreover, molecular dynamics (MD) performed on BasC-2-AIB unexpectedly showed how substrate when dissociated from the substrate binding site it simultaneously bound to K154 and Thr 16 (Errasti-Murugarren et al., 2019). This suggests that the binding between 2-AIB and K154 is the first transient step for the substrate to move to the cytosol. Thermostability-based binding assays indicate a reduction in the K154A L-Ala binding affinity compared with that of the WT. Thus, reinforcing the role of this residue in substrate interaction similarly as the Na2 in ion cotransporters.

Na1 and Na2 are involved in the alternating access mechanism, as they are needed for the TMs coordination for the conformational changes. Alternating

access mechanism is based on the exposure of the binding site from only one side at a time, either the extracellular or the cytosolic. To understand how the alternating access of transporters work for the APC superfamily, we need to pay special attention to the TMs that orchestrates the conformational changes (TMs 1, 5, 6, 7 and 10), further described (Nicolàs-Aragó et al., 2021; del Alamo et al., 2022).

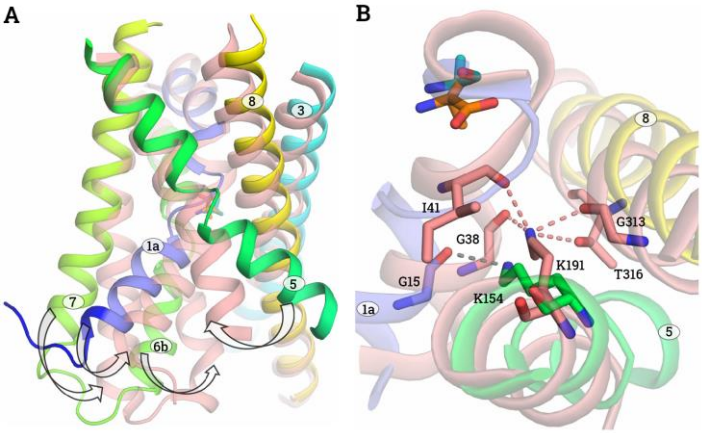

Figure 11. Substrate occlusion in inward facing SLC7 transporters. A. Comparison of the structures of BasC (rainbow) bound to 2-AIB (orange) (PDB ID: 6F2W) in non-occluded state and GkApcT (salmon) bound to L-Ala (cyan) (PDB ID: 5OQT) in occluded state. Tilting of TM1a and TM6b, together with the accompanying TM7, closes the substrate vestibule to occlude the substrate at the cytoplasmic side (arrows). Concomitantly, TM1a interacts and attracts TM5 in the occlusion state (arrow). Only TM1, 3, 5, 6, 7, and 8 are depicted for clarity. **B.** Detail of the interactions of K154 in BasC (grey dashed line) and K191 in GkApcT (salmon dashed lines) in the structures shown in a. Figure published in Errasti-Murrugaren et al., 2019.

Firstly, in the cytosolic side of the transporter, when comparing different conformation structures, it is noticed how extremely mobile are the bottom region of TM5 and the IL2 (Billesbølle et al., 2015; Stolzenberg et al., 2017) (Figure 12. A-B). This mobility is also illustrated with the difficulty to precisely solve the structure of these regions, specifically the IL2, in the APC superfamily members (e.g., GkApcT (Jungnickel et al., 2018)). Moreover, TM5 in outward facing conformations forms a thick gate together with the TM1a and TM6b that prevents accessibility to the binding site from the cytosol. TM1a is also one of the TMs showing larger tilts between conformations, as is the case for LeuT that has been reviewed how it pivots up to 45º (del Alamo et al., 2022) (Figure 13. A). This is also seen in for SERT and the APC family members, although in less amplitude for the latter (Coleman et al., 2019). TM1a tilting occurs at the same time as the TM6 in coordination with TM5 and 8 upon substrate binding from

the cytoplasmic side (Nicolàs-Aragó et al., 2021) with the exception of ApcT, solved in a fully occluded state without substrate, due to its non-obligatory AA exchange activity (Shaffer et al., 2009). This coordination between TM1, 5 and 8 is key for the function APC superfamily members. Finally, the cytoplasmic end of TM7 also shows bends, the biggest TM7 change is observed for LAT1 (Yan et al., 2021) (Figure 12. C), but is also described for the partially unfolding of it in LeuT (Kazmier et al., 2014; Merkle et al., 2018) and Metal Ion (Mn^{2+}-iron) Transporter (Nramp) family (Bozzi et al., 2019).

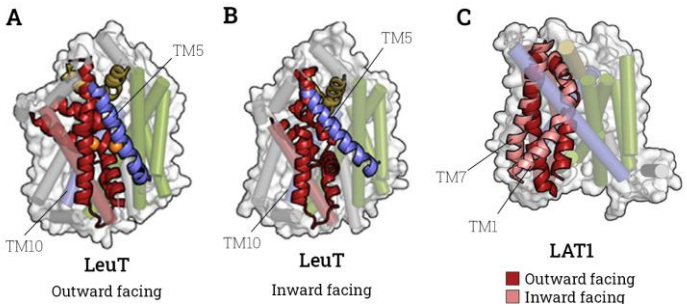

Figure 12. Mobile TMs in APC fold transporters. Cartoon schemes for APC fold transporters to compare in a simplified view the TMs tilts. **A-B.** LeuT outward (A) and inward (B) facing conformations sodium-bound (PDB ID 3TT1 and 3TT3, respectively). TM5 (front) and TM10 (back) are coloured blue, bundle domain, red and hash domain, green. **C.** LAT1 outward and inward facing conformations overlapped (see colour legend). TM1a and TM7 are highlighted opaque (PDB ID 7DSK and 6IRS for outward and inward facing conformations, respectively). Adapted from (del Alamo et al., 2022).

For the other hand, in the extracellular side, and regarding the symmetry of the APC fold, TM10 also tilts, symmetrically to TM5 (Figure 12. A-B), although less extensively. Members of the Betaine/Carnitine/Choline Transporter (BCCT) family and Nramps show a conserved helix-breaking Pro in the TM10 that facilitates this bend (Bozzi et al., 2019). A similar bend has been described for hLAT1, although this transporter does not have any conserved Pro promoting the bend of the TM10, as any of the hLATs nor BasC. TM1b and TM6a bends occluding the extracellular gate upon substrate binding have also been described, although for LeuT occur in a smaller range than other TM bends (Singh et al., 2008; Claxton et al., 2010). Comparison between AdiC and hLAT1 shows how this TM1 and 6 bend is also minimised in the eukaryotic transporters (16 º) respect the prokaryotic homologues (40º) of the APC family (Nicolàs-Aragó et al., 2021). TM1b and 6a tilt opening and closing the extracellular side of the transporter with the EL4, which bend is known, not only by structure comparison, as it might be biased by the impact of the detergent due to the conditions of sample preparations (Quick et al., 2009). EL4 bend has been analysed by dynamic assays on LeuT using electron paramagnetic resonance

(EPR) (Claxton et al., 2010; Kazmier et al., 2014) and transition metal ion FRET (tmFRET) (Billesbølle et al., 2016) concluding that EL4 can function as an extracellular lid that opens when sodium is present and closes when L-Leu binds.

All biological molecules can be subjected to structural changes in a broad range of time scales from femtoseconds' vibrations, through seconds-long structural rearrangements and even days-long domain swapping or aggregation processes (Lento and Wilson, 2021). Molecular mechanisms can be inferred from static structures solved through different techniques explained before and validated using biochemical and biophysical assays. Although these structural "snapshots" can identify distinct conformational states that macromolecules explore at equilibrium (e.g., apo vs. holo, inward facing vs. outward facing), they lack information on the interconversion dynamics between these states. Understanding the functional roles of these structures requires an exhaustive dynamic picture (Zhuang et al., 2000; Michalet et al., 2006; Pirchi et al., 2011). Dynamics of APC fold transporters have been studied in some cases as described below.

For the one hand, LeuT, which was already structurally solved in different conformational states, was assessed on immobilised LeuT molecules through total internal reflection fluorescence (TIRF) single molecule Florescence Resonance Energy Transfer (smFRET) analysis (TIRF-smFRET). LeuT dynamics were assessed tracking movements of the cytosolic gate labelling Cys7 (TM1a bottom) and Cys86 (IL1, i.e., TM3 bottom) (Figure 13. A). smFRET revealed two readily distinguished states in the presence of 200 mM K^+ and the nominal absence of Na^+ (Zhao et al., 2011). The high-FRET state, which would represent an inward closed conformation, and the low-FRET state, an inward open, differed by ~13 Å as solved structures shown (Table 5 and Figure 13. A). The distribution of these two different states was altered upon sodium addition (Figure 13. B), stabilising preferably the inward-closed state. However, under lower concentrations of Na^+ (2 mM), substrate addition (L-Ala) was not found to alter these states relative occupancies (Figure 13. C), but lowered the activation barrier needed for this conversion of states ($\Delta G^{\ddagger} \sim 80$ kJ / mol) increasing the transition rates between smFRET states by ~4 fold. Thus, L-Ala accelerates the opening-closing cycle of LeuT's cytosolic gate but not the equilibrium between these two different states.

It has been also described for some members of the APC superfamily a second substrate-binding site (S2) appart from the canonical one found in the unwound region of TM1 and 6, namely the S1. In SERT, an S2 was described as a low-affinity allosteric site when antidepressants acting as transporter inhibitors were found bound to it (Singh et al., 2007). This inhibitor bind to the S2 of SERT showed how it slowed their own dissociation rates from the S1. (Singh et al., 2007). Later, it was solved the structure of LeuT bound to L-Trp (PDB ID 3F3A) and to L-selenometionine (PDB ID 3F4I) in the S2 (Table 5) (Singh et al., 2008). Finally, Coleman and co-workers were able solve SERT structure by X-

ray in this occluded state bound to antagonists, antidepressants, in the S2 (Table 5) (Coleman et al., 2019; Coleman and Gouaux, 2018). In parallel, it was described an S2 after finding an octylglucoside molecule bound in MhsT, from the NSS family (Quick et al., 2009). In this regard, later, it was described for MhsT also the existence of two distinct substrate-binding sites (Quick et al., 2018). Not only structural information supports the existence of an S2, also MD simulations done on LeuT endorsed it (Shi et al., 2008).

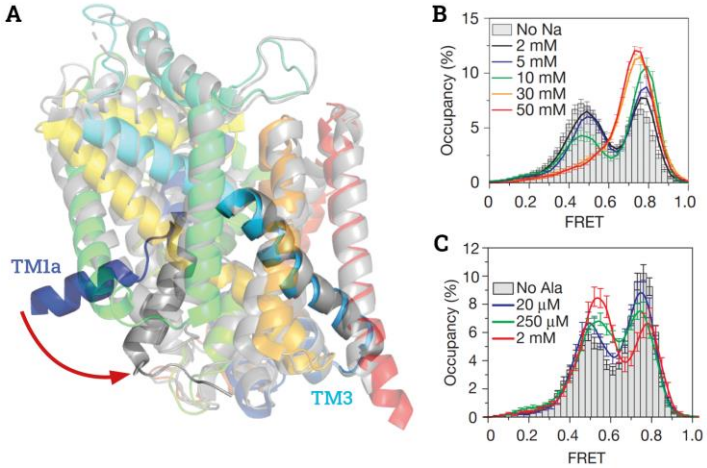

Figure 13. Dynamics assay by smFRET on LeuT. A. Overlapping LeuT structures in open to in (rainbow, PDB ID 3TT3) and open to out (grey, PDB ID 3TT1) conformations. TM1a (dark blue) and TM3 bottom (light blue) are highlighted translucent. TM1a tilt is evident in the cytosolic gate (red arrow). Figure created with Open-Source PyMol (The PyMOL Molecular Graphics System, Version 2.0 Schrödinger, LLC). **B-C.** FRET histograms traces collected varying concentrations of Na^+ (B) or L-Ala in presence of 2 mM Na^+ (C). Immobilised smFRET assessment performed on H7C/R86C-LeuT labelled with Cy3 and Cy5. Adapted from (Zhao et al., 2011).

Taking into consideration all what is has been explained above, the mechanism of transport (Figure 14) proposed here has been built on commonalities between sodium cotransporters (LeuT (Shi et al., 2008; Kazmier et al., 2014), MhsT (Quick et al., 2018), SERT (Coleman et al., 2016) and hSGLT1 (Loo et al., 2013)). The empty transporter is assumed to be negatively charged adopting an inward- or outward facing conformation depending on membrane voltage (Loo et al., 2013). The first sodium ion binding to the Na2 promotes a second sodium ion binding to the Na1 (Figure 14. A) (Loo et al., 2013). Once both Na^+ are bound, an outward facing conformation is stabilised, permitting the substrate to access from the extracellular compartment to the S1 (Figure 14. B), and later a second substrate molecule binds to the S2 (Figure 14. C). When substrate

binds to the S2 it triggers and opening of the cytosolic gate as a "symport effector" (Shi et al., 2008). It is only if both of the substrate-binding sites are bound to the substrate that this occurs (Coleman et al., 2016; Quick et al., 2018). Because inhibitors have been found interacting distinctly as substrates in the S2, they do no promote the substrate cotransport to the cytoplasm (Shi et al., 2008). Once both substrates and sodium ions are bound, the release to the cytoplasm of the sodium ion from the Na2 occurs first (Figure 14. D), enhancing the co-transport to the intracellular space of the substrate from the S1 plus the left sodium ion from the Na1 (Figure 14. E) (Kazmier et al., 2014).

The stoichiometry between substrate and ions co-transported depends on the transporter and its detailed mechanism of transport (e.g., vSGLT and Mhp1 only have one single sodium-binding site, the Na2 (Watanabe et al., 2010)). Speculations also let to the translocation of substrate from S2 to S1 once the cycle arrives at the last step in the presence of extracellular Na^+ (Zhao et al., 2011).

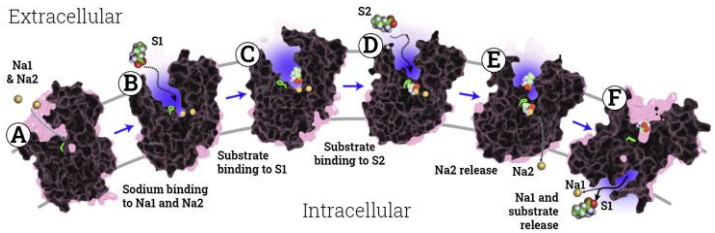

Figure 14. Schematic model of the proposed mechanism of transport by LeuT. First Na^+ binding to Na1 and Na2 are required (**A**). Then, substrate binds to S1 (**B and C**), a second molecule of substrate binds the S2 (**D**) triggering the release to the cytoplasm of the Na^+ from Na2 (**E**), finally the substrate in the S1 and Na+ in the Na1 are co-transported inside the membrane (**F**). Adapted from Shi et al., 2008.

We have seen how well stablished is the transport mechanism based on the alternate access for sodium cotransporters from the NSS family. Contrastingly, the steps for the substrate loading and release are unclear for the LAT family (Nicolàs-Aragó et al., 2021). In LATs, the double substrate-binding site has been speculated (Lee et al., 2019; Yan et al., 2021). An open space was first discovered in hLAT1 (PDB ID 6IRT and 6IRS) and was interpreted as a "distal-binding site" (Yan et al., 2019). A similar "distal-binding site" was the one where the hydrophobic tail of Diiodo-Tyr inhibitor was found stuck reaching the TM10 (Yan et al., 2021) (Figure 15. D). Lee and co-workers stated that the substrate binding site could have two pockets, one where to accommodate the primary side chains of the substrate and a "distal pocket" that could offer a promiscuous binding site for hydrophobic secondary substitutions, inhibitors (Lee et al., 2019). Similarly, in hLAT2 structure (PDB ID 7CMH and 7CMI), although it was seen a "distal cavity" connected to the central vestibule where to accommodate large side chains as in LAT1 (Yan et al., 2020b) (Figure 15. B), MD analysis did not predict any substrate occupying this

"distal cavity" (Rodriguez et al., 2021). Moreover, Rodriguez and co-workers stated that the recognition of the α-amino and carboxyl groups of the substrate by the substrate-binding site seemed incompatible with the occupancy of the putative distal site, even for AAs with large side chains such as L-Trp. And, in any case, there has been the evidence to bind two different substrate molecules simultaneously on the primary binding site and these putative "distal binding-sites" or "cavities" for LATs. Thus, the putative "distal binding-site" in LATs has nothing to relate with the S2 described for sodium symporters, where it has been described freely (Figure 15. A) or bound to inhibitors (Figure 15. C).

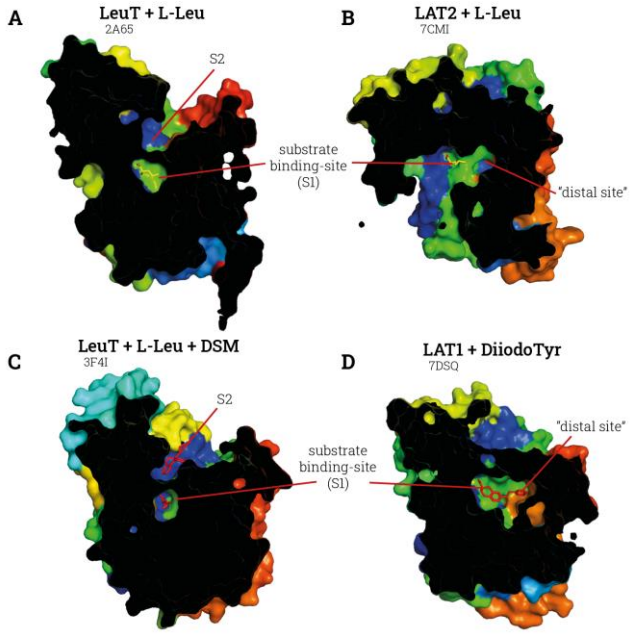

Figure 15. Substrate binding sites on APC fold transporters. Sliced structures of APC fold transporters. **A.** LeuT (PDBid 2A65) (Yamashita et al., 2005) in outward facing conformation substrate-bound (L-Leu). Presents a free-S2 above the S1 in the extracellular side. **B.** LAT2 (PDBid 7CMI) (Yan et al., 2020b) in inward facing conformation substrate-bound showing a distal site connected to the S1. **C.** LeuT (PDBid 3F4I) (Singh et al., 2008) in outward facing bound to susbtrate (L-Leu) in S1 and inhibitor (selenometionine (DSM)) in S2. **D.** LAT1 (PDBid 7DSQ) (Yan et al., 2021) in outward facing / occluded conformation inhibitor-bound (DiiodoTyr). All representations were built from the same point of view, permitting the visualisation of their substrate-binding sites (S1 and S2) and/or "distal sites". The S2 of LeuT (**A and C**) is located above the S1 facing the extracellular side, while the "distal site" described for hLATs is next to the S1 (**B and D**).

This thesis pretends to bring new insights about how we can translate the transport mechanism of the NSS family to the LAT family, considering the commonalities and divergences between them. As far as it is known, with LAT structures and bacterial homologues from the APC family, it can be described the states that LATs would adopt during its transport cycle (Figure 16) (Nicolàs-Aragó et al., 2021).

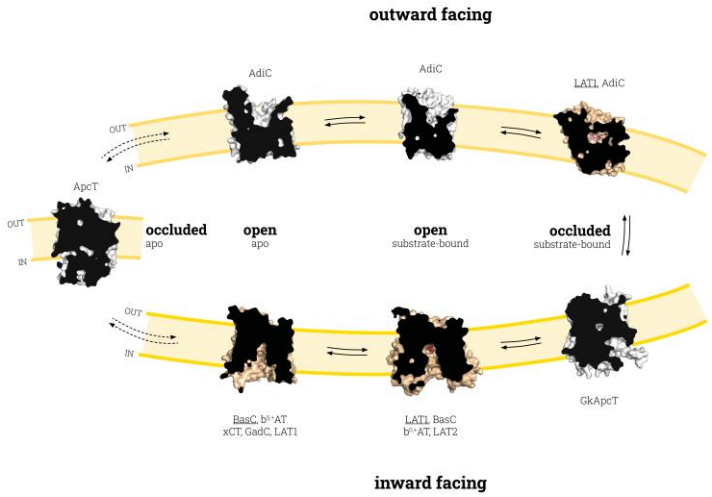

Figure 16. Structures solved of APC family members. Transport cycle with structures solved of LAT structures (brown) and APC family homologues (white). Only inward facing (open to in) conformations apo and substrate-bound, as outward facing (open to out) conformations occluded with inhibitor binding have been solved. (Nicolàs-Aragó et al., 2021)

Purpose of the research

Purpose of the research

i. Characterise the Nbs for their usage in the obtaining of a new BasC conformation structure and for the dynamic studies of the cytosolic gate.

ii. Elucidate the role of the conserved Lys among LATs in TM5, K154 in BasC, in the occlusion dynamics of the cytoplasmic gate.

Results

1. Nanobody characterisation

Nbs against BasC-GFP were generated as described previously (Pardon et al., 2014) and detailed in Experimental Procedures (Antibodies and derived products). Briefly, BasC-GFP reconstituted into empty PLs were injected into a llama in Instruct facility, Brussels, in collaboration with Jan Steyaert Lab, VIB-VUB. From all Nbs obtained, 29 were finally selected (information related to Nbs used are detailed in Appendix B. 2. Nanobodies).

1.1. Nanobodies binding

Surface Plasmon Resonance (SPR) was performed for all Nbs against BasC solubilised in 0.17 % (w/v) DM in Biacore™ T-100 device (Experimental Procedures 1.1). The objective of the screening was to study the affinity of these Nbs. SPR generates a full kinetic profile that permits to obtain the different constants related to binding: the equilibrium constant (K_D), and the constants of association and dissociation (k_a or k_{on} and k_d or k_{off}, respectively) (Table 7. A). The latter are the reflection of the rate of formation and decay of the complex. Thus, how fast the binding is occurring and how fast the binding is dismantled. The former describes the conditions where the association and dissociation rates are equal, is the quantitative measurement of affinity.

SPR also permits to elucidate the maximum response (R_{max}). This parameter reflects the amount of protein that the immobilised Nb is binding to. Thus, a high R_{max} means that the conformation recognised by the Nb is extensively adopted by BasC molecules and the sampling from the Nb is easy, while a low R_{max} means that the conformation recognised by the Nb is not really explored for BasC molecules and, therefore, Nb sampling is handicapped.

SPR was performed initially as a fast screening to identify the most affine Nbs to use for crystallisation, and it was performed for all of them against two distinct concentrations of BasC (K_D in grey in Table 7. A). Later, for the most promising Nbs, the SPR screening was repeated increasing the number of BasC concentrations until four (K_D in black in Table 7. A), providing more reliable binding parameters results.

Regarding the equilibrium constant, Nbs showing a K_D > 100 nM (Nb55, 57, 59, 66, 73 and 77) were considered low affine. Oppositely, the eight most affine Nbs with, with a K_D below 30 nM, are listed, from high to low, as if follows: Nb74, 50, 65, 69, 71, 53, 56 and 58.

Regarding all the other parameters, Nbs were sorted in five different categories: very high (dark green), high (light green), average (yellow), low (orange) and very low (red). The intervals for each parameter and category are listed in Table 7. B as legend for Table 7. A. These intervals were designed taking into account the distribution of the parameter values among all the Nbs. However, considering the three parameters simultaneously, no clear groups could be

formed as every single Nb has its own properties and distinct affinity behaviour. Finally, intervals permit the lector to interpret affinity data in a simpler manner.

For example, Nb71 has a high affinity to BasC (K_D < 30 nM), although it showed a very slow binding (very low k_a) and a very fast unbinding (k_d very high), and it also showed a very high R_{max}; thus, the conformation Nb71 detects is widely shared throughout BasC molecules. Oppositely, Nb52 shows a K_D of ~34 nM, with a very high binding (very high k_a) and a slow unbinding (low k_d), and with a very low R_{max}, which means that the conformation it recognised is not very commonly adopted among BasC molecules.

SPR was performed in both apo and holo (4 mM L-Ala) conditions, and no differences were observed with the comparison between them. A complete view for all Nbs and all parameters for apo and holo conditions is listed in Appendix C. Nanobodies SPR screening, Table C. 1. Is important to take into account that SPR was performed with BasC solubilised in detergent, while the Nbs were previously created against BasC reconstituted in PLs. Therefore, differences were expected all along the project between these two distinct amphipathic environments.

During the development and progress of this project, several attempts to obtain BasC-Nb complexes were carried out by size exclusion chromatography (SEC), while checking the feasibility to purify them solubilised in detergent, which constitutes a fact of paramount importance to solve BasC structure. Thus, a SEC summary is listed in Table 7. C, listing all the complexes tested by this technique. BasC-Nb complexes were checked solubilised in detergents (0.06 % (w/v) DM or 0.17 % (w/v) DM) by SEC, following the protocol in Experimental Procedures 2.2. Size exclusion chromatography. From the results, it can be assured that most of them were found to complex with BasC (e.g., 53, 58, 71 and 74) while a minority were unable to bind to BasC (e.g., 59 and 64).

A

Nb	SPR			
	K_D (nM)	R_{max}	k_a	k_d
50	5	-	↑	↑↑
51	36	-	↑	-
52	34	↓↓	↑↑	↓
53	26	-	-	↑
54	72	↓	↓	↑
55	101	↓	↑↑	↓↓
56	26	-	↓	↑↑
57	217	↓	-	↓
58	28	-	↓	↑↑
59	248	↓	↑	↓↓
60	19	-	↓	↑↑
61	33	↓↓	-	↑
62	undetectable			
63	undetectable			
64	undetectable			
65	11	-	↓	↑↑
66	115	↓	↑↑	↓↓
67	97	-	↑	↓
68	undetectable			
69	25	-	↓	↑↑
70	57	-	↓	↑
71	25	↑↑	↓↓	↑↑
72	85	↓	↑	↓
73	119	↓	↑↑	↓↓
74	4	↑	-	↑↑
75	undetectable			
76	undetectable			
77	115	-	↑	↓
78	55	-	-	↑

B

	R_{max} (R.U.)	k_a ($1/s^9$)	k_d ($1/s^3$)
↑↑	≥ 1000	≥ 1000	≥ 200
↑	[500 ; 1000)	[300 ; 1000)	[40 ; 200)
-	[100 ; 500)	[200 ; 300)	[15 ; 40)
↓	[20 ; 100)	[75 ; 200)	[5 ; 15)
↓↓	< 20	< 75	< 5

C

Nb	SEC
50	✓
51	✓
52	n.a.
53	✓
54	✓
55	✓
56	✓
57	✓
58	✓
59	✗
60	✓
61	✗
62	n.a.
63	✗
64	✗
65	✓
66	✗
67	n.a.
68	n.a.
69	n.a.
70	✓
71	✓
72	n.a.
73	n.a.
74	✓
75	n.a.
76	n.a.
77	✓
78	✓

Table 7. Nanobody affinity and binding characterisation. A. SPR affinity parameters measured for Nbs against BasC solubilised in 0.17 % (w/v) DM. K_D values are shown in absolute values and were obtained from two (grey) or four (black) distinct BasC concentrations. R_{max}, k_a and k_d are coloured according to each parameter categories as legend shows in (**B**). The detailed K_D, R_{max}, k_a and k_d values can be found in Appendix C. Nanobodies SPR screening, Table C. 1. **B.** Colour legend of interval categories designed to group Nbs by their R_{max}, k_a and k_d. **C.** Complex purification feasibility assayed by SEC in DM or DDM. A green tick or a red cross designate if complex was feasible to be purified by SEC or not, respectively. Cells containing n.a. are for non-assayed Nbs.

1.2. Nanobodies sidedness

To sort the 29 different Nb by their BasC side of interaction we performed influx and an efflux activity screening assays (Figure 17) based in previous experiments done with Nb74 (Errasti-Murugarren et al., 2019). The approach is based in BasC sidedness, which mean that it presents different substrate affinities for each side, and BasC reconstitution in random orientation (i.e., right-side-out and inside-out) (Bartoccioni et al., 2019). These two facts permit to classify the Nbs by their side of interaction when performing transport activities with high and low AA concentrations in the different sides of the PLs as shown in Figure 17. When Nbs are added in the extracellular solution, they will only inhibit half of BasC-GFP molecules and, depending their inhibition profile, influx or efflux, the BasC side of interaction can be deciphered.

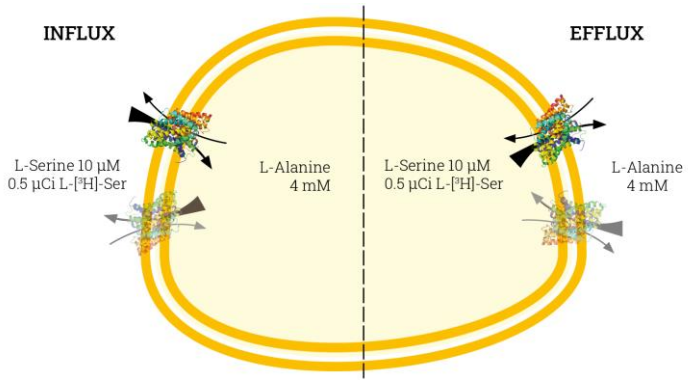

Figure 17. Screening assays on transport activity for nanobodies. Schematic representation for the influx and efflux transport activity assays. PLs are represented in yellow, with their lipid bilayer. Transporter sidedness is represented in black arrows (thick and thin for the high/low, extracellular/cytoplasmic, respectively). Active transporters are the ones facing with the high affinity side to the low AA concentration medium (opaque), the non-active are facing their low affinity side to the low AA concentration medium (transparent). Low AA concentration used in transport assays is 10 µM L-Ser + 0.5 µCi L-[^{3}H]-Ser and high AA concentration has 4 mM L-Ala.

Influx is based on measuring BasC transport activity with PLs loaded with high concentration of L-Ala (4 mM L-Ala) in a low concentration of L-Ser (10 µM L-Ser) medium. Efflux is approached as the opposite. In the former, it is measured the amount of radiolabelled L-Ser being transported inside the PLs while in the latter, the amount of radiolabelled L-Ser that is being exported from the PLs. During transport assays, only BasC molecules facing the high affinity side to the low AA concentration solution (10 µM L-Ser) will be actively transporting (i.e., right side up for the influx assays and inside out oriented for the efflux assays). Thus, Nbs added in the extra liposomal side that inhibit influx transport will be binding BasC

by the extracellular side, and the ones that inhibit the efflux will be binding by the cytoplasmic side (Figure 17).

Details on how the 29 Nbs were screened of their blocking effect on BasC-GFP in PLs, either influx or efflux as explained in Experimental procedures section 4.2 and 4.3, respectively.

For the one hand, influx was the first screening to be performed (Figure 18) using Nb74 as a control (Ctrl) as it was known to be a cytoplasmic binder. L-[^{3}H]-Ser influx against 4 mM L-Ala was measured with or without the addition of 15 µM Nb in the extra liposomal solution. Influx was let to occur for 5 s. Experimental duplicates were performed for all Nbs, while a third measure was performed for the ones that showed inhibition in one or both of the previous measurements. Four different Nbs were initially selected as inhibitors by the extracellular side: Nb58, Nb59, Nb64 and Nb78. In addition, Nb78 and 58 were selected as the efflux Ctrls, as they showed a high inhibition rate compared with Nb59 and 64. For the other hand, efflux transport conditions were adjusted based on the influx approach in order to solve unspecific inhibitions found and diminish the intrinsic loss of L-[^{3}H]-Ser from the intraliposomal solution detected. Because radiolabelled AA concentration inside the PLs was too high. Thus, Nb concentrations were lowered until 5 µM and transports allowed to occur for 30 s (Figure 18).

Influx dose responses were performed on the initially selected as extracellular binders (Nb58, 59, 64 and 68), as it was unclear why Nb59 and 64 presented such as weird profiles, inhibiting from both sides. Dose responses for Nb59 and 64 confirmed that they were actually inhibiting BasC transports by the extracellular side but with lower affinities than Nb58 and 78 and without reaching complete inhibitions (Figure 19). From these influx dose responses, Nb58 shows the highest affinity, with an IC_{50} of 9.44 ± 2.42 nM and reaching a complete inhibition, similarly as Nb78, which has less affinity, IC_{50} of 34.8 ± 8.01 nM. In the other side, Nb59 and 64 showed to be less affine, presenting lower IC_{50}s, 518 ± 170 and 362 ± 153 nM, respectively; and letting some residual transport activity of 36 and 30 %, respectively.

Figure 18. Nanobody blocking effect screening. Relative transport influx and efflux activity screening per each BasC-Nb complex. Influx and efflux were performed during 5 and 30 s, respectively on BasC-GFP reconstituted into PLs treated with 15 or 5 µM, respectively. Details for the assays described in the Experimental Procedures chapter. Mean ± s.e.m. plotted for each Nb treatment for a total of minimum of three independent experiments with the exception of the Nb that did not show influx inhibition below 70% during the first two trials. Multiple Dunett test comparisons were performed between each Nb (influx or efflux) against the non-treated relative activity. Multiple T-tests were performed between influx and efflux inhibition values within the same Nb. Statistical significance against the NT (100 %) is shown in asterisks and within the same Nb in hashes (* or # p.value < 0.0332, ** or ## p.value < 0.0021, *** or ### p.value < 0.0002 and **** or #### p.value < 0.0001).

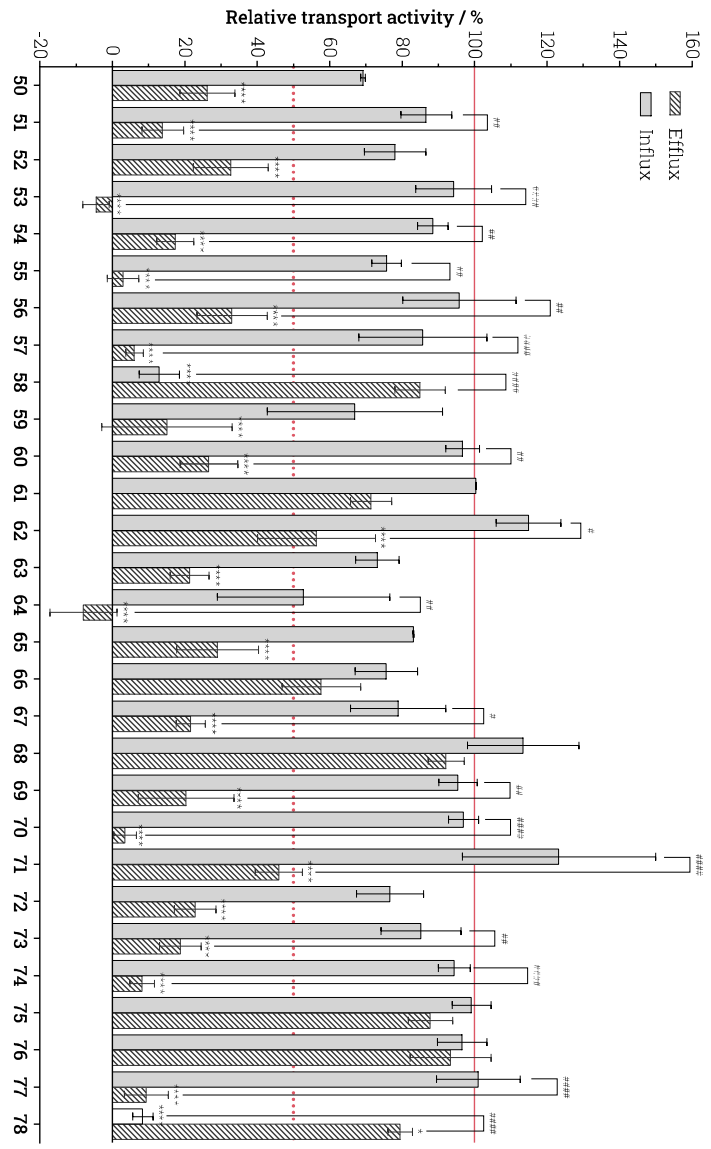
Relative transport activity / %
-20
0
20
40
60
80
100
120
140
160
Efflux
Influx
50 51 52 53 54 55 56 57 58 59 60 61 62 63 64 65 66 67 68 69 70 71 72 73 74 75 76 77 78

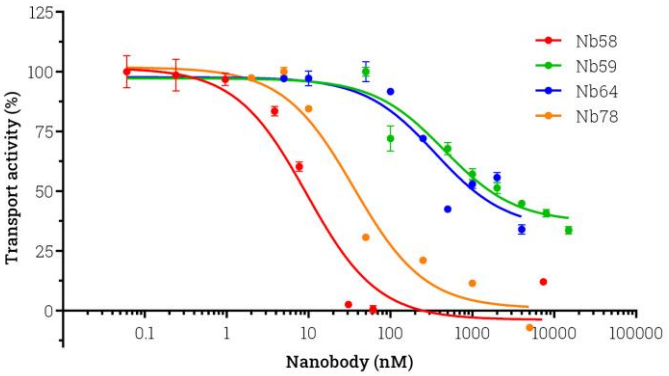

Figure 19. Influx dose responses. Nb58, 59, 64 and 78 influx dose responses. L-[^{3}H]-Ser uptake in 10 µM L-Ser against 4 mM L-Ala filled BasC-GFP PLs mean ± s.e.m. per each data point from a single experiment triplicates. Lower IC_{50}s were measured for Nb58 and 78 of 9.44 ± 2.42 and 34.8 ± 8.01 nM, respectively. Higher IC_{50}s were measured for Nb59 and 64 of 518 ± 170 and 362 ± 153 nM, respectively.

Yet, is not fully understood how Nb59 and 64 inhibited both efflux and influx, they may interacted non-specifically by the cytoplasmic side inhibiting the efflux transport activity of BasC. At this point, they were not be considered promising Nbs, although were kept being studied for compatibilities trying to solve this issue. Differently, as Nb58 and 78 showed a strong and clear inhibition effect, they were both selected for further characterisation, and possibility for being used in BasC structure solving and dynamics analysis, as they constituted the only two Nbs clearly binding from the extracellular side.

Finally, to categorise the interaction side of all Nbs, their influx and efflux effects were statistically compared between them, not only compared against the no treated measurement. Thus, Nbs were grouped finally into four different groups: non-inhibitors, influx inhibitors, efflux inhibitors and the weird inhibitors. Five no-inhibitor Nbs (Nb61, 66, 68, 75 and 76) were selected, which did not inhibit with statistical significance neither the influx nor efflux. Two Nbs were selected as influx inhibitors (Nb58 and 78) that inhibited the influx with statistical significance and did not show any inhibition effect on efflux. For the other hand, there were found 22 efflux inhibitors (Nb50-57, 60, 62-63, 65-67, 69-74 and 77) that showed statistical significance on efflux activity but did not affect significantly the influx activity. As this is the most populated group, the ones with better inhibition characteristics were the ones selected for further analysis. Lastly, a special group was created for two weird inhibitors (Nb59 and 64) that showed unexpected inhibition profiles as they inhibited BasC efflux activity with a statistical significance, but also they inhibited partially influx activity.

1.3. Nanobodies compatibilities

Once the interaction side of each Nb was deciphered, tertiary complexes assay by SEC was performed to study compatibilities between two Nbs interacting from opposite sides of BasC. Retention volumes between BasC incubated with none (BasC), one (BasC+Nb) or two Nbs (BasC-Nb+Nb) were compared. Nb were incubated for one hour at least, incubations with two Nbs were performed adding them sequentially with one hour of delay to allow the first incubation. So two different BasC-Nb+Nb samples were run on the SEC in different order of addition to see possible differences (e.g., BasC-58+74 designates that Nb53 was added first, and one hour later Nb74 was added). Comparing same-day SEC peaks, shifts observed between them are a clear Nb binding evidence. These shifts must be detected between BasC and BasC-Nb, and between this latter and BasC-Nb+Nb. When a tertiary complex was recognised, the conformations detected by these Nbs were defined as complementary.

Firstly, Nb compatibilities were studied between the extracellular binders (Nb58, 59, 64 and 78) and Nb74 (as BasC-conformation Ctrl) (Figure 20. E). BasC-58+74 resulted feasible (Figure 20. A), as also Nb78 (Figure 20. B), while Nb59 and 64 were not able to bind BasC. Heavier complexes were detected in tertiary complex of BasC-Nb58+74 and –Nb78+74 SEC profiles (indistinctly of the order of addition of the Nbs) (Figure 20. A-B, arrows). This means either that tertiary complexes were interacting between them or that these Nbs were able to bind more than once to BasC when they are added together with Nb74.

Then, Nb74-78 tertiary complex was studied in deep by MicroScale Thermophoresis (MST) on BasC labelled with sCy5 on the C427 solubilised in DDM (see Experimental Procedures 2.3, MicroScale Thermophoresis). MST results showed how Nb78 increased the affinity of Nb74 against BasC. The affinity measured by MST for Nb74 against BasC was 15.2 ± 8 nM (Figure 21. A), while its affinity for BasC-Nb78 increased until pM range, K_D = 74 ± 70 pM (Figure 21. B). Nb78 must do a conformational sampling in favour of Nb74 to lead this 4,500-fold increase of Nb74 K_D. The big s.e.m. comes to the high relative concentration of BasC used in the performed MST experiment regarding the very-low K_D found, lower BasC concentrations were unable to be used due to the consequent loss of fluorescence signal.

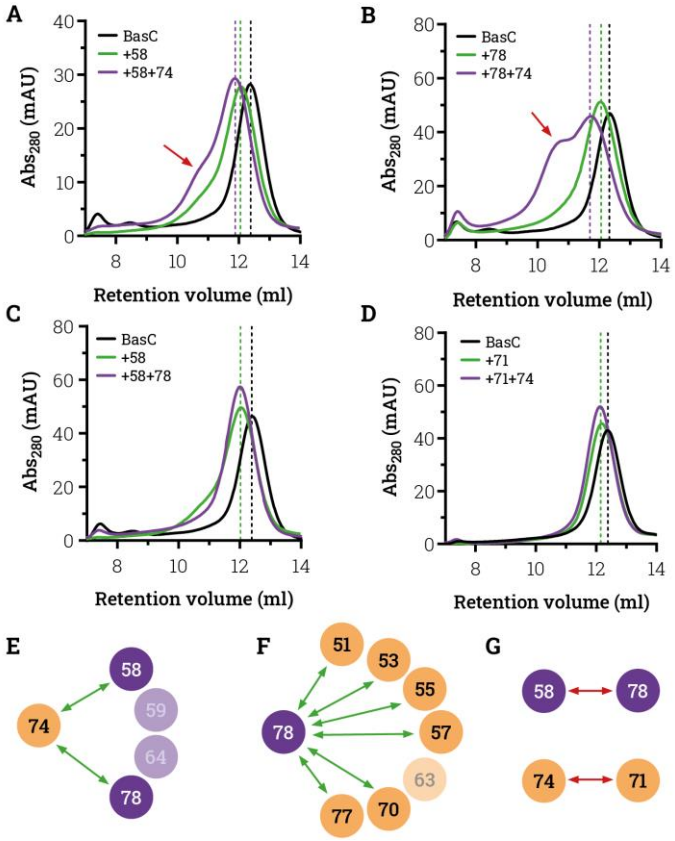

Figure 20. Nanobodies compatibilities. Representative results of compatibilities assay performed by SEC on a Superdex 200 10/300 GL column. Nb's of interest were assayed with Ctrls (Nb74 or 78) against BasC solubilised in DDM in a molar ratio of 1:1.5 (BasC:Nb). **A-D.** SEC profiles cut, normalised and overlapped for BasC (black), BasC+Nb (green) and BasC-Nb+Nb_{ctrl} (purple) are shown. Vertical dashed lines (same colour as SEC profiles) label each retention volume averages (of BasC+Nb with BasC+Nb_{ctrl}, and of BasC−Nb+Nb_{ctrl} with BasC-Nb_{ctrl}+Nb). **A-B.** Compatibility between Nb58 and 74 (**A**) and between Nb78 and 74 (**B**). Both also showed heavier complexes in the BasC-Nb+Nb_{Ctrl} sample (red arrows). **C-D.** Incompatibility between Nb58 and 78 (**C**), and Nb71 and 74 (**D**). Nbs binding from the same side were unable to form tertiary complexes. **E-G.** Schematic representation of compatibilities (green arrows) and incompatibilities (red arrows) between different cytoplasmic (orange) and extracellular (purple) Nbs. Those who did not bind to BasC are half-transparent. Schemes sorted by extracellular screening (**E**), cytoplasmic screening (**F**) and same-side trials (**G**).

Nb78 was selected as BasC-conformation Ctrl for the cytoplasmic compatibility screening coupled with the most efflux inhibitory Nbs (Nb51, 53, 54, 55, 57, 70 and 77) (Figure 20. F). All of the tested cytoplasmic inhibitors resulted to be compatible with Nb78. This means that they recognised either the same BasC conformation from opposite sides or different "side-conformations", which are compatible. For example, if a Nb binds from the extracellular side, it might permit BasC still to adopt distinct "cytoplasmic-conformations" (e.g., outward- and inward-closed, outward-closed inward-open…). Then, all the cytoplasmic Nbs that could bind to at the same time to one of these cytoplasmic-conformations would be detecting compatible conformations, even though they recognised different "cytoplasmic-conformations" between them.

Moreover, the compatibility between extracellular binders Nb58 and 78 and between intracellular binders Nb74 and 71 was also tested and they resulted to be incompatible (Figure 20. C-D). Same-side Nbs were expected to be incompatible, due to the steric effect they made one on the other. Thus, only one Nb seemed to be able to bind from the same side at the same time.

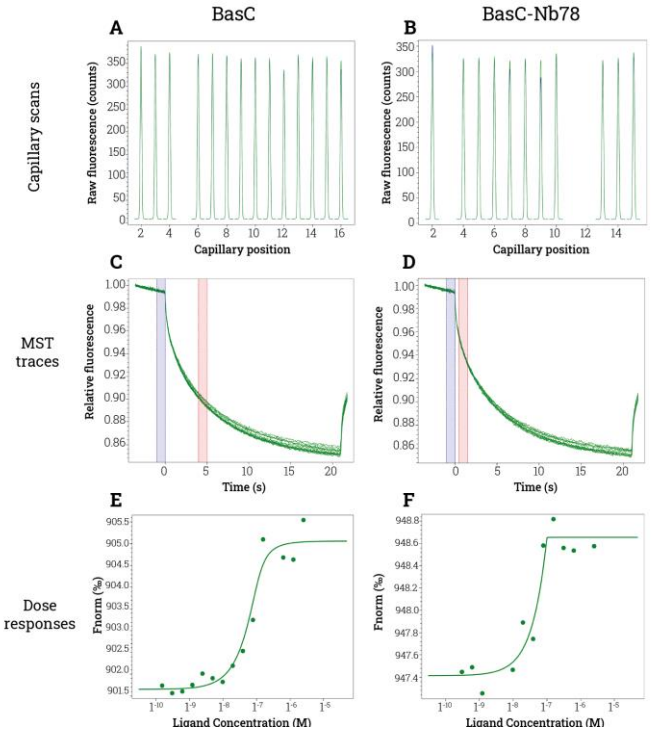

Figure 21. Nb78 effect on the binding of Nb74. Representative data of single MST assay performed on BasC WT variant labelled with sCy5. BasC concentration used was in the nM range, and it was screened against increasing concentrations of Nb74 when previously bound (BasC-Nb78 (**B, D and F**)) or not (BasC (**A, C and E**)) to Nb78 in Premium Capillaries. **A-B.** Capillary scan average of ~350 raw fluorescence counts per capillary. Spoiled capillaries (e.g., higher counts, lower counts…) were not used for the measurement. **C-D.** MST traces showing no aggregation and no ligand induced photo bleaching rate change. **E-F.** Dose responses with amplitudes of 3.4 and 1.2 points from normalised fluorescence. No significant signal to noise ratio with a measured. Triplicates performed for Nb74 against BasC (K_D = 15.2 ± 8 nM) and duplicates against BasC-Nb78 (K_D = 74 ± 70 pM).

1.4. BasC cytosolic gate dynamics

For the dynamics and conformational analysis Alternating Laser Excitation (ALEX)-single molecule Fluorescence Resonance Energy Transfer (smFRET) approach (Hohlbein et al., 2014) (ALEX-smFRET) was performed in collaboration with T. Cordes laboratory in LMU München. ALEX-smFRET is based in the excitation alternatively with lasers (561 and 640 nm) of two fluorophores attached to the residues selected. Intramolecular FRET populations' were measured as in Figure 14, analysing BasC double-Cys variants labelled in very low concentration (pM range) solubilised in DDM.

The aim of ALEX-smFRET measurements was to select from all the promising Nbs the ones that are able to freeze BasC in specific distances between TMs distinct from the ones present in apo conditions and/or forced by the Nb74. Further analysis comprised the effect of substrates on this closing and opening, then also the possible effect of Nb to block this substrates effect and finally an analysis of all this substrates effects on K154A LPI-related variant. For BasC, fluorophores were thought to be attached to it through maleimide bond to double-Cys variants basing this approach on Majumdar studies on LacY transporter (Majumdar et al., 2007) and Zhao's on LeuT (Zhao et al., 2011).

When this project started, the only known structures related to LATs were from LATs homologues. AdiC was, back then, the best candidate for modelling the light subunit of HATs. AdiC has around an 18 % SI to eukaryotic LATs and its atomic structure agrees fully with the previous low-resolution structural studies of the light subunits of HATs and hLATs (Rosell et al., 2014). Therefore, our Cys variants selection relied on the tilting differences between BasC inward open (PDB ID 6F2G) and AdiC outward open (PDB ID 3OB6): TM1a by the cytosolic gate (opened in BasC and occluded in AdiC) and TM6a by the extracellular gate (occluded in BasC and opened in AdiC).

When the first structures of eukaryotic LATs were solved, structural analysis was redone between LAT1 inward occluded structure (PDB ID: 7DSK) and BasC inward open (PDB ID: 6F2G). Thus, BasCs was modelled as LAT1 inward occluded and compared to the current BasC structure inward open (Figure 22. A). This new structural model comparison showed how TM1a tilted as expected (Figure 22. B), while TM6a did not clearly (Figure 22. C). Thus, the study was focused on the TM1a dynamics excluding the TM6a except for pairing with the TM1a. In parallel, different non-tilting TMs were selected to be paired with the TM1a. These non-tilting TMs selected from the structural model comparison were TM4 (Figure 22. D) and 12 (Figure 22. A); the latter not only for being static but also because contained the unique WT Cys – C427). With this selection, TM1a tilt analysis could be performed pairing it in three different ways, resulting in the following BasC double-Cys variants: TM1a-4, TM1a-6a, and TM1a-12.

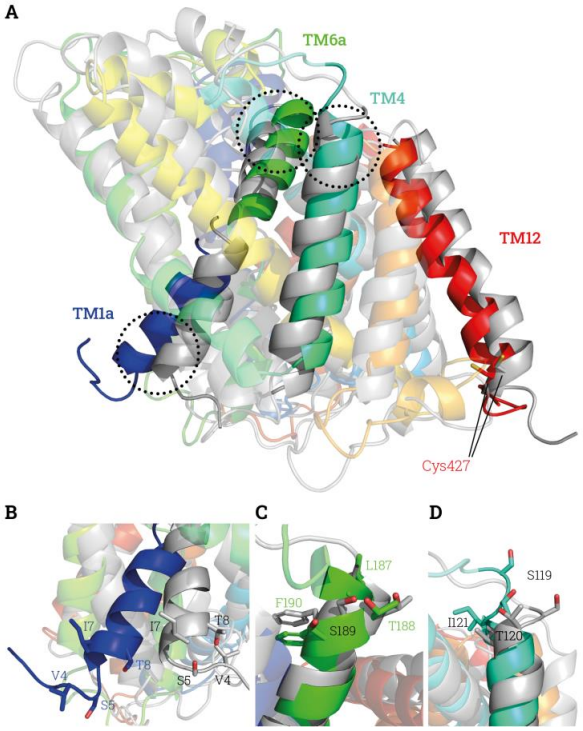

Figure 22. Inward to outward facing model. BasC inward facing structure (PDB ID: 6F2G) in rainbow and modelled BasC structure as LAT1 outward facing (PDB ID 7DSK) in grey. **A.** Complete view of the structural alignment of both structures. Selected TMs are highlighted in opaque for a simpler interpretation, TM1a in blue, TM4 in turquoise, TM6a in green and

TM12 in red. C427 in the TM12 is shown in sticks. Residues selected for Cys mutations are represented in sticks and labelled in the zoomed views (encircled areas) of TM1a (V4, S5, I7 and T8) (**B**), TM4 (L187, T188, S189 and F190) (**C**) and TM6a (S119, T120 and I121) (**D**). Figure created with Open-Source PyMol (The PyMOL Molecular Graphics System, Version 2.0 Schrödinger, LLC).

1.4.1. BasC cysteine variants

Different residues to be labelled were selected from the more exposed to the solved region of the selected TMs. The used double-Cys BasC variants were based on single-Cys mutants selected on each TM: V4, S5, I7 and T8 on TM1a; S119, T120 and I121 on TM4; and L187, T188, S189, F190 on TM6a (Figure 22). For the TM12 the WT Cys was used (C427), while for the double-Cys variants that did not need it, they were created on a Cys-less BasC variant (C427A).

All single-Cys mutants were generated on BasC C427A variant by site directed mutagenesis (Experimental Procedures 1.5). All BasC mutants were validated by sequencing, expressed, purified fused to GFP solubilised in DDM (Experimental Procedures 1.7) and reconstituted into liposomes for influx activity measurement (Experimental Procedures 3) (Figure 23) with the exception of S189C that presented a very low yield of purification and little amount protein was obtained for transport assays. The most active mutant on each TM was selected for double-Cys variants generation. Thus, I7C, T120C and L187C variants were selected for TM1a, 4 and 6a, respectively.

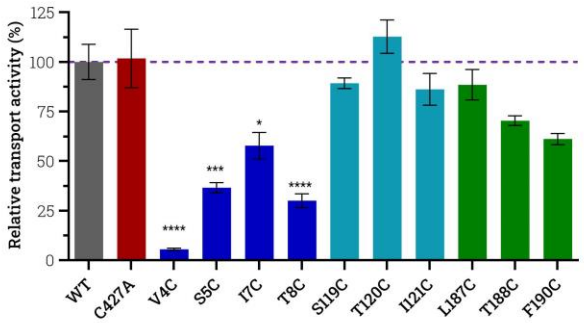

Figure 23. Relative transport activity for single-Cys BasC variants. Relative 10 µM L-[^{3}H]-Ser (1 µCi/µl) influx transport into BasC-GFP-PLs containing 4 mM L-Ala. BasC variants showed: WT (grey), C427A (red) and single-Cys variants: in TM1a (V4C, S5C, I7C and T8C in dark blue), in TM4 (S119C, T120C and I121C in turquoise) and in TM6a (L187C, T188C and F190C in dark green). Data shown (mean ± s.e.m.) is from single experiments triplicates. T-tests performed between relative transport activities of single-Cys variants and WT (* $p < 0.05$, *** $p < 0.005$, **** $p < 0.001$).

The double-Cys variants were generated as single-Cys from the selected residues for TM1a, 4 and 6a plus C427 in TM12. Used names from here on will be the names referring the TMs: TM1a-12 (I7C-C427), TM1a-4 (I7C-T120C-C427A), TM1a-6a (I7C-L187C-C427A), TM4-12 (T120C-C427), TM4-6a (T120C-L187C-C427A) and TM6a-12 (L187C-C427). All these BasC double-Cys variants were generated on BasC by site directed mutagenesis (Experimental Procedures 1.5). All mutants were validated by sequencing, expressed, purified fused to GFP solubilised in DDM (Experimental Procedures 1.7) and reconstituted into liposomes for influx activity measurement (Experimental Procedures 3) (Figure 24) and only TM1a-6a lost its activity until less than 50 %.

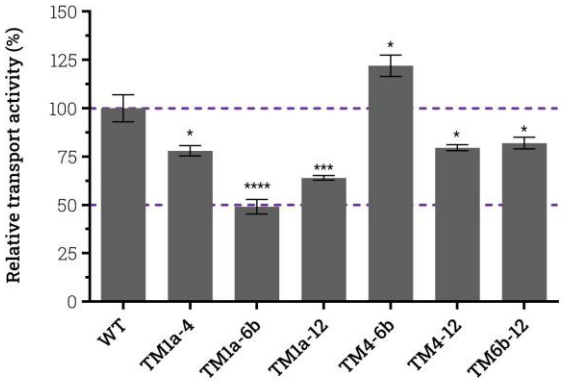

Figure 24. Relative transport activity for double-Cys BasC variants. Relative 10 µM L-[^{3}H]-Ser (1 µCi/µl) influx transport into BasC-GFP-PLs containing 4 mM L-Ala. BasC WT and double-Cys variants plotted. Horizontal dashed lines label the 100 and 50 % relative transport activity. Data shown (mean ± s.e.m.) is from single experiments triplicates. T-test performed between relative transport values of double-Cys mutants and WT (* p.value < 0.05, *** p.value < 0.005, **** p.value < 0.001).

1.4.2. BasC cytosolic gate model

BasC inward facing structure and outward facing model were used to measure and analyse the distances and changes between conformations between Cys pairs selected (Table 8. A). Distances were measured modelling the accessible volumes (AV) of each dye in each position measured with Olga software (Sindbert et al., 2011). Olga models these AVs with the flexibility that each dye would have in each position to be labelled (I7, T120, L187 and C427) taking into account their dimensions and linkers (Table 8. B). Then, with these AVs we can compare their average centre of the mass, the mathematical centre of all the possible positions the dye can assume. The comparison of the centres of the

mass of all the AVs between the two structures of BasC showed which positions were the ones that presented some tilt.

Analysing the AVs' centres of the mass, L187C (TM6a) showed a tiny tilt between conformations, of 1.9 Å, as predicted previously (Figure 22) and, therefore, this position will not be used to study the extracellular gate. Similarly, C427 (TM12) shows a small tilt between conformations, of 2.3 Å. This reinforces the use of this position as reference for the analysis of TM1a tilt, which shows a difference between conformations of 6.8 Å. As also predicted previously, this considerable change between conformations supports the use of this position, I7 in TM1a, to be analysed as a model for the closing and opening of the cytosolic gate. Surprisingly, even that TM4 did not show a clear shift between conformations (Figure 22), the centres of the mass of the AVs in T120C showed the biggest difference of all of them, a difference of 7.6 Å. This change of AVs centres of the mass is the responsible for the distances changes seen between TM4-6a and also increases the distance change observed between TM1a-4 in comparison of the change of distances between TM1a-12, that is less as C427 position is not tilting as much as T120C (Table 8).

A **Distances between dye accessible volume centres**

	sCy3-sCy5			Alexa 546-Alexa 647		
	Inward facing (Å)	Outward facing (Å)	Δ (Å)	Inward facing (Å)	Outward facing (Å)	Δ (Å)
TM1a-4	55.5	51.1	-4.4	55.8	51.4	-4.4
TM1a-6a	52.9	58.1	5.2	53.3	58.4	5.0
TM1a-12	59.7	57.8	-1.9	60.1	58.2	-1.9
TM4-6a	52.6	59.2	6.6	52.9	59.6	6.7
TM4-12	53.1	53.0	0.1	53.3	53.2	0.1
TM6a-12	56.9	58.3	1.4	57.1	58.5	1.4

B **Dye dimensions**

Dye	L_{linker} (Å)	W_{linker} (Å)	r_1 (Å)	r_2 (Å)	r_3 (Å)
Alexa 546 C_5	20.5	4.5	5	4.5	1.5
Alexa 647 C_2	21	4.5	11.0	4.7	1.5
Sulfo-Cy3	21	4.5	6.8	3.0	1.5
Sulfo-Cy5	21	4.5	11.0	3.0	1.5

Table 8. Distances between dye accessible volume centres. A. Distances measured in Angstroms (Å) between dye AVs centres according to inward open BasC structure (PDB ID 6F2W) and BasC modelled as LAT1 inward occluded (PDB ID 7DSK). For distances involving TM12, C-ter residues after C427 had to be removed. Selected residues were mutated to Cys with PyMol Open-Source Software (The PyMOL Molecular Graphics System, Version 2.0 Schrödinger, LLC) to be used as targets for maleimide dyes in the distances measurement with Olga software (Sindbert et al., 2011). Each distance was measured as the average of donor dye in each position with its acceptor in the other one and in the opposite direction. **B.** Dye dimensions in Å from their chemical structure used for modelling dye AVs, centres

and distances. Linker length (L_{linker}) and width (W_{linker}) are described as the distance from the attachment atom (carbon atom before the sulphur atom of the Cys) until the geometrical centre of the dye molecule and its thickness, respectively. Radius of the dye molecule (r_1, r_2 and r_3) are described each one per each of the space axes.

As the focus became the cytoplasmic gate and taking into consideration the tilting of each position and distances between Cys pairs, TM1a-4 and TM1a-12 were the final BasC double-Cys variants selected, excluding TM1a-6a as it lost more than 50 % activity. The most static pair is the TM4-12 as the distance between selected residues changes no much more than half an Angstrom. The biggest distance change is in the TM4-6a pair. Interestingly, when TM6a opens, its distances respect TM1a and 12 decrease oppositely of what happens for TM1a-4 and TM1a-12 that decreases the distance for the closing (Figure 25).

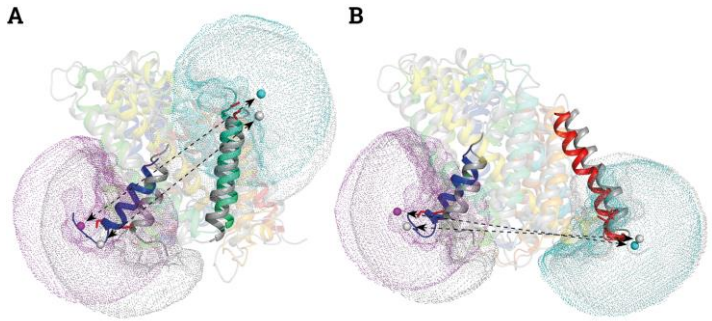

Figure 25. BasC double-Cys variants for TM1a tracking. BasC inward facing (PDB ID 6F2G) shown in rainbow, BasC modelled as LAT1 outward facing (PDB ID 7DSK) in grey. Cys residues to label are shown in red sticks, and representative AVs for sCy3 and sCy5 are shown in dots and their centre of the mass with a same-colour sphere. sCy3 AV is shown for position I7C in the TM1a (blue) in pink and grey for inward and outward facing conformations, respectively. **A.** BasC TM1a-4 variant labelled with sCy3-sCy5 model. sCy5 AV is shown on T120C position in TM4 (turquoise) in cyan and grey for the inward and outward facing conformations, respectively. Distances between positions are 55.5 and 51.1 Å for inward and outward facing conformations, respectively (dashed arrows). **B.** BasC TM1a-12 variant labelled with sCy3-sCy5 model. sCy5 AV is shown on C427 position in TM12 (red) in cyan and grey for inward and outward facing conformations, respectively. Distances between positions are 59.7 and 57.0 Å for inward and outward facing conformations, respectively (dashed arrows). Figure created with Open-Source PyMol (The PyMOL Molecular Graphics System, Version 2.0 Schrödinger, LLC), drawing AVs measured and simulated with Olga software (Sindbert et al., 2011).

Each ALEX-smFRET measurement was obtained in a complete apparent FRET efficiency (E^*) vs. apparent FRET stoichiometry (S^*) histogram where each data point is a single molecule lecture. Sample populations are fitted tak-

ing into account a stoichiometry (S^*) of 0.5 and compared to different conditions on same sample measured within the same day avoiding interferences on the results due to microscope alignment changes between datasets (Figure 26).

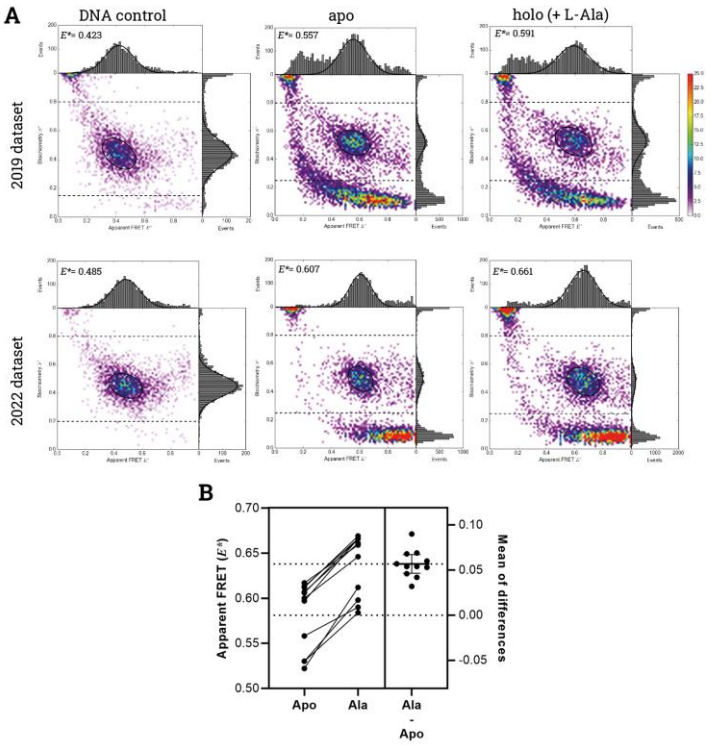

Figure 26. Microscope alignment difference between data sets. Same samples mean E^* differences observed between 2019 and 2022 datasets come from the different microscope alignment for samples labelled with sCy3-sCy5. **A.** Complete E^* vs S^* histograms of 2019 and 2022 datasets. Population mean E^* is labelled in each histogram. 18 base pairs length double strand deoxyribonucleic acid (DNA) Ctrl (DNA control) and BasC TM1a-4 variant labelled in apo and holo (300 mM L-Ala) conditions are shown per each dataset. **B.** Main population mean E^* of all dataset measurements of BasC TM1a-4 variant in apo and holo (300 mM L-Ala) conditions (left), their differences by same-day pairs (connecting lines), and the summary of the differences (right) coinciding even coming from different datasets.

Different burst search modes can be applied to raw data. All-Photon-Burst-Search (APBS) mode plots all the fluorescence signals measured from all the possible labelled molecules (i.e., D-A, only A and only D). But in some cases, if needed, Dual-Channel-Burst-Search (DCBS) mode was used, only plotting species detected as D-A (species measured when reading by the detectors from the A fluorophore when lasers were exciting the D). DCBS permit to decrease the background but with the side effect data loss. DCBS was only applied if needed for the proper population fittings.

BasC double-Cys variants selected for TM1a tilt studies were initially labelled on column during BasC purification in DDM indistinctly with sCy3-sCy5 or Alexa 546-Alexa 647 dye pairs. Thus, ALEX-smFRET results shown come from BasC TM1a-12 variant labelled with either sCy3-sCy5 or Alexa 546-Alexa 647 and BasC TM1a-4 variant with sCy3-sCy5.

Apo conditions were the first to be used for the ALEX-smFRET measurements. BasC TM1a-4 and TM1a-12 variants labelled with sCy3-sCy5 dye pair in apo conditions gave a single population at apparent FRET E^* (E^*), around 0.6 and 0.7, respectively (Figures 24. A and 25. A). Surprisingly BasC TM1a-12 variant labelled with Alexa 546-Alexa 647 dye pair in apo conditions gave already two distinct E^* populations (around 0.5 and 0.7 E^*, Figure 27. A), named from here on as high- and low-FRET populations. Interestingly, this population differences between BasC TM1a-12 variants labelled with sCy3-sCy5 or Alexa 546-Alexa 647 comes only from the different labelling.

1.4.3. Effect of nanobodies on BasC cytosolic gate

Nbs' effect on cytosolic gate position was performed by ALEX-smFRET experiments. This analysis comprised the Nbs selected during the first phase of this thesis. The aim was to compare their effects with Nb74's effect, to finally choose candidates to co-crystallise with BasC to obtain different conformations than the inward open structure published (PDB IDs 6F2G and 6F2W, (Errasti-Murugarren et al., 2019)).

Initially the selected Nbs, based on their binding and inhibition profile characterisation, were tested for some of the chosen BasC double-Cys variants and labelling for a fast screening trying to see by their effect on the E^*. Extracellular inhibitory Nbs (Nb58 and 78) were selected as also the most inhibitory from the intracellular side (Nb51, 53, 55, 57, 70, 73, 74 and 77). This selection excluded the Nbs that did not show binding or inhibition: Nb61, 63, 63, 64, 66, 68, 75 and 76. As also excluded the Nbs with mild inhibition profiles (above 20 % remaining activities): Nb50, 52, 56, 60, 65, 67, 69 and 72; with the exception of Nb71, which relevance comes from first ALEX-smFRET measurements screening. From the weird inhibitors, Nb64 was discarded for not being able to detect its binding upon SPR, thus Nb59 was selected despite showing a mild inhibition for influx (with dose response also performed (Figure X)) at the same time as inhibiting efflux in a strong manner.

Once the screening was done, here there are presented the results of the most relevant ones. From one side, the ones that increased the E^* of the BasC double-Cys variants and labelling tested were Nb53, 58, 78 and 74. From the other side, the ones that did reduce the E^* were Nb51, 59 and 71.

Firstly, for the BasC TM1a-4 variant labelled with sCy3-sCy5 (Figure 27), the single population measured in apo conditions (Figure 27. A-B) shifted to lower E^* for Nb71 and 51 in the same level with 0.032 points (Figure 27. B-C). While Nb59 did not show statistical differences and only the tendency to lower the E^* in 0.011 points. In the other way around, Nb74 showed an increase of the E^* of 0.044 (Figure 27. B-C). While Nb53 and 58 did also show increases, in lower and higher manners, of 0.010 (Figure 27. B-C) and 0.080, respectively. Nb78 did show also the tendency of increasing the E^* with 0.049 points. As Nb53 and 58 did show increases of E^* and were binding from opposite sites, they were also tested combined, and they did sum their effects and a higher E^* state was measured with an increase of 0.120 points. For a general overview of all these relevant Nbs performed on BasC TM1a-4 variant is shown in Figure 27. C.

The same Nbs were tested on BasC TM1a-12 variant labelled with sCy3-sCy5 (Figure 28). The reading of the results is similar because the single population shown in apo conditions (Figure 28. A-B) shifts to higher or lower E^* as the previous BasC TM1a-4 variant. Thus, Nb71 lowers it 0.061 points while Nb51 does the same effect lowering the E^* 0.067 points and Nb59 forces to decrease the E^* by 0.079 points (Figure 28. B-C). For all the opposite-effect Nbs, non-showed statistical significance, but they show a tendency to increase the E^*: Nb53 by 0.027 points (Figure 28. B-C). Nb58 by 0.024 points, Nb78 by 0.015 points and Nb74 not only increases the E^* by 0.011 points, but also wideners the population increasing the variability of E^* (Figure 28. B-C). For a general overview of all these relevant Nbs performed on BasC TM1a-12 variant is shown in Figure 28. C.

Finally, some of these relevant Nb were assayed binding to the third and last BasC TM1a-12 variant labelled with Alexa 546-Alexa 647. Here, BasC in apo conditions adopts by itself two populations (Figure 29. A). A low-FRET population with E^* = 0.519 and S^* = 0.454 and a high-FRET population with E^* = 0.699 and S^* = 0.416. The shifts of both populations occurred when Nbs were added (Figure 29. B). In this case, Nb71 did converge all the species into one single population at even lower E^* values than the lower-FRET apo population, decreasing its E^* by 0.039 points (Figure 29. B-C). The same effect was observed for Nb51 that showed the tendency to decrease the low-FRET apo population E^* by 0.060 points (Figure 27. B-C). Then, for the opposite-effect Nbs, Nb53 maintained the double population distribution as in apo conditions, but both positioned at higher E^* values, the tendency for the low-FRET population was to increase its E^* by 0.022 points and for the high-FRET population in increased for 0.036 points (Figure 29. B-C). Lastly, for the Nb74 a similar double population distribution was shown in the single experiment that was performed, with the difference of the high-FRET population decreasing E^*. Both Nb74 populations with this BasC variant and labelling are narrower between

them, there is the tendency of increase low-FRET population E^* by 0.100 points and decreased the high-FRET population E^* by 0.066 points (Figure 29. B-C).

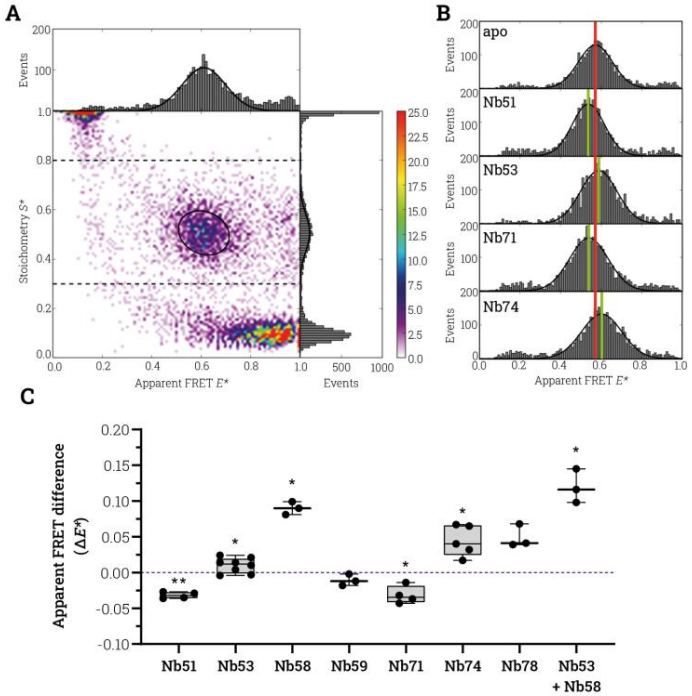

Figure 27. Effect of nanobodies on TM1a-4 variant labelled with sCy3-sCy5. Free-diffusion ALEX-smFRET analysis on BasC solubilised in DDM. **A.** Complete E^* vs. S^* histogram in APBS mode in apo conditions. Single population fitted with E^* = 0.612 and S^* = 0.505. **B.** Representative Events vs. E^* plots for apo, Nb51, 53, 71 and 74 conditions in DCBS mode measured within the same day. Nbs were added at least at 1 µM concentration. Red vertical line labels the population E^* of apo conditions and green vertical lines label each condition population E^*. **C.** All measurements for each condition were done adding Nb at least at 1 µM. Each data point is expressed as ΔE^* between Nb and apo conditions within the same day. Paired T-tests performed between same-day Nb and apo absolute values (* p.value < 0.05, ** p.value < 0.01).

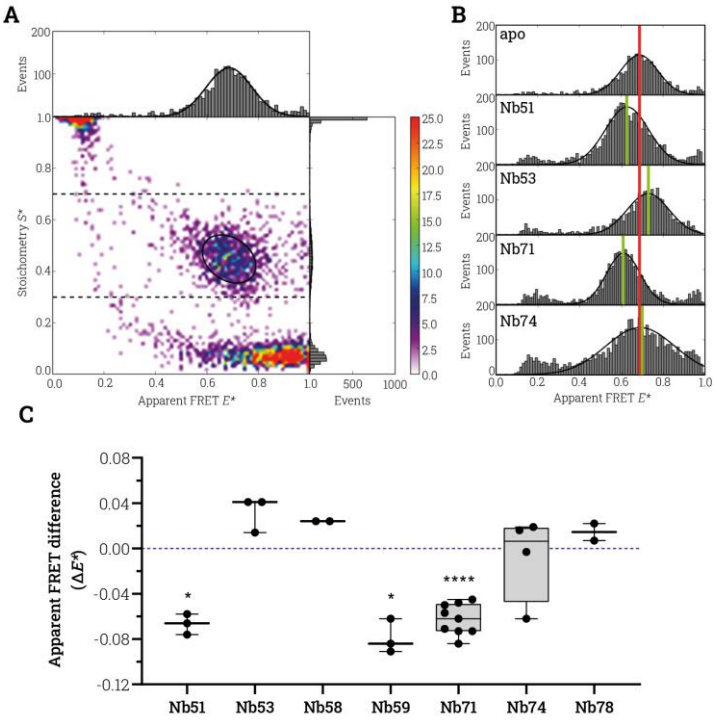

Figure 28. Effect of nanobodies on TM1a-12 variant labelled with sCy3-sCy5. Free-diffusion ALEX-smFRET analysis on BasC solubilised in DDM. **A.** Complete E^* vs. S^* histogram in APBS mode in apo conditions. Single population fitted with E^* = 0.687 and S^* = 0.447. **B.** Representative Events vs. E^* plots for apo, Nb51, 53, 71 and 74 conditions in APBS mode. Nbs were added at least at 1 µM concentration. Red vertical line labels the population E^* of apo conditions and green vertical lines label each condition population E^*. **C.** All measurements for each condition were done adding Nb at least at 1 µM. Each data point is expressed as ΔE^* between Nb and apo conditions within the same day. Statistical analysis performed with the absolute E^* in paired T-tests between Nb and apo conditions (* p.value < 0.05, **** p.value < 0.0001).

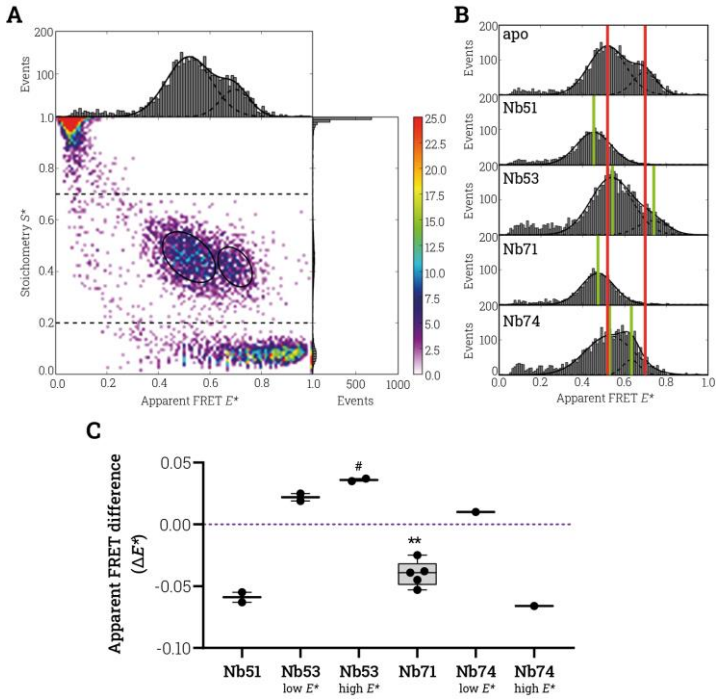

Figure 29. Effect of nanobodies on TM1a-12 variant labelled with Alexa 546-Alexa 647. Free-diffusion ALEX-smFRET analysis of BasC solubilised in DDM. **A.** Complete *E** vs. *S** histogram in APBS mode in apo conditions. Two distinct populations are shown fitted at *E** 0.519 and 0.699 and *S** of 0.454 and 0.416, respectively. **B.** Representative Events vs. *E** plots for apo, Nb51, 53, 71 and 74 conditions in APBS mode from different days. Nbs were added at least at 1 µM concentration. Red vertical lines label the mean *E** of apo condition low- and high-FRET populations and green vertical lines label each condition population *E**. **C.** All measurements for each condition were done adding Nb at least at 1 µM. Each data point is expressed as Δ*E** between Nb and apo conditions within the same day. Statistical analysis performed with the absolute *E** in paired T-tests between Nb and apo conditions (* p.value < 0.05, ** p.value < 0.01).

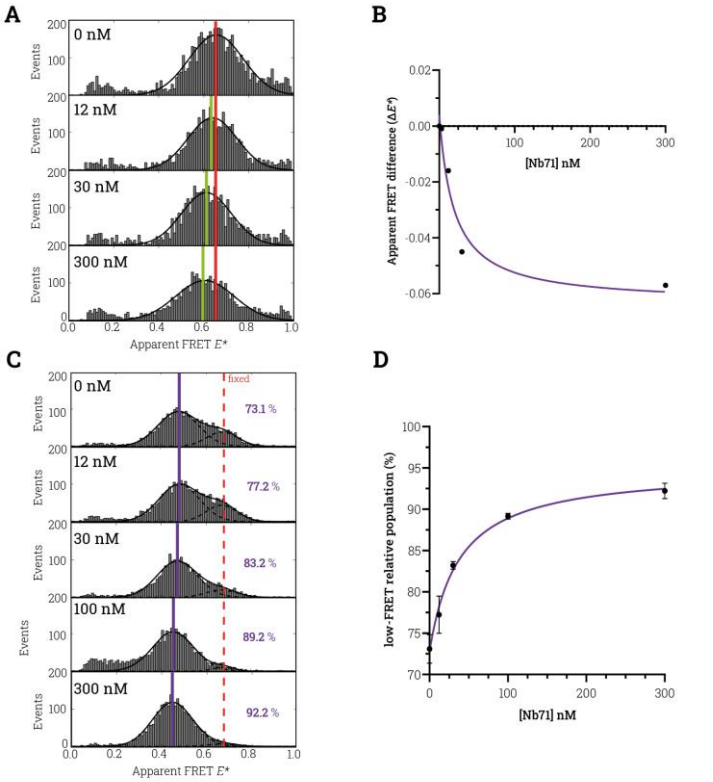

Figure 30. Nb71 effect titration. Nb71 titration by ALEX-smFRET effect on BasC TM1a-12 variants labelled with sCy3-sCy5 (A-B) and Alexa 546-Alexa 647 (C-D). **A.** Events vs. *E**histograms in DCBS mode at different Nb71 concentrations. Red vertical line labels apo (Nb71 0 nM) population *E**, green vertical lines label each condition population *E**. **B.** Single dose response experiment of Nb71 effect on *E**plotted. Fitting shows an IC_{50} measured of 19.6 ± 11.5 nM. **C.** Representative Events vs. *E**histograms in DCBS mode at different Nb71 concentration. Vertical red vertical line labels the apo high-FRET population *E**that was fixed for the fittings. Vertical purple lines label in each condition low-FRET population *E**. Percentage are labelled in the histogram. **D.** Mean ± s.e.m. of triplicate experiments plotted of Nb71 effect on low-FRET relative population. Fitting shows and IC_{50} of 37.4 ± 12 nM. The overall average K_D is 28.5 ± 8.9 nM.

Furthermore, Nb71 effect on BasC was analysed by dose response (Figure 30) to validate its effect was specific. Analysis was performed on BasC TM1a-12 variant labelled with sCy3-sCy5 (Figure 30. A-B) and with Alexa 546-Alexa 647

(Figure 29. B-C). For the first one, analysis was done measuring the apparent FRET difference change from apo state (0 % Nb71) until maximum concentration used (300 nM Nb71). IC_{50} measured for a single experiment was of 19.6 ± 11.5 nM. For the second one, analysis was done on the high-FRET relative population change from ~70 % in the apo state until ~100 % in Nb71 at high concentrations. It was done fixing the high-FRET *E** at the apo population *E**. The experiment was repeated trice different days and it resulted with an IC_{50} of 28.15 ± 3.49 nM. These IC_{50}s coincide with the K_D measured by SPR at the beginning of the Nbs characterisation process (K_D = 24.7 nM, Table 7. A).

1.5. In the search of BasC new conformation structure

From all previous Nb characterisation and their analysis by ALEX-smFRET, Nb53, Nb58 and Nb71 were selected for being used as chaperones in complex with BasC for its structure solving (Table 9). Nb53 was chosen as a high affinity Nb in DM (K_D = 26.4 nM, Table 7. A) that binds through the cytoplasmic side of BasC and highly inhibits its transport activity (Figure 18) and confers it with a closed TM1a (Figures 27-29). Nb58 was chosen as a high affinity Nb in DM (K_D = 28.1 nM, Table 7. A), extracellular binder as highly inhibits BasC transport activity (Figure 18) with high affinity in PLs (IC_{50} = 9.44 ± 2.4 nM, Figure 19), also confers BasC conformation with a closed TM1a (Figures 27-29). Finally, Nb71 was also selected for being a high affinity Nb in DM (K_D = 24.7 nM, Table 7. A). Although Nb71 binds from the cytoplasmic side with a mild inhibition effect on BasC transport activity (Figure 18) it showed an opening of the cytoplasmic gate (Figures 27-29) that was studied in deep (IC_{50} = 23.9 nM, Figure 30). Thus, for these Nbs, some further analysis on their effect blocking BasC transport activity was performed (Figure 31).

For the one side, Nb58 was assessed on BasC kinetic analysis parting from the effect that Nb74 did from the cytoplasmic side blocking the low affinity compound (Figure 8. B). It was seen that Nb58 binding from the extracellular side inhibited only the high-affinity component of BasC kinetic (Figure 31. A). Kinetics were performed on BasC-GFP reconstituted into PLs containing 4 mM L-Ala against increasing concentrations of L-Ala in the outer solution with the presence of 0.5 µCi L-[^{3}H]-Ala / 180 µl and the presence or absence of 15 µM Nb58. Transport was allowed for 5 s and stopped. In parallel, for Nb53 and Nb71 it was checked their dose response on efflux that was not performed previously for all cytoplasmic Nbs for the experimental trickiness of the assay. Thus, Nb53 and 71 resulted with an IC_{50} of 1.44 ± 1.0 and 11.9 ± 2.1 µM, respectively (Figure 31. B-C). For Nb71 was seen, then, that the concentrations used for the initial influx and efflux transport inhibition screening were far below its IC_{50}. Then, Nb71 was assayed again for its transport inhibition profile increasing its concentration until 100 µM and it showed a high blocking effect on efflux (Figure 31. D). Thus, Nb71 is not a mild efflux blocker, but it has very low affinity for BasC when reconstituted into PLs.

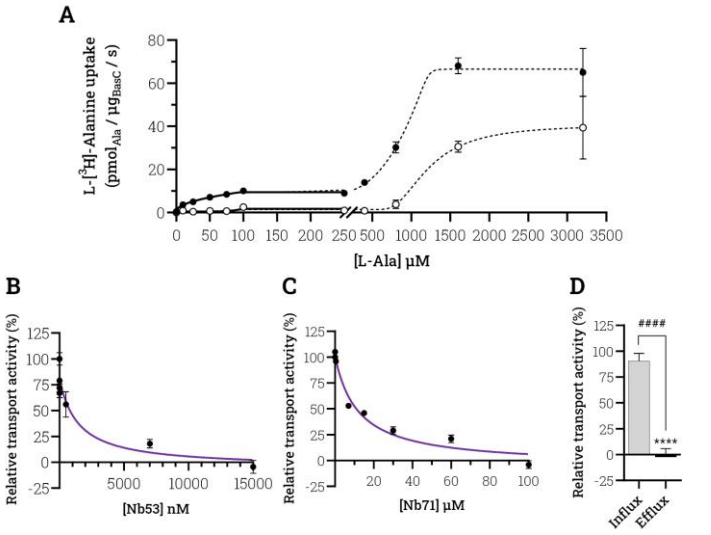

Figure 31. Nb53, Nb58 and Nb71 characterisation. A. Representative uptake kinetics of BasC-GFP PLs varying the extra liposomal concentration of L-Ala with the presence of 0.5 µCi / 180 µl of L-[^{3}H]-Ala. With the absence of Nb58 (black dots), the kinetics is complex with two components. Under the presence of 15 µM Nb58 (white dots), only the high-affinity component is depleted. Data (mean ± s.e.m.) correspond to triplicates. **B-C.** Representative Nb53 (B) and Nb71 (C) dose responses on efflux transport activity of BasC PLs. IC_{50} measured are 1.44 ± 1.0 and 11.9 ± 2.1 µM for Nb53 and Nb71, respectively. Data (mean ± s.e.m.) correspond to triplicates. **D.** Influx and efflux assays for Nb71 at 100 µM. Data (mean ± s.e.m.) correspond to three independent experiments. Statistical analysis performed by T-test Student with influx and efflux absolute values against NT PLs samples (asterisks, **** p.value < 0.001) and between relative transport activities of influx and efflux (hashes, ### p.value < 0.005).

		Nb53	Nb58	Nb71
	K_D (nM) Surface Plasmon Resonance Affinity	26.4	28.1	24.7
	IC_{50} (nM) Transport assays	1.4×10^3	9.4	$11{,}9 \times 10^3$
smFRET	**TM1a-4** sCy3-sCy5	↑ ΔE^* (*)	↑ ΔE^* (*)	↓ ΔE^* (*) IC_{50} = 28.5 nM
	TM1a-12 sCy3-sCy5	↑ ΔE^* (ns)	↑ ΔE^* (ns)	↓ ΔE^* (****)
	TM1a-12 Alexa 546-Alexa 647	↑ ΔE^* (ns)	↑ ΔE^* (ns)	↓ ΔE^* (**)

Table 9. Summary of selected Nbs for BasC structural studies. Summary of all data collected from the final selected Nb for structural studies in complex with BasC. Surface Plasmon Resonance K_D (nM) measured in 0.17 % (w/v) DM, IC_{50} (nM) of their blocking effect on influx (Nb58) or efflux (Nb53 and Nb71) BasC transport activity in PLs and their E^* changes (↑ increase or ↓ decrease) measured in the three different BasC double-Cys variants and dye pairs. Statistical significance for ALEX-smFRET measurements is indicated between brackets as explained in each results figure (ns, no statistical difference) and the IC_{50} of the dose response for Nb71 on TM1a dynamics.

Trials for structure acquisition were focused on Nb53 and Nb53-58 BasC complexes in crystallography and, in parallel, Nb71 complexes in cryo-EM. All of them performed solubilised in 0.17 % (w/v) DM.

1.5.1. BasC-Nb53-58

BasC was expressed and purified in DM without GFP (Experimental procedures 1.7) and incubated with Nb53 or Nb53 and 58 at high concentrations for complex formation for XRC (Experimental procedures 5) and they were screened on commercial and custom screening plates (Appendix E).

First trials were performed for BasC-Nb53 complexes purified by SEC on Superdex 200 10/300 GL column. Regular crystal screenings for membrane proteins were seeded in different conditions in 96 wells sitting drop plates (Experimental Procedures 6.1 X-ray crystallography and Appendix E. Crystallographic screening plates). Thin needle-like crystals (Figure 32. C) grown in wells E5 and E6 from PiPEG plate at 20 ºC, D6 well from PiPEG plate at 4 ºC and H3 well from MembGold2™ at 20 ºC. Optimisation plates based on these well conditions were made, and similar thin needle-like crystals were found without any clear improvement of crystal shapes or sizes. Diffraction of these crystals at ALBA Synchrotron (Cerdanyola, Barcelona, Spain) did not achieve resolutions below 8 Å.

To improve the contacts between molecules, Nb58 was added in order to co-crystallise the BasC-Nb53-58 tertiary complex. After SEC purification (Figure 32. A), presence of BasC and Nbs in the heaviest peak were checked by SDS-

PAGE (Figure 32. B). From regular screenings for membrane proteins, thick needle-like crystals (Figure 32. C) appeared on E6 well on PiPEG plates (50 mM ADA pH 6.8, 6.4 % (w/v) PEG MME 2000 and 17.1 % (w/v) PEG 3000) and optimisation plates were based on these conditions. Similar thick-needle-like crystals appeared, and they were diffracted in the ESRF (Grenoble, France). In this case, diffraction achieved an overall resolution of 6.14 Å (Figure 33. F). The crystal was indexed at H3 space group with the following cell parameters: 357.5, 357.5, and 74.1 Å cell dimensions (a, b and c, respectively), and 90, 90, and 120 º cell angles (α, β, and γ, respectively).

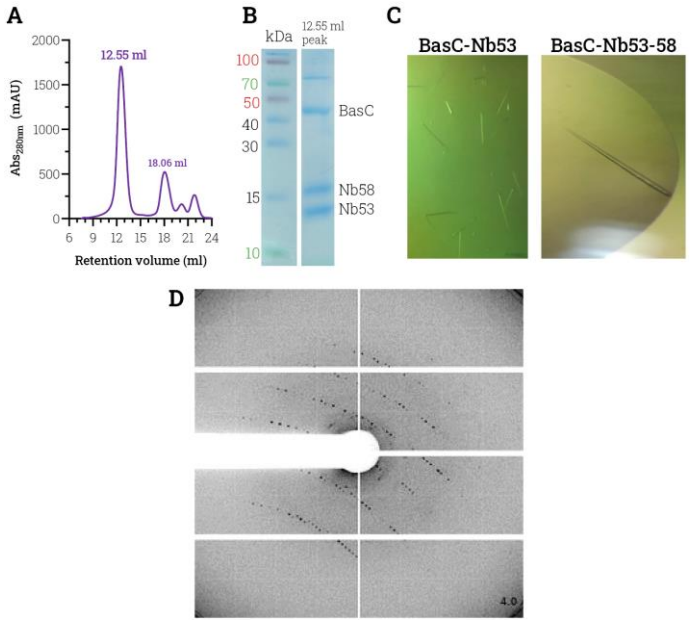

Figure 32. X-ray crystallography of BasC-Nb complexes. A. BasC-NB53-58 complex SEC run on a Superdex 200 10/300 GL column in DM buffer. Complex eluted at 12.55 ml, Nb53 and 58 excess, at 18.06 ml. **B.** SDS-PAGE of BasC-Nb53-58. Both proteins are shown in the 12.55 ml peak lane. Where both Nbs are detected, as BasC. Top band could be BasC dimers. **C.** Needle-like crystals of BasC-Nb53 (left) and BasC-Nb53-58 crystals (right). Note the improvement on length and thickness. **D.** Diffracting pattern of BasC-Nb53 needle-like crystals at 8 Å resolution. **D.** Representative diffraction pattern for BasC-Nb53-58 crystal.

Although the resolution achieved is not at atomic level, it can be extracted some information as the general position of the TMs. A general view of the structure shows how the conformation solved of BasC-Nb53-58 do not differ too much from the previously solved one with BasC-Nb74 complex (Errasti-

Murugarren et al., 2019) (Figure 33. A). Despite smFRET-ALEX predicted a more closed state (Figures 27-29), this has not been revealed in the electron density. It can be seen a nanobody binding by the cytosolic side (Nb53) and other by the opposite face (Nb58) (Figure 33), discerned between them by the inhibiting transport sidedness assays (Figure 18). Actually, contacts between complexes have been seen between Nb53 (Figure 33. A), which interacts with BasC through its CDRs against the IL4 (TM8-9) (Figure 33. B). By the opposite side, Nb58 interacts to BasC through its CDRs to the EL2 (TM3-4) and EL4 (TM7-8) (Figure 33. C).

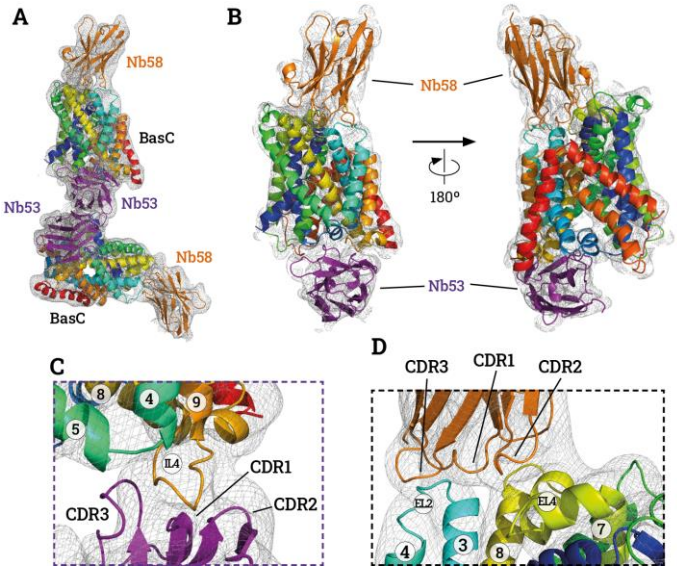

Figure 33. BasC-Nb53-58 structure. BasC-Nb53-58 X-ray electronic density where BasC (rainbow) from BasC-Nb74 structure (PDB ID 6F2W)) (Errasti-Murugarren et al., 2019) has been superposed, while Nb53 (purple) and 58 (orange) modelled. **A.** General view of interaction between complexes through Nb53. **B.** Side views of single complexes. Nb53 binds by the cytosolic side and Nb58 by the extracellular. Cytosolic cavity remain open and still accessible from the cytosol. Extracellular cavity remains closed. **C-D.** Electronic densities showing how Nb53 interacts through its CDRs against BasC IL4 (**C**) and Nb58 interacts through its CDR XX against EL3 and through its CDRs against EL4 (**D**).

1.5.2. BasC-Nb71

Cryo-EM assays were performed in collaboration with Dr. Oscar Llorca laboratory in the CNIO (Spanish National Cancer Research Centre, Madrid). BasC and Nb71 were produced at the IRB as described in Experimental procedures 1.7 and 1.8, respectively. After expression, BasC was concentrated until 75 or 150 µM and Nb71 until 300 µM, these both purified and concentrated proteins were sent to CNIO where Dr María Martínez Molledo and Dr. Jasminka Boskovic performed the complex purification, cryo-EM grid preparations, data collections and further analysis (Figure 34).

Cryo-EM grid preparation was carried out as explained in Experimental Procedures 6.2 Cryogenic-ElectroMicroscopy. First trials were carried with BasC concentration at 75 µM, while the second one was improved doubling its concentration until 150 µM. After purifying BasC-Nb71 complexes by SEC (Figure 34. A), checking presence of both proteins by SEC (Figure 34. B) and assessing the quality of the grids imaging through a 120 kV microscope (Figure 34. C) grids from the first and second trials were brought to 200 and 300 kV microscopes, respectively (Figure 34. D). Then, the final images were taken with the 300 kV microscope and low-resolution structure was solved (Figure 35).

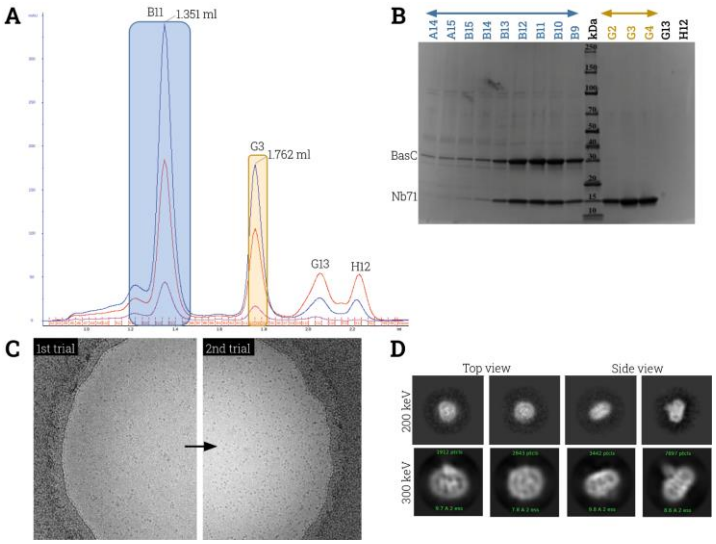

Figure 34. BasC-Nb71 complex for cryo-EM. (*Previous page*) **A.** High concentration BasC-Nb71 complex SEC profile in Superdex 200 increase 3.2/300 column equilibrated with DM buffer. SEC was performed injecting 60 µl sample in 50 µl loop at 0.05 ml/min flow. Fractionation was performed every 30 µl. **B.** SDS-PAGE of BasC-Nb71 complex SEC fractions. Excess of Nb71 elutes at 1.76 ml (yellow) and BasC-Nb71 complex at 1.35 ml (blue) **C.** Representative image of cryo-EM grid in JEM-2200FS microscope for the first (low concentration) and second (high concentration) trials. Note the increase of particle amount in the latter **D.** Representative BasC-Nb71 2D-class averages obtained from 200 and 300 kV microscopes from the first and second trials, respectively. 2D classification performed with CryoSPARC. Side views allow identifying the detergent micelle surrounding the TMs and some blurring in one side corresponding to Nb71.

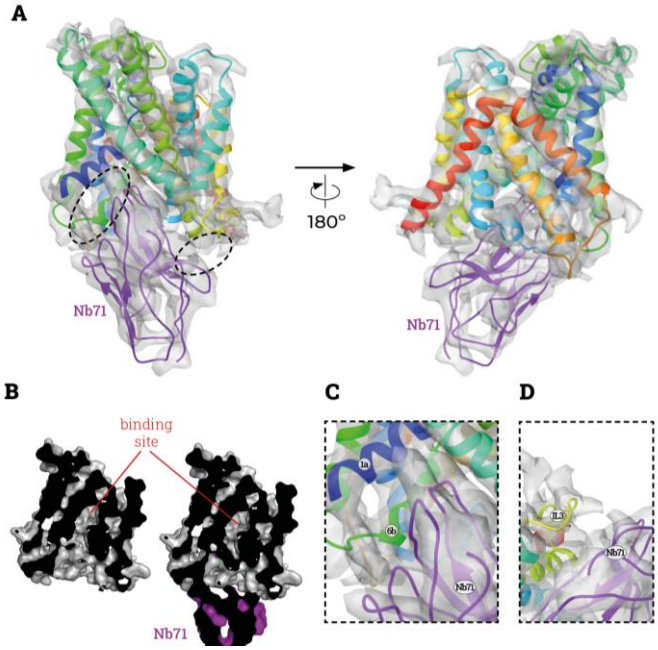

Figure 35. BasC-Nb71 cryo-EM structure. Modelled structure of BasC (rainbow) from BasC-Nb74 structure (PDB ID: 6F2W) (Errasti-Murugarren et al., 2019) and Nb71 (purple) within the electrostatic potential map (transparent). **A.** General view of BasC-Nb71 complex in inward facing apo conformation from side view. Nb71 interacts by the cytosolic side occupying the cytosolic cavity (**B**) and interacting with BasC through TM1a, 6b (**C**) and IL4 (TM8-9) (**D**). **B.** Cut side view of protein surface of BasC without Nb71 (left) and BasC-Nb71 complex (right). The entrance path from the cytosolic side to the substrate-binding site is clogged by Nb71. **C-D.** Electrostatic potential contacts between Nb71 CDRs and TM1a and 6b (**C**) and between Nb71-scaffold and IL4 (**D**). Figure created with UCSF Chimera (Resource for Biocomputing, Visualization, and Informatics at the University of California, San Francisco) (**A-B, D**) and Open-Source PyMol (The PyMOL Molecular Graphics System, Version 2.0 Schrödinger, LLC) (**C**).

The final BasC-Nb71 complex electrostatic potential map after data processing permitted fitting BasC from BasC-Nb74 (PDB ID 6F2W) (Errasti-Murugarren et al., 2019) and Nb71 model (Figure 35. A). Comparing this structure with BasC-Nb74 one, any conformational differences were detected, although ALEX-smFRET measurements predicted a more open state (Figures 25-27). What it was seen is that Nb71 occupies all the cytoplasmic cavity impeding the substrate to reach the substrate binding site from the cytoplasmic side (Figure 35. B) interacting with opposite sides of this cytosolic side. From the one hand its seen electrostatic potential bridges protruding from Nb71 CDRs 1, 2 and 3, to BasC TM1a and TM6b (Figure 35. C) and from the other hand there is also some electrostatic potential relating the scaffold structure of Nb71 with the IL4 (TM8-9) (Figure 35. C).

1.5.3. Nanobody effect on dye accessible volume clouds

After seeing no remarkable conformational changes on BasC-Nb71 and BasC-Nb53-58 solved structures, it was analysed how the presence of these Nbs (Nb53, 58 and 71) could affect the dye AVs clouds in the diverse labelled BasC double-Cys variants. There is a steric effect on AVs distribution due to Nb binding if the binding site and dye position are near. This was seen structures were solved, and it was checked how Nb71 was affecting the AVs of dyes on TM1a, representatively shown on sCy3 AV in Figure 36. Specifically, Nb71 increases distances between AV centres on BasC TM1a-4 variant, labelled with sCy3-sCy5. This distance increases from 55.47 to 57.33 Å when Nb71 binds.

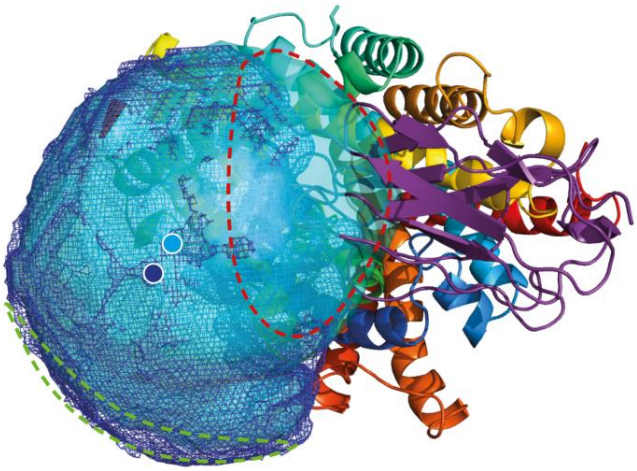

Figure 36. Nb71 effect on TM1a dye accessible volumes. (*Previous page*) Cytoplasmic view of BasC-Nb71 complex with the simulated AVs for sCy3 on TM1a (I7C) for BasC inward open structure (PDB ID: 6F2W) and BasC-Nb71 complex in cyan translucent surface and dark blue mesh, respectively. Nb71 displaces the AV centres (circumferences coloured as AVs) subtracting a volume near the cytoplasmic cavity (dashed red area) and pushing beyond the AV (green dashed area). Figure created with Open-Source PyMol (The PyMOL Molecular Graphics System, Version 2.0 Schrödinger, LLC), drawing AVs measured and simulated with Olga software (Sindbert et al., 2011).

2. Dynamics of the cytosolic gate of BasC

In order to decipher the dynamics of the inner gate of LATs through our bacterial model, BasC; the effect of substrates, the K154A variant and the combined effect of Nbs and substrates were analysed by ALEX-smFRET tracking BasC's TM1a.

2.1. Amino acids effect on BasC cytosolic gate

Substrates effect on TM1a were analysed on all BasC double-Cys variants and labelling. In all cases, the addition of substrates and inhibitors needed to be in high concentrations (above 100 mM) to reach the maximum effect possible. For this case BasC-GFP influx activity was tested in this high AA concentration conditions (Experimental Procedures 3.3) for two substrates (L-Ala and L-Ser) and L-Gln as no-substrate (Bartoccioni et al., 2019) (Figure 37). BasC-GFP was still able to transport both L-Ala and L-Ser at these conditions but was not transporting L-Gln.

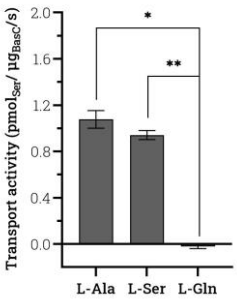

Figure 37. Substrates specificity at high concentration. Relative 10 µM L-[^{3}H]-Ser (1 µCi/µl) influx transport into BasC-GFP-PLs containing 100 mM AA. Transport was allowed for 5 s in solution containing 100 mM L-mannitol. Mean ± s.e.m. of three experiments. Results as expected according to previous work published in (Bartoccioni et al., 2019).

L-Ala was tested in all BasC double-Cys variants and increased the E^* for all of them. This effect was seen in BasC TM1a-4 variant labelled in sCy3-sCy5 as it increased the E^* in an average of 0.053 points (Figure 38. A-B). Also for BasC TM1a-12 variant labelled with sCy3-sCy5 dye pair where there can be clearly see the effect is related to L-Ala concentration. In this case L-Ala increased the E^* by 0.037 and 0.019 points for high and low concentrations of it, respectively (Figure 38. C-D). For BasC TM1a-12 variant labelled with Alexa 546-Alexa 647 the effect was the same but results come from another respective. As any statistic significant shift of E^* was observed, but low- and high-FRET populations experienced changes as high-FRET population relatively increased in number of events respect the low-FRET population. High-FRET population increased from an initial relative population of a 25 % in apo conditions to almost 50 % (49.5 %) for holo conditions (Figure 38. E). Furthermore, L-Ser was also used in high concentrations for BasC TM1a-4 variant and it gave an increase of E^* by 0.058 points (Figure 38. A-B). L-Ser in low-concentrations for BasC TM1a-TM12 variant also gave an increase of E^* by 0.040 points (Figure 38. C-D). As expected, L-Gln, which was not transporter, did not increase BasC TM1a-4 variant E^* (Figure 38. A.B).

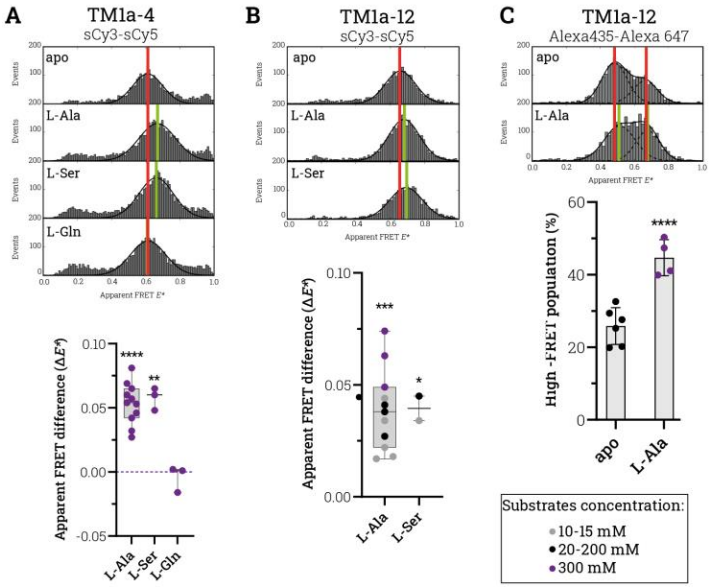

Figure 38. Amino acid effects on TM1a tilt. (*Previous page*). L-Ala, L-Ser and L-Gln dynamics effect by ALEX-smFRET on BasC TM1a-4 variant labelled with sCy3-sCy5 (**A**), BasC TM1a-12 variant labelled with sCy3-sCy5 (**B**) or Alexa 546-Alexa 647 (**C**). **A-C (top).** Events vs. *E** histograms for apo and holo conditions. Vertical red lines label apo population *E**, while green vertical lines label each holo condition population *E**. **A-C (bottom).** Mean ± s.e.m. of independent experiments (dots) are plotted. Single experiments AA concentration is labelled according to legend (low concentrations (10 to 15 mM) in grey, mid concentrations (20 to 200 mM) in black and high concentrations (300 mM) in purple). L-Ala and L-Ser increase the *E* (A-B)*, while L-Gln do not (A). L-Ala increase the events of the high-FRET population (C). Statistical analysis on A-B bottoms was performed using paired T-tests between each holo condition and its same-day apo condition in absolute values. Statistical analysis on C was performed using paired T-tests between high-FRET population relative population between apo and holo conditions of the same day (* p.value < 0.05, ** p.value < 0.01, *** p.value < 0.005 and **** p.value < 0.001).

In our laboratory, there has been a big effort to characterise BasC's substrate binding. Published results (Errasti-Murugarren et al., 2019) show L-Ala binding measured through thermostability on BasC-GFP WT variant solubilised in 0.17 % (w/v) DM. Measured K_D was 34.5 ± 2.1 mM. For BasC-GFP K154A variant, K_D was 61.4 ± 7.3 mM. As L-Ala effect was observed by ALEX-smFRET, and with the same aim to further describe binding, L-Ala was titrated on BasC TM1a-12 variant labelled with Alexa 546-Alexa 647. High-FRET population change in increasing concentrations of L-Ala (0 to 500 mM) resulted in an IC_{50} of ~50 mM, although saturation was not achieved (Figure 39. A). Then, L-Ala was also titrated on BasC TM1a-4 variant labelled with sCy3-sCy5, where saturation was reached. Apparent FRET difference change in increasing concentrations of L-Ala (0 to 500 mM) resulted in an IC_{50} of 40.4 ± 13.2 mM (Figure 39. B) (as the mean ± s.e.m. from three different experiments.

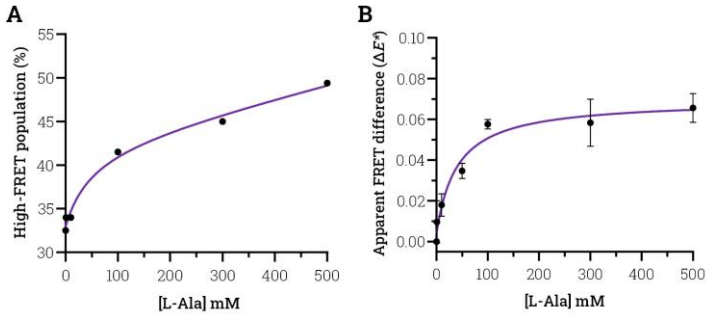

Figure 39. L-Ala titration for TM1a dynamics. L-Ala titration on ALEX-smFRET on BasC TM1a-12 labelled with Alexa 546-Alexa 647 (A) and TM1a-4 labelled with sCy3-sCy5 (B). **A.** Single experiment high-FRET relative population increase upon increase of L-Ala concentration. Saturation was not achieved. IC_{50} measured is around 50 mM. **B.** Apparent FRET difference respect apo conditions change upon increasing L-Ala concentrations. Mean ± s.e.m. of three experiments shown. Saturation was achieved. IC_{50} measured was 40.4 ± 13.2 mM.

Appart from the L-Ala titration performed by ALEX-smFRET, and keep trying to measure L-Ala binding to BasC same fluorophore labelled BasC sample was used to approach it through thermostability measured in Prometheus device (Experimental procedures 1.4). Prometheus is a nano differential scanning fluorimeter (nanoDSF) device used to characterise stability of proteins. It measures the intrinsic absorbance of Trp (Abs_{350}) and Tyr (Abs_{330}) change as the protein unfolds exposed to increasing temperatures from 19 to 95 ºC. Prometheus heating rate was set at 1 ºC/min and excitation power at 50 %. BasCs WT sequence has 8 Trp and 38 Tyr, enough from Prometheus to track absorbance increase and measure its thermostability. BasC WT and K154A variants showed T_m of 60.8 ± 0.3 and 52.7 ± 0.4 ºC, respectively (Figure 40. A), and upon L-Ala addition at 300 mM they increased until 68.9 ± 0.4 and 57.4 ± 0.6 ºC showing a clear increase of the thermostability when substrate is bound. Similar effect with Then, for BasC WT variant, L-Ala was titrated (Figure 40. B), the IC_{50}s obtained was 120.5 ± 16.9 mM. Although the range is maintained in the mM scale, it was described a 3-fold increase of the IC_{50} respect the previous thermostability assays and ALEX-smFRET measurements. These high IC_{50} justifies the use of high concentration substrates in ALEX-smFRET measurements with BasC labelled samples, as the saturation is difficult to achieve in this conditions.

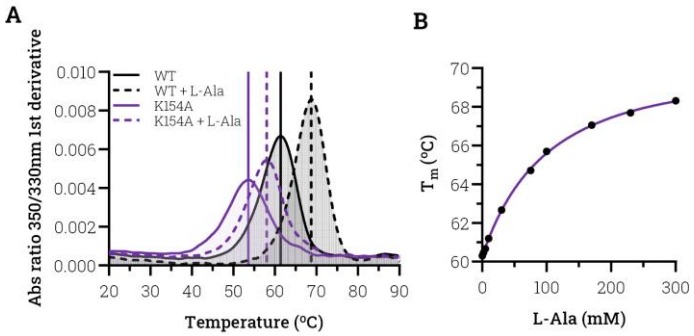

Figure 40. BasC thermostability assays. Thermostability assays performed on BasC WT and K154A variants TM1a-12 labelled with Alexa 546-Alexa 647 on Prometheus device by nanoDSF. **A.** Single experiment representative absorbance 330/350 ratio first derivatives for tested samples. Temperature melting (T_m) data points obtained from three experiments. Mean ± s.e.m. are shown for BasC WT and K154A variants ± L-Ala (300 mM). WT variant shows a T_m of 60.8 ± 0.3 ºC and K154A variant 52.7 ± 0.4 ºC. Upon L-Ala addition, WT increases its T_m until 68.9 ± 0.4 ºC and K154A variant until 57.4 ± 0.6 ºC. **B.** L-Ala titration on BasC WT variant T_m. Single experiment with triplicates per each data point. Measured IC_{50} is 120.5 ± 16.9 mM.

2.2. K154A inability to close BasC cytosolic gate

Once analysed the substrates effect on BasC WT variants, the LPI-related variant K154A was submitted to the same analysis. So, double-Cys variants were generated the same way as the previous on BasC K154A variant through site directed mutagenesis by PCR (Experimental procedures 1.5). For K154A ALEX-smFRET measurements, BasC double-Cys variants used were TM1a-4 and TM1a-12. Both were expressed in DDM (Experimental procedures 1.7) and labelled on resin (Experimental procedures 4.1), BasC K154A TM1a-4 variant was labelled with sCy3-sCy5 dye pair, while BasC K154A TM1a-12 variant was labelled with Alexa 546-Alexa 647 dye pair. After checking the labelling efficiencies, ALEX-smFRET measurements were performed on solution in very low concentrations (pM range).

BasC double-Cys K154A variants were analysed in in apo and holo (300 mM L-Ala) conditions. For the other hand, BasC K154A TM1a-4 variant labelled with sCy3-sCy5 did show the same population appearance than the WT protein in apo conditions slightly shifted to lower E^* (Figure 41. A). BasC K154A TM1a-4 variant did not show any effect upon substrate addition; it did not shift to higher E^*. Indeed, the difference of E^* between apo and holo populations measured was -0.002 points (Figure 41. A-B).

For the other hand, BasC K154A TM1a-12 variant labelled with Alexa 546 and Alexa 647 in apo conditions gave, from a very beginning, a different FRET population distribution from the BasC WT protein. BasC K154A variant did not show two distinct populations distribution (Figure 41. C) and it showed a single population fitting, although it was wider. This BasC K154A population gave a mean E^* below the low-FRET population for the WT variant by -0.036 points (Figure 41. C). Furthermore, upon substrate addition (300 mM L-Ala), this single BasC K154A population did not show any statistical difference; did not show the appearance of a second higher-FRET population neither a shift to higher E^* of itself. It can only be seen a tendency to shift to higher E^*, of 0.014 points (Figure 41. D).

With these measurements, it can be assumed that BasC K154A cannot close properly the cytosolic gate as it does with K154. BasC is not able to respond correctly under substrate addition. This constitutes the first experimental evidence of the conformational handicap that BasC explores, leading to a transport miss function that reduces the V_{max} and external substrate affinity (Bartoccioni et al., 2019). Thus, this dynamic misbehaviour of the LPI-related variant highlights the key role of K154 residue in BasC, the conserved Lys among all LATs.

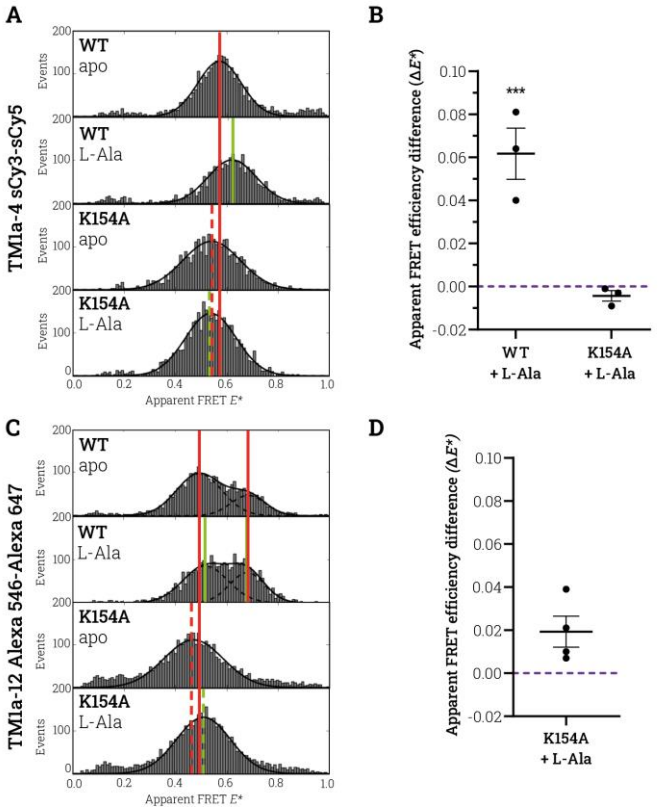

Figure 41. BasC K154A mutant behaviours upon substrate addition. ALEX-smFRET analysis of BasC K15A variant performed on BasC TM1a-4 (A) and TM1a-12 (B) variants labelled with sCy3-sCy5 and Alexa 546-Alexa 647, respectively. **A and C.** Representative events vs. *E** histograms for BasC WT and K154A ± L-Ala (300 mM L-Ala). Vertical red continuous lines label WT apo populations, green vertical lines the WT holo populations. Dashed lines same colour legend are for K154A populations. **B and D.** Comparison of WT and K154A BasC variants effect upon substrate addition (300 mM L-Ala). Triplicate experiments (dots) and mean ± s.e.m. are shown. T-tests performed on absolute values between same day apo and holo measurements per variant. Statistical significance was only detected on WT variant as shown previously (Figure 38); K154A did not show any significant change upon substrate addition in any case.

2.3. Nanobodies blocking the substrate-induced TM1a closing

Nbs used to solve BasC-Nb complex structure were analysed, as it was known to which regions of BasC they could be interacting. Then, Nb53, 71 and 74 were tested on BasC TM1a-4 variant with and without L-Ala at high concentration and it was found out that Nb71 did block completely TM1a tilt (Figure 42. B), opposite than Nb53 that could not at all (Figure 42. A), and while Nb74 permitted still the movement without a clear blocking effect but handicapping it somehow in terms of the amplitude of it, reducing it from an increase of 0.053 until a lower increase of 0.039 when Nb74 was present (Figure 42. C). Furthermore, Nb71 was also tested on BasC TM1a-12 variant labelled with Alexa 546-Alexa 647 and the blocking effect was also seen there (Figure 42. D).

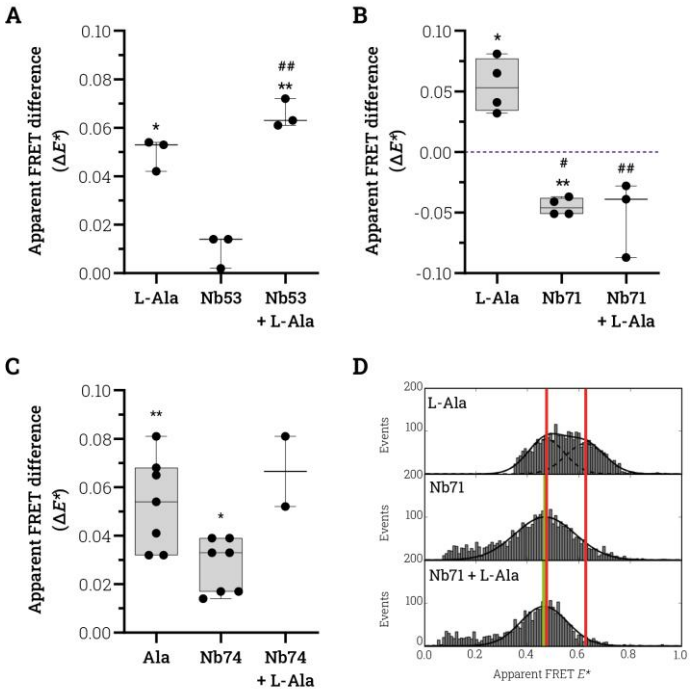

Figure 42. Nanobodies blocking L-Ala-induced effect. (*Previous page*). ALEX-smFRET of BasC TM1a-4 variant labelled with sCy3-sCy5 (**A-C**) and TM1a-12 variant labelled with Alexa 546-Alexa 647 (**D**). Nbs were added at least at 1 µM and L-Ala at 300 mM. **A.** The substrate-induced TM1a tilt had an amplitude of 0.055 and 0.049 points of *E**with presence or absence of Nb53, respectively. Nb53 did not block the substrate-induced TM1a tilt. **B.** There was not any *E** increase upon substrate addition when Nb71 was bound. It maintained a population with a decrease of ~0.05 points of *E**. Nb71 did block the substrate-induced TM1a tilt. **C.** The substrate-induced TM1a tilt was diminished in presence of Nb74 from 0.053 until 0.039 points of *E**. Nb74 still permitted the substrate-induced TM1a tilt, in less amplitude. **D.** Single experiment of Nb71 blocking substrate-induced TM1a tilt. Nb71 maintained a single population instead of an increase of the events in the high-FRET population. Statistical difference in A-C was performed using paired T-tests of each condition against the apo (asterisks) or L-Ala (hashes) of the same-day in absolute values. * p.value < 0.05 and ** or ## p.value < 0.01.

3. Future perspectives: nanodiscs

First attempts to reconstitute LATs in our research group were carried by Paloma Escudero Bravo. The protocol she settled for human LATs was the start point to be fully adapted when reconstituting BasC. This thesis permitted to settle the protocol for BasC reconstitution in nanodisc (ND) has been settled up in order to use it for solve BasC's structure and analyse it by ALEX-smFRET in this native-like lipid environment.

As the temperature for the self-assembly should be near the T_m of the lipid being used, 1-palmitoyl-2-oleoyl-sn-glycero-3-phosphocholine (POPC) solubilised in cholate was chosen as an appropriate candidate as its T_m is around 4 ºC. Thus, we can perform the reconstitution at 4 ºC without damaging neither BasC nor the membrane scaffold protein (MSP).

When reconstituting a MP into ND, one of the most critical steps is the detergent removal. In this case, it was opted the use of Bio-Beads (Experimental procedures 6.2) as most of the literature cases use them (Ritchie et al., 2009), although the first steps and optimisation were performed through dialysis (Experimental procedures 6.1).

First trials of BasC reconstitution into ND were performed with the aim to use them for solve its structure by cryo-EM. For this purpose, MSP1E3D1-his was used and reconstitution took place through dialysis. To check the correct removing of detergent, dialysis was applied to 500 µl BasC solubilised in DM buffer. After dialysis, sample was recovered from dialysis tubing, filtered through 0.45 µM-pore cellulose Eppendorf filters and injected on a Superdex 200 10:300 column. Comparing to BasC DM solubilised. The detergent was removed correctly as no other peak but aggregates eluted at 6.75 ml (Figure 43. A). In parallel, empty ND (Ø-ND) were reconstituted through dialysis in molar ratio 1:100 (MSP:POPC) and run in the same column (Figure 43. B), MSP1E3D1 was detected in the fraction peaks by SDS-PAGE (Figure 43. D). Then, different ratios were performed to optimise BasC reconstitution into MSP1E3D1-his. Molar ratios assayed between BasC and MSP

were 0.2:1, 0.5:1, 1:1 and 2:1. Molar ratios assayed between MSP:POPC were 1:100 and 1:80. All the different molar ratios BasC:MSP:POPC assayed (0.2:1:80, 0.5:1:80, 1:1:80 and 2:1:80) gave similar profiles with different. Void appeared at ~7.6 ml and the main ND peak at ~10.30 ml, between these two peaks, it always appeared some other species (Figure 43. C), possibly due to the reconstitution of multiple number of BasC molecules one a single ND, or even aberrant NDs (Shih et al., 2007).

Finally, BasC:MSP:POPC selected was the 1:1:80 (Figure 43. C), BasC and MSP1E3D1 was detected at the main peak at 10.16 ml (Figure 43. E). At this point protocol was changed to use BioBeads instead of using dialysis for detergent removal. In addition, the column used for SEC was changed to Superose 6 10/300 in order to separate better the peaks observed in the Superdex 200 10/300 GL column SEC (Figure 43. C).

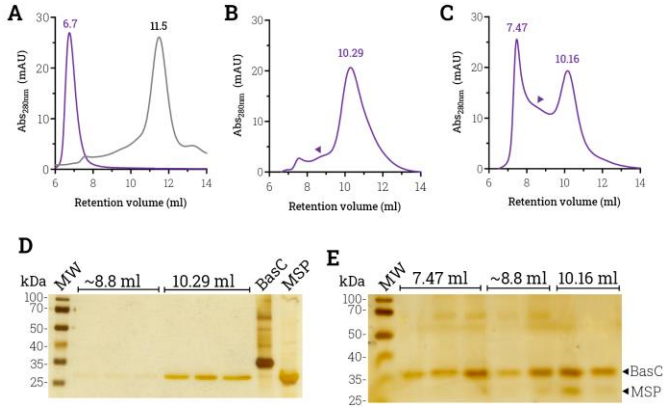

Figure 43. Nanodisc optimisation. A-C. SEC profiles on Superdex 200 10/300 GL for the different Ctrls performed after dialysis reconstitution. **A.** BasC Ctrls, BasC in DM buffer (grey) and after dialysis in Tris buffer (purple). Elimination of detergent works properly as BasC precipitates completely. **B.** Ø-MSP1E3D1-ND run in Tris buffer. Ø-NDs elute at 10.29 ml with a previous shoulder at around 8.8 ml (arrow). SDS-PAGE of peak and shoulder fractions in (D). **C.** BasC-MSP1E3D1-ND at 1:1:80 molar ratio (BasC:MSP:POPC) run in Tris buffer. Huge void appears at 7.47 ml, main peak at 10.16 ml and some species elutes between them at around 8.8 ml (arrow). SDS-PAGE of void, shoulder and ND peak fractions on (E). **D-E.** SDS-PAGEs at 12.5 % acrylamide for ND samples silver stained. **D.** ~8.8 and 10.29 ml peak fractions of Ø-MSP1E3D1-NDs SEC (B). MSP1E3D1 appears mainly in the peak, although in the previous shoulder is also present. **E.** 7.47, ~8.8 and 10.16 ml peak fractions of BasC-MSP1E3D1-ND (C). BasC is precipitates more than the MSP; both proteins are present at the rest of the peaks. Empty and full ND elute at almost the same retention volume. BasC must not protrude much from the lipid bilayer.

Same selected ratio, MSP was reconstituted in BioBeads, and sample was run in a Superose 6 10/300 column (Figure 44. A) and the presence of full ND was

checked by SDS-PAGE (Figure 44. B). Subsequently, negative staining was performed (Figure 44. C) before cryo-EM grids preparation in order to check sample quality. Finally, low-resolution cryo-EM imaging obtained in a 100 kV microscope (Tecnai G2 microscope with TVIPS CMOS detector) in collaboration with Dr. Oscar Llorca Lab (CNIO, Madrid). Images showed a high heterogeneity of the sample. Different sizes of NDs were seen from ~64 until ~150 Å (Figure 44. D) Improvement needed to be done to reduce this heterogeneity of the sample.t was needed an improvement of the ND.

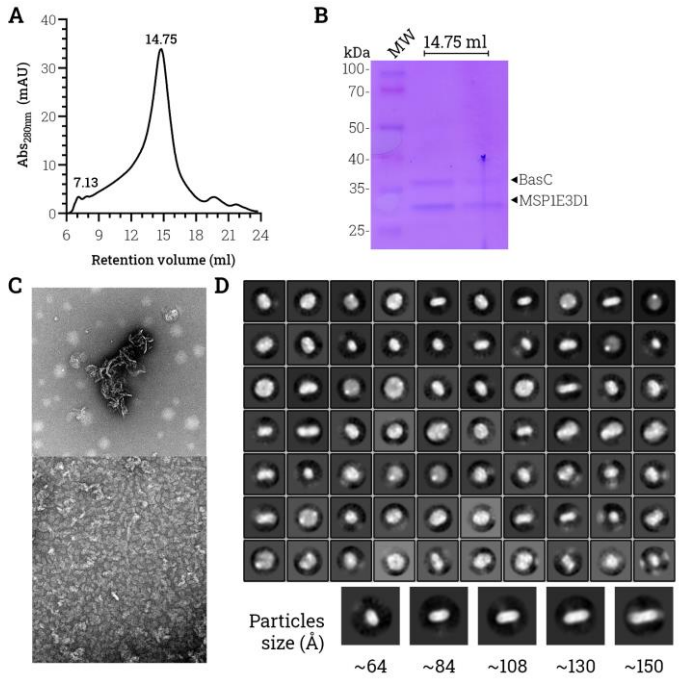

Figure 44. BasC into MSP1E3D1 nanodiscs. A. BasC-MSP1E3D1-ND at 1:1:80 molar ratio (BasC:MSP:POPC) SEC profile on a Superose 6 10/300 GL after dialysis reconstitution. Void is reduced compared to previous protocol (Figure 36. C). NDs elute at 14.75 ml, while there is still some previous shoulder. **B.** SEC peak fraction (14.75 ml) run on a 12.5 % acrylamide SDS-PAGE and coomassie blue stained. Both BasC and MSP are detected in it. **C.** Negative staining of SEC void fraction (top) and ND peak fraction (bottom). Lipid aggregates are visible in void fraction while ND particles are in good concentration. **D.** BasC-MSP1E3D1 ND 2D-class averages from CryoSPARC. Images obtained with a Tecnai G2 100 kV microscope with TVIPS CMOS detector. Particles size in Å are shown from a lateral perspective.

Notice the molar ratio is 1:1 between BasC and MSP, quite high comparing with the literature, that use MP:MSP ratios of 0.5:1:100 for $b^{0,+}$AT (Lee et al., 2022) or 0.1:1:50 and 0.05:1:50 for LeuT (Nasr and Singh, 2014), among others. Here, it was followed the idea to fulfil as much as possible the ND with BasC molecules to avoid Ø-ND and it did not succeed. We need to take into account that BasC diameter is ~45 Å. As MSP1E3D1 offers a ND of ~120 Å diameter, two molecules of BasC would fit in each, and even three.

In order to reduce the availability of ND with more than one BasC molecule several changes were applied. First, MSP was changed to MSP1D1 TEV cleaved without its His-tag, which constitute smaller ND with 9.7 nm of diameter. BasC-GFP was reconstituted permitting its His-tag to be used for the selection of full ND eliminating the presence of the empty ones. GFP permits the differentiation of species (BasC-ND vs. Ø-ND) (Figure 43. A), as its stands out the lipid bilayer, and permits to track BasC-GFP along the SEC profile by its absorbance at 488 nm. In addition, the molar ratio was lowered 10 fold, until BasC:MSP:POPC of 0.1:1:50, lowering both BasC and POPC relative concentrations. Finally, BioBeads were used instead of dialysis, reducing also the time needed for reconstitution. This experimental approach (Experimental procedures 6.2) permits to select full ND out of all the pull of ND to discard Ø-ND (Figure 43. A). Eluted SEC fractions from pre- and post-selection samples were run in an SDS-PAGE (Figure 43. B). Same reconstitution protocol was followed changing the final Ni-NTA elution. 3C protease was used to elute BasC-ND without GFP for cryo-EM grid preparation and image acquisition (Figure 43. C) An improvement on sample homogeneity was detected as species size range is from ~85 to ~112 Å.

This protocol can be used to reconstitute BasC for Cryo-EM structure solving and dynamics studies by ALEX-smFRET. Improvements can be done, as adjusting the lipid composition to mimic better the bacterial membrane, generating a better physiological-like environment (Do et al., 2021; Ganapathy et al., 2020).

BasC WT TM1a-4 variant labelled with sCy3-sCy5 (Figure 46. A) was reconstituted into MSP1D1-ND following the latter experimental design seen (Experimental procedures 4.2) in a molar ratio lower than 0.1:1:50 (BasC:MSP:POPC) as the concentration of labelled BasC was too low that was not possible to measure. After BioBeads incubation, Superdex 200 increase 3.2/300 column showed fluorophore signal in the full ND fraction (1.49 ml) (Figure 46. A) separately from the Ø-ND (1.65 ml). Full ND fraction was collected, snap frozen in liquid nitrogen (LN) and stored at -80 °C until ALEX-smFRET experiments. Sample was highly diluted and only permitted to study it in apo and holo conditions (Figure 46. B-C). Surprisingly, BasC in ND showed an E^* value higher than the same variant and labelling solubilised in DDM (Figure 27 and 30. A). ALEX-smFRET experiments for BasC in ND in apo conditions concluded with an E^* of 0.665, (Figure 46. B), while in DDM it was an E^* of 0.598 (from 2022 dataset). Moreover, this apparent closed state did not show any shifts to higher values upon substrate addition (Figure 46. C).

By the one hand, this apparent immobile closed state suggests that POPC molecules in the ND could be constraining BasC mobility. That would lead to the impossibility of BasC to close properly the cytosolic gate when embedded in a lipid bilayer. However, this idea contradicts with the fact that BasC is able to adopt diverse conformations during the transport assays, when is reconstituted in total lipid extract PLs. Unless there was a distinct interaction between BasC and POPC from the interaction between BasC and total *E.coli* lipid extract phospholipids. However, is hard to think that BasC dynamically constrained in MSP1D1-ND when no one in the literature has ascertained it when reconstituting MPs on ND.

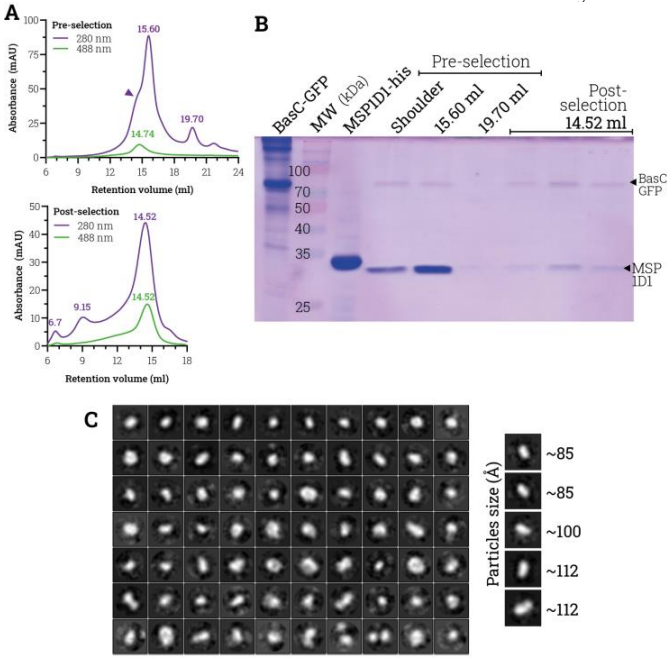

Figure 43. BasC into MSP1D1 nanodiscs. A. BasC-GFP-his reconstituted into MSP1D1 (His-tag free) at molar ratios 0.1:1:50 (BasC:MSP:POPC), samples injected pre-selection by Ni-NTA (top) and post-selection (bottom). All SEC profiles show the UV at 280 nm (purple) and 488 nm (green). Shoulder is detected in pre-selection profile, as full ND and Ø-ND differ in SEC retention volumes due to GFP anchored to BasC. Ø-NDs elute at 15.60 ml (top) while BasC-GFP-NDs elute at 14.52 ml (bottom). Peak at 9.15 ml must be some MSP aggregates, as it does not absorb at 488 nm. **B.** SDS-PAGE coomassie stained loaded with peak fractions of pre- and post-selection SEC. MSP and BasC can be detected in all fractions except the pre-selection peak at 19.70 ml that contains some free MSP. Bands intensity analysis reinforces the presence of one single molecule of BasC-GFP per two molecules of MSP1D1 after selection by NiNTA (post-selection fractions). **C.** BasC-MSP1D1 ND 2D-class averages classified with CryoSPARC. Particles size in Å are shown from a lateral perspective.

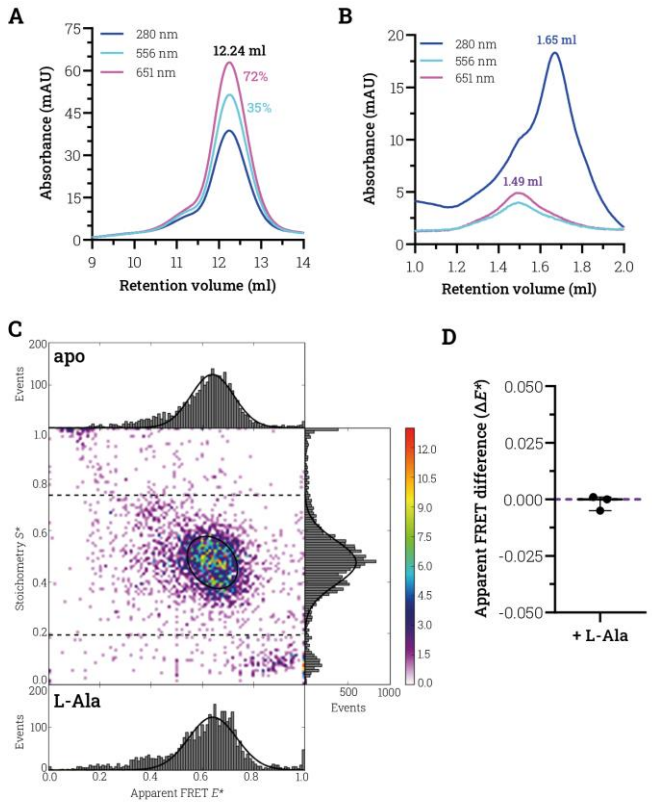

Figure 46. TM1a dynamics analisis on BasC reconstituted in MSP1D1-ND. Labelled BasC TM1a-4 variant labelled with sCy3-sCy5 was reconstituted in MSP1D1-ND and studied by free diffusion ALEX-smFRET. **A.** Superdex 200 10/300 GL column SEC profile of labelled BasC in DDM. BasC elutes at 12.24 ml where protein and dye absorbance are simultaneously detected. Donor and acceptor labelling efficiencies are indicated next to their peak. **B.** Superdex 200 increase 3.2/300 GL column SEC profile of labelled BasC-MSP1D1-ND purification. Dye absorbance are detected in the retention volume corresponding to full ND (1.49 ml). Empty ND elute at 1.65 ml. **C.** Representative complete E^* vs. S^* histogram in APBS algorithm of BasC in MSP1D1-ND in apo conditions (top) and Events vs. E^* histogram for holo conditions (300 mM L-Ala) (bottom). Single population is detected at E^*= 0.640 and 0.641 for apo and holo (300 mM L-Ala) conditions, respectively. **D.** Mean +- s.e.m. of triplicate measurements of apparent FRET efficiency between apo and holo (300 mM L-Ala) conditions of BasC in MSP1D1-ND. No statistical difference is detected when performing T-test between apo and holo conditions in absolute values.

In the other hand, more reasonable and feasible, it could take place a steric impediment generated by the phospholipid molecules. A simulated DPPC bilayer around BasC structure showed how I7 and T120 residues are positioned within the lipid bilayer (Figure 47). Residues being inside the bilayer could affect directly sCy3-sCy5 AVs to be one more nearby the other, resulting in the seen higher and immobile E^*values measured by ALEX-smFRET (Figure 46).

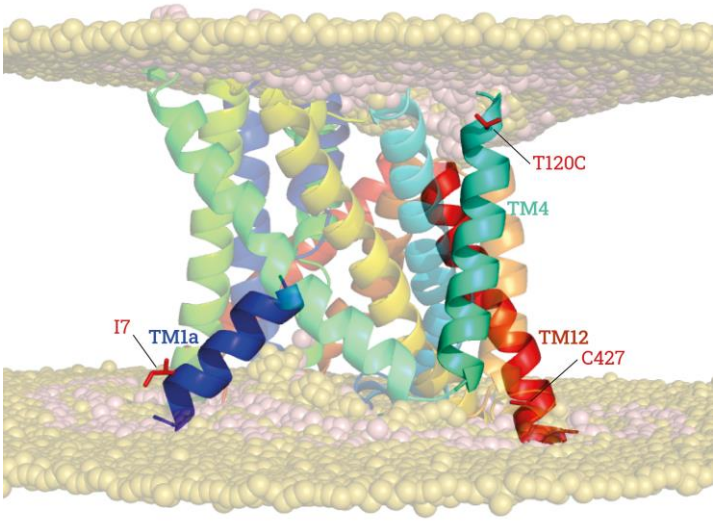

Figure 47. Lipid bilayer simulation. Simulation of BasC (rainbow) embedded in a DPPC lipid bilayer with its limits labelled with spheres. I7 (TM1a), T120 (TM4) and C427 (TM12) remain inside the bilayer. Simulation done by MD on MemProtMD database (http://memprotmd.bioch.ox.ac.uk) creative commons 4.0 of Thomas D. Newport, Mark S.P. Sansom and Philip J. Stansfeld.

Discussion

In the search of new LAT conformations

We have seen although the efforts made by the scientific community to solve MPs structures all along the time since it was started through XRC how difficult is to obtain them. First of all, in order to stabilise MPs, these proteins have majority been studied solubilised in detergents, an alternative amphipathic environment far away of mimicking a native-like surrounding as the lipid bilayer offers. Despite these characteristics, detergents play a significant role in structural and functional characterisation of MPs and can maintain the native conformation of proteins successfully. Despite of the key function of detergents, currently the use of other amphipathic environments more likely a lipid membrane, as ND, are being used for structure solving using cryo-EM. This new approach permits to obtain diverse conformational states with a single sample preparation and, also important, structures are solved in a native-like environment distinct from the one that detergents offer. Will this approach confirm what detergents have helped us to know, or will it tremble all what has been build?

Regarding the structures solved until now for members of the LAT subfamily, we have to take into account that most of them have been solved in the same inward facing conformation. This highlights the probably most stable and predominant conformation of the LAT transport cycle in detergents. Nevertheless, detergents would not be the main responsible for this fact, because $b^{0,+}$AT-rBAT was solved in the same conformation although it was reconstituted into ND, in a native-like environment. The only structures that have been solved in an outward facing conformation were achieved for LAT1 with inhibitors. Thus, the use of inhibitors seems to be to date the only choice to trap LATs in other conformations rather than inward facing.

All along this thesis, we have seen a similar output, while we thought that the use of Nbs would increase the chance to freeze BasC in another conformational state, it was not enough with the approach we build. In this regard, firstly, we saw the disproportioned amount of Nbs that were binding BasC by its cytoplasmic side instead of the extracellular. Only two of the Nbs, out of 29, were clearly identified as extracellular binders. This would mean either that BasC exposes a wider surface out the PLs membrane through the cytosol rather than the extracellular space, or that the mobility of both BasC's sides is not balanced, and that the cytosolic side is more stable and accessible for Nbs' binding than the extracellular. Even more, while screening Nbs for the effect they did on TM1a dynamics, we could not detect any Nb that forced BasC to close it in a similar amplitude as the substrate did.

In this thesis, ALEX-smFRET approach has shown some unexpected factors that could have been considered previously; these factors may have blurred the true conformational effects of the Nb on the TM1a dynamics.

One of these factors is the steric effect that comes from the binding of the Nb itself to labelled species of BasC. As at the beginning of the project we only knew their side of interaction, we did not know if they would affect the AV of the dyes

when performing the ALEX-smFRET measurements. Actually, this is what was seen for Nb71, which clearly sterically interferes with the AV of dyes anchored in the I7C position. To reduce this effect, fully cytosolic or extracellular double-Cys labelled pairs would be needed to assay opposite side Nb binders to avoid at maximum this steric effect.

Another factor is the unclear effect that detergent micelles surrounding BasC may influence the AV of dyes. As there have not been published any study regarding this issue, we still unknown how DDM molecules interact with maleimide dyes used in our assays. The only reference of detergent side-effect on smFRET measurements is from the studies carried for LeuT (Zhao et al., 2011), where OG molecules inhibited intracellular gating dynamics, although is not due to the micelle solubilisation, but the interaction of an OG molecule with S2 as it was found in structures bound there (Quick et al., 2009). Blanchard and co-work have never described any possible effect of detergent micelles into dyes AVs. This builds one of the relevant factors that would have been considered. To minimise any presumed interaction between detergent micelles and maleimide dyes, smallest detergent possible would be a better choice (DM rather than DDM).

Similarly, if we discuss about the effect of the detergent of choice with ALEX-smFRET results, we must analyse also the effect of a lipid environment on the TM1a dynamic measurements done on BasC reconstituted into MSP1D1-ND with POPC. BasC when reconstituted into ND showed by ALEX-smFRET a more closed state of the TM1a in the cytosolic gate than when solubilised in DDM. Even more, BasC did not respond upon substrate addition, 300 mM L-Ala, in this native-like environment. Simulating a lipid bilayer around BasC we could check the localisation of the residues labelled within it. With this simulation we ascertained that I7, C427 and T120 were found immerse the hydrophobic region of the protein, thus, inside the bilayer. Therefore, when these residues are mutated to Cys and labelled, before the reconstitution, with the maleimide dyes, once labelled BasC is reconstituted in the ND, the AV of the dyes will be restrained by the POPC molecules and forced to maintain a more narrow distance between them. That would be the possible cause of the ALEX-smFRET measurement as a more closed-state. Moreover, this restrain by the lipid membrane does not permit to detect the closing of the inner gate when substrate binds. We cannot say that the closing of the inner gate is not happening in a lipid environment, as it must occur since we can measure activity transport in PLs, unless the lipid of choice for the ND, POPC, is not suitable for a proper BasC's dynamics.

In this regard, new residues would need to be selected in positions more distant from the hydrophobic region for anchoring the maleimide dyes. This would avoid affinity effects of detergent micelles or lipid molecules, as it was done for P-type ATPase smFRET measurements in PLs labelling the EDs and not the transporter (Dyla et al., 2017). Lipid composition of bacterial membranes needs a special attention to keep improving the ND reconstitution process. For example, considering the fundamental role of phosphatidylglycerol and cholesterol as negatively charged lipids in bacterial membranes, which seem indispensable for membrane insertion (Opekarová and Tanner, 2003). Distinct type of lipids could be used for

BasC reconstitution in ND to go to a more comfortable lipid bilayer to permit BasC mobility as in a physiologic environment while also try to avoid interferences with dye AVs.

Deciphering K154 role on the occlusion of the cytoplasmic gate

Regarding the studies performed on WT variants of APC fold transporters and their structures solved, we can hypothesise about which conformational state of the transport cycle they prefer to adopt, bearing in mind the alternate access it has been described for their shared transport mechanism.

In fact, sodium symporters have been repeatedly solved facing to the extracellular space easily than LATs, which have been solved preferentially in inward facing conformations. In this regard is common to expect that sodium symporters prefer to be in outward facing states rather than inward facing. This theory is reinforced by TIRF measurements performed on LeuT cytosolic double-Cys TM1a-3 variant (Zhao et al., 2011). In this study, in apo conditions, LeuT showed a double population profile, high- and low-FRET populations representing the closed and an opened cytosolic side state respectively. The fact is that the high-FRET population, cytosolic gate closed, had more events than the low-FRET, opened. This biased distribution of the events between was displaced even more in favour of the high-FRET population when increasing sodium concentration (Figure 13).

Oppositely, what has been seen in the present study is how this transporter in apo conditions prefers to adopt an inward facing conformation taking into account the ALEX-smFRET measurements performed on BasC (Figures 27-30, 38-39 and 41), which was able to close the cytosolic thick gate only when substrates (L-Ser or L-Ala) were added (Figure 38). The difference of populations seen (single or double) with the different BasC double-Cys variants must rely on the physical-chemical properties of the dyes used. Probably, sCy3-sCy5 do not permit to distinguish between the two states while Alexa 546-Alexa 647 do allow it. The closing effect induced by substrates (L-Ala and L-Ser) but not by the inhibitor (L-Gln) did not abolish completely the existence of the open state, meaning that they may increase the rate of switching from one state to the other but not trapping the transporter in one single state. Substrate induced dynamics seen make sense taking into account that LATs have a substrate affinity sidedness with the high affinity side facing the extracellular space, while the cytosolic is the less affine for the substrate (Meier et al., 2002; Bartoccioni et al., 2019). That leads to the fact that in apo conditions LATs are more often facing the cytosol rather than the extracellular space and that they must export to adopt an outward facing stat. Once they face the extracellular space, its conformation will be fast switched to the inward facing state again due to the high affinity of the extracellular side. That would explain our ALEX-smFRET results and the vast majority of the structures solved in the same inward facing conformation.

Regarding the blocking or non-blocking effect of Nb53, 71 and 74 on substrate induced effect on TM1a dynamics, we can infer their blocking ability through the structures solved for BasC-Nb71, BasC-Nb53-58 and the published BasC-Nb74 (Errasti-Murugarren et al., 2019). For the one hand we have to bear in mind which are the interactions occurring between the Nbs and BasC. For the other hand we have to understand which is the TM1a mobility they allow upon substrate addition when bind BasC.

Firstly, let us analyse Nb71, the only Nb of the three that blocked totally the mobility of the TM1a upon substrate addition. We saw its blocking effect with BasC TM1a-4 and TM1a-12 variants (Figure 42). In the former, BasC remained in a lower-FRET state when both Nb71 and L-Ala were added, in a similar way as when Nb71 was added alone. The addition of L-Ala induced in this BasC variant a closing of the TM1a to the centre of the BasC molecule. Paying attention to the cryo-EM solved structure of BasC-Nb71; we can see how this Nb occupies the open cytosolic cavity, clogging it so perfectly that the substrate cannot reach the substrate-binding site through it. Moreover, Nb71 is interacting directly with the TM1a, the one that is being tracked by ALEX-smFRET, together with the TM6b in the same region of the cytosolic gate; in addition, Nb71 seems also to be interacting with the opposite region of this cytosolic cavity, the IL3. Therefore, Nb71 is acting like a scaffolding prop impeding sterically the cytoplasmic gate to close the inner cavity while it is also filling the latter impeding the access of substrate to the centre of the molecule. Overall, BasC-Nb71 low-resolution structure and Nb71 blocking effect of the induced-closing of the cytosolic gate permit to verify that all the ALEX-smFRET measurements carried out throughout this project have been tracking the TM1a as Nb71 was able to block it as it is shown in Figure 35.

Secondly, Nb53 permitted what it seemed a complete TM1a tilt when substrate was added (Figure 42), considering also that Nb53 when bound to BasC still allowed the existence of two distinct FRET populations when measuring on BasC TM1a-12 variant labelled with Alexa 546-Alexa 647 (Figure 29). Therefore, although Nb53 blocked transport activity of BasC in PLs (Figure 18), it still permitted what it seems a functional movement of the TM1a. Of course, this TM1a tilt is not the only conformational change needed to allow the transport mechanism. The XRC structure solved for BasC-Nb53-58 (Figure 33) shows how Nb53 interacts to BasC through the cytosolic side in a different manner as Nb71. Nb53 seem to only interact with one particular region of the cytosolic side, the IL2 and IL3, at the contrary side from TM1a at the cytosolic cavity. These interactions would still permit the substrate induced tilt of the TM1a, as measured by ALEX-smFRET, because Nb53 does not physically impede the entrance of substrate to its binding site nor the TM1a tilt to close the cytosolic gate. For a functional closing of the cytosolic gate, it has been stated that TM1a forms the thick gate with TM6b, 5 and 7. Therefore, if Nb53 is interacting with the IL2, for sure it impedes the cytosolic tilt of the cytosolic end of the TM5 to complete the mechanism of transport.

Finally, but not least, Nb74 seems to be in between of the effect made by Nb71 and Nb53. By ALEX-smFRET, when bound to BasC, Nb74 permitted the bend of TM1a

upon substrate addition (Figure 41), although it seemed not completely as the L-Ala effect on BasC without Nb. The movement the Nb74 permits of the TM1a seems restricted somehow as it showed also the populations appearing with the ALEX-smFRET measurements on the BasC TM1a-12 variant labelled with Alexa 546-Alexa 647. Nb74 in this measurements changed the two apo populations maintaining the low-FRET population as the apo one and lowering the E* of the low-FRET population while reducing the number of events of it (Figure 29). Thus, by ALEX-smFRET, TM1a is able to bend even when Nb74 is bound to it but it cannot reach the same closing state and it remains halfway. This can be explained by the interactions between Nb74 and BasC in BasC-Nb74 complex structure published (PDB IDs 6F2G and 6F2W) (Figure 9) (Errasti-Murugarren et al., 2019). This structure shows Nb74 interacting to BasC in the cytosol side through the cytosolic ends of TM2, 6b, 8 and IL4. As Nb71, from opposite regions in the cytosolic cavity, TM2 and 6b from one side and TM8 and IL4 in the other. Differently than Nb71, Nb74 still permits the substrate to access the binding site from the cytosol, and Nb74 is not interacting with TM1a. Therefore, Nb74 is not directly restricting this TM to bend. Nevertheless, this TM1a pivot cannot be complete, as Nb74 is partially occupying the cytosolic cavity, and interacting with other TMs involved in the thick gate (i.e., TM1a, 5 and 6), which are needed to complete the occlusion of the cytosolic gate.

Moreover, this inward facing state of LATs was the only one seen when submitting the K154A variant of BasC to ALEX-smFRET measurements. This dynamic study on BasC comparing both WT and LPI-related variants permitted to gather the first experimental evidence of the dynamical and structural miss function of the disease variant regarding the closure of the cytosolic gate upon substrate addition. This result highlights the key role of the mutant analysed, homologue of K191E in y^+LAT1, the variant K154A in BasC. This conserved Lys residue among the LATs (Bartoccioni et al., 2019) is located in a region of paramount importance for the transport mechanism in the APC fold MPs, the TM5, one of the "arms" that, together with TM10, is partially responsible of the conformational changes in the APC fold members mechanism of transport, as described until now.

The mechanism studied for sodium symporters has showed that the unwinding of the TM5 allows a solvation pathway for water molecules reach the Na2 site and an opportunity for this Na^+ to translocate to the cytosol. This sodium release allows TM5 to reform and triggers the TM1a to swing out to complete the translocation of the substrate and sodium from S1 and Na1, respectively (Malinauskaite et al., 2014; Singh et al., 2008). This unwinding occurs facilitated by the conserved GX_nP motif among the APC fold transporters, GX_9P for bacterial members of the NSS family.

The conserved Lys among the LATs is located in the TM5 and it could substitute the role of Na2 in sodium symporters. This Lys interacts with the TMs 1a and 8 (Figure 11). Not surprisingly, this Lys in BasC is placed within the GX_nP motif (G144-X_{10}-P157 in BasC) (Figure 48. A-B). Note that BasC still conserves this GX_nP motif not as the human LATs, which only contain the conserved Lys (e.g., K204 in LAT1, Figure 48. C). In sodium symporters there is also a conserved a Lys or Arg

conserved inside the GX_nP motif (Malinauskaite et al., 2014), although this residue is not related functionally to LATs' conserved Lys, as in sodium symporters is located downstream the TM5, away from the Na2 site extending its lateral chain outwards the protein (Figure 48. A).

The fact that BasC still contains the GX_nP motif in TM5 strengthen the use of this bacterial LAT homologue as a model to decipher the human LAT mechanism of transport, while building it on previous studies on distant related APC fold transporters. Thus, BasC offers the possibility to bridge from the transport mechanism of sodium symporters from the NSS family to the transport mechanism of hLATs with the shared APC fold as the basis of their commonalities.

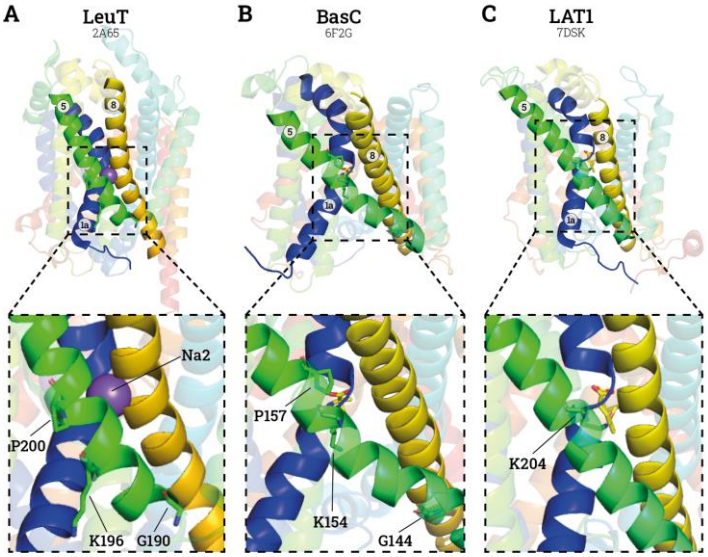

Figure 48. TM5 residues comparison between APC fold transporters. Structures of LeuT in outward facing state (PDB ID 2A65) (Yamashita et al., 2005) (**A**), BasC inward facing state (PDB ID 6F2G) (Errasti-Murugarren et al., 2019)(**B**) and LAT1 outward facing state (PDB ID 7DSK) (Yan et al., 2021) (**C**). Only TMs involved in the TM5 interactions regarding the Na2 or conserved Lys in LATs are shown for a simpler interpretation (TM1a in blue, TM5 in green and TM8 in yellow). Substrates and inhibitors are also shown in yellow sticks, 2-AIB (poor substrate) in BasC structure (**B**) and JX-075 (inhibitor) is shown in LAT1 structure (**C**). Zoomed views detail the residues involved in the diverse GX_nP motifs shown for LeuT and BasC (**A and B**), the Lys conserved among the NSS family members (K196 in (**A**)) and the conserved Lys involved in the substitution of the Na2 in LATs, K154 in BasC (**B**) and K204 in LAT1 (**C**).

By ALEX-smFRET, we have proved experimentally that the closing of the TM1a is not feasible when K154 is mutated to Ala. Thus, the expected interaction between TM1a, 5 and 8 in BasC is crucial for the closing of the thick gate in the cytosolic cavity. As it was seen since the structural comparison performed between BasC inward facing open state and GkApcT inward facing closed state (Figure 11) showed GkApcT with the thick gate closed and its conserved Lys in the TM5 interacting with TM1a and 8 (Errasti-Murugarren et al., 2019). Therefore, if K154 is essential for the closing of the inner gate, is also vital for the opening of the extracellular gate, regarding the alternate access that APC fold transporters have. Thus, the inability of BasC-K154A variant to close the cytosolic gate consequentially to open to the extracellular space is functionally supported by the ~10-fold decrease of the apparent extracellular affinity. Functional studies published previously showed how the extracellular K_M increased from 45 ± 5 µM to 474 ± 42 µM when K154 was mutated to Ala, while the intracellular K_M remained barely the same (Errasti-Murugarren et al., 2019).

Moreover, and as previously published (Errasti-Murugarren et al., 2019), MD showed how the substrate (L-Ala) in BasC structure (PDB ID 6F2G) when bound to the substrate-binding site, before being translocated into the cytosol, it would interact with K154. The interaction between the substrate and K154 would be the trigger for the opening of the thick gate. And not only these, because the K154 seems to be pulling the whole

If we reverse the steps, starting from the inward facing conformation, substrate before binding to the substrate-binding site would need to be interact first with K154 and after move to the substrate-binding site itself. This would permit the K154 to interact with TM1a and TM8 similarly as seen in GkApcT and, recently, with LAT1 (Figure 49). Here, the interactions between substrate and TM1a residues compete with the interactions between TM5 and TM1a residues. Thus K154 in BasC would probably pass from interacting with TM1a (G15) in the open to in state to interact also with the backbone of S280 in TM8 as in LAT1 K204 (TM5) interacts with S334 (TM8) (Figure 49).

The triggering between one state and the other regarding the K154 interactions between the inward and outward facing rely on the affinities and strengths of this K154 as it pulls the substrate out of the substrate-binding site to translocate it to the cytosol. As in LATs sodium does not play any role at all, this must rely on the protonation or deprotonation state of this conserved residue, as it was hypothesised for ApcT Lys158 that is also described as the substitute of the Na2 site (Stolzenberg et al., 2017).

The translocation of the substrate to the extracellular side remain unclear yet, as the preferred inward facing conformation for LATs and the sidedness of this transporters lead to explore easily the cytoplasmic side rather than the extracellular, as it is expected to switch fast to the inward as soon as it gets to the outward facing state.

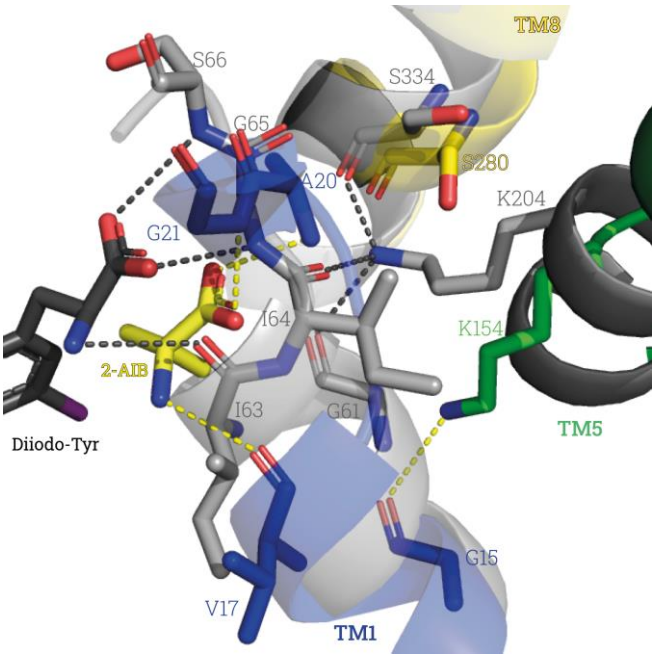

Figure 49. K154 and susbtrate interactions with TM1a. Structural representation for BasC (coloured) in inward facing conformation bound to 2-AIB (yellow) (PDB ID 6F2G) (Errasti-Murugarren et al., 2019) superposed to LAT1 (grey) in outward facing conformation bound to DiiodoTyr (black) (PDB ID 7DSQ) (Yan et al., 2021). Only TM1a (blue), TM5 (green) and TM8 (yellow) are shown for simplicity of the interpretation. Interactions between TM1a and substrate and/or TM5/8 are shown (yellow for BasC and black for LAT1), while the residues involved in them are labelled.

To further describe LAT dynamics and bring new insights to their transport mechanism, new positions in distinct TMs would be necessary and this approach could be applied beyond BasC, and analyse and measure ALEX-smFRET on hLATs. It would be interesting to start deciphering the dynamics and mechanism in the extracellular side of LATs, as well as other TMs involved in thick gate of the cytosolic side (e.g., TM6b, 7, 5…). Following a similar approach as it has been done here, basing the study on the described transport mechanism of NSS family symporters (Shi et al., 2008) and targeting the mobile TMs from comparing LATs structures (Nicolàs-Aragó et al., 2021).

Another further step in the dynamic studies for LATs would be the implementation of TIRF microscopy. TIRF permits to measure, not only the populations and main conformations seen in the free-diffusion ALEX-smFRET measurements,

but to analyse the rate of change between them and unveil the possible hindered states that free-diffusion mode does not allow to do. In addition, it offers the possibility to check how specific residue variants, disease-related or not, can affect the stabilisation or destabilisation of some states. Similarly as what it has been done for other transporters such as LeuT when analysing residues responsible for substrate selectivity (Levine et al., 2019). Recently, since COVID-19 pandemic, TIRF has been used to analyse spike protein of the virus interaction with the human receptors, immobilising directly the viral particle, unveiling up to 4 different states of it (Lu, 2021).

Appart from the type of smFRET chosen to analyse LATs dynamics, both methodologies (free-diffusing or immobilised) can be carried on a transporter solubilised in detergent or reconstituted into ND or PLs. We have seen the feasibility of LATs to be reconstituted in ND to solve their structures for $b^{0,+}$AT-rBAT heterotetramers (Lee et al., 2022) and for BasC in this present work (Results 3. Future perspectives: nanodiscs). These new approach would bring new insights on BasC dynamics, as for hLATs. In addition, the effect of the different amphipathic environments used, when comparing, for example, detergent solubilised measurements with ND or PLs reconstituted molecules. In addition, more interestingly, TIRF would also permit to see the details of the miss functions of disease variants

Conclusions

Conclusions

i. Inward-open and -closed states coexist in apo conditions for BasC reconstituted in n-Dodecyl-β-Maltoside (DDM).

ii. The preferred conformational state for BasC is the inward-open.

iii. L-Alanine and L-Serine trigger the closing of the cytosolic gate as substrates. L-Glutamine does not as inhibitor.

iv. The LPI-related variant BasC-K154A is not able to close properly the cytosolic gate.

v. The combination of ALEX-smFRET studies with nanobodies, substrates and disease-related mutants is a very useful tool to decipher transport mechanism insights of transporters.

vi. Steric effect of nanobodies and interactions with detergent micelles and lipid must be taken into consideration regarding the accessible volumes of attached dyes to MPs.

vii. A single molecule of BasC can be reconstituted into MSP1D1-ND with POPC.

Experimental Procedures

1. Molecular Biology

1.1. Buffers

- **Tris buffer**: 20 mM Tris, pH 7.4, 150 mM NaCl.
- **High Salt buffer**: 20 mM Tris, pH 7.4, 350 mM NaCl.
- **Lysis buffer**: 20 mM Tris, pH 7.4, 350 mM NaCl, DNase 1/500x, 1 cOmplete ethylthyimidine diphosphate (EDTA)-free Protease Inhibitor Cocktail tablet per each 50 ml.
- **Membranes buffer**: 20 mM Tris, pH 7.4, 150 mM NaCl, 10 % glycerol.
- **DDM buffer**: 20 mM Tris, pH 7.4, 150 mM NaCl, pH 7.4, 0.06 % (w/v) DDM.
- **DM buffer**: 20 mM Tris, pH 7.4, 150 mM NaCl, 0.17 % (w/v) DM.
- **Washing buffer 1**: 20 mM Tris, pH 7.4, 150 mM NaCl, 10 mM imidazole.
- **Washing buffer 2**: 20 mM Tris, pH 7.4, 150 mM NaCl, 20 mM imidazole.
- **Washing buffer 3**: 20 mM Tris, pH 7.4, 150 mM NaCl, 30 mM imidazole.
- **Imidazole elution buffer**: 20 mM Tris, pH 7.4, 150 mM NaCl, 300 mM imidazole.
- **3C buffer**: 20 mM Tris, pH 7.4 , 150 mM NaCl, 1 mM DTT, 1 mM EDTA
- **TES buffer**: 200 mM Tris-Base, 0.5 mM EDTA, 500 mM sucrose.
- **PE buffer**: 50 mM Tris-Base pH 8.0, 1 mM EDTA, 150 mM NaCl, 20 % sucrose.
- **TfB I**: 100 mM RbCl, 50 mM $MnCl_2$, 30 mM potassium acetate, 10 mM $CaCl_2$, 15 % glycerol, pH 5.8, sterilised by filtration.
- **TfB II**: 10 mM MOPS, 10 mM RbCl, 75 mM $CaCl_2$, 15 % glycerol, pH 6.8, sterilised by filtration.
- **PBS** (phosphate-buffered saline): 137 mM NaCl, 2,7 mM KCl, 10 mM Na_2HPO_4 , 1,8 mM KH_2PO_4, pH 7.4.

1.2. Culture mediums

- **SOB medium**: for 1 litre, 0.5 g NaCl, 20 g Tryptone, 10 ml KCl 250 mM until 995 ml with H_2O_{mq}. Just before use add 5 ml $MgCl_2$ 2 M previously sterilised by autoclaving.
- **Luria Broth medium** (LB): for 1 litre, 25 g LB broth mix.
- **Terrific Broth medium** (TB) **for Nb**: for 1 litre, 2.3 g KH_2PO_4, 16.4 g $K_2HPO_4{\cdot}3H_2O$, 12 g Tryptone, 24 g yeast extract, 4 ml glycerol 100 %.
- **Terrific Broth medium** (TB) **for MSP**: for 1 litre, 2.3 g KH_2PO_4, 16.4 g $K_2HPO_4{\cdot}3H_2O$, 12 g Peptone, 24 g yeast extract.
- **TY medium**: for 1 litre, 16 g Tryptone, 10 g yeast extract and 5 g NaCl.

1.3. Competent cells preparation

This experimental procedure was used for obtaining new competent cells of the *E.coli* TOP10, BL21 (DE3), and WK6 (Su-) strains. *E.coli* Rosetta cells were obtained from Protein Expression Facility (IRB Barcelona).

Firstly, cells were plated two consecutive times in LB agar plates and incubated at 37 ºC ON (for *E.coli* WK6 (Su-) cell culture plates contained 0.1 mg/ml streptomycin). 1 ml SOB medium was inoculated with five different colonies and incubated at 37 ºC in agitation for 5 minutes, without adding antibiotic. Then, 200 ml SOB medium was inoculated with the grown starter culture and incubated at 37 ºC agitated at 240 rpm for TOP10 and BL21 or 180 rpm for WK6 until first turbid floccules appeared avoiding an extreme cell growth.

Cultures were split in 50 ml falcon and incubated for 10 min in ice and cells were recovered by centrifugation at 1800 × relative centrifuge force (RCF, g from here on) for 10 min at 4 ºC. Cells were resuspended in 15 ml of TfB I Buffer per each 50 ml culture and incubated again 10 minutes on ice. Final cell recuperation was performed by centrifugation at 1800 × g for 10 min at 4 ºC. Cells were resuspended with a final volume of 10 ml of TfB II Buffer per each 200 ml of initial culture. 50 µl aliquots for WK6 (Su-) and 100 µl for *E.coli* TOP10 or BL21 (DE3) were made into -20 ºC pre-chilled tubes that were snap-frozen in LN and stored at -80 ºC until use.

1.4. Heat shock cell transformation

Depending on the purpose, different *E.coli* strains have been used. For DNA amplification, *E.coli* TOP10 strain; for BasC expression, *E.coli* BL21 Star (DE3); for Nb and Mb expression, *E.coli* WK6; and for MSP expression, *E.coli* Rosetta. Sequences and vectors used in this thesis are listed all along the Appendix B.

Firstly, aliquots of competent cells were mixed with 2 µl cDNA at 200 ng/µl or 10 µl PCR product and incubated in ice for 20 min. Heat shock was carried for 1 min incubation at 42 ºC followed of 2 min incubation in ice. Finally, 900 µl LB antibiotic-free was added and incubated at 37 ºC in agitation for at least one hour. Cells were recovered by centrifugation at 4,000 × g for 10 min at room temperature (RT). After discarding almost all the supernatant (SN), pelleted cells were resuspended and plated in LB agar plates supplemented with the appropriate antibiotics and substrates 100 mg/L ampicillin for BasC transformed cells, 100 mg/L ampicillin and 2 % (w/v) glucose for Nbs or Mbs transformed cells and 50 mg/L kanamycin for MSPs transformed cells. Finally, plates were incubated at 37 ºC ON ready for the following step, DNA amplification or protein expression.

1.5. Mutagenesis

All BasC double-Cys variants were performed with their respective primers (Appendix B. 1. Bacterial alanine-serine-cysteine, Table B. 1) with QuikChange site-directed mutagenesis kit by PCR in 25 µl of mix. Mix contained Cloned Pfu DNA polymerase reaction buffer 1x, 4 % dimethyl sulfoxide (DMSO), 1 mM $MgCl_2$, 500 µM FP, 500 µM RP, 100 mM deoxynucleoside triphosphates (dNTPs) (25 mM each) and 1.25 U of PfuTurbo DNA polymerase. Finally, the DNA template was added at 25 ng/µl.

Sixteen PCR cycles were carried on a thermocycler with an initial 60 s step at 95 ºC followed by 30 s at 95 ºC, 1 min at 55 ºC and 14 min at 68 ºC per cycle and a final step of 10 min at 68 ºC. Then, each sample was supplemented with 5 U DpnI and incubated ON at 37 ºC. *E.coli* TOP10 cells were transformed by heat shock (Experimental procedures 1.5), plated into LB agar plates supplemented with 0.1 mg/ml ampicillin and incubated at 37 ºC ON.

1.6. cDNA amplification

cDNA amplification was performed to check sequences by sequencing or just amplifying verified ones. Single *E.coli* TOP10 transformed colonies were picked and used to inoculate 3 ml LB supplemented with 0.1 mg/ml ampicillin and incubated at 37 ºC ON agitated at 240 rpm. Cells were recovered by centrifugation and cDNA extracted by NucleoSpin mini kit. All obtained DNAs sequences were checked by Sanger sequencing at Macrogen facilities (Macrogen Spain, Madrid, ES) using the appropriate sequencing primers (Appendix B. 4 Sequencing Primers, Table B. 3).

1.7. BasC expression and purification

Three or four fresh transformed *E.coli* star (DE3) colonies were used to inoculate the LB starter culture (20 ml each 800 ml of culture) supplemented with 0.1 mg/ml ampicillin and incubated at 37 ºC ON at 240 rpm agitation in non-baffled flasks. 800 ml LB medium in non-baffled flasks were inoculated with 20 ml starter culture, supplemented with 0.1 mg/ml and incubated at 37 ºC at 240 rpm agitation until an optical density at 600 nm (OD_{600}) = 0.5 AU. Induction of the expression was performed supplementing the culture with 0.1 mM Isopropyl β-D-1-thiogalactopyranoside (IPTG) and incubated at 37 ºC ON at 240 rpm agitation.

Cells were recovered by centrifugation at 5,000 × g for 30 min at 4 ºC and resuspended adding 20 ml High Salt Buffer per 800 ml of culture. A second centrifugation was performed at 3,500 × g for 30 min at 4 ºC and recovered cells were resuspended again in 25 ml lysis buffer per each 800 ml of culture. Cells were lysate by four cycles at 35 kPSI in the Cell Disruptor.

Non-lysed cells were discarded by centrifugation at 23,600 × g for 1 hour at 4 ºC. The membranes fraction present in the SN was recovered by centrifugation at 200,000 × g for 2 hour at 4 ºC and resuspended in membranes buffer until 5-15 mg/ml concentration measured by Pierce™ BCA Protein Assay Kit. Samples were aliquot, snap-frozen in LN and stored at -80 ºC until use.

The use of different detergent (DDM or DM) depended on the purpose of the purification. DDM was generally used at 0.06 % (w/v) and DM at 0.17 % (w/v) if it is not specified the opposite. In both cases, they were above the double of their critical micelle concentration (CMC). By the one hand, DDM was used for Binding assays (Experimental Procedures 2), BasC reconstitution in PLs (Experimental Procedures 3) and ALEX-smFRET measurements (Experimental Procedures 4). By the other hand, DM was used for Structural studies (Experimental procedures 5) and BasC reconstitution into nanodiscs (Experimental procedures 6).

Membranes were diluted until 3 mg/ml in Tris buffer supplemented with 1 % (w/v) DDM or 2 % (w/v) DM and incubated for one hour at 4 ºC. Solubilised membranes were recovered in the SN after centrifugation at 200,000 × g for 2 h and supplemented with 0.5 ml Ni^{2+}-NTA Superflow beads per each 10 ml of diluted membranes. Nickel beads were previously washed with 2 × 10 CV H_2O_{mq} and equilibrated with 2 × 10 CV Tris buffer supplemented with either 0.06 % (w/v) DDM or 0.17 % (w/v) DM. BasC-GFP incubation with Nickel beads was carried for at least 3 h at 4 ºC. Resin was washed with 10 CV each washing buffer (I, II and III) supplemented with DM or DDM. Elution type (imidazole or protease-cut) depended on the purpose of the purification.

By the one hand, for BasC-GFP elution, imidazole was used. Then, after washing resin, BasC-GFP was eluted with elution buffer supplemented with DM or DDM. Buffer was finally exchanged to DM or DDM buffer. Eluted BasC-GFP was finally concentrated with Amicon Ultra filter of 100,000 kDa cut-off.

By the other hand, for BasC elution, HRV-3C-protease was used. After washing the resin, this was further equilibrated with 2 × 10 CV of 3C buffer, and resin was supplemented with 900 µl 3C buffer supplemented with the used detergent plus 100 µl HRV-3C-protease per each millilitre of resin. Digestion was allowed ON at 4 ºC in mild rotation. Direct elution was allowed and further 2 CV washes, if needed, further 2 CV Tris buffer supplemented with the used detergent were applied until concentration of purified BasC decreased. Finally, eluted BasC was concentrated through Amicon Ultra filter of 50,000 kDa cut-off.

Once BasC or BasC-GFP was purified, solubilised in the desired detergent, it was either used freshly or snap-frozen in LN and stored at -80 ºC until use.

1.8. Antibodies derived products

Antibodies (Abs) were first reported in 1890 after the detection of a component in the blood with the capacity to neutralize the diphtheria toxin. This agent was later named Antikörper. Abs, also named Immunoglobulins (Igs), are heterodimeric glycoproteins that bind to specific antigen epitopes with high specificity (Hassanzadeh-Ghassabeh et al., 2013).

Monoclonal antibodies (MAbs) are those obtained from a single B cell that produces a unique antibody against an epitope of a single antigen. MAbs have made a striking contribution to the development of scientific tools and human therapeutics. The first MAb was approved by the Food and Drug Administration (FDA) in the U.S. in the 1986. As of November 2020, the FDA and the European Medicines Agency (EMA) had approved **95 therapeutic MAbs**. Moreover, during the COVID-19 pandemic alone, more than 10 MAbs were authorized. Furthermore, the number of MAbs in the global Phase 1, 2 and 3 clinical trials amount to 453, 290 and 88, respectively (Kaplon and Reichert, 2021) (as of November 2020). These data bring to light the increasing development of MAbs as drugs and their relevance for clinical therapeutics.

The structure of Abs is highly conserved among mammals (Figure 51. A). The variable domains (from both heavy and light chains) are responsible for the binding to antigens (Schroeder and Cavacini, 2010) and they can be divided into three regions of sequence variability, namely the complementarity-determining regions (CDRs), and four framework regions with a relatively constant sequence. The CDRs of the heavy chain are paired with the CDRs of the light chain to form the antigen-binding site, as classically defined. In contrast, constant domains are organised similarly in all isotypes, each isotype being defined by its constant domains (i.e., IgM, IgG, IgA...) (Jr et al., 2001). The fragment-crystallisable region, or effector region, designates the function exerted by the Ab (e.g., IgG triggers the destruction of harmful germs).

An Ab has a molecular weight of approximately 160 kDa. Smaller antigen binding fragments can be derived from its structure; such as fragment antigen-binding (Fab) or single-chain variable fragment (scFv) (Figure 51. A), with molecular weights of 50 and 30 kDa, respectively. The smallest fragment, scFv, is a synthetic product composed of an N-ter variable domain of the heavy chain (V_H) and light chain (V_L), joined by a short peptide linker (Figure 51. A). As smaller the antigen-binding molecule is, smaller the epitope will be recognised and, therefore, more distinct epitopes will exist. Efforts to express single-chain variable fragment (scFv) in microorganisms have given low yields, and attempts have also been made to use single soluble V_H or V_L libraries and also man-made scaffolds, all of which are accompanied by their respective advantages and disadvantages (Hassanzadeh-Ghassabeh et al., 2013).

Abs and their derivatives are widely used for research purposes, with applications ranging from the detection of specific molecules through the western blot technique to their use as chaperones in crystallography (Koide, 2009). Indeed, the

first application of chaperone-assisted crystallography in MPs involved the use of a recombinant scFv (Ostermeier et al., 1995). Abs and their derivatives can be used to lock the most flexible regions of proteins or the whole protein in a more fixed conformation that is easier to crystallise. Polar contacts are primarily responsible for the formation of the crystal lattices of MPs, and the binding of Ab fragments increases the polar surface area, which is very important, especially for unstable MPs or membrane complexes where only a few, mild detergents can be used. As Abs are conformation-specific, they might "freeze" the target in a given conformation, thereby leading to a more homogeneous preparation

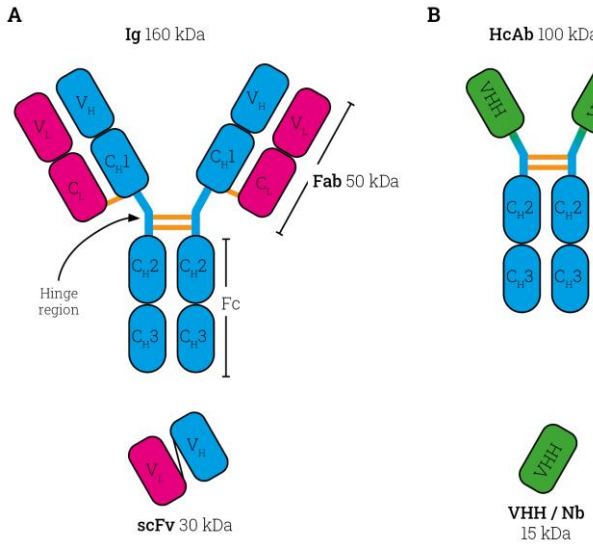

Figure 51. Monoclonal and heavy chain-only antibodies derivatives. Light domains coloured in pink, heavy in blue and VHH in green. Variable and constant domains are indicated with V or C, respectively. **A.** Classical four chain structure of an Ig (i.e., Ab) and its derivatives (Fab and scFv). Two identical light chains (V_L-C_L) and two identical heavy chains (V_H-C_H1-C_H2-C_H3), which are held together by disulphide bonds to form a flexible Y shape. Flexibility is also conferred for the hinge region. **B.** Camelid or heavy chain-only antibody (HcAb) and its derivate or VHHs or Nb.

In 1993, it was reported, almost serendipitously, that Abs devoid of a light chain naturally occur in camelid species (e.g., camels, dromedaries, llamas and alpacas) (Hamers-Casterman et al., 1993). Similar single chained Abs are found in sharks. These antibodies are also named heavy chain-only antibodies (HcAbs) and they weight ~100 kDa. HcAbs are folded into three domains: an N-terminal domain that is variable in sequence (i.e., VHH for camelids and VNAR for sharks), bound to two constant domains through a hinge region (Figure 51. B). Therefore, the

equivalent of the first constant domain of the heavy chain of a conventional antibody (C_H1) is missing in HcAbs (Hassanzadeh-Ghassabeh et al., 2013).

Therefore, as HcAbs are single chained, these natural camelid Abs can be used to obtain the smallest Ig antigen-binding from the variable domain of a heavy-chain Ab (VHHs), called also nanobody (Nb) (Muyldermans et al., 2001) (Figure 51. B). Nbs are effectively generated through a semi-synthetic approach. VHHs are the smallest Ig, with only 125 residues and weighting no more than 15 kDa. Functionally, Nbs have a strong tendency to bind to preformed clefts, while for conventional mammal Abs and their derivatives is less pronounced due to their larger antigen binding area (Genst et al., 2006). Thus, Nbs can be used as complementary chaperones to target distinct types of epitopes.

The production of specific Nbs against our target protein is relatively simple and fast. After vaccinating a camelid to raise an H_2-type Ab response, the VHH gene fragments from lymphocytes are amplified by PCR, ligated in phage display vectors, and transformed in bacteria to construct an immune VHH library. Antigen-specific VHHs on immobilized antigens in two or three rounds of panning allows the identification, with a high success rate, of Nbs targeting a wide variety of antigens with nanomolar to even picomolar affinities (Vincke et al., 2012). The retrieved Nbs are successfully expressed in microorganisms, thereby providing an easy route to obtain large amounts of *in vivo* affinity-matured, antigen specific single-domain Abs. This is an important advantage over scFv or man-made scaffolds (Hassanzadeh-Ghassabeh et al., 2013).

Nbs are impermeable to lipid membranes. In this regard, considerable research effort are being channelled into achieving transducing Nbs. Such Nbs could be used to produce 'Trojan horses' with therapeutic uses that direct drugs specifically to their targets (Hassanzadeh-Ghassabeh et al., 2013). In 2016, Bruce and cowork hypothesised that the sequence resurfacing of Nbs to polycationic AAs could be used to transduce these Nbs as was previously shown in other investigations with different therapeutic binders and proteins (Fuchs and Raines, 2007; Cronican et al., 2010; Thompson et al., 2012; Chapman and McNaughton, 2014). Bruce and co-workers succeeded when mutating several residues out of the CDRs and out of the essential structure regions (Bruce et al., 2016).

The most important feature of Nbs is that do not induce non-native conformations as they are matured *in vivo*. Therefore, Nbs will always recognise native states of the antigen (protein target), as long as the quality and conditions of the target were optimal when vaccinating the camelid. Immature B cells expressing antibodies would have to pay a substantial energetic penalty for distorting the antigen structure and would have a lower probability of proliferation and differentiation (Pardon et al., 2014).

1.8.1. Nanobodies expression and purification

Three or four fresh transformed *E.coli* WK6 (Su-) strain colonies were used to inoculate the LB starter culture (20 ml per litre of culture) supplemented with 0.1 mg/ml ampicillin 2 % glucose and 1 mM $MgCl_2$ and incubated at 37 °C ON at 190 rpm agitation in 50 ml falcons. 3 × 330 ml of autoclaved TB culture were supplemented with 0.1 mg/ml ampicillin, 0.1 % glucose, 2 mM $MgCl_2$ in one litre baffled flask. Medium was inoculated with 3 ml of grown starter culture and grown at 37 °C, shaking at 190 rpm, until an OD_{600} between 0.7 and 1.1 AU. Overexpression was performed adding 1 mM IPTG and incubating ON at 190 rpm at 28 °C.

OD_{600} of 1/50 diluted was measured and cells were recovered by centrifugation at 4,500 × g for 30 min at 4 °C. Cells were resuspended with 15 ml TES buffer per each initial litre for an OD_{600} = 25 AU and incubated for at least one hour at 4 °C magnetically stirred. 30 ml of ¼ TES buffer in H_2O were added per each litre of culture for an OD_{600} = 25 AU and incubated for 45 min at 4 °C magnetically stirred.

Periplasm was obtained from the SN after centrifugation at 15,000 × g for 30 min. Per each litre of culture, 1 ml of Ni^{2+}-NTA Superflow beads previously washed twice with H_2O_{mq} and equilibrated with Tris buffer was added and incubated for at least 3 h at 4 °C in stirring or rotation. A second osmotic shock was applied resuspending cells again on 25 ml TES buffer and incubating ON at 4 °C magnetically stirred repeating all steps.

Resin was washed 3 × 10 CV with washing buffer I and Nb was eluted 4 × 2 CV with elution buffer. Buffer was exchanged and Nb concentrated through an Amicon Ultra filter of 3,000 kDa cut-off. Nbs snap-frozen in LN and stored at -80 °C until use.

1.9. Membrane scaffold protein expression and purification

Three-four fresh transformed *E.coli* Rosetta strain colonies were used to inoculate the TB starter culture (25 ml per litre of culture) supplemented with 0.05 mg/ml kanamycin and incubated at 37 °C ON at 250 rpm agitation in non-baffled flasks. 800 ml of autoclaved TB were supplemented with 0.05 mg/ml Kanamycin and inoculated with 25 ml of the grown starter culture at 37 °C and 250 rpm until an OD_{600} between 2.5 and 3 AU. Overexpression induction was performed adding 1 mM IPTG and incubating for 3,5 h at 37 °C at 250 rpm.

Cells were recovered centrifuging at 4,500 × g for 15 min resuspended in 50 ml of high salt buffer per litre of culture and centrifuged again at 3,000 × g for 15 min. Centrifuged cells without medium nor buffer were stored at -20 °C until purification.

Purification cells started resuspending cells with 30 ml of PBS supplemented with 0.2 % Triton™ X-100, 0.1 mM Pefabloc, protease inhibitor cocktail cOmplete

EDTA-free and 20 kunits/ml DNase. After 20 min incubation at 4 ºC cells were disrupted through two cycles of 35,000 kPSI in the Cell Disruptor. Disrupted cells were supplemented until 1 % of Triton™ X-100 and incubated in stirring for 10 min at 4 ºC. Finally, periplasmic fraction was recovered in the SN after centrifugation at 20,000 rpm for 30 min at 4 ºC. Periplasmic fraction was incubated at least 2 h at 4 ºC with 500 µl of Ni^{2+}-NTA Superflow beads per litre of culture previously washed 2 × 10 CV of H_2O_{mq} and equilibrated 2 × 10 CV 40 mM Tris, 300 mM NaCl.

Resin was washed first with 20 CV 40 mM Tris, 300 mM NaCl, pH 7.4, 1 % Triton™ X-100; then with 20 CV 40 mM Tris, 300 mM NaCl, pH 7.4, 20 mM imidazole, 50 mM cholate; and finally with 20 CV 40 mM Tris, 300 mM NaCl, pH 7.4, 50 mM imidazole. Elution was performed distinctly depending on the need of the His-tag. By the one hand and for keeping the His-tag, imidazole elution was performed trice with 1 CV 20 mM Tris, 150 mM NaCl, pH 7.4, 40 mM Sodium Cholate, 0.5 mM EDTA, 300 mM imidazole. Imidazole was eliminated through desalting PD-10 columns equilibrated with Tris buffer supplemented with 40 mM Sodium Cholate Eluted and buffer changed MSP-his was concentrated using Amicon Ultra filters of 10,000 Da cut-off. By the other hand, to obtain MSP without His-tag, TEV cleavage elution was performed. Resin was equilibrated with 2 × 10 CV TEV buffer (Tris buffer supplemented with 40 mM Sodium Cholate, 0.5 mM DTT and 0.5 mM EDTA). Resin was resuspended in 2 CV TEV buffer supplemented with 500 µl of TEV protease and incubated for a first 2 h at RT and 15 h at 4 ºC. Eluted MSP was concentrated using Amicon Ultra filters of 10,000 Da cut-off, snap-frozen in LN and stored at -80 ºC until use.

2. Binding assays

2.1. Surface Plasmon Resonance

Due to the hydrophobic characteristics of the transporter and the difficulties found when having to use detergent in all immobilising buffers, SPR screening was designed immobilising the Nb through their His-tag avoiding the use of detergents during the first steps of this technique. Then, different concentrations of BasC with and without L-Ala were flowed on over the channels.

SPR was carried out on Biacore T-100 immobilising the 29 Nbs (3 – 20 µg/ml) until reaching 200 resonance units (RU). For binding against BasC expressed and purified in DM. Immobilising injections were performed for 20 s at 5 µl/min flowrate on CM5 Sensor Chip previously coated with an anti-His antibody (His capture kit; GE Healthcare, Chicago, IL) and regenerated with 10 mM HCl in running buffer (PBS, 0.17 % DM). BasC purified in DM was assayed between 2.5 and 500 nM in running buffer.

2.2. Size exclusion chromatography

BasC purified in DM or DDM was diluted at the desired concentration and incubated for 1 h at 4 ºC with the selected Nb at molar ratios 1:1.5 (BasC:Nb). For double Nb trials, a second incubation with the other Nb was performed the same way. Same amount of solubilised BasC without any Nb was also used.

All samples were filtered through centrifuge tube cellulose filters with 0.22 µm pore size and directly injected to a Superdex 200 10/300 GL column to perform in an ÄKTA purification system. UV monitor was performed at 280 nm and samples were recovered by fractionation, 250 µl each, for further SDS-PAGE analysis if needed.

2.3. Micro Scale Thermophoresis

100 µl of 60 µM purified BasC in DDM were supplemented with 10 mM DTT and incubated for 1 h at 4 ºC. DTT was eliminated through desalting using 0.5 ml Zeba Spin columns and sCy5 was immediately added at molar ratio 1:1,5 (BasC:sCy5). Maleimide reaction between sCy5 and BasC-Cys427 took place ON at 4 ºC in rotation protected from light.

BasC-sCy5 was purified through SEC on a Superdex 200 10/300 GL column. Fractions collected were directly used to perform the analysis on MST device using premium capillaries. Pre-test analysis optimal concentration giving between 300-400 counts of raw fluorescence was used for the affinity analysis against BasC and BasC-Nb78.

BasC concentration used for affinity analysis was around 100 nM. For BasC-Nb78, same amount of BasC was supplemented at molar ratio 1:1.5 (BasC:Nb78) and incubated for 1 h at 4 ºC. Capillary scan outliners were discarded for a proper dose response measurement.

2.4. Thermostability

BasC double-Cys variants labelled and purified samples were directly used at pM range concentration for nanoDSF assays on Prometheus device in premium capillaries. Samples obtained from labelling SEC fractionation were solubilised in 0.06 % (w/v) DDM and diluted at different folds in order to check the optimal concentration to be used in each case. Then, once dilution was adjusted, triplicate T_m measurements were performed per each sample loading three different premium capillaries of BasC WT and K154A TM1a-4 and TM1a-12 variants labelled with sCy3-sCy5 and Alexa 546-Alexa 647, respectively. Finally, L-Ala was titrated on BasC TM1a-12 variant to measure its binding through this technique.

Prometheus settings: 19-95 ºC temperature range, 1 ºC/min heating rate and 50 % excitation power.

3. Transport activity assays

3.1. BasC reconstitution in PLs

E.coli total polar lipids extract powder was dissolved in chloroform until 50 mg/ml for aliquoting and were dried in small glass avoiding the generation of bubbles under a stream of N_2. Once a thin layer of lipids was stacked in the glass, the tubes were let under the N_2 stream for three hours at RT. Once the lipids were fully dried, they were resuspended under sonication until 40 mg/ml in Tris buffer.

Resuspended lipids were finally mixed with BasC at concentration ratio 1:100 (protein:lipid). Octylglucoside was finally added to the mix at 1.25 % and incubated for 30 min at 4 ºC. Sample was dialysed in dialysis tubing for 40 h at 4 ºC against 100 × volumes of Tris buffer. After dialysing, PLs were recovered and snap-frozen in LN and stored at -80 ºC until use.

3.2. Influx and efflux

PLs were filled up adding 4 mM L-Ala for influx, and 10 µM L-Ser and 0.5 µCi/point L-[^{3}H]-Ser for efflux, in both cases through six freeze and thaw cycles. Empty liposomes for influx were just performed directly without adding any AA. After 30 min incubation in ice, PLs were pulled down with ultracentrifugation at 100,000 × g for 1 h at 4 ºC. Medium was discarded and PLs were resuspended in Tris buffer until one third or half of the initial volume depending on the batch.

Transport was allowed during 5 s for influx or 30 s for efflux after mixing 20 µl of PLs with 180 µl of transport buffer (Tris buffer with 10 µM L-Ser and 0.5 µCi/180 µl of L-[^{3}H]-Ser for the influx or Tris buffer with 4 mM L-Ala for the efflux). Transport was stopped with 3 ml ice-cold Tris buffer for efflux or supplemented with 10 mM L-Ser for influx. Finally, PLs were filtrated through 0.45 µm pore-size membrane filters and cleaned adding 2 × 3 ml ice-cold stop buffer. Filters were let dry completely at RT and submerged in scintillation liquid to count tritium radioactivity trapped inside the PLs for 3 min.

For the Nb screening, 15 and 5 µM were added in transport solutions and PLs preparations for influx and efflux, respectively, letting a 20 min incubation prior to transport assay.

To obtain the net AA exchange in influx, time zero Ctrls were performed for empty and L-Ala PLs, adding from the beginning the first 3 ml of stop solution at 4 ºC to the transport solution, before adding the PLs. In addition, transport measured in empty PLs was subtracted from each L-Ala data point. Influx measurements were finally normalised to the BasC protein concentration determined by SDS-PAGE and expressed in pmol of radiolabelled AA per µg of protein and time ($pmol_{AA}/\mu g_{BasC}/s$).

In order to measure the net exchange in efflux, the loss of counts was measured respect the initial Ctrl at times zero (adding the 20 µl of PLs in ice-cold Tris buffer directly). In addition, Ø Ctrls for 30 s (adding the 20 µl of PLs in ice-cold Tris buffer directly for 30 s) were performed at the beginning and continuously at different times all along the assay. Transport measurements were expressed in relation to non-treated samples as SDS-PAGE of radiolabelled PLs were unable to be performed.

3.3. High concentration amino acid transport assay

AA screenings at high concentration were performed as the influx transport activity assay. PLs were filled with six freeze-thaw cycles adding 100 mM AA. After 30 min incubation in ice, they were pulled down with ultracentrifugation at 100,000 × g for 1 h at 4 ºC. Medium was discarded and PLs were resuspended in Tris buffer until the desired concentration, until one third or half of the initial volume. All extra liposomal solutions and empty PLs were supplemented until 100 mM AA concentration with L-Mannitol.

Transport was permitted for 5 s mixing 20 µl of PLs with 180 µl of transport buffer (Tris buffer with 10 µM L-Ser and 0.5 µCi/180 µl of L-[^{3}H]-Ser). Transport was stopped adding 3 ml ice-cold stop buffer (Tris buffer with 100 mM L-Mannitol). Finally, PLs were filtrated through 0.45 µm pore-size membrane filters and cleaned adding 2 × 3 ml ice-cold stop buffer. Filters were let dry completely at RT and submerged in scintillation liquid in scintillation vials. Tritium radioactivity trapped inside the PLs was counted for 3 min each vial.

To obtain the net AA exchange and normalise, Ctrls and measurements were performed as explained previously in influx (Experimental procedures 2.3).

4. Single-molecule FRET

Although FRET is still named Förster Resonance Energy Transfer in honour of Theodor Förster (1910-1974), in this thesis FRET is used to refer to Fluorescence Resonance Energy Transfer (for more information regarding this issue, see Appendix D. 3. Statement on antifascism).

FRET is a distance-dependent, non-radiative energy transfer process that occurs between a fluorophore and a chromophore as a consequence of long-range dipole–dipole coupling (Förster, 1948). FRET is a physical process whereby the excited state energy of one chromophore molecule can be transferred to a neighbouring chromophore in the ground state (Clegg, 2006; Roy et al., 2008) (Figure 52. C). The number of publications with FRET as the topic reflects both the advancement and growing diversity of FRET methods available. PubMed shows how until 2000, the topic of FRET appeared in 290 publications, increasing to over 14,780 in 2021 (Data accessed on 26 May 2022).

Although other non-optical techniques have higher resolution (e.g., XRC), they are generally more technically complex and more restrictive with respect to sample preparation and measurement conditions (Algar et al., 2019). In contrast, FRET has minimal limitations as, since its development, it has been used as a molecular ruler extensively, both *in vivo* (König et al., 2015) and *in vitro* (Majumdar et al., 2007).

In most cases, the chromophore is also a fluorophore and the probes can be induced in a single biomolecule. After excitation of the high-energy fluorophore or donor (D) via an external light source, the energy can be transferred to a low-energy fluorophore or acceptor (A) (Figure 52. D-E) as long as the following two preconditions are fulfilled (Hwang et al., 2009; Algar et al., 2019):

- The emission spectrum of D overlaps with the absorption spectrum of A. (Figure 52. A)
- The two fluorophores are close enough (1-10 nm) (Figure 52. B)

Because of energy transfer, the emission intensity of D decreases ("donor quenching") and the emission intensity of A increases ("acceptor sensitization"). The FRET process is often represented by a simplified Jablonski chart, which is a free-energy state diagram that illustrates the electronic states of the fluorophores and the transitions between them (Figure 52. C).

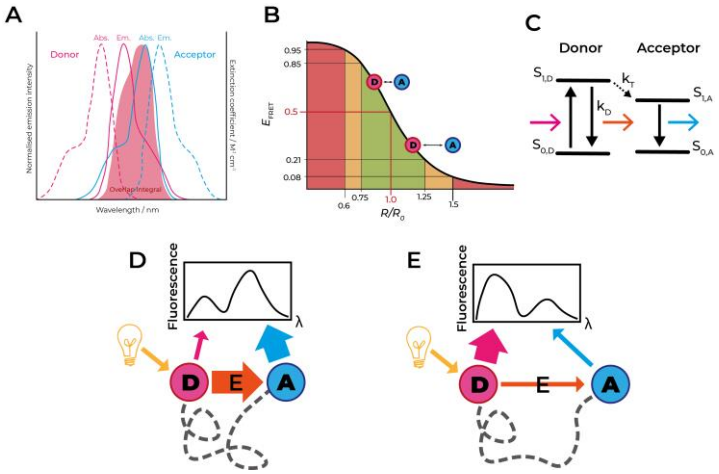

Figure 52. Fluorescence Resonance Energy Transfer principles. A. Absorbance (Abs.) and emission (Em.) normalised spectrums for D in pink and A in blue and the resulting spectral overlap (red). **B.** FRET-efficiency (E_{FRET}) as a function of inter-dye distance relative to their Förster radius (R/R_0). D dye directly excited with incident laser (**D-E**) either fluoresces or transfers energy to A dye, depending upon its proximity. At $R = R_0$, $E = 0.5$ (red lines) but at smaller distances, it is > 0.5 and vice versa, according to the function (black). Notice the linearity of the E values adjacent to $R/R_0 = 1.0$. The dynamic range decreases from the

green to the yellow to the red zones. **C.** Simplified Jablonski diagram showing the transition pathways occurring in the energy transfer process. After excitation of the D dye (pink arrow) into its first excited singlet state, two processes can occur: the D system can either relax to its ground state by emitting a green photon with a rate constant k_D, or the energy can be transferred to the A molecule with a rate constant of k_T (orange arrow). In the last case, the A relaxes by emitting a red photon (blue arrow). Other electronic transitions, such as bleaching and intersystem crossing, are neglected. **D.** Example of how a light source directly excites the D. As long as the A is in close proximity, the energy (E) can be transferred non-radioactively from the D to the A, resulting in increased emission intensity for the A spectrum. **E.** Opposite example when the distance between the D and the A is increased, the fraction transferred E decreases, resulting in increased the emission intensity of the spectrum corresponding to the D.

With a proper design of the dye positions, distances between fluorophores can be estimated from FRET efficiency, taking into account the Förster Radius (R_0) of the fluorophore pair (Roy et al., 2008) (Figure 52. B). R_0 describes the D-to-A distance where FRET efficiency equals 50 % and takes values between 2 and 7 nm (Selvin, 2000) for common pairs of fluorophores.

Depending on the number of particles labelled, two different approaches can be used as single molecule FRET (smFRET) techniques. On the one hand, there is intermolecular FRET. This technique is widely used to label different species in order to track and study binding or oligomerisation (Mori et al., 2003), and it can also be used to study the conformation dynamic effects of these processes (Lu et al., 2019). On the other hand, there is intramolecular FRET, the technique used in this thesis. This approach allows the study of the conformation dynamics of a protein where both fluorophores are bound and tracked. This approach has been used several times for MPs (LeVine et al., 2019; Mächtel et al., 2019; Majumdar et al., 2007; Terry et al., 2018; Zhao et al., 2011). In this regard, Majumdar and co-work used it to study LacY transporter from MFS in detergent micelles and we have already seen studies on LeuT through TIRF-smFRET in Introduction 2.4 Transport Mechanism.

The advantage of being a single-molecule technique is the simplicity offered to study free diffusing or surface-immobilised molecules. Thus, in a free diffusion manner through confocal microscopy (Figure 53. A), intramolecular FRET is a powerful technique to study population distributions of inter-dye distances (Majumdar et al., 2007) (Figure 53. B). Nevertheless, FRET efficiencies can also be tracked in real-time when the labelled molecules are surface-immobilised, and their conformational dynamics can then be obtained through TIRF microscopy (Lu et al., 2019) (Figure 53. C). In that last case, transition density plots can be extracted from the fluorescence traces (Figure 53. D) obtained. In these plots, the relative frequency of state-to-state transitions is indicated. Since the first smFRET measurement in 1996 (Ha et al., 1996), the technique has contributed substantially to our understanding of biological molecules and processes by probing the structure and dynamics of nucleic acids, proteins, and complexes between these molecules (Hwang et al., 2009).

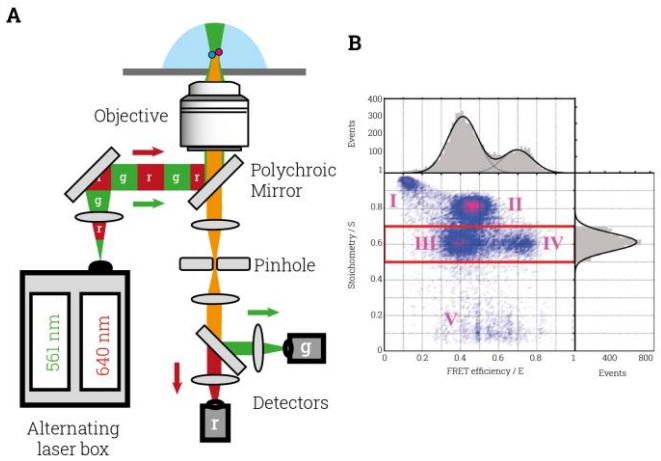

Figure 53. Implementation of the alternating-laser excitation scheme in confocal microscopy. A. The laser box in the excitation pathway contains two mouldable table lasers in order to provide well-defined sequences of red (r) and green (g) illumination. After collimating the laser light with a lens and reflecting the laser by a polychroic mirror, an objective with high numerical aperture is used to generate a diffraction limited excitation spot in the sample volume. Fluorescence, originating from fluorescent dyes attached to biomolecules diffusing through the confocal spot, is collected by the same objective and spatially filtered with a pinhole before it is spectrally split into a green and a red detection channel. During the transit of a single biomolecule through the focus, the periods of green (g) and red (r) excitation alternate much faster than the corresponding diffusion time. Upon direct excitation of the D, some energy can be transferred to the A via FRET. The existence of the A is probed during red excitation. Use of confocal microscopy results in E vs S Histograms (C). **B.** E vs S histogram for simulated data of five different species diffusing through a confocal volume using solution-based ALEX. The parameters used for the simulation were adjusted to mimic experimental conditions as closely as possible. Whereas the two-dimensional ES histogram allows differentiating all species unambiguously, the one-dimensional histogram of the transfer efficiency after single-colour excitation would have been too convoluted to separate species II and III. The one-dimensional bar histograms represent the data as defined by the red box (Hohlbein et al., 2014).

4.1. BasC labelling in-resin and purification

BasC-GFP double-Cys variants were purified with DDM as explained previously in Experimental Procedures 1.7 with the only difference that 10 mM DTT were added to all buffers and steps to prevent Cys reduction. Then, just after the third wash of the resin, DTT was eliminated equilibrating the column with 10 CV of DDM buffer. Immediately after the equilibration fluorophores* were added at the

desired concentration in a final volume of 200 µl DDM buffer. Maleimide reaction was allowed for 15 h at 4 ºC in vigorous agitation and light-protected. Dye excess was washed away with 6 × 10 CV DDM buffer and resin was then equilibrated with 2 × 10 CV 3C buffer supplemented with 0.06 % (w/v) DDM.

** Fluorophores were stored dried in 25 nmol aliquots. Resuspension with 2 µl DMSO was needed before the correct dissolving in DDM buffer. Fluorophore concentration may be adjusted depending on the amount of protein in the resin, double-Cys variant and fluorophore type. In addition, addition delays between D and A may be applied.*

To elute labelled-BasC 25 µl of HRV 3C protease was added in 250 µl 3C buffer and incubated 3 h at 4 ºC in rotation and light-protected. The elution was collected by mild centrifugation (30 s at 900 × g) and a second 250 µl elution was performed through centrifugation adding 250 µl of DDM buffer. Finally, labelled-BasC was purified and completely cleaned from free dyes through SEC on a Superdex 200 10/300 GL column in DDM buffer. Labelling efficiency can be measured using the following formula from the absorbance profiles at 280 nm and each dyes absorbance maximum wavelengths.

4.2. Free-diffusion ALEX-smFRET experiments

Free diffusion ALEX-smFRET experiments were performed on a home-built confocal microscope (Figure 53) on Thorben Cordes Lab (LMU, München, Deutschland). Detailed information of confocal microscope characteristics can be found at (Gebhardt et al., 2021). Briefly, all samples were studied focusing the water immersion objective of the microscope into a 100 µl sample drop at pM concentration of BasC in DDM buffer on a glass coverslip (*Tris buffer was used for ND samples*). Coverslips were previously coated for 60 s with 1 mg/mL bovine serum albumin to prevent fluorophore and/or protein interactions with it. Donor species were excited by a 532 nm diode laser at 60 µW power while acceptor ones were excited at 640 nm and 25 or 30 µW power for Alexa 546-Alexa 647 or sCy3-sCy5 dye-pairs, respectively. Both lasers were alternated at 20 kHz frequency.

The extremely low concentration of labelled BasC permitted to get an enough high signal-to-noise ratio for data collection (Hohlbein et al., 2014). DNA Ctrls with same fluorophores in DDM buffer were performed to check microscope alignment between datasets and buffer interferences. Comparisons between conditions were only done if their data was collected on the same day.

Data analysis was performed using home-written software package described in (Gouridis et al., 2015). Single-molecule events were identified and represented using the all-photon-burst-search (APBS) algorithm with a minimum total photon number between 100 and 150. For a cleaner histograms representation, events vs. *E**histograms shown in this thesis, figures can be represented using the double-count-search-mode (DCBS) algorithm.

5. The amphipathic environment

The quality of the membrane-solubilizing agent used to remove MPs from their natural environment (i.e., the cellular lipid bilayer) is critical for preserving the native structure and function of these proteins.

Detergents have played a significant role in this field. These compounds are surface acting agents (i.e., surfactants) that lower the tension between two immiscible liquids (hydrophobic and hydrophilic), thanks to their hydrophilic polar head group and a hydrophobic non-polar tail group (Anandan and Vrielink, 2016). The most successful detergents for MPs crystallisation are N,N-dimethyldodecylamine-N-oxide (LDAO), n-octyl-β-D-glucopyranoside (OG), octyltetraoxyethylene (C_8E_4), n-decyl-β-D-maltopyranoside (DM) and n-dodecyl-β-D-maltopyranoside (DDM) (Privé, 2007).

In this thesis, BasC was solubilised in two different maltoside detergents, namely DM and DDM. These detergents are glycosides with a maltose, of 10 and 12 carbons, respectively. Maltosides are lipid-like non-ionic detergents. They are the most widely used detergents as they preserve MP function well and present a low UV absorption. Above the CMC, DM and DDM self-assemble in micelles of ~33 and ~72 kDa, respectively. In water, CMC_{DM} and CMC_{DDM} are 1.8 mM or 0.087 % and 0.17 mM or 0.0087 %, respectively (Oliver et al., 2013). The higher the CMC, the easier it is for the detergent to detach from the MP. In this regard, DM is less harsh than DDM.

However, detergents can interfere in some procedures as detergent-only micelles can appear in addition to the detergent-MP micelles. Also, although the use of detergents yields a small particle size, the resultant structure undergoes dynamic fluctuations as it lacks the lipid bilayer (Nichols, 1988).

Detergents provide a hydrophobic environment rather than a native-like lipid environment and this property may bias the structure or completely denature the MP. To overcome this, MPs are commonly reconstituted in PLs or in NDs (i.e., nanoparticulate phospholipid bilayer disks).

On the one hand, phospholipids have the capacity to self-assemble into bilayer structures upon desolvation. A typical form of phospholipid bilayer is the liposome, which is a spherical closed bilayer having an aqueous interior and a high resemblance to a cell membrane. PLs, which are liposomes containing reconstituted MPs, are extensively used for functional studies. The phospholipids of PLs can provide a true lipid environment and, more importantly, they offer a dual differentiated space. However, PLs may not be fully advantageous for other techniques as the mass is highly biased to phospholipids and the variability in size and number of proteins reconstituted per PL is the most significant impairment for structural procedures.

On the other hand, ND are assembled from phospholipids and a class of amphipathic helical proteins termed membrane scaffold proteins (MSP) (Figure 54),

which were created based on the natural amphipathic α-helical protein (Apolipoprotein A-1 (Apo A1)) present in the plasma lipoproteins. The two amphipathic α-helical proteins wrap the edge of a leaflet and stabilises the complete lipid bilayer (Atkinson et al., 1976; Wlodawer et al., 1979; Koppaka et al., 1999). However, for lipoprotein-lipid aggregates, the predominant natural form is a spherical particle with additional protein domains required for interaction with cellular receptors and enzymes.

Stephen G. Sligar's group has been working with NDs and MSPs since 2002, when they removed the globular N-ter domain from Apo A1 (Figure 54. B) (Bayburt et al., 2002). Their studies had a huge impact around on the field (Bayburt et al., 2002; Denisov et al., 2004; Ritchie et al., 2009; Bayburt and Sligar, 2010; Bayburt et al., 2011; Schuler et al., 2013; Denisov and Sligar, 2016, 2017), providing the scientific community with a new powerful approach to study MPs in a native-like environment. The MSPs used in this thesis (MSP1D1 and MSP1E3D1) come from the original MSP1 (Ritchie et al., 2009), forming NDs of 6.5-9.7 and 12.1 nm in diameter, respectively. Both MSP lead to ND around 4.5-5.6 nm thick (Figure 54. A).

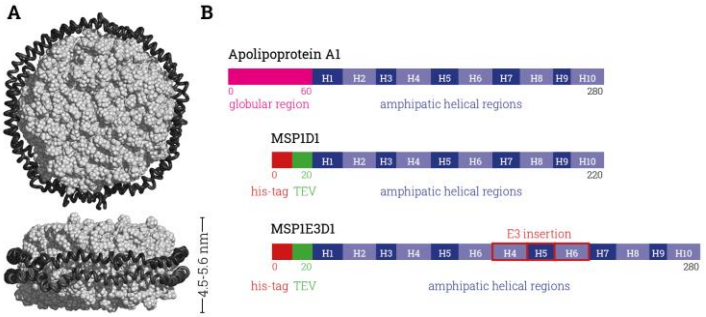

Figure 54. Nanodiscs structure and membrane scaffold proteins. A. Structure of NDs, modelled with POPC as lipid. Lipid bilayer fragment (grey space filling) is encircled by two amphipathic helices of MSP (black ribbon) (Ritchie et al., 2009). **B.** Comparison between Sigma Aldrich products human Apolipoprotein A1 (Apo A1) and MSPs 1D1 and 1E3D1. Aldrich products). Instead of the globular region (pink) of the human Apo A1, His-tag and TEV cleaving site are present in both MSP constructs. Repetitions of α-helices 4, 5 and 6 are only found in MSP1E3D1 construct (E3 insertion). NDs generated from MSP1D1 and MSP1E3D1 are 9.5-9.7 and 12.9 nm diameter, respectively (adapted from Sigma Aldrich Product Information).

To date, a huge number of MPs, ranging from Cytochrome P450 (Bayburt et al., 2002) to G-protein coupled receptors (Leitz et al., 2006), among many others, have been reconstituted in NDs; recently, the structure of $b^{0,+}$AT-rBAT heterotetramer reconstituted in MSP1E3D1 ND was solved (Lee et al., 2022). The potential of NDs is exemplified by their utility in diverse biochemical and biophysical methodologies, including solid state NMR (Li et al., 2006; Kijac et al., 2008), single molecule

fluorescence (Nath et al., 2008), and solubilizing functional receptors (Leitz et al., 2006; Bayburt et al., 2007; Boldog et al., 2007; Mi et al., 2008).

Otherwise, NDs-like particles can be formed using other small amphipathic compounds like diglucosides or styrene maleic-acid. The former is formed by a diglucoside polar head group and a carbonic chain (Mahler et al., 2021). The latter are similar to detergents but retain the lipid bilayer around MPs creating what is called as styrene maleic-acid lipid particles (SMALPs) (Hesketh et al., 2020). These recent amphipathic alternative compounds offer the advantage of ND formation directly from the membranes where the MPs are expressed.

5.1. BasC reconstitution into ND with dialysis

BasC was expressed and purified solubilised in DM (Experimental procedures 1.7) Purified BasC was mixed with MSP1E3D1 and POPC (both solubilised in 40 mM of Sodium Cholate) at the desired molar ratio. Mixtures were supplemented with 1 % (w/v) DM and incubated for 1 h at 4 ºC.

After the first incubation, samples were transferred into 50 kDa 12 mm flat width dialysis tubing and they were incubated for 72 h at 4 ºC with a magnetic stirrer submerged in at least 100 x times the sample volume in Tris buffer for dialysis.

After the dialysis, samples were recovered and purified via SEC on a Superdex 200 10/300 GL column previously equilibrated with Tris buffer. Run was performed at 0.4 ml/min in Tris buffer and 250 µl fractions were collected all along the elution for further analysis by SDS-PAGE.

5.2. BasC reconstituted into ND with BioBeads

BasC was expressed and purified solubilised in DM (Experimental procedures 1.7) Purified BasC was mixed in a final volume of 500 µl with MSP (MSP1E3D1 or MSP1D1) and POPC (both solubilised in 40 mM of Sodium Cholate) at the desired molar ratio. Mixtures were supplemented with 1 % (w/v) DM and incubated for 1 h at 4 ºC.

After the first incubation, samples were supplemented with 80 % (w/v) of Bio-Beads SM-2 resin and they were incubated one hour at 4 ºC in ice followed by four hours at 4 ºC in the cold chamber at mild rotation.

After the incubation, the sample was recovered through 44 µm Eppendorf filters and kept ON at 4 ºC. After, the reconstituted ND were analysed by SEC on Tris buffer equilibrated Superose 6 10/300 GL column at 0.4 ml/min in Tris buffer.

For labelled BasC samples to reconstitute ND for ALEX-smFRET measurements, as protein concentration was very low, less mix volume was achievable (100 µl ND mix), and Tris buffer equilibrated Superdex 200 increase 3.2/300 column was used at 0.07 ml/min in Tris buffer.

Finally, ND SEC fractions were collected for further analysis by SDS-PAGE, to prepare cryo-EM grids or assay by ALEX-smFRET.

6. Structural studies

Until mid '90s, insights into structural biology came mainly from static macromolecular structures obtained by X-ray crystallography (XRC) (Brünger, 1997; Zewail, 2005; Lento and Wilson, 2021). However, a biomolecule can adopt many diverse conformations. Nuclear magnetic resonance (NMR) spectroscopy allows the identification of structures even in multiple conformation states from a dynamic perspective. Cryogenic electron microscopy (cryo-EM) facilitates also the determination of multiple conformations of macromolecular structures in the ensemble with near-atomic resolution (Bharat et al., 2015; Cheng, 2015).

6.1. X-ray crystallography

Protein crystallization dates back to 1840 (Giegé, 2013). Back then, it was conceived as a tool to prepare biological substances. It is now an efficient method for XRC.

The most widely known X-ray diffraction pattern is the Photo 51 published by Rosalind Franklin and it was used to determine the structure of DNA. This Photo 51 and the data it contained, together with the data obtained by Maurice Wilkins (Franklin and Gosling, 1953; Watson and Crick, 1953; Wilkins et al., 1953) was used by James Dewey Watson and Francis Crick to deduce the double-helix model of DNA. Published in the same issue of Nature (April 1953), these three aforementioned articles, all from King's College London, marked one of the most important scientific discoveries ever made, yet one of the most controversial. For more information regarding this issue, see Appendix D. 1 Statement on feminism and cooperativeness.

The first protein structures obtained by XRC were myoglobin (Kendrew et al., 1960) and haemoglobin (Perutz et al., 1960), which showed structural similarity. This similarity was one of the first pieces of evidence of the narrow link between protein function and structure. All the structure determinations done in the following years highlighted the enormous variability of protein structure but also similar patterns of folding shown by distinct proteins that may or may not have a related function or recognisably homologous sequences (Matthews, 1976).

XRC has been the technique of choice for structure determination of proteins and biological macromolecules. Until now, 167,765 structures, out of 190,841 (> 85 %), have been solved by XRC (data retrieved from Protein Data Bank www.rcsb.org on 26th of May, 2022). This technique is indeed the approach most widely used to obtain full atomistic protein structures. All branches of the biological sciences require structural information to shed light on previously unanswered questions.

Moreover, this structural information can provide a more detailed focus for future research (Smyth and Martin, 2000).

It was not until 1985 that the first integral MP structure was elucidated from its natural source, the protein subunits in the photosynthetic reaction centre of *Rhodopseudomonas viridis* (Deisenhofer et al., 1985). Almost a decade later, the first MP obtained from heterologous expression, namely the potassium channel KcsA, was solved (Doyle et al., 1998). These studies highlight the effort that has to be made to crystallise a MP, as solubilisation in detergents out of the native physiological conditions hinders a proper organisation of molecules suitable for a successful result.

In this thesis, XRC have been performed either in synchrotron ALBA in Cerdanyola del Vallès (Barcelona, Spain) and the European Synchrotron Radiation Facility (ESRF) in Grenoble (France).

6.1.1. BasC by X-ray crystallography

For structural studies by XRC, BasC was purified with DM and freshly used as it follows. Purified BasC was concentrated until 6 mg/ml using Amicon Ultra filters of 100,000 kDa cut-off previously equilibrated with DM buffer. Complex formation was performed adding the desired Nb at molar ratio 1:1.2 (BasC:Nb) and incubated for 1 h at 4 ºC. BasC-Nb complex was then purified by SEC in an equilibrated Superdex 200 10/300 GL column with DM buffer at 0.5 ml/min flow collecting the complex peak fractions. Fractions were merged and concentrated if needed until 2 mg/ml using Amicon Ultra filters of 100,000 kDa cut-off. The presence of both proteins (i.e., BasC and Nb53) was validated by sodium dodecyl sulphate-polyacrylamide gel electrophoresis (SDS-PAGE).

BasC-Nb complexes samples between 1.2 and 1.9 mg/ml ± L-Ser 100 mM were screened for different precipitation agents in following commercial and non-commercial plates: Pi-PEG, MemGold™, MemGold2™, PAC13, PAC22 (Appendix E. Crystallographic screening plates). Crystals were grown on sitting- or hanging-drop with vapour diffusion at 4 and 20 ºC. Drops were created in a ratio 1:1 (v/v) between sample and reservoir solution. The final drop volume depended on the total amount of protein achieved after the purification of the complex process.

The different conditions of wells that gave crystals were further used for optimisation plates to repeat the crystallisation process to improve crystals, expanding the range above and below the original condition components concentrations. Finally, crystals grown in the screening and/or optimisation plates were collected, cryo-protected in clean reservoir solution and snap-frozen in LN for further X-ray diffraction and data collection.

Data collection was carried out at the ALBA synchrotron light source (Cerdanyola del Vallès, SPAIN) XALOC beamline and the European Synchrotron Radiation Facility (Grenoble, France) beamlines ID30A-3 (microbeam

(Theveneau et al., 2013; von Stetten et al., 2020)), ID23-1 (Nurizzo et al., 2006), and ID23-2 (microbeam (Nanao et al., 2022)). Data obtained from the ID23-1 beamline was the used one for the structure solving of BasC-Nb53-58 complex structure (Figure 33), special care was taken in data collection to overcome the inherent crystal anisotropy. To this end, crystals were aligned to minimize this effect by using tilted loops with automatic re-centering.

Data was processed with AutoProc toolbox (Vonrhein et al., 2011), Phases are obtained by molecular replacement using PHASER (McCoy et al., 2007) and the structures of BasC and Nb74 (PDBid: 6F2G) as templates. Model building into the electron density map was per-formed in COOT (Emsley et al., 2010), with structure refinement carried out in REFMAC5 (Winn et al., 2011). Images were prepared using Open-Source PyMol (The PyMOL Molecular Graphics System, Version 2.0 Schrödinger, LLC.).

6.2. Cryogenic electron microscopy

Single-particle cryogenic electron microscopy (Cryo-EM) has been used for the structure determination of biological complexes with molecular masses up to megadaltons. Rather than determining structures from the diffraction of three dimension (3D) crystals, cryo-EM determines structures by computationally combining images of many individual macromolecules in identical or similar conformations.

Here, samples of purified molecules in solution are applied to a cryo-EM grid covered with a thin holey carbon film and blotted by a filter paper to remove most of solution so that the a thin liquid layer is formed across the holes in the carbon film. This is followed by plunge-frozen in liquid ethane cooled by LN. Finally, frozen-hydrated molecules are embedded in a thin layer of vitreous ice that preserves the native structure to the atomic level. Molecules embedded in the commented above thin layer of vitreous ice adopt a range of orientations, which are then imaged using an electron beam. Each particle image is a 2D projection of a molecule, whose spatial orientation and position are defined by six geometric parameters. After further correction for aberrational errors of the microscope, a 3D structure can be reconstructed by combining images of many molecules that have been aligned to each other. The resolution of the reconstruction is improved iteratively by refining the data to higher accuracies. The final 3D reconstruction is a Coulomb potential density map that can be interpreted in the same way as the electron density maps obtained from the XRC (Cheng, 2015).

Cryo-EM was originally developed by Dubochet and colleagues in 1982 (Dubochet et al., 1982), years after the first computers became available. High-performance computers are needed iteratively to refine the huge amount of data needed to obtain a 3D Coulomb potential density map at the highest resolution possible. Without computers, Cryo-EM would not be possible. In this regard, I would like to thank

Dr. A.M. Turing, considered the father of modern informatics, for his work. However, he tragically died as a criminal for his homosexuality (to see more of this issue see Appendix D. 2. Statement on LGBTIQ+).

Lower molecular masses represent a technical challenge for cryo-EM structure studies. Nevertheless, the use of Volta phase plates has recently opened new possibilities in cryo-EM for the structure determination of MPs with molecular weights of only 110 to 120 kDa. Alternatively, chaperone proteins can be used to enlarge the total molecular mass of the protein of interest, thereby favouring the solvation of the structure. Indeed, this is how Simon Newstead lab solved their PepT2-Nb complex structure (PDBid 7NQK), which has a molecular weight of ~100 kDa (Parker et al., 2021b).

6.2.1. BasC by Cryo-EM

Cryo-EM experiments were performed in collaboration with Dr. Oscar Llorca laboratory in the CNIO (Spanish National Cancer Research Center, Madrid). Proteins expression and purification was carried at the IRB and complex purification, grid preparation and imaging was carried at the CNIO by Dr. María Martínez Molledo and Dr. Jasminka Boskovik.

Purified BasC was mixed with Nb71 at molar ratios 1:1.67 (BasC:Nb71) in 60 µl final volume supplementing the sample with 0.17 % (w/v) DM and were incubated over-night (ON) at 4 ºC. Prior to complex purification, samples were spun down for 20 min at 4 ºC at maximum speed in a tabletop centrifuge. Then, SEC was run on Superdex 200 Increase 3.2/300 and fractions at 1.35 were taken for grid preparation. Presence of both proteins was checked by SDS-PAGE. Cryo-EM grids were prepared with ThermoFisher Vitrobot Mark IV (CNIO, Madrid) and analysed in a 120 kV microscope at the CNIO.

After first analysis at 120 kV the presence of complex molecules was assessed and experiment continued at 200 kV microscope at the CNIO if it was not good enough or 300 kV for good-quality samples (Electron Microscopy Unit in the University of Leeds, UK).

Grid preparation improving by increasing concentration was needed to eventually fill more the grid-holes and finally obtain high-end data in a 300 kV microscope. Then, same previous described protocol was used, but mixing BasC and Nb71 until a final volume of 120 µl instead of 60, and prior to injection, sample was concentrated until 60 µl through a 30 kDa cut-off Amicon Ultra filter. Sample presented a best particle distribution (Figure 34. C) on-grid holes and seven grids were stored for data collection on a 300 kV microscope (Electron Microscopy Unit in the University of Leeds, UK). Then, images were 2D classified with CryoSPARC (Figure 34. D), and density map was obtained (Figure 35).

BasC and Nbs expression and purification for cryo-EM experimental procedure is detailed in results section as each trial was performed distinctly. Generally, as detailed in Experimental Procedures 1.7, BasC was expressed and purified in DM.

Bibliography

Bibliography

- Adibi, S.A., Gray, S.J., Menden, E., 1967. The Kinetics of Amino Acid Absorption and Alteration of Plasma Composition of Free Amino Acids After Intestinal Perfusion of Amino Acid Mixtures. Am. J. Clin. Nutr. 20, 24–33. https://doi.org/10.1093/ajcn/20.1.24
- Algar, W.R., Hildebrandt, N., Vogel, S.S., Medintz, I.L., 2019. FRET as a biomolecular research tool — understanding its potential while avoiding pitfalls. Nat. Methods 16, 815–829. https://doi.org/10.1038/s41592-019-0530-8
- Almeida, J.G., Preto, A.J., Koukos, P.I., Bonvin, A.M.J.J., Moreira, I.S., 2017. Membrane proteins structures: A review on computational modeling tools. Biochim. Biophys. Acta BBA - Biomembr. 1859, 2021–2039. https://doi.org/10.1016/j.bbamem.2017.07.008
- Almén, M.S., Nordström, K.J., Fredriksson, R., Schiöth, H.B., 2009. Mapping the human membrane proteome: a majority of the human membrane proteins can be classified according to function and evolutionary origin. BMC Biol. 7, 50. https://doi.org/10.1186/1741-7007-7-50
- AltschuP, S.F., Gish, W., Miller, W., Myers, E.W., Lipman, D.J., 1990. Basic Local Alignment Search Tool. ET J. 8.
- Anandan, A., Vrielink, A., 2016. Detergents in Membrane Protein Purification and Crystallisation. Adv. Exp. Med. Biol. 922, 13–28. https://doi.org/10.1007/978-3-319-35072-1_2
- Atkinson, D., Smith, H.M., Dickson, J., Austin, J.P., 1976. Interaction of Apoprotein from Porcine High-Density Lipoprotein with Dimyristoyl Lecithin. Eur. J. Biochem. 64, 541–547. https://doi.org/10.1111/j.1432-1033.1976.tb10334.x
- Bai, X., Moraes, T.F., Reithmeier, R.A.F., 2017. Structural biology of solute carrier (SLC) membrane transport proteins. Mol. Membr. Biol. 34, 1–32. https://doi.org/10.1080/09687688.2018.1448123
- Bartoccioni, P., Fort, J., Zorzano, A., Errasti-Murugarren, E., Palacín, M., 2019. Functional characterization of the alanine-serine-cysteine exchanger of Carnobacterium sp AT7. J. Gen. Physiol. 151, 505–517. https://doi.org/10.1085/jgp.201812195
- Bartoccioni, P., Rius, M., Zorzano, A., Palacín, M., Chillarón, J., 2008. Distinct classes of trafficking rBAT mutants cause the type I cystinuria phenotype. Hum. Mol. Genet. 17, 1845–1854. https://doi.org/10.1093/hmg/ddn080
- Bayburt, T.H., Grinkova, Y.V., Sligar, S.G., 2002. Self-Assembly of Discoidal Phospholipid Bilayer Nanoparticles with Membrane Scaffold Proteins. Nano Lett. 2, 853–856. https://doi.org/10.1021/nl025623k
- Bayburt, T.H., Leitz, A.J., Xie, G., Oprian, D.D., Sligar, S.G., 2007. Transducin Activation by Nanoscale Lipid Bilayers Containing One and Two Rhodopsins*,. J. Biol. Chem. 282, 14875–14881. https://doi.org/10.1074/jbc.M701433200
- Bayburt, T.H., Sligar, S.G., 2010. Membrane protein assembly into Nanodiscs. FEBS Lett. 584, 1721–1727. https://doi.org/10.1016/j.febslet.2009.10.024
- Bayburt, T.H., Vishnivetskiy, S.A., McLean, M.A., Morizumi, T., Huang, C., Tesmer, J.J.G., Ernst, O.P., Sligar, S.G., Gurevich, V.V., 2011. Monomeric Rhodopsin Is Sufficient for Normal Rhodopsin Kinase (GRK1) Phosphorylation and Arrestin-1 Binding. J. Biol. Chem. 286, 1420–1428. https://doi.org/10.1074/jbc.M110.151043
- Bharat, T.A.M., Russo, C.J., Löwe, J., Passmore, L.A., Scheres, S.H.W., 2015. Advances in Single-Particle Electron Cryomicroscopy Structure Determination applied to Sub-tomogram Averaging. Structure 23, 1743–1753. https://doi.org/10.1016/j.str.2015.06.026
- Billesbølle, C.B., Krüger, M.B., Shi, L., Quick, M., Li, Z., Stolzenberg, S., Kniazeff, J., Gotfryd, K., Mortensen, J.S., Javitch, J.A., Weinstein, H., Loland, C.J., Gether, U., 2015. Substrate-induced Unlocking of the Inner Gate Determines the Catalytic Efficiency of a Neurotransmitter:Sodium Symporter*. J. Biol. Chem. 290, 26725–26738. https://doi.org/10.1074/jbc.M115.677658
- Billesbølle, C.B., Mortensen, J.S., Sohail, A., Schmidt, S.G., Shi, L., Sitte, H.H., Gether, U., Loland, C.J., 2016. Transition metal ion FRET uncovers K+ regulation of a neurotransmitter/sodium symporter. Nat. Commun. 7, 12755. https://doi.org/10.1038/ncomms12755
- Bodoy, S., Sotillo, F., Espino-Guarch, M., Sperandeo, M.P., Ormazabal, A., Zorzano, A., Sebastio, G., Artuch, R., Palacin, M., 2019. Inducible Slc7a7 Knockout Mouse Model Recapitulates Lysinuric Protein Intolerance Disease. Int. J. Mol. Sci. 20. https://doi.org/10.3390/ijms20215294

- Boldog, T., Li, M., Hazelbauer, G.L., 2007. [14] - Using Nanodiscs to Create Water-Soluble Transmembrane Chemoreceptors Inserted in Lipid Bilayers, in: Simon, M.I., Crane, B.R., Crane, A. (Eds.), Methods in Enzymology, Two-Component Signaling Systems, Part B. Academic Press, pp. 317–335. https://doi.org/10.1016/S0076-6879(07)23014-9
- Borsani, G., Bassi, M.T., Sperandeo, M.P., Grandi, A.D., Buoninconti, A., Riboni, M., Manzoni, M., Incerti, B., Pepe, A., Andria, G., Ballabio, A., Sebastio, G., 1999. SLC7A7, encoding a putative permease-related protein, is mutated in patients with lysinuric protein intolerance. Nat. Genet. 21, 297–301. https://doi.org/10.1038/6815
- Bozzi, A.T., Zimanyi, C.M., Nicoludis, J.M., Lee, B.K., Zhang, C.H., Gaudet, R., 2019. Structures in multiple conformations reveal distinct transition metal and proton pathways in an Nramp transporter. eLife 8, e41124. https://doi.org/10.7554/eLife.41124
- Brechtel, C.E., King, S.C., 1998. 4-Aminobutyrate (GABA) transporters from the amine-polyamine-choline superfamily: substrate specificity and ligand recognition profile of the 4-aminobutyrate permease from Bacillus subtilis. Biochem. J. 333, 565–571. https://doi.org/10.1042/bj3330565
- Bröer, S., 2008. Amino Acid Transport Across Mammalian Intestinal and Renal Epithelia. Physiol. Rev. 88, 249–286. https://doi.org/10.1152/physrev.00018.2006
- Bröer, S., Bröer, A., 2017. Amino acid homeostasis and signalling in mammalian cells and organisms. Biochem. J. 474, 1935–1963. https://doi.org/10.1042/BCJ20160822
- Bröer, S., Palacin, M., 2011. The role of amino acid transporters in inherited and acquired diseases. Biochem. J. 436, 193–211. https://doi.org/10.1042/BJ20101912
- Brown, J.M., Hunihan, L., Prack, M.M., Harden, D.G., Bronson, J., Dzierba, C.D., Gentles, R.G., Hendricson, A., Krause, R., Macor, J.E., Westphal, R.S., 2014. In vitro Characterization of a small molecule inhibitor of the alanine serine cysteine transporter -1 (SLC7A10). J. Neurochem. 129, 275–283. https://doi.org/10.1111/jnc.12618
- Bruce, V.J., Lopez-Islas, M., McNaughton, B.R., 2016. Resurfaced penetrating nanobodies: A potentially general scaffold for intracellularly targeted protein discovery 9.
- Brünger, A.T., 1997. X-ray crystallography and NMR reveal complementary views of structure and dynamics. Nat. Struct. Biol. 4 Suppl, 862–865.
- Calonge, M.J., Gasparini, P., Chillarón, J., Chillón, M., Gallucci, M., Rousaud, F., Zelante, L., Testar, X., Dallapiccola, B., Di Silverio, F., Barceló, P., Estivill, X., Zorzano, A., Nunes, V., Palacín, M., 1994. Cystinuria caused by mutations in rBAT, a gene involved in the transport of cystine. Nat. Genet. 6, 420–425. https://doi.org/10.1038/ng0494-420
- Chapman, A.M., McNaughton, B.R., 2014. Resurfaced Shape Complementary Proteins That Selectively Bind the Oncoprotein Gankyrin. ACS Chem. Biol. 9, 2223–2228. https://doi.org/10.1021/cb5003834
- Cheng, Y., 2015. Single-Particle Cryo-EM at Crystallographic Resolution. Cell 161, 450–457. https://doi.org/10.1016/j.cell.2015.03.049
- Christensen, H.N., 1990. Role of amino acid transport and countertransport in nutrition and metabolism. Physiol. Rev. 70, 43–77. https://doi.org/10.1152/physrev.1990.70.1.43
- Christensen, H.N., 1984. Organic ion transport during seven decades the amino acids. Biochim. Biophys. Acta BBA - Rev. Biomembr. 779, 255–269. https://doi.org/10.1016/0304-4157(84)90012-1
- Chung, W.J., Lyons, S.A., Nelson, G.M., Hamza, H., Gladson, C.L., Gillespie, G.Y., Sontheimer, H., 2005. Inhibition of Cystine Uptake Disrupts the Growth of Primary Brain Tumors. J. Neurosci. 25, 7101–7110. https://doi.org/10.1523/JNEUROSCI.5258-04.2005
- Claxton, D.P., Quick, M., Shi, L., de Carvalho, F.D., Weinstein, H., Javitch, J.A., Mchaourab, H.S., 2010. Ion/substrate-dependent conformational dynamics of a bacterial homolog of neurotransmitter:sodium symporters. Nat. Struct. Mol. Biol. 17, 822–829. https://doi.org/10.1038/nsmb.1854
- Clegg, R.M., 2006. The History of Fret, in: Geddes, C.D., Lakowicz, J.R. (Eds.), Reviews in Fluorescence 2006, Reviews in Fluorescence. Springer US, Boston, MA, pp. 1–45. https://doi.org/10.1007/0-387-33016-X_1
- Cob, M., 2015. Sexism in science: did Watson and Crick really steal Rosalind Franklin's data? The Guardian.
- Coleman, J.A., Gouaux, E., 2018. Structural basis for recognition of diverse antidepressants by the human serotonin transporter. Nat. Struct. Mol. Biol. 25, 170–175. https://doi.org/10.1038/s41594-018-0026-8
- Coleman, J.A., Green, E.M., Gouaux, E., 2016. X-ray structures and mechanism of the human serotonin transporter. Nature 532, 334–339. https://doi.org/10.1038/nature17629

- Coleman, J.A., Navratna, V., Antermite, D., Yang, D., Bull, J.A., Gouaux, E., 2020. Chemical and structural investigation of the paroxetine-human serotonin transporter complex. eLife 9, e56427. https://doi.org/10.7554/eLife.56427
- Coleman, J.A., Yang, D., Zhao, Z., Wen, P.-C., Yoshioka, C., Tajkhorshid, E., Gouaux, E., 2019. Serotonin transporter–ibogaine complexes illuminate mechanisms of inhibition and transport. Nature 569, 141–145. https://doi.org/10.1038/s41586-019-1135-1
- Copelant, B.J., 2004. The Essential Turing: Seminal Writings in Computing, Logic, Philosophy, Artificial Intelligenec, and Artificial Life: Plus The Secrets of Enigma. Oxford University Press.
- Cronican, J.J., Thompson, D.B., Beier, K.T., McNaughton, B.R., Cepko, C.L., Liu, D.R., 2010. Potent delivery of functional proteins into Mammalian cells in vitro and in vivo using a supercharged protein. ACS Chem. Biol. 5, 747–752. https://doi.org/10.1021/cb1001153
- Deisenhofer, J., Epp, O., Miki, K., Huber, R., Michel, H., 1985. Structure of the protein subunits in the photosynthetic reaction centre of Rhodopseudomonas viridis at 3Å resolution. Nature 318, 618–624. https://doi.org/10.1038/318618a0
- del Alamo, D., Meiler, J., Mchaourab, H.S., 2022. Principles of Alternating Access in LeuT-fold Transporters: Commonalities and Divergences. J. Mol. Biol. 434, 167746. https://doi.org/10.1016/j.jmb.2022.167746
- del Amo, E.M., Urtti, A., Yliperttula, M., 2008. Pharmacokinetic role of L-type amino acid transporters LAT1 and LAT2. Eur. J. Pharm. Sci. 35, 161–174. https://doi.org/10.1016/j.ejps.2008.06.015
- Denisov, I.G., Baas, B.J., Grinkova, Y.V., Sligar, S.G., 2007. Cooperativity in cytochrome P450 3A4: linkages in substrate binding, spin state, uncoupling, and product formation. J. Biol. Chem. 282, 7066–7076. https://doi.org/10.1074/jbc.M609589200
- Denisov, I.G., Grinkova, Y.V., Lazarides, A.A., Sligar, S.G., 2004. Directed self-assembly of monodisperse phospholipid bilayer Nanodiscs with controlled size. J. Am. Chem. Soc. 126, 3477–3487. https://doi.org/10.1021/ja0393574
- Denisov, I.G., Sligar, S.G., 2017. Nanodiscs in Membrane Biochemistry and Biophysics. Chem Rev 45.
- Denisov, I.G., Sligar, S.G., 2016. Nanodiscs for structural and functional studies of membrane proteins. P ERS P ECTI V E 23, 6.
- Derndorfer, C., 2004. Who was Alan Turing?
- Do, H.Q., Bassil, C.M., Andersen, E.I., Jansen, M., 2021. Impact of nanodisc lipid composition on cell-free expression of proton-coupled folate transporter. PLOS ONE 16, e0253184. https://doi.org/10.1371/journal.pone.0253184
- Doyle, D.A., Morais Cabral, J., Pfuetzner, R.A., Kuo, A., Gulbis, J.M., Cohen, S.L., Chait, B.T., MacKinnon, R., 1998. The structure of the potassium channel: molecular basis of K+ conduction and selectivity. Science 280, 69–77. https://doi.org/10.1126/science.280.5360.69
- Dvorak, V., Wiedmer, T., Ingles-Prieto, A., Altermatt, P., Batoulis, H., Bärenz, F., Bender, E., Digles, D., Dürrenberger, F., Heitman, L.H., IJzerman, A.P., Kell, D.B., Kickinger, S., Körzö, D., Leippe, P., Licher, T., Manolova, V., Rizzetto, R., Sassone, F., Scarabottolo, L., Schlessinger, A., Schneider, V., Sijben, H.J., Steck, A.-L., Sundström, H., Tremolada, S., Wilhelm, M., Wright Muelas, M., Zindel, D., Steppan, C.M., Superti-Furga, G., 2021. An Overview of Cell-Based Assay Platforms for the Solute Carrier Family of Transporters. Front. Pharmacol. 12.
- Dyla, M., Terry, D.S., Kjaergaard, M., Sørensen, T.L.-M., Lauwring Andersen, J., Andersen, J.P., Rohde Knudsen, C., Altman, R.B., Nissen, P., Blanchard, S.C., 2017. Dynamics of P-type ATPase transport revealed by single-molecule FRET. Nature 551, 346–351. https://doi.org/10.1038/nature24296
- Emsley, P., Lohkamp, B., Scott, W.G., Cowtan, K., 2010. Features and development of Coot. Acta Crystallogr. D Biol. Crystallogr. 66, 486–501. https://doi.org/10.1107/S0907444910007493
- Errasti-Murugarren, E., Fort, J., Bartoccioni, P., Díaz, L., Pardon, E., Carpena, X., Espino-Guarch, M., Zorzano, A., Ziegler, C., Steyaert, J., Fernández-Recio, J., Fita, I., Palacín, M., 2019. L amino acid transporter structure and molecular bases for the asymmetry of substrate interaction. Nat. Commun. 10, 1807. https://doi.org/10.1038/s41467-019-09837-z
- Espino Guarch, M., Font-Llitjós, M., Murillo-Cuesta, S., Errasti- Murugarren, E., Celaya, A.M., Girotto, G., Vuckovic, D., Mezzavilla, M., Vilches, C., Bodoy, S., Sahún, I., González, L., Prat, E., Zorzano, A., Dierssen, M., Varela-Nieto, I., Gasparini, P., Palacín, M., Nunes, V., 2018. Mutations in L-type amino acid transporter-2 support SLC7A8 as a novel gene involved in age-related hearing loss. eLife 7, e31511. https://doi.org/10.7554/eLife.31511

- Estévez, R., Camps, M., Rojas, A.M., Testar, X., Devís, R., Hediger, M.A., Zorzano, A., Palacín, M., 1998. The amino acid transport system y+L/4F2hc is a heteromultimeric complex. FASEB J. 12, 1319–1329. https://doi.org/10.1096/fasebj.12.13.1319
- Faham, S., Watanabe, A., Besserer, G.M., Cascio, D., Specht, A., Hirayama, B.A., Wright, E.M., Abramson, J., 2008. The Crystal Structure of a Sodium Galactose Transporter Reveals Mechanistic Insights into Na+/Sugar Symport. Science 321, 810–814. https://doi.org/10.1126/science.1160406
- Fairweather, S.J., Shah, N., Bröer, S., 2020. Heteromeric Solute Carriers: Function, Structure, Pathology and Pharmacology, in: Advances in Experimental Medicine and Biology. Springer US, New York, NY. https://doi.org/10.1007/5584_2020_584
- Fang, Y., Jayaram, H., Shane, T., Kolmakova-Partensky, L., Wu, F., Williams, C., Xiong, Y., Miller, C., 2009. Structure of a prokaryotic virtual proton pump at 3.2 Å resolution. Nature 460, 1040–1043. https://doi.org/10.1038/nature08201
- Feliubadaló, L., Font, M., Purroy, J., Rousaud, F., Estivill, X., Nunes, V., Golomb, E., Centola, M., Aksentijevich, I., Kreiss, Y., Goldman, B., Pras, M., Kastner, D.L., Pras, E., Gasparini, P., Bisceglia, L., Beccia, E., Gallucci, M., de Sanctis, L., Ponzone, A., Rizzoni, G.F., Zelante, L., Bassi, M.T., George Jr, A.L., Manzoni, M., De Grandi, A., Riboni, M., Endsley, J.K., Ballabio, A., Borsani, G., Reig, N., Fernández, E., Estévez, R., Pineda, M., Torrents, D., Camps, M., Lloberas, J., Zorzano, A., Palacín, M., 1999. Non-type I cystinuria caused by mutations in SLC7A9, encoding a subunit (bo,+AT) of rBAT. Nat. Genet. 23, 52–57. https://doi.org/10.1038/12652
- Fernández, E., Torrents, D., Zorzano, A., Palacín, M., Chillarón, J., 2005. Identification and Functional Characterization of a Novel Low Affinity Aromatic-preferring Amino Acid Transporter (arpAT): ONE OF THE FEW PROTEINS SILENCED DURING PRIMATE EVOLUTION*. J. Biol. Chem. 280, 19364–19372. https://doi.org/10.1074/jbc.M412516200
- Förster, T., 2012. Energy migration and fluorescence. J. Biomed. Opt. 17, 011002. https://doi.org/10.1117/1.JBO.17.1.011002
- Förster, T., 1946. Energiewanderung und Fluoreszenz. Naturwissenschaften 33, 166–175. https://doi.org/10.1007/BF00585226
- Förster, Th., 1948. Zwischenmolekulare Energiewanderung und Fluoreszenz. Ann. Phys. 437, 55–75. https://doi.org/10.1002/andp.19484370105
- Fort, J., de la Ballina, L.R., Burghardt, H.E., Ferrer-Costa, C., Turnay, J., Ferrer-Orta, C., Usón, I., Zorzano, A., Fernández-Recio, J., Orozco, M., Lizarbe, M.A., Fita, I., Palacín, M., 2007. The Structure of Human 4F2hc Ectodomain Provides a Model for Homodimerization and Electrostatic Interaction with Plasma Membrane*. J. Biol. Chem. 282, 31444–31452. https://doi.org/10.1074/jbc.M704524200
- Fort, J., Nicolàs-Aragó, A., Palacín, M., 2021. The Ectodomains of rBAT and 4F2hc Are Fake or Orphan α-Glucosidases. Molecules 26, 6231. https://doi.org/10.3390/molecules26206231
- Fotiadis, D., Kanai, Y., Palacín, M., 2013. The SLC3 and SLC7 families of amino acid transporters. Mol. Aspects Med. 34, 139–158. https://doi.org/10.1016/j.mam.2012.10.007
- Franklin, R.E., Gosling, R.G., 1953. Molecular configuration in sodium thymonucleate. Nature 740–741. https://doi.org/10.1038/171740a0
- Fuchs, S.M., Raines, R.T., 2007. Arginine grafting to endow cell permeability. ACS Chem. Biol. 2, 167–170. https://doi.org/10.1021/cb600429k
- Fukasawa, Y., Segawa, H., Kim, J.Y., Chairoungdua, A., Kim, D.K., Matsuo, H., Cha, S.H., Endou, H., Kanai, Y., 2000. Identification and Characterization of a Na+-independent Neutral Amino Acid Transporter That Associates with the 4F2 Heavy Chain and Exhibits Substrate Selectivity for Small Neutral d- and l-Amino Acids*. J. Biol. Chem. 275, 9690–9698. https://doi.org/10.1074/jbc.275.13.9690
- Ganapathy, S., Opdam, L., Hontani, Y., Frehan, S., Chen, Q., Hellingwerf, K.J., de Groot, H.J.M., Kennis, J.T.M., de Grip, W.J., 2020. Membrane matters: The impact of a nanodisc-bilayer or a detergent microenvironment on the properties of two eubacterial rhodopsins. Biochim. Biophys. Acta BBA - Biomembr. 1862, 183113. https://doi.org/10.1016/j.bbamem.2019.183113
- Gao, X., Lu, F., Zhou, L., Dang, S., Sun, L., Li, X., Wang, J., Shi, Y., 2009. Structure and Mechanism of an Amino Acid Antiporter. Science 324, 1565–1568. https://doi.org/10.1126/science.1173654
- Gao, X., Zhou, L., Jiao, X., Lu, F., Yan, C., Zeng, X., Wang, J., Shi, Y., 2010. Mechanism of substrate recognition and transport by an amino acid antiporter. Nature 463, 828–832. https://doi.org/10.1038/nature08741
- Gebhardt, C., Lehmann, M., Reif, M.M., Zacharias, M., Gemmecker, G., Cordes, T., 2021. Molecular and Spectroscopic Characterization of Green and Red Cyanine Fluorophores from the Alexa Fluor and AF Series. Chemphyschem 22, 1566–1583. https://doi.org/10.1002/cphc.202000935

- Genst, E.D., Silence, K., Decanniere, K., Conrath, K., Loris, R., Kinne, J., Muyldermans, S., Wyns, L., 2006. Molecular basis for the preferential cleft recognition by dromedary heavy-chain antibodies. Proc. Natl. Acad. Sci. 103, 4586–4591. https://doi.org/10.1073/pnas.0505379103
- Giegé, R., 2013. A historical perspective on protein crystallization from 1840 to the present day. FEBS J. 280, 6456–6497. https://doi.org/10.1111/febs.12580
- Giroud-Gerbetant, J., Sotillo, F., Couso, J., Zorzano, A., Weiss, G., Palacín, M., Bodoy, S., 2021. Erythropoietin supplementation ameliorates the immunological and hematological deficiencies of lysinuric protein intolerance in mice 38.
- Gouridis, G., Schuurman-Wolters, G.K., Ploetz, E., Husada, F., Vietrov, R., de Boer, M., Cordes, T., Poolman, B., 2015. Conformational dynamics in substrate-binding domains influences transport in the ABC importer GlnPQ. Nat. Struct. Mol. Biol. 22, 57–64. https://doi.org/10.1038/nsmb.2929
- Ha, T., Enderle, T., Ogletree, D.F., Chemla, D.S., Selvin, P.R., Weiss, S., 1996. Probing the interaction between two single molecules: fluorescence resonance energy transfer between a single donor and a single acceptor. Proc. Natl. Acad. Sci. 93, 6264–6268. https://doi.org/10.1073/pnas.93.13.6264
- Hamers-Casterman, C., Atarhouch, T., Muyldermans, S., Robinson, G., Hammers, C., Songa, E.B., Bendahman, N., Hammers, R., 1993. Naturally occurring antibodies devoid of light chains. Nature 363, 446–448. https://doi.org/10.1038/363446a0
- Hassanzadeh-Ghassabeh, G., Devoogdt, N., De Pauw, P., Vincke, C., Muyldermans, S., 2013. Nanobodies and their potential applications. Nanomed. 8, 1013–1026. https://doi.org/10.2217/nnm.13.86
- Hesketh, S.J., Klebl, D.P., Higgins, A.J., Thomsen, M., Pickles, I.B., Sobott, F., Sivaprasadarao, A., Postis, V.L.G., Muench, S.P., 2020. Styrene maleic-acid lipid particles (SMALPs) into detergent or amphipols: An exchange protocol for membrane protein characterisation. Biochim. Biophys. Acta BBA - Biomembr. 1862, 183192. https://doi.org/10.1016/j.bbamem.2020.183192
- Hohlbein, J., Craggs, T.D., Cordes, T., 2014. Alternating-laser excitation: single-molecule FRET and beyond. Chem Soc Rev 43, 1156–1171. https://doi.org/10.1039/C3CS60233H
- Hu, L.A., King, S.C., 1998. Functional Significance of the "Signature Cysteine" in Helix 8 of the Escherichia coli 4-Aminobutyrate Transporter from the Amine-Polyamine-Choline Superfamily: RESTORATION OF CYS-300 TO THE CYS-LESS GabP*. J. Biol. Chem. 273, 20162–20167. https://doi.org/10.1074/jbc.273.32.20162
- Hwang, L.C., Hohlbein, J., Holden, S.J., Kapanidis, A.N., 2009. Single-Molecule FRET: Methods and Biological Applications, in: Hinterdorfer, P., Oijen, A. (Eds.), Handbook of Single-Molecule Biophysics. Springer US, New York, NY, pp. 129–163. https://doi.org/10.1007/978-0-387-76497-9_5
- Ilgü, H., Jeckelmann, J.-M., Gapsys, V., Ucurum, Z., de Groot, B.L., Fotiadis, D., 2016. Insights into the molecular basis for substrate binding and specificity of the wild-type L-arginine/agmatine antiporter AdiC. Proc. Natl. Acad. Sci. 113, 10358–10363. https://doi.org/10.1073/pnas.1605442113
- Jack, D.L., Paulsen, I.T., Saier, M.H., 2000. The amino acid/polyamine/organocation (APC) superfamily of transporters specific for amino acids, polyamines and organocations. Microbiology 146, 1797–1814. https://doi.org/10.1099/00221287-146-8-1797
- Jersin, R.Å., Tallapragada, D.S.P., Madsen, A., Skartveit, L., Fjære, E., McCann, A., Dyer, L., Willems, A., Bjune, J.-I., Bjune, M.S., Våge, V., Nielsen, H.J., Thorsen, H.L., Nedrebø, B.G., Busch, C., Steen, V.M., Blüher, M., Jacobson, P., Svensson, P.-A., Fernø, J., Rydén, M., Arner, P., Nygård, O., Claussnitzer, M., Ellingsen, S., Madsen, L., Sagen, J.V., Mellgren, G., Dankel, S.N., 2021. Role of the Neutral Amino Acid Transporter SLC7A10 in Adipocyte Lipid Storage, Obesity, and Insulin Resistance. Diabetes 70. https://doi.org/10.2337/db20-0096
- Jr, C.A.J., Travers, P., Walport, M., Shlomchik, M.J., Jr, C.A.J., Travers, P., Walport, M., Shlomchik, M.J., 2001. Immunobiology, 5th ed. Garland Science.
- Jungnickel, K.E.J., Parker, J.L., Newstead, S., 2018. Structural basis for amino acid transport by the CAT family of SLC7 transporters. Nat. Commun. 9, 550. https://doi.org/10.1038/s41467-018-03066-6
- Kalayil, S., Schulze, S., Kühlbrandt, W., 2013. Arginine oscillation explains Na+ independence in the substrate/product antiporter CaiT. Proc. Natl. Acad. Sci. 110, 17296–17301. https://doi.org/10.1073/pnas.1309071110
- Kandasamy, P., Gyimesi, G., Kanai, Y., Hediger, M.A., 2018. Amino acid transporters revisited: New views in health and disease. Trends Biochem. Sci. 43, 752–789. https://doi.org/10.1016/j.tibs.2018.05.003
- Kaplon, H., Reichert, J.M., 2021. Antibodies to watch in 2021. mAbs 13, 1860476. https://doi.org/10.1080/19420862.2020.1860476

- Kazmier, K., Sharma, S., Quick, M., Islam, S.M., Roux, B., Weinstein, H., Javitch, J.A., Mchaourab, H.S., 2014. Conformational dynamics of ligand-dependent alternating access in LeuT. Nat. Struct. Mol. Biol. 21, 472–479. https://doi.org/10.1038/nsmb.2816
- Kendrew, J.C., Dickerson, R.E., Strandberg, B.E., Hart, R.G., Davies, D.R., Phillips, D.C., Shore, V.C., 1960. Structure of Myogobin, a three-dimensional fourier synthesis at 2 A resolution. Nature 422–427. https://doi-org.sire.ub.edu/10.1038/185422a0
- Kijac, A., Li, Y., Sligar, S.G., Rienstra, C.M., 2008. Magic-Angle Spinning Solid-State NMR Spectroscopy of Nanodisc– Embedded Human CYP3A4 15.
- Knöpfel, E.B., Vilches, C., Camargo, S.M.R., Errasti-Murugarren, E., Stäubli, A., Mayayo, C., Munier, F.L., Miroshnikova, N., Poncet, N., Junza, A., Bhattacharya, S.S., Prat, E., Berry, V., Berger, W., Heon, E., Moore, A.T., Yanes, Ó., Nunes, V., Palacin, M., Verrey, F., Kloeckener-Gruissem, B., 2019. Dysfunctional LAT2 Amino Acid Transporter Is Associated With Cataract in Mouse and Humans. Front. Physiol. 10, 688. https://doi.org/10.3389/fphys.2019.00688
- Koide, S., 2009. Engineering of recombinant crystallization chaperones. Curr. Opin. Struct. Biol. 19, 449–457. https://doi.org/10.1016/j.sbi.2009.04.008
- König, I., Zarrine-Afsar, A., Aznauryan, M., Soranno, A., Wunderlich, B., Dingfelder, F., Stüber, J.C., Plückthun, A., Nettels, D., Schuler, B., 2015. Single-molecule spectroscopy of protein conformational dynamics in live eukaryotic cells. Nat. Methods 12, 773–779. https://doi.org/10.1038/nmeth.3475
- Koppaka, V., Silvestro, L., Engler, J.A., Brouillette, C.G., Axelsen, P.H., 1999. The Structure of Human Lipoprotein A-I: EVIDENCE FOR THE "BELT" MODEL*. J. Biol. Chem. 274, 14541–14544. https://doi.org/10.1074/jbc.274.21.14541
- Koshy, C., Schweikhard, E.S., Gärtner, R.M., Perez, C., Yildiz, Ö., Ziegler, C., 2013. Structural evidence for functional lipid interactions in the betaine transporter BetP. EMBO J. 32, 3096–3105. https://doi.org/10.1038/emboj.2013.226
- Kowalczyk, L., Ratera, M., Paladino, A., Bartoccioni, P., Errasti-Murugarren, E., Valencia, E., Portella, G., Bial, S., Zorzano, A., Fita, I., Orozco, M., Carpena, X., Vazquez-Ibar, J.L., Palacin, M., 2011. Molecular basis of substrate-induced permeation by an amino acid antiporter. Proc. Natl. Acad. Sci. 108, 3935–3940. https://doi.org/10.1073/pnas.1018081108
- Krishnamurthy, H., Gouaux, E., 2012. X-ray structures of LeuT in substrate-free outward-open and apo inward-open states. Nature 481, 469–474. https://doi.org/10.1038/nature10737
- Lam, V.H., Lee, J.-H., Silverio, A., Chan, H., Gomolplitinant, K.M., Povolotsky, T.L., Orlova, E., Sun, E.I., Welliver, C.H., Saier, M.H., 2011. Pathways of Transport Protein Evolution: Recent Advances. Biol. Chem. 392, 5–12. https://doi.org/10.1515/BC.2011.018
- Lee, Y., Wiriyasermkul, P., Jin, C., Quan, L., Ohgaki, R., Okuda, S., Kusakizako, T., Nishizawa, T., Oda, K., Ishitani, R., Yokoyama, T., Nakane, T., Shirouzu, M., Endou, H., Nagamori, S., Kanai, Y., Nureki, O., 2019. Cryo-EM structure of the human L-type amino acid transporter 1 in complex with glycoprotein CD98hc. Nat. Struct. Mol. Biol. 26, 510–517. https://doi.org/10.1038/s41594-019-0237-7
- Lee, Y., Wiriyasermkul, P., Kongpracha, P., Moriyama, S., Mills, D.J., Kühlbrandt, W., Nagamori, S., 2022. Ca2+-mediated higher-order assembly of heterodimers in amino acid transport system b0,+ biogenesis and cystinuria. Nat. Commun. 13, 2708. https://doi.org/10.1038/s41467-022-30293-9
- Leitz, A.J., Bayburt, T.H., Barnakov, A.N., Springer, B.A., Sligar, S.G., 2006. Functional reconstitution of β2-adrenergic receptors utilizing self-assembling Nanodisc technology. BioTechniques 40, 601–612. https://doi.org/10.2144/000112169
- Lento, C., Wilson, D.J., 2021. Subsecond Time-Resolved Mass Spectrometry in Dynamic Structural Biology. Chem. Rev. acs.chemrev.1c00222. https://doi.org/10.1021/acs.chemrev.1c00222
- LeVine, M.V., Terry, D.S., Khelashvili, G., Siegel, Z.S., Quick, M., Javitch, J.A., Blanchard, S.C., Weinstein, H., 2019. The allosteric mechanism of substrate-specific transport in SLC6 is mediated by a volumetric sensor. Proc. Natl. Acad. Sci. 116, 15947–15956. https://doi.org/10.1073/pnas.1903020116
- Li, Y., Kijac, A.Z., Sligar, S.G., Rienstra, C.M., 2006. Structural Analysis of Nanoscale Self-Assembled Discoidal Lipid Bilayers by Solid-State NMR Spectroscopy. Biophys. J. 91, 3819–3828. https://doi.org/10.1529/biophysj.106.087072
- Lo, M., Wang, Y.-Z., Gout, P.W., 2008. The x cystine/glutamate antiporter: A potential target for therapy of cancer and other diseases. J. Cell. Physiol. 215, 593–602. https://doi.org/10.1002/jcp.21366
- Lodish, H., Berk, A., Zipursky, S.L., Matsudaira, P., Baltimore, D., Darnell, J., 2000. Molecular Cell Biology, 4th ed. W. H. Freeman.

- Loo, D.D.F., Jiang, X., Gorraitz, E., Hirayama, B.A., Wright, E.M., 2013. Functional identification and characterization of sodium binding sites in Na symporters. Proc. Natl. Acad. Sci. 110, E4557–E4566. https://doi.org/10.1073/pnas.1319218110
- Lu, M., 2021. Single-Molecule FRET Imaging of Virus Spike–Host Interactions. Viruses 13, 332. https://doi.org/10.3390/v13020332
- Lu, M., Ma, X., Castillo-Menendez, L.R., Gorman, J., Alsahafi, N., Ermel, U., Terry, D.S., Chambers, M., Peng, D., Zhang, B., Zhou, T., Reichard, N., Wang, K., Grover, J.R., Carman, B.P., Gardner, M.R., Nikić-Spiegel, I., Sugawara, A., Arthos, J., Lemke, E.A., Smith, A.B., Farzan, M., Abrams, C., Munro, J.B., McDermott, A.B., Finzi, A., Kwong, P.D., Blanchard, S.C., Sodroski, J.G., Mothes, W., 2019. Associating HIV-1 envelope glycoprotein structures with states on the virus observed by smFRET. Nature 568, 415–419. https://doi.org/10.1038/s41586-019-1101-y
- Ma, D., Lu, P., Yan, C., Fan, C., Yin, P., Wang, J., Shi, Y., 2012. Structure and mechanism of a glutamate–GABA antiporter. Nature 483, 632–636. https://doi.org/10.1038/nature10917
- Ma, J., Lei, H.-T., Reyes, F.E., Sanchez-Martinez, S., Sarhan, M.F., Hattne, J., Gonen, T., 2019. Structural basis for substrate binding and specificity of a sodium–alanine symporter AgcS. Proc. Natl. Acad. Sci. 116, 2086–2090. https://doi.org/10.1073/pnas.1806206116
- Mächtel, R., Narducci, A., Griffith, D.A., Cordes, T., Orelle, C., 2019. An integrated transport mechanism of the maltose ABC importer. Res. Microbiol. 170, 321–337. https://doi.org/10.1016/j.resmic.2019.09.004
- Mahler, F., Meister, A., Vargas, C., Durand, G., Keller, S., 2021. Self-Assembly of Protein-Containing Lipid-Bilayer Nanodiscs from Small-Molecule Amphiphiles. Small 17, 2103603. https://doi.org/10.1002/smll.202103603
- Maimaiti, M., Sakamoto, S., Sugiura, M., Kanesaka, M., Fujimoto, A., Matsusaka, K., Xu, M., Ando, K., Saito, S., Wakai, K., Imamura, Y., Nakayama, K., Kanai, Y., Kaneda, A., Ikehara, Y., Ikeda, J.-I., Anzai, N., Ichikawa, T., 2021. The heavy chain of 4F2 antigen promote prostate cancer progression via SKP-2. Sci. Rep. 11, 11478. https://doi.org/10.1038/s41598-021-90748-9
- Majumdar, D.S., Smirnova, I., Kasho, V., Nir, E., Kong, X., Weiss, S., Kaback, H.R., 2007. Single-molecule FRET reveals sugar-induced conformational dynamics in LacY. Proc. Natl. Acad. Sci. 104, 12640–12645. https://doi.org/10.1073/pnas.0700969104
- Malinauskaite, L., Quick, M., Reinhard, L., Lyons, J.A., Yano, H., Javitch, J.A., Nissen, P., 2014. A mechanism for intracellular release of Na+ by neurotransmitter/sodium symporters. Nat. Struct. Mol. Biol. 21, 1006–1012. https://doi.org/10.1038/nsmb.2894
- Malinauskaite, L., Said, S., Sahin, C., Grouleff, J., Shahsavar, A., Bjerregaard, H., Noer, P., Severinsen, K., Boesen, T., Schiøtt, B., Sinning, S., Nissen, P., 2016. A conserved leucine occupies the empty substrate site of LeuT in the Na+-free return state. Nat. Commun. 7, 11673. https://doi.org/10.1038/ncomms11673
- Mariotti, F., Huneau, J.-F., Mahé, S., Tomé, D., 2000. Protein metabolism and the gut: Curr. Opin. Clin. Nutr. Metab. Care 3, 45–50. https://doi.org/10.1097/00075197-200001000-00008
- Maschalidi, S., Mehrotra, P., Keçeli, B.N., De Cleene, H.K.L., Lecomte, K., Van der Cruyssen, R., Janssen, P., Pinney, J., van Loo, G., Elewaut, D., Massie, A., Hoste, E., Ravichandran, K.S., 2022. Targeting SLC7A11 improves efferocytosis by dendritic cells and wound healing in diabetes. Nature 1–9. https://doi.org/10.1038/s41586-022-04754-6
- Masters, B.R., 2014. Paths to Förster's resonance energy transfer (FRET) theory. Eur. Phys. J. H 39, 87–139. https://doi.org/10.1140/epjh/e2013-40007-9
- Mastroberardino, L., Spindler, B., Pfeiffer, R., Skelly, P.J., Loffing, J., Shoemaker, C.B., Verrey, F., 1998. Amino-acid transport by heterodimers of 4F2hc/CD98 and members of a permease family. Nature 395, 288–291. https://doi.org/10.1038/26246
- Matthews, B.W., 1976. X-ray Crystallographic Studies of Proteins. Annu. Rev. Phys. Chem. 27, 493–493. https://doi.org/10.1146/annurev.pc.27.100176.002425
- Mauhin, W., Habarou, F., Gobin, S., Servais, A., Brassier, A., Grisel, C., Roda, C., Pinto, G., Moshous, D., Ghalim, F., Krug, P., Deltour, N., Pontoizeau, C., Dubois, S., Assoun, M., Galmiche, L., Bonnefont, J.-P., Ottolenghi, C., de Blic, J., Arnoux, J.-B., de Lonlay, P., 2017. Update on Lysinuric Protein Intolerance, a Multi-faceted Disease Retrospective cohort analysis from birth to adulthood. Orphanet J. Rare Dis. 12, 3. https://doi.org/10.1186/s13023-016-0550-8
- McCoy, A.J., Grosse-Kunstleve, R.W., Adams, P.D., Winn, M.D., Storoni, L.C., Read, R.J., 2007. Phaser crystallographic software. J. Appl. Crystallogr. 40, 658–674. https://doi.org/10.1107/S0021889807021206
- Meier, C., Ristic, Z., Klauser, S., Verrey, F., 2002. Activation of system L heterodimeric amino acid exchangers by intracellular substrates. EMBO J. 21, 580–589. https://doi.org/10.1093/emboj/21.4.580

- Merkle, P.S., Gotfryd, K., Cuendet, M.A., Leth-Espensen, K.Z., Gether, U., Loland, C.J., Rand, K.D., 2018. Substrate-modulated unwinding of transmembrane helices in the NSS transporter LeuT. Sci. Adv. 4, eaar6179. https://doi.org/10.1126/sciadv.aar6179
- Mi, L.-Z., Grey, M.J., Nishida, N., Walz, T., Lu, C., Springer, T.A., 2008. Functional and Structural Stability of the Epidermal Growth Factor Receptor in Detergent Micelles and Phospholipid Nanodiscs. Biochemistry 47, 10314–10323. https://doi.org/10.1021/bi801006s
- Michalet, X., Weiss, S., Jäger, M., 2006. Single-Molecule Fluorescence Studies of Protein Folding and Conformational Dynamics. Chem. Rev. 106, 1785–1813. https://doi.org/10.1021/cr0404343
- Milne, M.D., 1964. Disorders of Amino-Acid Transport. Br. Med. J. 1, 327–336.
- Mori, H., Tsukazaki, T., Masui, R., Kuramitsu, S., Yokoyama, S., Johnson, A.E., Kimura, Y., Akiyama, Y., Ito, K., 2003. Fluorescence Resonance Energy Transfer Analysis of Protein Translocase: SecYE FROM *THERMUS THERMOPHILUS* HB8 FORMS A CONSTITUTIVE OLIGOMER IN MEMBRANES. J. Biol. Chem. 278, 14257–14264. https://doi.org/10.1074/jbc.M300230200
- Morth, J.P., Poulsen, H., Toustrup-Jensen, M.S., Schack, V.R., Egebjerg, J., Andersen, J.P., Vilsen, B., Nissen, P., 2009. The structure of the Na $^{+}$,K $^{+}$-ATPase and mapping of isoform differences and disease-related mutations. Philos. Trans. R. Soc. B Biol. Sci. 364, 217–227. https://doi.org/10.1098/rstb.2008.0201
- Muyldermans, S., Cambillau, C., Wyns, L., 2001. Recognition of antigens by single-domain antibody fragments: the superfluous luxury of paired domains. Trends Biochem. Sci. 26, 230–235. https://doi.org/10.1016/S0968-0004(01)01790-X
- Mykkänen, J., Torrents, D., Pineda, M., Camps, M., Yoldi, M.E., Horelli-Kuitunen, N., Huoponen, K., Heinonen, M., Oksanen, J., Simell, O., Savontaus, M.-L., Zorzano, A., Palacín, M., Aula, P., 2000. Functional analysis of novel mutations in y+LAT-1 amino acid transporter gene causing lysinuric protein intolerance (LPI). Hum. Mol. Genet. 9, 431–438. https://doi.org/10.1093/hmg/9.3.431
- Nanao, M., Basu, S., Zander, U., Giraud, T., Surr, J., Guijarro, M., Lentini, M., Felisaz, F., Sinoir, J., Morawe, C., Vivo, A., Beteva, A., Oscarsson, M., Caserotto, H., Dobias, F., Flot, D., Nurizzo, D., Gigmes, J., Foos, N., Siebrecht, R., Roth, T., Theveneau, P., Svensson, O., Papp, G., Lavault, B., Cipriani, F., Barrett, R., Clavel, C., Leonard, G., 2022. ID23-2: an automated and high-performance microfocus beamline for macromolecular crystallography at the ESRF. J. Synchrotron Radiat. 29, 581–590. https://doi.org/10.1107/S1600577522000984
- Napolitano, L., Scalise, M., Koyioni, M., Koutentis, P., Catto, M., Eberini, I., Parravicini, C., Palazzolo, L., Pisani, L., Galluccio, M., Console, L., Carotti, A., Indiveri, C., 2017. Potent inhibitors of human LAT1 (SLC7A5) transporter based on dithiazole and dithiazine compounds for development of anticancer drugs. Biochem. Pharmacol. 143, 39–52. https://doi.org/10.1016/j.bcp.2017.07.006
- Nasr, M.L., Singh, S.K., 2014. Radioligand Binding to Nanodisc-Reconstituted Membrane Transporters Assessed by the Scintillation Proximity Assay. Biochemistry 53, 4–6. https://doi.org/10.1021/bi401412e
- Nath, A., Koo, P.K., Rhoades, E., Atkins, W.M., 2008. Allosteric Effects on Substrate Dissociation from Cytochrome P450 3A4 in Nanodiscs Observed by Ensemble and Single-Molecule Fluorescence Spectroscopy. J. Am. Chem. Soc. 130, 15746–15747. https://doi.org/10.1021/ja805772r
- Navratna, V., Gouaux, E., 2019. Insights into the mechanism and pharmacology of neurotransmitter sodium symporters. Curr. Opin. Struct. Biol., Folding and Binding • Proteins:3D structures 54, 161–170. https://doi.org/10.1016/j.sbi.2019.03.011
- Nichols, J.W., 1988. Phospholipid transfer between phosphatidylcholine-taurocholate mixed micelles. Biochemistry 27, 3925–3931. https://doi.org/10.1021/bi00411a006
- Nicolàs-Aragó, A., Fort, J., Palacín, M., Errasti-Murugarren, E., 2021. Rush Hour of LATs towards Their Transport Cycle. Membranes 11, 602. https://doi.org/10.3390/membranes11080602
- Nurizzo, D., Mairs, T., Guijarro, M., Rey, V., Meyer, J., Fajardo, P., Chavanne, J., Biasci, J.-C., McSweeney, S., Mitchell, E., 2006. The ID23-1 structural biology beamline at the ESRF. J. Synchrotron Radiat. 13, 227–238. https://doi.org/10.1107/S0909049506004341
- Oda, K., Lee, Y., Wiriyasermkul, P., Tanaka, Y., Takemoto, M., Yamashita, K., Nagamori, S., Nishizawa, T., Nureki, O., 2020. Consensus mutagenesis approach improves the thermal stability of system xc− transporter, xCT, and enables cryo-EM analyses. Protein Sci. 29, 2398–2407. https://doi.org/10.1002/pro.3966
- Ohgimoto, S., Tabata, N., Suga, S., Nishio, M., Ohta, H., Komada, H., Kawano, M., Watanabe, N., Ito, Y., 1995. Molecular characterization of fusion regulatory protein-1 (FRP-1) that induces multinucleated giant cell formation of monocytes and HIV gp160-mediated cell fusion. FRP-1 and 4F2/CD98 are identical molecules. J. Immunol. 9.

- Ohtsuki, S., Yamaguchi, H., Kang, Y.-S., Hori, S., Terasaki, T., 2010. Reduction of L-type amino acid transporter 1 mRNA expression in brain capillaries in a mouse model of Parkinson's disease. Biol. Pharm. Bull. 33, 1250–1252. https://doi.org/10.1248/bpb.33.1250
- Oliver, R.C., Lipfert, J., Fox, D.A., Lo, R.H., Doniach, S., Columbus, L., 2013. Dependence of Micelle Size and Shape on Detergent Alkyl Chain Length and Head Group. PLoS ONE 8, e62488. https://doi.org/10.1371/journal.pone.0062488
- Opekarová, M., Tanner, W., 2003. Specific lipid requirements of membrane proteins—a putative bottleneck in heterologous expression. Biochim. Biophys. Acta BBA - Biomembr., Overexpression of Integral Membrane Proteins 1610, 11–22. https://doi.org/10.1016/S0005-2736(02)00708-3
- Ostermeier, C., Iwata, S., Ludwig, B., Michel, H., 1995. F v fragment-mediated crystallization of the membrane protein bacterial cytochrome c oxidase. Nat. Struct. Biol. 2, 842–846. https://doi.org/10.1038/nsb1095-842
- Overington, J.P., Al-Lazikani, B., Hopkins, A.L., 2006. How many drug targets are there? Nat. Rev. Drug Discov. 5, 993–996. https://doi.org/10.1038/nrd2199
- Owada, T., Kurasawa, K., Endou, H., Fujita, T., Anzai, N., Hayashi, K., 2022. LAT1-specific inhibitor ameliorates severe autoimmune arthritis in SKG mouse. Int. Immunopharmacol. 109, 108817. https://doi.org/10.1016/j.intimp.2022.108817
- Oxender, D.L., Christensen, H.N., 1963. Distinct Mediating Systems for the Transport of Neutral Amino Acids by the Ehrlich Cell. J. Biol. Chem. 238, 3686–3699. https://doi.org/10.1016/S0021-9258(19)75327-7
- Palacín, M., 1994. A new family of proteins (rBAT and 4F2hc) involved in cationic and zwitterionic amino acid transport: a tale of two proteins in search of a transport function. J. Exp. Biol. 196, 123–137. https://doi.org/10.1242/jeb.196.1.123
- Palacín, M., Estévez, R., Bertran, J., Zorzano, A., 1998a. Molecular Biology of Mammalian Plasma Membrane Amino Acid Transporters. Physiol. Rev. 78, 969–1054. https://doi.org/10.1152/physrev.1998.78.4.969
- Palacín, M., Estévez, R., Bertran, J., Zorzano, A., 1998b. Molecular Biology of Mammalian Plasma Membrane Amino Acid Transporters. Physiol. Rev. 78, 969–1054. https://doi.org/10.1152/physrev.1998.78.4.969
- Palacín, M., Kanai, Y., 2004. The ancillary proteins of HATs: SLC3 family of amino acid transporters. Pflugers Arch. 447, 490–494. https://doi.org/10.1007/s00424-003-1062-7
- Palacín, M., Nunes, V., Font-Llitjós, M., Jiménez-Vidal, M., Fort, J., Gasol, E., Pineda, M., Feliubadaló, L., Chillarón, J., Zorzano, A., 2005. The Genetics of Heteromeric Amino Acid Transporters. Physiology 20, 112–124. https://doi.org/10.1152/physiol.00051.2004
- Pardon, E., Laeremans, T., Triest, S., Rasmussen, S.G.F., Wohlkönig, A., Ruf, A., Muyldermans, S., Hol, W.G.J., Kobilka, B.K., Steyaert, J., 2014. A general protocol for the generation of Nanobodies for structural biology. Nat. Protoc. 9, 674–693. https://doi.org/10.1038/nprot.2014.039
- Parker, J.L., Deme, J.C., Kolokouris, D., Kuteyi, G., Biggin, P.C., Lea, S.M., Newstead, S., 2021a. Molecular basis for redox control by the human cystine/glutamate antiporter system xc−. Nat. Commun. 12, 1–11. https://doi.org/10.1038/s41467-021-27414-1
- Parker, J.L., Deme, J.C., Wu, Z., Kuteyi, G., Huo, J., Owens, R.J., Biggin, P.C., Lea, S.M., Newstead, S., 2021b. Cryo-EM structure of PepT2 reveals structural basis for proton-coupled peptide and prodrug transport in mammals. Sci. Adv. 7, eabh3355. https://doi.org/10.1126/sciadv.abh3355
- Penmatsa, A., Gouaux, E., 2014. How LeuT shapes our understanding of the mechanisms of sodium-coupled neurotransmitter transporters. J. Physiol. 592, 863–869. https://doi.org/10.1113/jphysiol.2013.259051
- Penmatsa, A., Wang, K.H., Gouaux, E., 2013. X-ray structure of the dopamine transporter in complex with tricyclic antidepressant. Nature 503, 85–90. https://doi.org/10.1038/nature12533
- Perez, C., Faust, B., Mehdipour, A.R., Francesconi, K.A., Forrest, L.R., Ziegler, C., 2014. Substrate-bound outward-open state of the betaine transporter BetP provides insights into Na + coupling. Nat. Commun. 5, 4231. https://doi.org/10.1038/ncomms5231
- Perez, C., Koshy, C., Ressl, S., Nicklisch, S., Krämer, R., Ziegler, C., 2011. Substrate specificity and ion coupling in the Na+/betaine symporter BetP. EMBO J. 30, 1221–1229. https://doi.org/10.1038/emboj.2011.46
- Perez, C., Koshy, C., Yildiz, Ö., Ziegler, C., 2012. Alternating-access mechanism in conformationally asymmetric trimers of the betaine transporter BetP. Nature 490, 126–130. https://doi.org/10.1038/nature11403

- Perheentupa, J., Visakorpi, J.K., 1965. Protein intolerance with deficient transport of basic aminoacids. Another inborn error of metabolism. Lancet Lond. Engl. 2, 813–816. https://doi.org/10.1016/s0140-6736(65)92446-3
- Perutz, M.F., Rossmann, M.G., Cullis, A.F., Muirhead, H., Will, G., North, A.C.T., 1960. Structure of Hæmoglobin: A Three-Dimensional Fourier Synthesis at 5.5-Å. Resolution, Obtained by X-Ray Analysis. Nature 185, 416–422. https://doi-org.sire.ub.edu/10.1038/185416a0
- Pfeiffer, R., Spindler, B., Loffing, J., Skelly, P.J., Shoemaker, C.B., Verrey, F., 1998. Functional heterodimeric amino acid transporters lacking cysteine residues involved in disulfide bond. FEBS Lett. 439, 157–162. https://doi.org/10.1016/S0014-5793(98)01359-3
- Pineda, M., Font, M., Bassi, M.T., Manzoni, M., Borsani, G., Marigo, V., Fernández, E., Río, R.M. del, Purroy, J., Zorzano, A., Nunes, V., Palacín, M., 2004. The amino acid transporter asc-1 is not involved in cystinuria. Kidney Int. 66, 1453–1464. https://doi.org/10.1111/j.1523-1755.2004.00908.x
- Pirchi, M., Ziv, G., Riven, I., Cohen, S.S., Zohar, N., Barak, Y., Haran, G., 2011. Single-molecule fluorescence spectroscopy maps the folding landscape of a large protein. Nat. Commun. 2, 493. https://doi.org/10.1038/ncomms1504
- Privé, G.G., 2007. Detergents for the stabilization and crystallization of membrane proteins. Methods, Structural Biology of Membrane Proteins 41, 388–397. https://doi.org/10.1016/j.ymeth.2007.01.007
- Quick, M., Abramyan, A.M., Wiriyasermkul, P., Weinstein, H., Shi, L., Javitch, J.A., 2018. The LeuT-fold neurotransmitter:sodium symporter MhsT has two substrate sites. Proc. Natl. Acad. Sci. 115, E7924–E7931. https://doi.org/10.1073/pnas.1717444115
- Quick, M., Winther, A.-M.L., Shi, L., Nissen, P., Weinstein, H., Javitch, J.A., 2009. Binding of an octylglucoside detergent molecule in the second substrate (S2) site of LeuT establishes an inhibitor-bound conformation. Proc. Natl. Acad. Sci. 106, 5563–5568. https://doi.org/10.1073/pnas.0811322106
- Reddy, V.S., Shlykov, M.A., Castillo, R., Sun, E.I., Saier, M.H., 2012. The major facilitator superfamily (MFS) revisited. FEBS J. 279, 2022–2035. https://doi.org/10.1111/j.1742-4658.2012.08588.x
- Ressl, S., Terwisscha van Scheltinga, A.C., Vonrhein, C., Ott, V., Ziegler, C., 2009. Molecular basis of transport and regulation in the Na+/betaine symporter BetP. Nature 458, 47–52. https://doi.org/10.1038/nature07819
- Ritchie, T.K., Grinkova, Y.V., Bayburt, T.H., Denisov, I.G., Zolnerciks, J.K., Atkins, W.M., Sligar, S.G., 2009. Reconstitution of Membrane Proteins in Phospholipid Bilayer Nanodiscs 23.
- Rodriguez, C.F., Escudero-Bravo, P., Díaz, L., Bartoccioni, P., García-Martín, C., Gilabert, J.G., Boskovic, J., Guallar, V., Errasti-Murugarren, E., Llorca, O., Palacín, M., 2021. Structural basis for substrate specificity of heteromeric transporters of neutral amino acids. Proc. Natl. Acad. Sci. U. S. A. 118, e2113573118. https://doi.org/10.1073/pnas.2113573118
- Rosell, A., Meury, M., Álvarez-Marimon, E., Costa, M., Pérez-Cano, L., Zorzano, A., Fernández-Recio, J., Palacín, M., Fotiadis, D., 2014. Structural bases for the interaction and stabilization of the human amino acid transporter LAT2 with its ancillary protein 4F2hc. Proc. Natl. Acad. Sci. 111, 2966–2971. https://doi.org/10.1073/pnas.1323779111
- Roy, R., Hohng, S., Ha, T., 2008. A practical guide to single-molecule FRET. Nat. Methods 5, 507–516. https://doi.org/10.1038/nmeth.1208
- Rullo-Tubau, J., Bartoccioni, P., Llorca, O., Errasti-Murugarren, E., Palacín, M., 2022. HATs meet structural biology. Curr. Opin. Struct. Biol. 74, 102389. https://doi.org/10.1016/j.sbi.2022.102389
- Saier, M.H., 2000. A Functional-Phylogenetic Classification System for Transmembrane Solute Transporters. Microbiol. Mol. Biol. Rev. 64, 354–411. https://doi.org/10.1128/MMBR.64.2.354-411.2000
- Saier, M.H., Jr, Reddy, V.S., Tsu, B.V., Ahmed, M.S., Li, C., Moreno-Hagelsieb, G., 2016. The Transporter Classification Database (TCDB): recent advances. Nucleic Acids Res. 44, D372–D379. https://doi.org/10.1093/nar/gkv1103
- Saier, M.H., Tam, R., Reizer, A., Reizer, J., 1994. Two novel families of bacterial membrane proteins concerned with nodulation, cell division and transport. Mol. Microbiol. 11, 841–847. https://doi.org/10.1111/j.1365-2958.1994.tb00362.x
- Sakimura, K., Nakao, K., Yoshikawa, M., Suzuki, M., Kimura, H., 2016. A novel Na+-Independent alanine-serine-cysteine transporter 1 inhibitor inhibits both influx and efflux of D-Serine. J. Neurosci. Res. 94, 888–895. https://doi.org/10.1002/jnr.23772
- Sato, H., Tamba, M., Ishii, T., Bannai, S., 1999. Cloning and expression of a plasma membrane cystine/glutamate exchange transporter composed of two distinct proteins. J. Biol. Chem. 274, 11455–11458. https://doi.org/10.1074/jbc.274.17.11455

- Savaskan, N.E., Eyüpoglu, I.Y., 2010. xCT modulation in gliomas: Relevance to energy metabolism and tumor microenvironment normalization. Ann. Anat. - Anat. Anz., SPECIAL SECTION: NUCLEAR IMAGING 192, 309–313. https://doi.org/10.1016/j.aanat.2010.07.003
- Scalise, M., Pochini, L., Console, L., Pappacoda, G., Pingitore, P., Hedfalk, K., Indiveri, C., 2018. Cys Site-Directed Mutagenesis of the Human SLC1A5 (ASCT2) Transporter: Structure/Function Relationships and Crucial Role of Cys467 for Redox Sensing and Glutamine Transport. Int. J. Mol. Sci. 19, 648. https://doi.org/10.3390/ijms19030648
- Schroeder, H.W., Cavacini, L., 2010. Structure and function of immunoglobulins. J. Allergy Clin. Immunol., 2010 Primer on Allergic and Immunologic Diseases 125, S41–S52. https://doi.org/10.1016/j.jaci.2009.09.046
- Schuler, M.A., Denisov, I.G., Sligar, S.G., 2013. Nanodiscs as a new tool to examine lipid-protein interactions. Methods Mol. Biol. Clifton NJ 974, 415–433. https://doi.org/10.1007/978-1-62703-275-9_18
- Schulze, S., Köster, S., Geldmacher, U., Terwisscha van Scheltinga, A.C., Kühlbrandt, W., 2010. Structural basis of Na + -independent and cooperative substrate/product antiport in CaiT. Nature 467, 233–236. https://doi.org/10.1038/nature09310
- Selvin, P.R., 2000. The renaissance of fluorescence resonance energy transfer. Nat. Struct. Biol. 7, 730–734. https://doi.org/10.1038/78948
- Shaffer, P.L., Goehring, A., Shankaranarayanan, A., Gouaux, E., 2009. Structure and Mechanism of a Na+-Independent Amino Acid Transporter. Science 325, 1010–1014. https://doi.org/10.1126/science.1176088
- Shi, L., Quick, M., Zhao, Y., Weinstein, H., Javitch, J.A., 2008. The Mechanism of a Neurotransmitter:Sodium Symporter—Inward Release of Na+ and Substrate Is Triggered by Substrate in a Second Binding Site. Mol. Cell 11.
- Shih, A.Y., Freddolino, P.L., Sligar, S.G., Schulten, K., 2007. Disassembly of Nanodiscs with Cholate. Nano Lett. 7, 1692–1696. https://doi.org/10.1021/nl0706906
- Shimamura, T., Weyand, S., Beckstein, O., Rutherford, N.G., Hadden, J.M., Sharples, D., Sansom, M.S.P., Iwata, S., Henderson, P.J.F., Cameron, A.D., 2010. Molecular Basis of Alternating Access Membrane Transport by the Sodium-Hydantoin Transporter Mhp1. Science 328, 470–473. https://doi.org/10.1126/science.1186303
- Silbernagl, S., 1988. The renal handling of amino acids and oligopeptides. Physiol. Rev. 68, 97.
- Silbernagl, S., 1979. Renal transport of amino acids. Klin. Wochenschrifft 57, 1009–1019.
- Silbernagl, S., Foulkes, E.C., Deetjen, P., 1975. Renal transport of amino acids, in: Reviews of Physiology, Biochemistry and Pharmacology, Volume 74: Ergebnisse Der Physiologie, Biologischen Chemie Und Experimentellen Pharmakologie Volume: 74, Reviews of Physiology, Biochemistry and Pharmacology. Springer, Berlin, Heidelberg, pp. 105–167. https://doi.org/10.1007/3-540-07483-X_20
- Silk, D.B.A., Grimble, G.K., Rees, R.G., 1985. Protein digestion and amino acid and peptide absorption. Proc. Nutr. Soc. 44, 63–72. https://doi.org/10.1079/PNS19850011
- Simmons, K.J., Jackson, S.M., Brueckner, F., Patching, S.G., Beckstein, O., Ivanova, E., Geng, T., Weyand, S., Drew, D., Lanigan, J., Sharples, D.J., Sansom, M.S., Iwata, S., Fishwick, C.W., Johnson, A.P., Cameron, A.D., Henderson, P.J., 2014. Molecular mechanism of ligand recognition by membrane transport protein, Mhp1. EMBO J. 33, 1831–1844. https://doi.org/10.15252/embj.201387557
- Sindbert, S., Kalinin, S., Nguyen, H., Kienzler, A., Clima, L., Bannwarth, W., Appel, B., Müller, S., Seidel, C.A.M., 2011. Accurate Distance Determination of Nucleic Acids via Förster Resonance Energy Transfer: Implications of Dye Linker Length and Rigidity. J. Am. Chem. Soc. 133, 2463–2480. https://doi.org/10.1021/ja105725e
- Singh, S.K., Piscitelli, C.L., Yamashita, A., Gouaux, E., 2008. A Competitive Inhibitor Traps LeuT in an Open-to-Out Conformation. Science 322, 1655–1661. https://doi.org/10.1126/science.1166777
- Singh, S.K., Yamashita, A., Gouaux, E., 2007. Antidepressant binding site in a bacterial homologue of neurotransmitter transporters. Nature 448, 952–956. https://doi.org/10.1038/nature06038
- Smyth, M.S., Martin, J.H.J., 2000. x Ray crystallography. Mol. Pathol. 53, 8–14.
- Sperandeo, M.P., Andria, G., Sebastio, G., 2008. Lysinuric protein intolerance: update and extended mutation analysis of theSLC7A7 gene. Hum. Mutat. 29, 14–21. https://doi.org/10.1002/humu.20589

- Stolzenberg, S., Li, Z., Quick, M., Malinauskaite, L., Nissen, P., Weinstein, H., Javitch, J.A., Shi, L., 2017. The role of transmembrane segment 5 (TM5) in Na2 release and the conformational transition of neurotransmitter:sodium symporters toward the inward-open state. J. Biol. Chem. 292, 7372–7384. https://doi.org/10.1074/jbc.M116.757153
- Tang, L., Bai, L., Wang, W., Jiang, T., 2010. Crystal structure of the carnitine transporter and insights into the antiport mechanism. Nat. Struct. Mol. Biol. 17, 492–496. https://doi.org/10.1038/nsmb.1788
- Tărlungeanu, D.C., Deliu, E., Dotter, C.P., Kara, M., Janiesch, P.C., Scalise, M., Galluccio, M., Tesulov, M., Morelli, E., Sonmez, F.M., Bilguvar, K., Ohgaki, R., Kanai, Y., Johansen, A., Esharif, S., Ben-Omran, T., Topcu, M., Schlessinger, A., Indiveri, C., Duncan, K.E., Caglayan, A.O., Gunel, M., Gleeson, J.G., Novarino, G., 2016. Impaired Amino Acid Transport at the Blood Brain Barrier Is a Cause of Autism Spectrum Disorder. Cell 167, 1481-1494.e18. https://doi.org/10.1016/j.cell.2016.11.013
- Tavoulari, S., Margheritis, E., Nagarajan, A., DeWitt, D.C., Zhang, Y.-W., Rosado, E., Ravera, S., Rhoades, E., Forrest, L.R., Rudnick, G., 2016. Two Na+ Sites Control Conformational Change in a Neurotransmitter Transporter Homolog. J. Biol. Chem. 291, 1456–1471. https://doi.org/10.1074/jbc.M115.692012
- Terry, D.S., Kolster, R.A., Quick, M., LeVine, M.V., Khelashvili, G., Zhou, Z., Weinstein, H., Javitch, J.A., Blanchard, S.C., 2018. A partially-open inward-facing intermediate conformation of LeuT is associated with Na+ release and substrate transport. Nat. Commun. 9, 230. https://doi.org/10.1038/s41467-017-02202-y
- Theveneau, P., Baker, R., Barrett, R., Beteva, A., Bowler, M.W., Carpentier, P., Caserotto, H., Sanctis, D. de, Dobias, F., Flot, D., Guijarro, M., Giraud, T., Lentini, M., Leonard, G.A., Mattenet, M., McCarthy, A.A., McSweeney, S.M., Morawe, C., Nanao, M., Nurizzo, D., Ohlsson, S., Pernot, P., Popov, A.N., Round, A., Royant, A., Schmid, W., Snigirev, A., Surr, J., Mueller-Dieckmann, C., 2013. The Upgrade Programme for the Structural Biology beamlines at the European Synchrotron Radiation Facility – High throughput sample evaluation and automation. J. Phys. Conf. Ser. 425, 012001. https://doi.org/10.1088/1742-6596/425/1/012001
- Thompson, D.B., Cronican, J.J., Liu, D.R., 2012. Engineering and identifying supercharged proteins for macromolecule delivery into mammalian cells. Methods Enzymol. 503, 293–319. https://doi.org/10.1016/B978-0-12-396962-0.00012-4
- Tian, J., Li, X., Jiang, Y., Gao, F., Ju, B., Chen, J., Zhu, W., He, L., Meng, L., Lu, S., 2022. SLC7A5 expression is up-regulated in peripheral blood T and B lymphocytes of systemic lupus erythematosus patients, associating with renal damage. Clin. Immunol. 237, 108987. https://doi.org/10.1016/j.clim.2022.108987
- Torrents, D., Mykkänen, J., Pineda, M., Feliubadaló, L., Estévez, R., Cid, R. de, Sanjurjo, P., Zorzano, A., Nunes, V., Huoponen, K., Reinikainen, A., Simell, O., Savontaus, M.-L., Aula, P., Palacín, M., 1999. Identification of SLC7A7, encoding y+LAT-1, as the lysinuric protein intolerance gene. Nat. Genet. 21, 293–296. https://doi.org/10.1038/6809
- Tsumura, H., Suzuki, N., Saito, H., Kawano, M., Otake, S., Kozuka, Y., Komada, H., Tsurudome, M., Ito, Y., 2003. The targeted disruption of the CD98 gene results in embryonic lethality. Biochem. Biophys. Res. Commun. 308, 847–851. https://doi.org/10.1016/S0006-291X(03)01473-6
- Uhlén, M., Fagerberg, L., Hallström, B.M., Lindskog, C., Oksvold, P., Mardinoglu, A., Sivertsson, Å., Kampf, C., Sjöstedt, E., Asplund, A., Olsson, I., Edlund, K., Lundberg, E., Navani, S., Szigyarto, C.A.-K., Odeberg, J., Djureinovic, D., Takanen, J.O., Hober, S., Alm, T., Edqvist, P.-H., Berling, H., Tegel, H., Mulder, J., Rockberg, J., Nilsson, P., Schwenk, J.M., Hamsten, M., Feilitzen, K. von, Forsberg, M., Persson, L., Johansson, F., Zwahlen, M., Heijne, G. von, Nielsen, J., Pontén, F., 2015. Tissue-based map of the human proteome. Science 347. https://doi.org/10.1126/science.1260419
- Verrey, F., Closs, E.I., Wagner, C.A., Palacín, M., Endou, H., Kanai, Y., 2004. CATs and HATs: the SLC7 family of amino acid transporters. Pflugers Arch. 447, 532–542. https://doi.org/10.1007/s00424-003-1086-z
- Verrey, F., Jack, D.L., Paulsen, I.T., Saier, Jr., M.H., Pfeiffer, R., 1999. New Glycoprotein-Associated Amino Acid Transporters. J. Membr. Biol. 172, 181–192. https://doi.org/10.1007/s002329900595
- Verrey, F., Meier, C., Rossier, G., Kühn, L.C., 2000. Glycoprotein-associated amino acid exchangers: broadening the range of transport specificity. Pflüg. Arch. 440, 503–512. https://doi.org/10.1007/s004240000274
- Vincke, C., Gutiérrez, C., Wernery, U., Devoogdt, N., Hassanzadeh-Ghassabeh, G., Muyldermans, S., 2012. Generation of single domain antibody fragments derived from camelids and generation of manifold constructs. Methods Mol. Biol. Clifton NJ 907, 145–176. https://doi.org/10.1007/978-1-61779-974-7_8
- Vinothkumar, K.R., Henderson, R., 2010. Structures of membrane proteins. Q. Rev. Biophys. 43, 65–158. https://doi.org/10.1017/S0033583510000041

- von Stetten, D., Carpentier, P., Flot, D., Beteva, A., Caserotto, H., Dobias, F., Guijarro, M., Giraud, T., Lentini, M., McSweeney, S., Royant, A., Petitdemange, S., Sinoir, J., Surr, J., Svensson, O., Theveneau, P., Leonard, G.A., Mueller-Dieckmann, C., 2020. ID30A-3 (MASSIF-3) – a beamline for macromolecular crystallography at the ESRF with a small intense beam. J. Synchrotron Radiat. 27, 844–851. https://doi.org/10.1107/S1600577520004002
- Vonrhein, C., Flensburg, C., Keller, P., Sharff, A., Smart, O., Paciorek, W., Womack, T., Bricogne, G., 2011. Data processing and analysis with the autoPROC toolbox. Acta Crystallogr. D Biol. Crystallogr. 67, 293–302. https://doi.org/10.1107/S0907444911007773
- Wallin, E., Heijne, G.V., 1998. Genome-wide analysis of integral membrane proteins from eubacterial, archaean, and eukaryotic organisms. Protein Sci. 7, 1029–1038. https://doi.org/10.1002/pro.5560070420
- Wang, K.H., Penmatsa, A., Gouaux, E., 2015. Neurotransmitter and psychostimulant recognition by the dopamine transporter. Nature 521, 322–327. https://doi.org/10.1038/nature14431
- Watanabe, A., Choe, S., Chaptal, V., Rosenberg, J.M., Wright, E.M., Grabe, M., Abramson, J., 2010. The mechanism of sodium and substrate release from the binding pocket of vSGLT. Nature 468, 988–991. https://doi.org/10.1038/nature09580
- Watson, J.D., Crick, F.H.C., 1953. Molecular structure of nucleic acids, a structure for deoxyribose nucleic acid. Nature 737–738. https://doi.org/10.1038/171737a0
- Wells, R.G., Lee, W.-S., Kanai, Y., Laiden, J.M., Hediger, M.A., 1992. The 4F2 antigen heavy chain induces uptake of neutral and dibasic amino acids in Xenopus oocytes. J. Biol. Chem. 267, 4. https://doi.org/10.1016/S0021-9258(19)49531-8
- Weyand, S., Shimamura, T., Yajima, S., Suzuki, S., Mirza, O., Krusong, K., Carpenter, E.P., Rutherford, N.G., Hadden, J.M., O'Reilly, J., Ma, P., Saidijam, M., Patching, S.G., Hope, R.J., Norbertczak, H.T., Roach, P.C.J., Iwata, S., Henderson, P.J.F., Cameron, A.D., 2008. Structure and Molecular Mechanism of a Nucleobase–Cation–Symport-1 Family Transporter. Science 322, 709–713. https://doi.org/10.1126/science.1164440
- Wilkins, M.H.F., Stokes, A.R., Wilson, H.R., 1953. Molecular structure of nucleic acids: molecular structure of deoxypentose nucleic acids. Nature 738–740.
- Winn, M.D., Ballard, C.C., Cowtan, K.D., Dodson, E.J., Emsley, P., Evans, P.R., Keegan, R.M., Krissinel, E.B., Leslie, A.G.W., McCoy, A., McNicholas, S.J., Murshudov, G.N., Pannu, N.S., Potterton, E.A., Powell, H.R., Read, R.J., Vagin, A., Wilson, K.S., 2011. Overview of the CCP4 suite and current developments. Acta Crystallogr. D Biol. Crystallogr. 67, 235–242. https://doi.org/10.1107/S0907444910045749
- Wissler, L., Gadau, J., Simola, D.F., Helmkampf, M., Bornberg-Bauer, E., 2013. Mechanisms and Dynamics of Orphan Gene Emergence in Insect Genomes. Genome Biol. Evol. 5, 439–455. https://doi.org/10.1093/gbe/evt009
- Wlodawer, A., Segrest, J.P., Chung, B.H., Chiovetti, R., Weinstein, J.N., 1979. High-density lipoprotein recombinants: evidence for a bicycle tire micelle structure obtained by neutron scattering and electron microscopy. FEBS Lett. 104, 231–235. https://doi.org/10.1016/0014-5793(79)80821-2
- Wong, F.H., Chen, J.S., Reddy, V., Day, J.L., Shlykov, M.A., Wakabayashi, S.T., Milton H. Saier, J., 2012. The Amino Acid-Polyamine-Organocation Superfamily. Microb. Physiol. 22, 105–113. https://doi.org/10.1159/000338542
- Wu, D., Grund, T.N., Welsch, S., Mills, D.J., Michel, M., Safarian, S., Michel, H., 2020. Structural basis for amino acid exchange by a human heteromeric amino acid transporter. Proc. Natl. Acad. Sci. U. S. A. 117, 21281–21287. https://doi.org/10.1073/pnas.2008111117
- Yamashita, A., Singh, S.K., Kawate, T., Jin, Y., Gouaux, E., 2005. Crystal structure of a bacterial homologue of Na + /Cl - -dependent neurotransmitter transporters. Nature 437, 215–223. https://doi.org/10.1038/nature03978
- Yan, R., Li, Y., Müller, J., Zhang, Y., Singer, S., Xia, L., Zhong, X., Gertsch, J., Altmann, K.-H., Zhou, Q., 2021. Mechanism of substrate transport and inhibition of the human LAT1-4F2hc amino acid transporter. Cell Discov. 7, 16. https://doi.org/10.1038/s41421-021-00247-4
- Yan, R., Li, Y., Shi, Y., Zhou, J., Lei, J., Huang, J., Zhou, Q., 2020a. Cryo-EM structure of the human heteromeric amino acid transporter b $^{0,+}$ AT-rBAT. Sci. Adv. 6, eaay6379. https://doi.org/10.1126/sciadv.aay6379
- Yan, R., Xie, E., Li, Y., Li, J., Zhang, Y., Chi, X., Hu, X., Xu, L., Hou, T., Stockwell, B.R., Min, J., Zhou, Q., Wang, F., 2022. The structure of erastin-bound xCT–4F2hc complex reveals molecular mechanisms underlying erastin-induced ferroptosis. Cell Res. 1–4. https://doi.org/10.1038/s41422-022-00642-w
- Yan, R., Zhao, X., Lei, J., Zhou, Q., 2019. Structure of the human LAT1–4F2hc heteromeric amino acid transporter complex. Nature 568, 127–130. https://doi.org/10.1038/s41586-019-1011-z

- Yan, R., Zhou, J., Li, Y., Lei, J., Zhou, Q., 2020b. Structural insight into the substrate recognition and transport mechanism of the human LAT2–4F2hc complex. Cell Discov. 6, 82. https://doi.org/10.1038/s41421-020-00207-4
- Young, J.A., Freedman, B.S., 1971. Renal Tubular Transport of Amino Acids. Clin. Chem. 17, 245–266. https://doi.org/10.1093/clinchem/17.4.245
- Zewail, A.H., 2005. Diffraction, crystallography and microscopy beyond three dimensions: structural dynamics in space and time. Philos. Trans. R. Soc. Math. Phys. Eng. Sci. 363, 315–329. https://doi.org/10.1098/rsta.2004.1513
- Zhang, G., Cao, L., 2017. New mutations in the SLC7A7 gene of two chinese sisters with lysinuric protein intolerance. Pediatr. Pulmonol. 52, E94–E96. https://doi.org/10.1002/ppul.23760
- Zhao, Y., Terry, D.S., Shi, L., Quick, M., Weinstein, H., Blanchard, S.C., Javitch, J.A., 2011. Substrate-modulated gating dynamics in a Na+-coupled neurotransmitter transporter homologue. Nature 474, 109–113. https://doi.org/10.1038/nature09971
- Zhou, Z., Zhen, J., Karpowich, N.K., Goetz, R.M., Law, C.J., Reith, M.E.A., Wang, D.-N., 2007. LeuT-Desipramine Structure Reveals How Antidepressants Block Neurotransmitter Reuptake. Science 317, 1390–1393. https://doi.org/10.1126/science.1147614
- Zhuang, X., Bartley, L.E., Babcock, H.P., Russell, R., Ha, T., Herschlag, D., Chu, S., 2000. A Single-Molecule Study of RNA Catalysis and Folding. Science 288, 2048–2051. https://doi.org/10.1126/science.288.5473.2048

Appendix

Appendix contents

Appendix A. Tables of contents

Appendix A.1. Reagents

Product name	Stock conditions	Working conditions	Application	Source
[^{3}H] L-alanine	250 µCi	0.5 µCi	Transport activity assay	PerkinElmer, Massachusetts, US
[^{3}H] L-serine	250 µCi	0.5 µCi	Transport activity assay	PerkinElmer, Massachusetts, US
Alexa Fluor™ 546 C5	25 nmol dried	0.06-0.25 nmol/µl	Maleimide labelling	Thermo Fisher Scientific, Waltham, US
Alexa Fluor™ 647 C2	25 nmol dried	0.06-0.25 nmol/µl	Maleimide labelling	Thermo Fisher Scientific, Waltham, US
Ampicillin	100 mg/ml	100 mg/L	Antibiotic	Merck, Darmstadt, Germany
Bacteriological Peptone	Powder	12 g/L	Culture medium	Laboratorios Conda, Madrid, ES
Chloroform	≥99 %	≥99 %	Organic solvent	Merck, Darmstadt, Germany
Cloned Pfu DNA polymerase reaction buffer	10x	1x	Site-directed mutagenesis by PCR	Agilent Technologies, Santa Clara, US
cOmplete EDTA-free	Solid tablets	1 tablet / 50 ml	BasC purification	Merck, Darmstadt, Germany
cOmplete mini	Solid tablets	1 tablet / 50 ml	Mb purification	Merck, Darmstadt, Germany
Cy3 maleimide	25 nmol dried	0.06-0.25 nmol/µl	Maleimide labelling	Lumiprobe, Hannover, Germany
Cy5 maleimide	25 nmol dried	0.06-0.25 nmol/µl	Maleimide labelling	Lumiprobe, Hannover, Germany
D-(+)-Glucose	Powder	2 % (w/v)	WK6 cells medium	Merck, Darmstadt, Germany
DDM	Powder	0.06-1 % (w/v)	Solubilising	Anatrace, Ohio, US
DM	Powder	0.17-2 % (w/v)	Solubilising	Anatrace, Ohio, US
DMSO (dimethyl sulfoxide)	≥99.9 %	≥99.9 %	Organic solvent	Merck, Darmstadt, Germany
DNase I	40 U/µl	200 U/mg_{cells}	Cell disruption	Thermo Fisher Scientific, Waltham, US
dNTPs	10 mM each	2 mM	Site-directed mutagenesis by PCR	Merck, Darmstadt, Germany

DPN I	200 U/µl	50 U/µl	Site directed mutagenesis	Agilent Technologies, Santa Clara, US
***E.coli* total lipid extract**	50 mg/ml	Dried and buffer resuspended	Proteoliposomes preparation	Avanti Polar Lipids, Alabama, US
Ecoscint Ultra Biodegradable Liquid Scintillation Cocktail	Commercial	Commercial	Radioactivity transport assays	Scientific Laboratory Supplies, Hessle, UK
EDTA	Disodium salt powder	Soluble	Buffer preparation	Merck, Darmstadt, Germany
HRV 3C protease	2 mg/ml	0.2 mg/ml	Protein specific digestion	(IRB Barcelona Protein Expression Core Facility, Barcelona, Spain)
Hydrocloric Acid	37 %	Different dilutions	pH buffer adjustment	Panreac Química, Barcelona, Spain
Imidazole	Powder / 3 M	10-500 mM	His-tagged proteins elution	
InstantBlue® Coomassie Protein Stain	Commercial	Commercial	Protein SDS-PAGE Staining	Abcam plc, Cambridge, UK
IPTG	1 M	1 mM	Protein expression inducer	Merck, Darmstadt, DE
Kanamycin	50 mg/ml	50 mg/L	Antibiotic	Merck, Darmstadt, DE
LB	Powder	25 g/L	Culture medium	Laboratorios Conda, Madrid, ES
Lysozyme	≥30,000 FP-U/mg	0.2 mg/ml	Mb purification	Merck, Darmstadt, DE
$MgCl_2$	Powder			
NaCl	Powder			
Ni-NTA Agarose	Et-OH 20 % suspension		Affinity purification for His-tagged proteins	QIAGEN, Hilden, Germany
n-octyl-b-D-glucopyranoside				Quimigen, Madrid, ES
Pefabloc® SC	Commercial	Commercial	Protease inhibitor, protein purification	Merck, Darmstadt, DE
PfuTurbo DNA polymerase	100 U, 2.5 U/µl	1.25 U / 25 µl	Site-directed mutagenesis by PCR	Agilent Technologies, Santa Clara, US
Pierce™ BCA Protein Assay Kit	Commercial	Commercial	Protein quantification	Thermo Fisher Scientific, Waltham, US

Pierce™ Silver Stain Kit	Commercial	Commercial	Protein SDS-PAGE Staining	Thermo Fisher Scientific, Waltham, US
POPC	50 mg/ml	Dried and buffer resuspended	NDs preparation	Avanti Polar Lipids, Alabama, US
SCy3 maleimide	25 nmol dried	0.06-0.25 nmol/µl	Maleimide labelling	Lumiprobe, Hannover, DE
SCy5 maleimide	25 nmol dried	0.06-0.25 nmol/µl	Maleimide labelling	Lumiprobe, Hannover, DE
Sodium hydroxide	Pellets	Soluble	Buffer preparation	Panreac Química, Barcelona, ES
Streptomycin	100 mg/ml	100 mg/L	Antibiotic	Thermo Fisher Scientific, Waltham, US
Sucrose	Powder		Nb purification (osmotic shock)	Merck, Darmstadt, Germany
TEV protease	2 mg/ml	0.2 mg/ml	Protein specific digestion	IRB Barcelona Protein Expression Core Facility, Barcelona, ES
Tris-HCl	Powder	20-100 mM	Buffer preparation	Roche Diagnostics, S.L., Barcelona, ES
Triton™ X-100	Commercial	Commercial	Detergent, protein purification	Merck, Darmstadt, DE
Tryptone	Powder	12-20 g/L	Culture medium	Laboratorios Conda, Madrid, ES
Yeast extract	Powder	24 g/L	Culture medium	Laboratorios Conda, Madrid, ES

Table A. 1. Reagens. List of most used reagents along the thesis.

Appendix A.2. Materials

Product name	Details	Application	Source
HisTrap HP	1 and 5 ml prepacked columns	His-tagged proteins purification	Cytiva, Marlborough, US
Amicon Ultra Centrifugal Filters	15 or 4 ml filters of 30,000, 50,000 or 100,000 kDa cut-off	Protein concentration and buffer exchange	Merck, Darmstadt, Germany
Sensor Chip CM5	Matrix: carboxymethylated dextran covalently attached to a gold surface.	Biacore sensor chip	Cytiva, Marlborough, US
His Capture Kit	Reagent kit based with anti-His antibodies	Immobolisation of His-tagged proteins on biacore sensor chips	Cytiva, Marlborough, US
Superdex 200 10/300 GL column	CV = 24.6 ml; always stored with 20 % Ethanol	Size Exclusion Chromatography	Cytiva, Marlborough, US
Superose 6 10/300 GL column	CV = 24.6 ml; always stored with 20 % Ethanol	Size Exclusion Chromatography	Cytiva, Marlborough, US
PD 10 Desalting	Pre-packed columns for 1.75-2.5 ml volume samples	Desalting	Cytiva, Marlborough, US
PD MidiTrap G-25	Pre-packed columns for 0,75-1 ml volume samples	Desalting	Cytiva, Marlborough, US
Dialysis tubing	50 kDa MWCO, 16 mm flat-with tubes	Dialysis	Repligen, Waltham, US
Bio-Beads SM-2 Resin	Bio-Beads SM-2 nonpolar polystyrene adsorbents	ND reconstitution	
Eppendorf cellulos filters			
Monolith NT.115 Premium Capillaries	High precission crystal capillaries covalently coeated with polymer to prevent surface adsorption of molecules.	Microscale Thermophoresis (MST)	Nanotemper Technologies, München, Germany
NucleoSpin mini kit	NucleoSpin Plasmid, Mini kit for plasmid DNA	(minipreps) cDNA obtention	Macherey-Nagel, Düren, Germany
Prometheus High Sensitivity Capillaries	High sensitivity capillaries for for low protein concentrations.	Thermostability	Nanotemper Technologies, München, Germany

Product name	Details	Application	Source
0.45 µm pore-size membrane filters	Regenerated Cellulose Membrane Filters 47 mm diameter 0.45 µm pore size	Transport assays	Sartorius Stedim Biotech, Cedex, France
Pony Vials	6 ml HDPE scintillation vials	Liquid scintillation counting	PerkinElmer, Massachusetts, US
Zeba Spin Columns	0.5 ml Spin Columns of 7 kDa cut-off for 30-130 µl volume sample	Desalting	Thermo Fisher Scientific, Waltham, US

Table A. 2 Materials. List of most used materials along the thesis.

Appendix A.3. Devices

Device	Details	Application	Source
Cell disruptor	French press type cell disruptor able to work in continuous (for volumes > 20 ml) or by batches (for small volumes < 20 ml).	Protein purification	Constant Systems Ltd., Daventry, UK
Nanodrop spectrophotometer		Protein and DNA quantification	Thermo Fisher Scientific, Waltham, US
ÄKTA pure 25 M	ÄKTA pure system with pumps, injection valve, and pressure, multi-wavelength UV, and conductivity monitors. With fraction collector F9-C and sample pump S9.	Size Exclusion Chromatography	Cytiva, Marlborough, US
Biacore™ T-100	Biacore™ T-100 system	Surface Plasmon Resonance	Cytiva, Marlborough, US
Incubator shaker	Incubator Shaker Series I 26	Protein expression	Thermo Fisher Scientific, Waltham, US
Thermocycler	GeneAmp PCR System 2700	Site directed mutagenesis by PCR	Thermo Fisher Scientific, Waltham, US
Monolith	Detects the mobility of fluorescent labelled proteins to detect binding, conformational changes, etc.	Binding characterisation by MST	Nanotemper Technologies, München, Germany
Prometheus	Detects intrinsic fluorescence of proteins to measure their fold and unfold rates.	Thermostability by nanoDSF	Nanotemper Technologies, München, Germany
Espectrophotometer	UV-VIS spectrophotometer UVmini-1240 CE	Cell cultures growth measurement	Schimadzu Corporation, Kyoto, Japan
High-Speed Centrifuges	- Avanti J-26 XPI - Avanti JHC - Avanti J-25	Centrifugation below 21,000 rpm	Backman Coulter Life Sciences, Indianapolis, US
Ultracentrifuge	- Optima L-90K - Optima XL-100K	Large volumes ultracentrifugation	Backman Coulter Life Sciences, Indianapolis, US
Tabletop Ultracentrifuge	- OPTIMA MAX XP - Optima TLX-B	Eppendorf ultracentrifugation	Backman Coulter Life Sciences, Indianapolis, US

Device	Details	Application	Source
70 Ti Rotor	Type 70 Ti fixed-angle titanium rotor, 8 x 39 ml tubes, maximum rpm: 70,000	Ultracentrifugation	Backman Coulter Life Sciences, Indianapolis, US
70.1 Ti Rotor	Type 70.1 Ti fixed-angle titanium rotor, 12 x 14 ml tubes, maximum rpm: 70,000	Ultracentrifugation	Backman Coulter Life Sciences, Indianapolis, US
TLA-55 Rotor	TLA-55 fixed-angle rotor, 12 x 2 ml tubes, maximum rpm: 55,000	Tabletop ultracentrifugation	Backman Coulter Life Sciences, Indianapolis, US
JA-30.50	JA-30.50 Ti fixed-angle titanium rotor, 8 x 50 ml tubes, maximum rpm: 30,000	High-speed centrifugation	Backman Coulter Life Sciences, Indianapolis, US
JA-10 Rotor	JA-10 fixed angle aluminium rotor, 6 x 500 ml tubes, maximum rpm: 10,000	High-speed centrifugation	Backman Coulter Life Sciences, Indianapolis, US
JA-14 Rotor	JA-14 fixed angle aluminium rotor, 6 x 250 ml tubes, maximum rpm: 14,000	High-speed centrifugation	Backman Coulter Life Sciences, Indianapolis, US
JLA-8.1000	J-LITE JLA-8.1000 fixed-angle aluminium rotor, 6 x 1000 ml tubes, maximum rpm: 8,000	High-speed centrifugation	Backman Coulter Life Sciences, Indianapolis, US
120 kV microscope	Thermo Fisher Tecnai 12 equiped with 4kx4k TemCam-F416 CMOS camera (TVIPS)	Cryo-EM imaging	CNIO, Madrid, ES
200 kV microscope	JEOL JEM-2200FS 200 kV equiped wit K3 direct electron detector	Cryo-EM imaging	CNIO, Madrid, ES

Table A. 3. Devices. List of most used devices along the thesis.

Appendix B: vectors and primers sequences

This Appendix aims to list the sequences for BasC variants, Nbs and MSPs as describe their expression vectors and primers used during the mutagenesis and sequencing.

Appendix B. 1. Bacterial alanine-serine-cysteine transporter

BasC sequence is cloned in pTTQ18 expressing vector between EcoRI and PstI sites (Figure A. 1). BasC is fused at C-ter in frame to a GFP variant and in between them the HRV-3C-protease site, additionally a 10 × His-tag is added at C-ter. pTTQ18 vector contains Ampicillin resistance and LacZ promoter.

All single and double-Cys variants were performed on cys-less versions (C427A) of BasC WT sequence or K154A variant. Single point mutations were carried out using the QuickChange site directed mutagenesis kit (Experimental Procedures 1.3) using the specific primers (Table A. 1). Cys positions, Lys154, and Cys427 can be clearly identified in Figure A. 2.

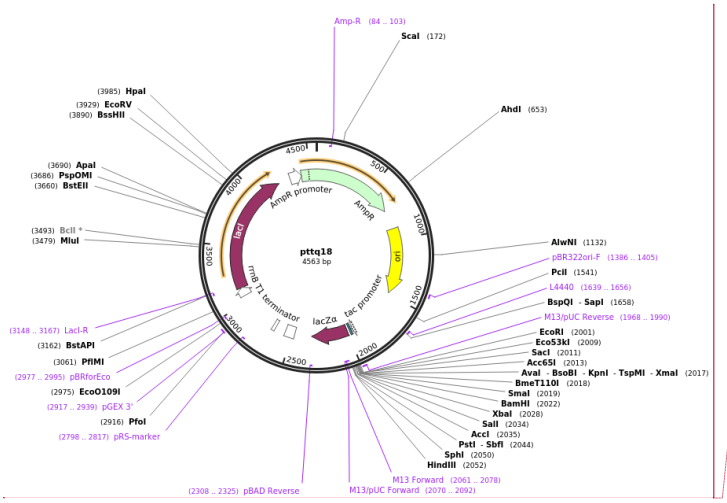

Figure B. 1. PTTQ18 vector map. Original map of PTTQ18 expression vector (Addgene plasmid #69122).

Commented [ANA1]: No veig PstI! EL vector modificat PTTQ18 el té?

BasC DNA sequence:

```
   1 ATG AAA GAA GTG AGC GGC ATT ACC GCA CTG ACG GTG GTT
  40 GTG GGT ACG GTG ATT GGC GCG GGT ATC TTT TTC AAA CCG
  79 ACC GCC GTT TAT GGT GCG GCC GGT GCG CCG GGT CTG GGT
 118 CTG CTG GCA TGG TTT GTG GCA GGC ATT ATC ACG ATC GCA
 157 GGC GGT CTG ACC GTT GCG GAA ATT GGT ACG ATC TAC CCG
 196 CAG ACC GGC GGT ATG ATG ATT TAT CTG GAA AAA GTG TAC
 235 GGC CGT TGG CTG GGT TTT CTG GTG GGC TGG GCG CAG ATG
 274 GTT ATC TAT TAC CCG GCC AAT ATT GCA GCG CTG GCG ATT
 313 ATC TTT GCC ACC CAG TTC GTG AAC CTG TTT GCC CTG AGT
 352 GAT AGC ACC ATC GTT CCG ACG GCA ATT CTG ACC TCT ATC
 391 TTC CTG ATG GGT GTT AAT TTT CTG GGC ACC AAA TAT AGT
 430 GGT TGG ATT CAG ACC CTG GCG ACG ATT CTG AAA CTG ATC
 469 CCG CTG GTT GTG ATT ATT GTG GCG GGT CTG CTG TAT CCG
 508 GGC GGT GGC GTT ATT CGT CTG GTG CCG TTT AGC GTT GAA
 547 ACG CAT CCG GTT CTG ACC TCT TTC GGC AGT GCA CTG ATC
 586 GCG ACG CTG TTT GCC TAT GAT GGT TGG ATT AAT GTG GGT
 625 ACC CTG GCA GGC GAA ATG AAA AAC CCG GGT AAA ATG CTG
 664 CCG AAA GTT ATT ATC GGT GGC CTG TCT ATC GTT ATG GCA
 703 GTG TAT CTG CTG ACC AAT ATT GCG TAC CTG TTT GTG CTG
 742 GAT AGC TCT CAG CTG GCC GGT ACC GAT ACC CCG GCC GCA
 781 CTG GTT GCC AGC CAC CTG TTC GAA GGC ATC GGT TCT AAA
 820 CTG GTG ACC ATT GGT ATC CTG ATT AGT GTT TTT GGT GGC
 859 ATT AAC GGC TAT ATT ATT AGC GGT CTG CGC GTG CCG TAT
 898 GCC CTG GCA ACC CAG AAA ATG CTG CCG TTC AGC GAT TGG
 937 TTT GCG CGC ATC AAC CCG AAA ACC AAT CTG CCG ATT AAC
 976 GGT GGC CTG GTG ATG CTG GGC ATC GCG ATT GTT ATG ATT
1015 CTG ACG GGC CAG TTC AAC CAG CTG ACC GAT CTG ATC GTT
1054 TTC GTG ATC TGG TTT TTC ATC ACC CTG ACG TTC ATC GCG
1093 GTG ATT ATC CTG CGT AAA ACC CAG CCG GAT ATT GAA CGT
1132 CCG TAT CGC GTG CCG TTT TAC CCG GTT ATT CCG CTG ATC
1171 GCA ATT ATC GGT GGC CTG TAT ATT ATC TTC AAT ACG CTG
1210 ATT GTG CAG CCG AAA AAC GCC TTT ATC GGC ATT CTG CTG
1249 ACC CTG ATC GGT ATT CCG ATC TAT TTC TAC TGC AAG AAA
1288 AAA TAT GGC AGC CCG GAA stop
```

BasC protein sequence:

```
  1 MKEVSGITAL TVVVGTVIGA GIFFKPTAVY GAAGAPGLGL LAWFVAGIIT
 51 IAGGLTVAEI GTIYPQTGGM MIYLEKVYGR WLGFLVGWAQ MVIYYPANIA
101 ALAIIFATQF VNLFALSDST IVPTAILTSI FLMGVNFLGT KYSGWIQTLA
151 TIIKLIPLVV IIVAGLLYPG GGVIRLVPFS VETHPVLTSF GSALIATLFA
201 YDGWINVGTL AGEMKNPGKM LPKVIIGGLS IVMAVYLLTN IAYLFVLDSS
251 QLAGTDTPAA LVASHLFEGI GSKLVTIGIL ISVFGGINGY IISGLRVPYA
301 LATQKMLPFS DWFARINPKT NLPINGGLVM LGIAIVMILT GQFNQLTDLI
351 VFVIWFFITL TFIAVIILRK TQPDIERPYR VPFYPVIPLI AIIGGLYIIF
401 NTLIVQPKNA FIGILLTLIG IPIYFYCKKK YGSPE
```

Figure B. 2. BasC DNA and protein sequences. Residue and codon of ALEX-SsmFRET Cys mutants (7, 120, 187, 427) are coloured in red, other Cys candidates tested in black bold and K154 in yellow.

Variant	Primer-template duplexes	Details
V4C	5'-aggaaacagcgatggaattcatgaaagaa**tgc**agcggcattaccgca-3' tcctttgtcgctaccttaagtactttctt**cac**tcgccgtaatggcgt aggaaacagcgatggaattcatgaaagaa**gtg**agcggcattaccgca 3'-tcctttgtcgctaccttaagtactttctt**acg**tcgccgtaatggcgt-5'	47 nt 79.07 °C
S5C	5'-aattcatgaaagaagtg**tgc**ggcattaccgcactg-3' ttaagtactttcttcact**cg**ccgtaatggcgtgac aattcatgaaagaagtg**agc**ggcattaccgcactg 3'-ttaagtactttcttcac**acg**ccgtaatggcgtgac-5'	35 nt 78.10 °C
I7C	5'-gaaagaagtgagcggc**tgt**accgcactgacggtg-3' ctttcttcactcgccg**taa**tggcgtgactgccac gaaagaagtgagcggc**att**accgcactgacggtg 3'-ctttcttcactcgccg**aca**tggcgtgactgccac-5'	34 nt 83.00 °C
T8C	5'-tcatgaaagaagtgagcggcatt**tgc**gcactgacggt-3' agtactttcttcactcgccgtaa**tgg**cgtgactgccacca tcatgaaagaagtgagcggcatt**acc**gcactgacggtggt 3'-agtactttcttcactcgccgtaa**acg**cgtgactgcca-5'	37 nt 78.91 °C
S119C	5'-gtttgccctgagtga**ttg**caccatcgttccg-3' caaacgggactcact**atc**gtggtagcaaggc gtttgccctgagtga**tag**caccatcgttccg 3'-caaacgggactcact**aac**gtggtagcaaggc-5'	31 nt 78.98 °C
T120C	5'-gccctgagtgatagc**tgc**atcgttccgacggc-3' cgggactcactatcg**tgg**tagcaaggctgccg gccctgagtgatagc**acc**atcgttccgacggc 3'-cgggactcactatcg**acg**tagcaaggctgccg-5'	32 nt 79.78 °C
I121C	5'-ccctgagtgatagcacc**tgc**gttccgacggcaattc-3' gggactcactatcgtgg**tag**caaggctgccgttaag ccctgagtgatagcacc**atc**gttccgacggcaattc 3'-gggactcactatcgtgg**acg**caaggctgccgttaag-5'	36 nt 79.97 °C
L187C	5'-agcgttgaaacgcatccggtt**tgc**acctctttcggcagtg-3' tcgcaactttgcgtaggccaa**gac**tggagaaagccgtcac agcgttgaaacgcatccggtt**ctg**acctctttcggcagtg 3'-tcgcaactttgcgtaggccaa**acg**tggagaaagccgtcac-5'	40 nt 78.65 °C
T188C	5'-acgcatccggttctg**tgc**tctttcggcagtgc-3' tgcgtaggccaagac**tgg**agaaagccgtcacg acgcatccggttctg**acc**tctttcggcagtgc 3'-tgcgtaggccaagac**acg**agaaagccgtcacg-5'	32 nt 78.50 °C
S189C	5'-tccggttctgacc**tgt**ttcggcagtgcac-3' aggccaagactgg**aga**aagccgtcacgtg tccggttctgacc**tct**ttcggcagtgcac 3'-aggccaagactgg**aca**aagccgtcacgtg-5'	29 nt 78.81 °C
F190C	5'-gcatccggttctgacctct**tgc**ggcagtgcac-3' cgtaggccaagactggaga**aag**ccgtcacgtg gcatccggttctgacctct**ttc**ggcagtgcac 3'-cgtaggccaagactggaga**acg**ccgtcacgtg-5'	32 nt 81.62 °C

C427A	5'-gtattccgatctatttctac**gcc**aagaaaaaatatggcagcccg-3' cataaggvtagataaagatg**acg**ttctttttttataccgtcgggc gtattccgatctatttctac**tgc**aaagaaaaaatatggcagcccg 3'-cataaggctagataaagatg**cgg**ttctttttttataccgtcgggc-5'	44 nt 78.80 ºC
K154A	5'-cctggcgacgattctg**gca**ctgatcccgctggtt-3' ggaccgctgctaagac**ttt**gactagggcgaccaa cctggcgacgattctg**aaa**ctgatcccgctggtt 3'-ggaccgctgctaagac**cgt**gactagggcgaccaa-5'	34 nt 87.10 ºC

Table B. 1. Mutagenesis primers used for Cys and LPI-related variants. Forward (FP) and reverse (RP) primers shown in primer-template duplexes. Codon involved in the mutation is highlighted in bold and its matches and mismatches are represented by green or red bars, respectivelly. T_m in ºC and primer length in nucleotides (nt) are shown in the details column.

Appendix B. 2. Nanobodies

All Nbs are cloned in pMESy4 vector (Figure A. 3, GenBank KF415192) that confers transformed *E.coli* strain WK6 with ampicillin resistance. Nb sequences (Table A. 3) carry a C-ter 6 × His-tag and CaptureSelect C-tag. All Nbs are cloned behind a pelB pre-signal that directs their expression to the periplasm.

The Nb reference number (Table A. 2), e.g. CA11050, names the plasmid construct encoding for each Nb; whereas Nb number, e.g. Nb50, is the last two digits of the reference number. Nb families are described as groups of Nbs with their variable regions with similarity criteria.

The occurrence (Table A. 2) gives an idea on how many times a family was found after ELISA and sequence analysis. In our case, in total, 88 clones were screened in ELISA. The 73 positive clones are the ones that were analysed.

Four different selection conditions are used to select the specific binders. Selection was done in PBS supplemented or not with 4 mM L-Ala on BasC PLs solid phase coated in $NaHCO_3$ buffer pH 8.2 or PBS.

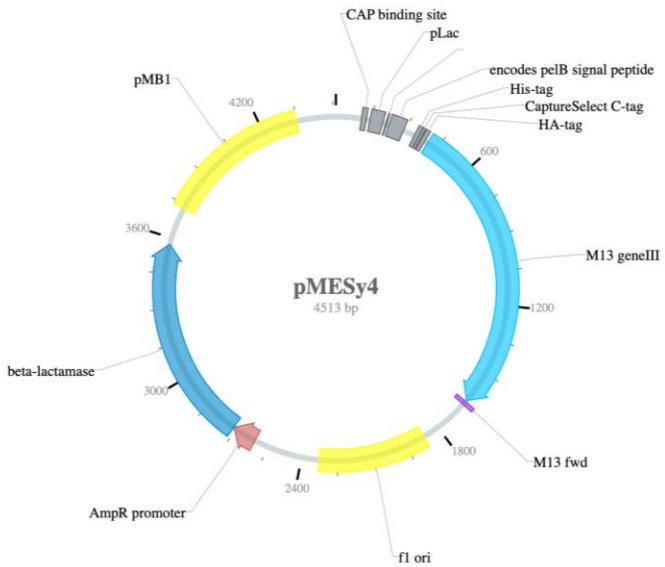

Figure B. 3. NovoPro complete pMESy4 vector map. Reference number V004763# (GenBank KF415192).

Reference no.	Family	Occ.	Selection conditions			
			Without L-Ala		With L-Ala	
			$NaHCO_3$	PBS	$NaHCO_3$	PBS
CA11050	1	11	X	X	X	X
CA11051						
CA11826						
CA11827						
CA11828						
CA11829						
CA11830						
CA11831						
CA11832						
CA11053	2	6	X	X	X	X
CA11845						
CA11846						
CA11052	3	7	X	X		X
CA11836						
CA11837						
CA11838						
CA11839						
CA11058	4	3	X	X		X
CA11844						
CA11060	5	3	X	X		X
CA11847						
CA11848						
CA11054	6	4		X	X	
CA11833						
CA11834						
CA11835						
CA11057	7	3		X	X	
CA11843						
CA11061	8	2		X		X
CA11062						
CA11056	9	3	X			
CA11841						
CA11842						
CA11059	10	3	X			
CA11063	11	2	X			
CA11066	12	1	X			
CA11073	13	1	X			
CA11074	14	1	X			
CA11078	15	1	X			
CA11055	16	3		X		
CA11840						
CA11065	17	1		X		
CA11069	18	1		X		
CA11072	19	1		X		
CA11077	20	1		X		
CA11064	21	2			X	
CA11068	22	1			X	
CA11070	23	1			X	
CA11071	24	1			X	
CA11075	25	1			X	
CA11076	26	1			X	
CA11067	27	1				X

Table B. 2. List of nanobodies. Nbs grouped in the 27 families, the 29 best candidates are highlighted in bold (from 50 to 78). *Occ. = occurrence.*

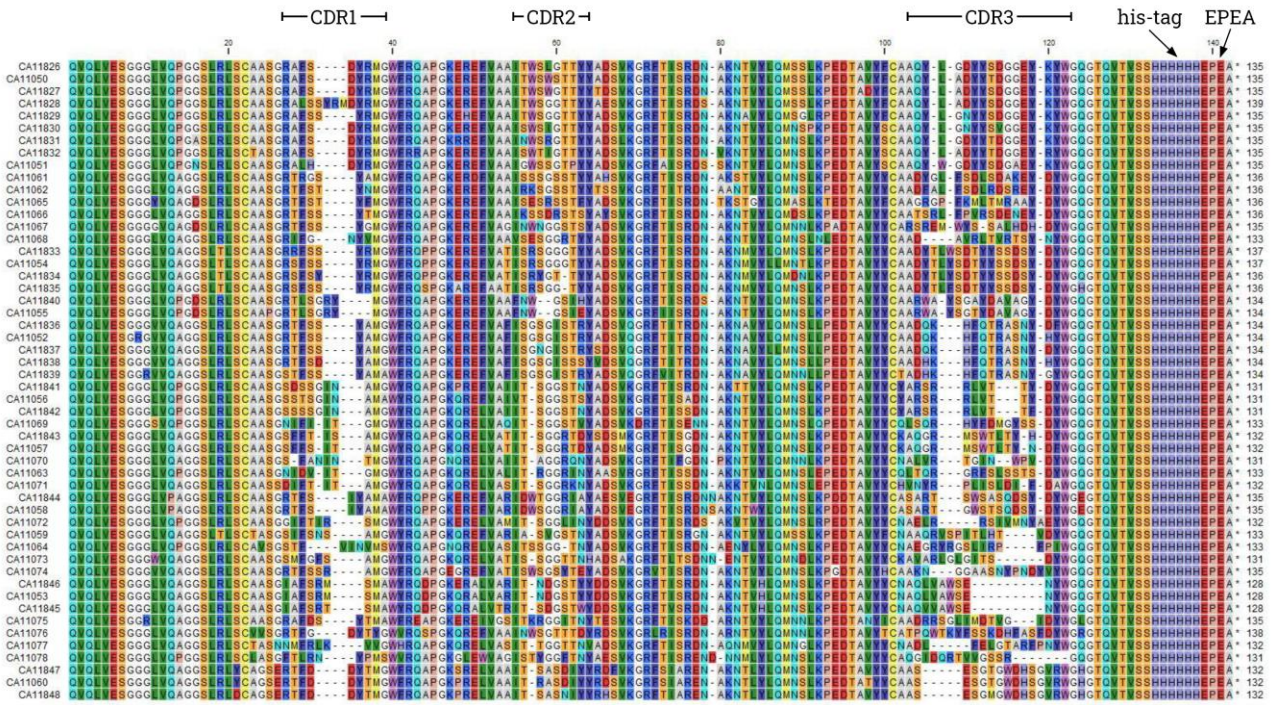

Figure B.4. Alignement of amino acid sequences of nanobodies. Alignement by similarity of all Nb AA sequences. CDRs 1, 2 and 3 are highlighted above; notice the difference of sequence in the CDR regions. All 29 selected Nbs have at C-ter 6 × His-tag and EPEA-tag.

Appendix B. 3. Membrane Scaffold Proteins

MSPs used in this thesis are MSP1D1 and MSP1E3D1, generated from Apolipoprotein A1. Both MSPs are cloned inserted into pET 28a plasmids with T7 promotor and terminus and resistance to Kanamycin. pMSP1D1 and pMSP1E3D1 were obtained from Prof. Dr. Rafa Leiro (CNIO, Madrid, Spain). Addgene plasmids #20061 (Denisov et al., 2007) and #20066 (Denisov et al., 2004) (Figures B. 5 and B. 6).

MSPs final constructs have a 7 × His-tag in frame at N-ter and TEV-cleavage site between the MSP and the purification tag. Full sequences are represented in Figures B. 7 and B. 8.

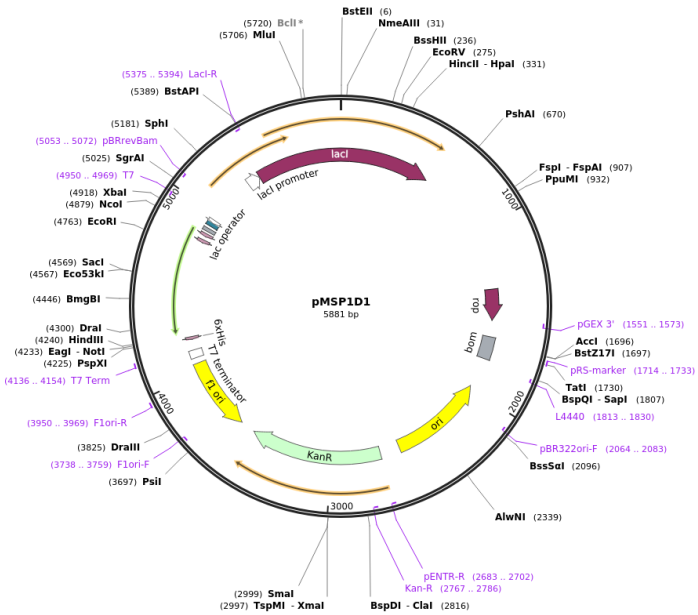

Figure B. 5. Addgene complete map for pMSP1D1. Reference number #20061.

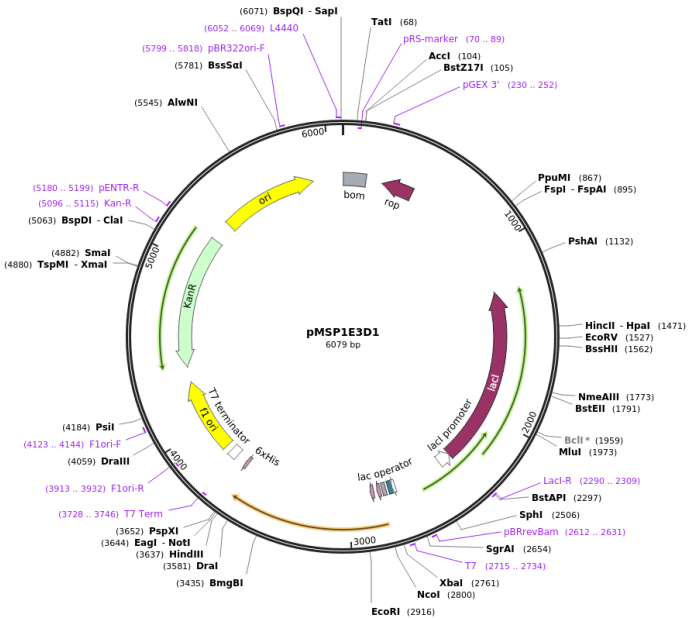

Figure B. 6. Addgene complete map for pMSP1E3D1. Reference number #20061.

MSP1D1:

DNA sequence:

```
  1 ATG GGT CAT CAT CAT CAT CAT CAT CAC GAT TAT GAT ATT CCT ACT ACT
 49 GAG AAT TTG TAT TTT CAG GGT TCT ACC TTC AGT AAA CTT CGC GAA CAA
 97 CTG GGC CCC GTG ACG CAG GAA TTC TGG GAC AAC CTG GAA AAA GAA ACC
145 GAG GGA CTG CGT CAG GAA ATG TCC AAA GAT TTA GAA GAG GTG AAG GCC
193 AAG GTT CAG CCA TAT CTC GAT GAC TTT CAG AAA AAA TGG CAG GAA GAG
241 ATG GAA TTA TAT CGT CAA AAG GTG GAA CCG CTG CGT GCG GAA CTG CAA
289 GAG GGG GCA CGC CAA AAA CTC CAT GAG CTC CAA GAG AAG CTC AGC CCA
337 TTA GGC GAA GAA ATG CGC GAT CGC GCC CGT GCA CAT GTT GAT GCA CTC
385 CGG ACT CAT TTG GCG CCG TAT TCG GAT GAA CTT CGC CAG CGT TTG GCC
433 GCA CGT CTC GAG GCG CTG AAA GAA AAC GGG GGT GCC CGC TTG GCT GAG
481 TAC CAC GCG AAA GCG ACA GAA CAC CTG AGC ACC TTG AGC GAA AAA GCG
529 AAA CCG GCG CTG GAA GAT CTA CGC CAG GGC TTA TTG CCT GTT CTT GAG
577 AGC TTT AAA GTC AGT TTT CTG TCA GCT CTG GAA GAA TAT ACT AAA AAG
625 CTG AAT ACC CAG TAA
```

Protein sequence:

```
  1 MGHHHHHHHD YDIPTTENLY FQGSTFSKLR EQLGPVTQEF WDNLEKETEG
 51 LRQEMSKDLE EVKAKVQPYL DDFQKKWQEE MELYRQKVEP LRAELQEGAR
101 QKLHELQEKL SPLGEEMRDR ARAHVDALRT HLAPYSDELR QRLAARLEAL
151 KENGGARLAE YHAKATEHLS TLSEKAKPAL EDLRQGLLPV LESFKVSFLS
201 ALEEYTKKLN TQ-
```

Figure B. 7. Membrane scaffold protein 1D1 DNA and protein sequences. 7x His-tag (red) and TEV-cleavage site ENLYFQ|S(G,A) (green) can be found on N-ter. TMs are alternatively highlighted in underline in protein sequence.

MSP1E3D1:

DNA sequence:

```
  1 ATG GGT CAT CAT CAT CAT CAT CAT CAC GAT TAT GAT ATT CCT ACT ACT
 49 GAG AAT TTG TAT TTT CAG GGT TCT ACC TTC AGT AAA CTT CGC GAA CAA
 97 CTG GGC CCC GTG ACG CAG GAA TTC TGG GAC AAC CTG GAA AAA GAA ACC
145 GAG GGA CTG CGT CAG GAA ATG TCC AAA GAT TTA GAA GAG GTG AAG GCC
193 AAG GTT CAG CCA TAT CTC GAT GAC TTT CAG AAA AAA TGG CAG GAA GAG
241 ATG GAA TTA TAT CGT CAA AAG GTG GAA CCG CTG CGT GCG GAA CTG CAA
289 GAG GGG GCA CGC CAA AAA CTC CAT GAG CTC CAA GAG AAG CTC AGC CCA
337 TTA GGC GAA GAA ATG CGC GAT CGC GCC CGT GCA CAT GTT GAT GCA CTC
385 CGG ACT CAT TTG GCG CCA TAT CTC GAT GAC TTT CAG AAA AAA TGG CAG
433 GAA GAG ATG GAA TTA TAT CGT CAA AAG GTG GAA CCG CTG CGT GCG GAA
481 CTG CAA GAG GGG GCA CGC CAA AAA CTC CAT GAG CTC CAA GAG AAG CTC
529 AGC CCA TTA GGC GAA GAA ATG CGC GAT CGC GCC CGT GCA CAT GTT GAT
577 GCA CTC CGG ACT CAT TTG GCG CCG TAT TCG GAT GAA CTT CGC CAG CGT
625 TTG GCC GCA CGT CTC GAG GCG CTG AAA GAA AAC GGG GGT GCC CGC TTG
673 GCT GAG TAC CAC GCG AAA GCG ACA GAA CAC CTG AGC ACC TTG AGC GAA
721 AAA GCG AAA CCG GCG CTG GAA GAT CTA CGC CAG GGC TTA TTG CCT GTT
769 CTT GAG AGC TTT AAA GTC AGT TTT CTG TCA GCT CTG GAA GAA TAT ACT
817 AAA AAG CTG AAT ACC CAG TAA
```

Protein sequence:

```
  1 MGHHHHHHHD YDIPTTENLY FQGSTFSKLR EQLGPVTQEF WDNLEKETEG
 51 LRQEMSKDLE EVKAKVQPYL DDFQKKWQEE MELYRQKVEP LRAELQEGAR
101 QKLHELQEKL SPLGEEMRDR ARAHVDALRT HLAPYLDDFQ KKWQEEMELY
151 RQKVEPLRAE LQEGARQKLH ELQEKLSPLG EEMRDRARAH VDALRTHLAP
201 YSDELRQRLA ARLEALKENG GARLAEYHAK ATEHLSTLSE KAKPALEDLR
251 QGLLPVLESF KVSFLSALEE YTKKLNTQ-
```

Figure B. 8. Membrane scaffold protein sequences. MSP1E3D1 DNA and AA sequences. 7x His-tag (red) and TEV-cleavage site ENLYFQ|S(G,A) (green) can be found on N-ter. TMs are alternatively highlighted in underline in protein sequence. E3 repetition (helixes 4, 5 and 6) is labelled in purple.

Appendix B. 4. Sequencing primers

Different standard and custom primers have been used in this thesis to verify sequences of BasC, Nb, Mb and MSP.

Standard primers		
Name	**Binding site**	**Sequence**
pQE (FP)	5′ of MCS in pQE vectors	5′-CCCGAAAAGTGCCACCTG-3′
pTI2-1-1 (FP)	LacZ promoter	5′-GGCAAATATTCTGAAATGAGC-3′
M13 (RP)	LacZ promoter	5′-CAGGAAACAGCTATGAC-3′
M13 (FP)	LacZ promoter	5′-TGTAAAACGACGGCCAGT-3′
M13pUC (FP)	LacZ promoter	5′-CCCAGTCACGACGTTGTAAAACG-3′
M13F-pUC (FP)	LacZ promoter	5′-GTTTTCCCAGTCACGAC-3′
M13 pUC (RP)	LacZ promoter	5′-AGCGGATAACAATTTCACACAGG-3′
T7 (FP)	T7 promoter	5′-TAATACGACTCACTATAGGG-3′
T7 term (RP)	T7 terminator	5′-GCTAGTTATTGCTCAGCGG-3′

Custom primers		
Name	**Binding site**	**Sequence**
BasC_2 (FP)	Middle of BasC sequence	5′-GTGGCGTTATTCGTCTG-3′
Nb_F (FP)	Before Nb promotor	5′-TTATGCTTCCGGCTCGTATG-3′
Nb_R (RP)	After Nb sequence	5′-CCACAGACAGCCCTCATAG-3′

Table B. 3. Sequencing primers. Standard and custom primers used when sequencing by Sanger in GATC and/or Macrogen services. FP and RP designates de forward and reverse primers, respectively.

Appendix C. Nanobodies SPR screening

	SPR							
	Apo				Holo			
	K_D (nM)	R_{max}	k_a (1/Gs)	k_d (1/ms)	K_D (nM)	R_{max}	k_a (1/Gs)	k_d (1/ms)
50	4.9	379	471	2.3	23.1	928	110	2,6
51	36.1	>200	619	22.4	111	518	264	29.5
52	34.3	17	1,210	41.7	undetectable			
53	26.4	341	231	6.1	57.8	762	126	7.3
54	72.0	51	79	5.7	67.8	53	65.8	4.5
55	101.1	70	1,790	1815	7.1	10.1	334	2.4
56	26.3	>200	128	2.2	14.0	835	171	2.4
57	216.6	80	230	49.9	238	71	203	48.4
58	28.1	289	99	2,8	43.1	717	167	7.2
59	248	80	606	606	157	36	226	35.5
60	18.6	260	162	3.0	86.3	2290	39.9	3.5
61	33.0	15	260	8.6	undetectable			
62	undetectable				undetectable			
63	undetectable				undetectable			
64	undetectable				undetectable			
65	11.5	241	173	2.0	26.5	621	78.1	2.1
66	115	50	1×10^{9}	1×10^{8}	16.7	9,1	258	4.3
67	97.0	220	476	46.5	89.3	194	937	83.7
68	undetectable				32.3	28.3	114	3.7
69	24.9	218	126	3.1	69.3	332	41.4	2.9
70	57.,0	120	151	8.0	224	191.9	33.5	7.5
71	135	1550	26	3.4	173	1,630	23.6	4.1
72	84.9	80	750	63,0	102	31.8	132	13.5
73	119	100	2,800	330	70.4	42.4	34,100	2,400
74	3.87	746	254	1.5	21.0	845.8	54,8	1.2
75	undetectable				undetectable			
76	undetectable				undetectable			
77	115	140	390	44.8	92.5	84.5	419,000	38,800
78	55.3	200	217	12.0	178	229.1	30.1	5.3

Table C. 1. Surface Plasmon Resonance screening. Complete table for each apo and holo (4 mM L-Ala) assay per each Nb Biacore against BasC solubilised in 0.17 % (w/v) DM. Equilibrium constant (K_D), maximum Biacore response (R_{max}), association rate (k_a) and dissociation rate (k_d) values are shown. Undetectable Nb responses are labelled. Results done with only two or four BasC concentrations are written in grey or black, respectively.

Appendix D. Political statements

Some scientists hesitate to acknowledge the fact that science is political. Scientific research does not take place in a vacuum; it can only happen with society's blessing. In this way, science is a political institution de facto, governed by society and beholden to its political will.

Adapted from "Science has always been inseparable from politics" by Ubadah Sabbagh, on April 25th, 2017 (Scientific American ©)

Appendix D. 1. Statement on feminism and cooperativeness

According to Watson, Photo 51 provided the vital clue to the double helix. However, all the main issues, such as the number of strands and above all the precise chemical organisation of the molecule, remained a mystery. What Watson and Crick needed was far more than the idea of a helix – they needed precise observations from X-ray crystallography. Those numbers were unwittingly provided by Franklin herself, including them in a brief informal report that was given to Max Perutz who, in 1953, passed the report to Bragg and, hence, to Watson and Crick. The report was not confidential, and there is no question that Watson and Crick acquired it dishonestly (Cob, 201 5).

Rosalind died four years before this distinct price was awarded to them and not to her and his PhD student **Raymond Gosling**, who actually took the Photo 51. We will never know if she could have been awarded also if she had still being alive. The fact is that Franklin not only did not receive the Nobel Prize for Physiology or Medicine in 1962 while Crick and Watson did; in addition and surprisingly, Wilkins also was awarded with the Nobel on 1962, which crystallographic data was, by far, poorer than data from Franklin. It is clear than Perutz, Bragg, Watson, Crick and Wilkins behaviour was driven by a sexist disdain driven also by their competitiveness. Moreover, they did never tell anyone at King's what they were doing, and they did not ask Franklin for permission to interpret her data.

Later on, Francis Crick stated in 2001 "*It is important to remember that all the really relevant experimental work on X-ray diffraction patterns of DNA fibres was done by Rosalind Franklin and Maurice Wilkins and their co-workers.*" Nevertheless, Franklin story lasted cruelly short, perhaps because of her repeated exposure to radiation; she developed ovarian cancer and died in 1958.

From this entire story, the current thesis wants to be a **clamour for feminism and cooperativeness** not only in science research, but also in the rest of our culture, where this two attributes are ignored, still now.

Left: **Raymond Gosling** (1926-2015) in his student years. *Right*: **Rosalind Franklin** (1920-1958) in 1950. Photos from King's College Archive.

Appendix D. 2. Statement on LGBTIQ+

When the time to talk about computational arrives this moment of the thesis, where I want to honour **Alan Mathison Turing**, considered the father of the modern informatics and one of the idols of the LGBTIQ+ collective without him being conscious.

During World War II Turing played a key-role in the cracking of the Enigma code, which Nazi Germany's army used to communicate between them. He created the **Bombe device** based in the Bomba device created by the Polish Cipher Bureau. Bombe was simply an electro-mechanical device made from wire rotors. Actually, this device and the involvement in finishing the World War II made him **Officer of the Most Excellent Order of the British Empire**.

Nevertheless, in 1952, Alan Turing was arrested on the charges of having a homosexual relationship. The public embarrassment combined with the negative side effects of the hormones injections and the general disappointment seems to have had a devastating effect on Alan Turing. Alan Turing was found dead on 8 June 1954 after eating an apple, which contained the poison cyanide. Actually, this cruel story served as inspiration to create Apple INC logo.

His ideas led to early versions of modern computing and helped win World War II. Yet he died as a criminal for his **homosexuality** (Copelant, 2004; Derndorfer, 2004).

Trying to revert this shocking story into freedom, this thesis supports the belief that a better world is possible, as a discrimination-free environment in science and research.

Left: **Alan Mathieu Turing** (1912-1954). *Right*: Apple Inc. logo used from 1977 to 1998 designed by Rob Janoff.

Appendix D. 3. Statement on anti-fascism

FRET is still named as **Förster Resonance Energy Transfer** in honour of **Theodor Förster** (1910-1974) a German physical chemist known for his big contribution to the understanding of FRET, mainly in 1946-48 (Förster, 1946, 2012, 1948) when he developed this theory which later proved to be transformative in the fields of chemistry, biochemistry, and biology.

Nevertheless, after Adolf Hitler became the Chancellor of Germany, just the same year Förster took the Ph.D. under Erwin Madelung at the University of Frankfurt in 1933, he joined the *Nationalsozialistische Deutsche Arbeiterpartei* – NSDAP (National Socialist German Workers Party) and the *Sturmabteilung* - SA (Stormtroopers), the paramilitary wing of the Nazi Party) (Masters, 2014).

Left: **NSDAP insignia**. *Centre:* **Iron Front** (German paramilitary organisation) **Three Arrows** (Social Democratic Political Symbol) on NSDAP insignia. *Right:* SA flag.

After his qualification, in 1940, he became a lecturer in Leipzig. Following his research and teaching activities in Leipzig, he became a professor at the State University of Poznan (1942).

For his narrow relationship with the Nazi Party and the III Reich, FRET will be referred from Fluorescence Resonance Energy Transfer in this entire thesis as an anti-fascist statement claiming for a democratic world.

Years after Adolf Hitler and Francisco Franco shake their hands; to make an apology to Nazism is punished in Germany. The country where the production, distribution and exhibition of Nazi ideology is fully forbidden. At the same time, in Spain these type of conducts are freely permitted and, yet, becoming popular even deep-seated in the government parliament.

Theodor Förster
at the age of 45 in 1955.

Appendix E. Crystallographic screening plates

Commercial screening plates used are MemGold™ (MD1-29-ECO) and MemGold 2™ (MD1-37-ECO) from Molecular Dimensions and Pi-PEG (CS-128) from Jena Bioscience. Custom non-commercial plates used are PAC13 and PAC22, both prepared at home at the *Plataforma Automàtica de Cristal·lografia* (PAC; Automated Chrystallographic Platform), service shared between IBMB-CSIC (Molecular Biology Institute of Barcelona from Consejo Superior de Investigaciones Científicas) and the IRB Barcelona (Institute for Research in Biomedicine of Barcelona). The detailed composition of each well for these plates is as follows.

Appendix E. 1. MemGold™ Eco Screen conditions (MD1-29-ECO)

MemGold™ is based on crystallization conditions data obtained from MPs in the Protein Data Bank. It contains 96 conditions covering a range of pH, PEGs and salt additives.

Well	Buffer	pH	Precipitant	Additive
A1	0.1 M SPG	4	25 % w/v PEG 1500	
A2	0.1 M SPG	5	25 % w/v PEG 1500	
A3	0.1 M SPG	6	25 % w/v PEG 1500	
A4	0.1 M SPG	7	25 % w/v PEG 1500	
A5	0.1 M SPG	8	25 % w/v PEG 1500	
A6	0.1 M SPG	9	25 % w/v PEG 1500	
A7	0.1 M Sodium acetate	5	20 % w/v PEG 6000	0.2 M Sodium chloride
A8	0.1 M Sodium acetate	5	20 % w/v PEG 6000	0.2 M Ammonium chloride
A9	0.1 M Sodium acetate	5	20 % w/v PEG 6000	0.2 M Lithium chloride
A10	0.1 M Sodium acetate	5	20 % w/v PEG 6000	0.2 M Magnesium chloride hexahydrate
A11	0.1 M Sodium acetate	5	20 % w/v PEG 6000	0.2 M Calcium chloride dihydrate
A12	0.1 M Sodium acetate	5	20 % w/v PEG 6000	0.01 M Zinc chloride
B1	0.1 M MIB	4	25 % w/v PEG 1500	
B2	0.1 M MIB	5	25 % w/v PEG 1500	
B3	0.1 M MIB	6	25 % w/v PEG 1500	
B4	0.1 M MIB	7	25 % w/v PEG 1500	
B5	0.1 M MIB	8	25 % w/v PEG 1500	
B6	0.1 M MIB	9	25 % w/v PEG 1500	
B7	0.1 M MES	6	20 % w/v PEG 6000	0.2 M Sodium chloride
B8	0.1 M MES	6	20 % w/v PEG 6000	0.2 M Ammonium chloride
B9	0.1 M MES	6	20 % w/v PEG 6000	0.2 M Lithium chloride
B10	0.1 M MES	6	20 % w/v PEG 6000	0.2 M Magnesium chloride hexahydrate
B11	0.1 M MES	6	20 % w/v PEG 6000	0.2 M Calcium chloride dihydrate
B12	0.1 M MES	6	20 % w/v PEG 6000	0.01 M Zinc chloride
C1	0.1 M PMTP	4	25 % w/v PEG 1500	
C2	0.1 M PMTP	5	25 % w/v PEG 1500	
C3	0.1 M PMTP	6	25 % w/v PEG 1500	
C4	0.1 M PMTP	7	25 % w/v PEG 1500	
C5	0.1 M PMTP	8	25 % w/v PEG 1500	
C6	0.1 M PMTP	9	25 % w/v PEG 1500	
C7	0.1 M HEPES	7	20 % w/v PEG 6000	0.2 M Sodium chloride
C8	0.1 M HEPES	7	20 % w/v PEG 6000	0.2 M Ammonium chloride
C9	0.1 M HEPES	7	20 % w/v PEG 6000	0.2 M Lithium chloride

C10	0.1 M HEPES	7	20 % w/v PEG 6000	0.2 M Magnesium chloride hexahydrate
C11	0.1 M HEPES	7	20 % w/v PEG 6000	0.2 M Calcium chloride hexahydrate
C12	0.1 M HEPES	7	20 % w/v PEG 6000	0.01 M Zinc chloride
D1	0.1 M MMT	4	25 % w/v PEG 1500	
D2	0.1 M MMT	5	25 % w/v PEG 1500	
D3	0.1 M MMT	6	25 % w/v PEG 1500	
D4	0.1 M MMT	7	25 % w/v PEG 1500	
D5	0.1 M MMT	8	25 % w/v PEG 1500	
D6	0.1 M MMT	9	25 % w/v PEG 1500	
D7	0.1 M Tris	8	20 % w/v PEG 6000	0.2 M Sodium chloride
D8	0.1 M Tris	8	20 % w/v PEG 6000	0.2 M Ammonium chloride
D9	0.1 M Tris	8	20 % w/v PEG 6000	0.2 M Lithium chloride
D10	0.1 M Tris	8	20 % w/v PEG 6000	0.2 M Magnesium chloride hexahydrate
D11	0.1 M Tris	8	20 % w/v PEG 6000	0.2 M Calcium chloride dihydrate
D12	0.1 M Tris	8	20 % w/v PEG 6000	0.002 M Zinc chloride
E1			20 % w/v PEG 3350	0.2 M Sodium fluoride
E2			20 % w/v PEG 3350	0.2 M Sodium bromide
E3			20 % w/v PEG 3350	0.2 M Sodium iodide
E4			20 % w/v PEG 3350	0.2 M Potassium thiocyanate
E5			20 % w/v PEG 3350	0.2 M Sodium nitrate
E6			20 % w/v PEG 3350	0.2 M Sodium formate
E7			20 % w/v PEG 3350	0.2 M Sodium acetate trihydrate
E8			20 % w/v PEG 3350	0.2 M Sodium sulfate
E9			20 % w/v PEG 3350	0.2 M Potassium sodium tartrate tetrahydrate
E10			20 % w/v PEG 3350	0.02 M Sodium/potassium phosphate
E11			20 % w/v PEG 3350	0.2 M Sodium citrate tribasic dihydrate
E12			20 % w/v PEG 3350	0.2 M Sodium malonate dibasic monohydrate
F1	0.1 M Bis-Tris propane	6.5	20 % w/v PEG 3350	0.2 M Sodium fluoride
F2	0.1 M Bis-Tris propane	6.5	20 % w/v PEG 3350	0.2 M Sodium bromide
F3	0.1 M Bis-Tris propane	6.5	20 % w/v PEG 3350	0.2 M Sodium iodide
F4	0.1 M Bis-Tris propane	6.5	20 % w/v PEG 3350	0.2 M Potassium thiocyanate
F5	0.1 M Bis-Tris propane	6.5	20 % w/v PEG 3350	0.2 M Sodium nitrate
F6	0.1 M Bis-Tris propane	6.5	20 % w/v PEG 3350	0.2 M Sodium formate
F7	0.1 M Bis-Tris propane	6.5	20 % w/v PEG 3350	0.2 M Sodium acetate trihydrate
F8	0.1 M Bis-Tris propane	6.5	20 % w/v PEG 3350	0.2 M Sodium sulfate
F9	0.1 M Bis-Tris propane	6.5	20 % w/v PEG 3350	0.2 M Potassium sodium tartrate tetrahydrate
F10	0.1 M Bis-Tris propane	6.5	20 % w/v PEG 3350	0.02 M Sodium/potassium phosphate
F11	0.1 M Bis-Tris propane	6.5	20 % w/v PEG 3350	0.2 M Sodium citrate tribasic dihydrate
F12	0.1 M Bis-Tris propane	6.5	20 % w/v PEG 3350	0.2 M Sodium malonate dibasic monohydrate
G1	0.1 M Bis-Tris propane	7.5	20 % w/v PEG 3350	0.2 M Sodium fluoride
G2	0.1 M Bis-Tris propane	7.5	20 % w/v PEG 3350	0.2 M Sodium bromide
G3	0.1 M Bis-Tris propane	7.5	20 % w/v PEG 3350	0.2 M Sodium iodide
G4	0.1 M Bis-Tris propane	7.5	20 % w/v PEG 3350	0.2 M Potassium thiocyanate
G5	0.1 M Bis-Tris propane	7.5	20 % w/v PEG 3350	0.2 M Sodium nitrate
G6	0.1 M Bis-Tris propane	7.5	20 % w/v PEG 3350	0.2 M Sodium formate
G7	0.1 M Bis-Tris propane	7.5	20 % w/v PEG 3350	0.2 M Sodium acetate trihydrate
G8	0.1 M Bis-Tris propane	7.5	20 % w/v PEG 3350	0.2 M Sodium sulfate
G9	0.1 M Bis-Tris propane	7.5	20 % w/v PEG 3350	0.2 M Potassium sodium tartrate tetrahydrate
G10	0.1 M Bis-Tris propane	7.5	20 % w/v PEG 3350	0.02 M Sodium/potassium phosphate
G11	0.1 M Bis-Tris propane	7.5	20 % w/v PEG 3350	0.2 M Sodium citrate tribasic dihydrate

G12	0.1 M Bis-Tris propane	7.5	20 % w/v PEG 3350	0.2 M Sodium malonate dibasic monohydrate
H1	0.1 M Bis-Tris propane	8.5	20 % w/v PEG 3350	0.2 M Sodium fluoride
H2	0.1 M Bis-Tris propane	8.5	20 % w/v PEG 3350	0.2 M Sodium bromide
H3	0.1 M Bis-Tris propane	8.5	20 % w/v PEG 3350	0.2 M Sodium iodide
H4	0.1 M Bis-Tris propane	8.5	20 % w/v PEG 3350	0.2 M Potassium thiocyanate
H5	0.1 M Bis-Tris propane	8.5	20 % w/v PEG 3350	0.2 M Sodium nitrate
H6	0.1 M Bis-Tris propane	8.5	20 % w/v PEG 3350	0.2 M Sodium formate
H7	0.1 M Bis-Tris propane	8.5	20 % w/v PEG 3350	0.2 M Sodium acetate trihydrate
H8	0.1 M Bis-Tris propane	8.5	20 % w/v PEG 3350	0.2 M Sodium sulfate
H9	0.1 M Bis-Tris propane	8.5	20 % w/v PEG 3350	0.2 M Potassium sodium tartrate tetrahydrate
H10	0.1 M Bis-Tris propane	8.5	20 % w/v PEG 3350	0.02 M Sodium/potassium phosphate
H11	0.1 M Bis-Tris propane	8.5	20 % w/v PEG 3350	0.2 M Sodium citrate tribasic dihydrate
H12	0.1 M Bis-Tris propane	8.5	20 % w/v PEG 3350	0.2 M Sodium malonate dibasic monohydrate

Appendix E. 2. MemGold2™ Eco Screen conditions (MD1-63-ECO)

MemGold2™ contains an absolute brand new set of 96 conditions and is particularly suited for Prokaryotic and Eukaryotic α-helical MPs.

Well	Buffer	pH	Precipitants	Additives
A1	0.1 M Sodium acetate	4,5	50 % w/v PEG 400	0.2 M Lithium sulfate
A2	0.1 M Sodium citrate	5,5	20 % w/v PEG 3000	
A3			20 % w/v PEG 3350	0.2 M Ammonium citrate dibasic
A4	0.1 M Sodium acetate	4,6	30 % v/v MPD	0.02 M Calcium chloride dihydrate
A5			20 % w/v PEG 3350	0.2 M Magnesium formate dihydrate
A6	0.1 M Phosphate/citrate	4,2	20 % w/v PEG 1000	0.2 M Lithium sulfate
A7	0.1 M CHES	9,5	20 % w/v PEG 8000	
A8			20 % w/v PEG 3350	0.2 M Ammonium formate
A9			20 % w/v PEG 3350	0.2 M Ammonium chloride
A10			20 % w/v PEG 3350	0.2 M Potassium formate
A11	0.1 M Tris	8,5	50 % v/v MPD	0.2 M Ammonium phosphate monobasic
A12			20 % w/v PEG 3350	0.2 M Potassium nitrate
B1	0.1 M Citrate	4		0.8 M Ammonium sulfate
B2			20 % w/v PEG 3350	0.2 M Sodium thiocyanate
B3	0.1 M BICINE	9	20 % w/v PEG 6000	
B4	0.1 M HEPES	7,5	10 % w/v PEG 8000 + 8 % v/v Ethylene glycol	
B5	0.1 M MES	6,5	40 % v/v MPD + 5 % w/v PEG 8000	
B6	0.1 M Phosphate/citrate	4,2	40 % v/v Ethanol + 5 % w/v PEG 1000	
B7	0.1 M Sodium acetate	4,6	8 % w/v PEG 4000	
B8	0.1 M Tris	7	10 % w/v PEG 8000	0.2 M Magnesium chloride hexahydrate
B9	0.1 M Citrate	5	20 % w/v PEG 6000	
B10	0.1 M MES	6,5	50 % v/v PEG 200	0.2 M Magnesium chloride hexahydrate

B11		6,5		1.6 M Sodium citrate tribasic dihydrate
B12			20 % w/v PEG 3350	0.2 M Potassium citrate tribasic monohydrate
C1	0.1 M Phosphate/citrate	4,2	20 % w/v PEG 8000	0.2 M Sodium chloride
C2	0.1 M Citrate	4	20 % w/v PEG 6000	1 M Lithium chloride
C3			20 % w/v PEG 3350	0.2 M Ammonium nitrate
C4	0.1 M HEPES	7	10 % w/v PEG 6000	
C5	0.1 M Sodium HEPES	7,5		0.8 M Sodium phosphate monobasic monohydrate + 0.8 M Potassium phosphate monobasic
C6	0.1 M Phosphate/citrate	4,2	40 % v/v PEG 300	
C7	0.1 M Sodium acetate	4,5	10 % w/v PEG 3000	0.2 M Zinc acetate dihydrate
C8	0.1 M Tris	8,5	20 % v/v Ethanol	
C9	0.1 M Sodium/potassium phosphate	6,2	25 % v/v 1.2-Propanediol + 10 %v/v Glycerol	
C10	0.1 M BICINE	9	20 % w/v PEG 6000	
C11	0.1 M Sodium acetate	4,6	20 % w/v PEG 6000	2 M Ammonium sulfate
C12			10 % w/v PEG 1000 + 10 % w/v PEG 8000	
D1			24 % w/v PEG 1500 + 20 % v/v Glycerol	
D2	0.1 M Sodium HEPES	7,5	30 % v/v PEG 400	0.2 M Magnesium chloride hexahydrate
D3	0.1 M Sodium/potassium phosphate	6,2	50 % v/v PEG 200	0.2 M Sodium chloride
D4	0.1 M Sodium acetate	4,5	30 % w/v PEG 8000	0.2 M Lithium sulfate
D5	0.1 M HEPES	7,5	70 % v/v MPD	
D6	0.1 M Tris	8,5	20 % w/v PEG 8000	0.2 M Magnesium chloride hexahydrate
D7	0.1 M Tris	8,5	40 % v/v PEG 400	0.2 M Lithium sulfate
D8	0.1 M Tris	8	40 % v/v MPD	
D9			25.5 % w/v PEG 4000 + 15 % v/v Glycerol	0.17 M Ammonium sulfate
D10	0.1 M MES	6,5	40 % v/v PEG 300	0.2 M Calcium acetate hydrate
D11	0.07 M Sodium acetate	4,6	14 % v/v 2-Propanol + 30 % v/v Glycerol	0.14 M Calcium chloride dihydrate
D12			16 % w/v PEG 8000 + 20 % v/v Glycerol	0.04 M Potassium phosphate monobasic
E1	0.1 M MES	6,5		1 M Sodium citrate tribasic dihydrate
E2	0.1 M MES	6,5		2 M Ammonium sulfate + 0.2 M Sodium chloride
E3	0.1 M HEPES	7,5	10 % v/v 2-Propanol	0.2 M Sodium chloride
E4	0.1 M Tris	8,5		1.26 M Ammonium sulfate
E5	0.1 M CAPS	11	40 % v/v MPD	
E6	0.1 M Imidazole	8	20 % w/v PEG 3000	0.2 M Zinc acetate dihydrate
E7	0.1 M MES	6,5	10 % v/v 2-Propanol	0.2 M Zinc acetate dihydrate
E8	0.1 M Sodium acetate	4,5		1 M Ammonium phosphate dibasic
E9	0.1 M MES	6,5		1.6 M Magnesium sulfate heptahydrate
E10	0.1 M BICINE	9	10 % w/v PEG 6000	

E11	0.08 M MES	6,5	14.4 % w/v PEG 8000 + 20 % v/v Glycerol	0.16 M Calcium acetate hydrate
E12	0.1 M Imidazole	8	10 % w/v PEG 8000	
F1	0.1 M MES	6,5	30 % v/v Jeffamine® M-600	0.05 M Cesium chloride
F2	0.1 M Citrate	5		3.2 M Ammonium sulfate
F3	0.1 M Tris	8	20 % v/v MPD	
F4	0.1 M HEPES	7,5	20 % v/v Jeffamine® M-600	
F5	0.1 M Tris	8,5	50 % v/v Ethylene glycol	0.2 M Magnesium chloride hexahydrate
F6	0.1 M BICINE	9	10 % v/v MPD	
F7		7		0.8 M Succinic acid
F8		7		2.1 M DL-Malic acid
F9		7		2.4 M Sodium malonate dibasic monohydrate
F10	0.1 M HEPES	7	0.5 % v/v Jeffamine® ED-2003	1.1 M Sodium malonate dibasic monohydrate
F11	0.1 M HEPES	7	1 % w/v PEG 2000 MME	1 M Succinic acid
F12	0.1 M HEPES	7	30 % v/v Jeffamine® M-600	
G1	0.1 M HEPES	7	30 % v/v Jeffamine® ED-2003	
G2	0.1 M HEPES	7,5	22 % w/v Poly(acrylic acid sodium salt) 5100	0.02 M Magnesium chloride hexahydrate
G3	0.1 M Tris	8,5	20 % w/v Polyvinylpyrolidone	0.01 M Cobalt(II) chloride hexahydrate
G4	0.1 M Tris	8,5	20 % w/v PEG 2000 MME	0.2 M TMAO
G5	0.1 M HEPES	7,5	12 % w/v PEG 3350	0.005 M Cobalt(II) chloride hexahydrate 0.005 M Cadmium chloride hemi(pentahydrate) 0.005 M Magnesium chloride hexahydrate 0.005 M Nickel(II) chloride hexahydrate
G6			20 % w/v PEG 3350	0.2 M Sodium malonate dibasic monohydrate
G7			15 % w/v PEG 3350	0.1 M Succinic acid
G8			20 % w/v PEG 3350	0.15 M DL-Malic acid
G9			30 % w/v PEG 2000 MME	0.1 M Potassium thiocyanate
G10			30 % w/v PEG 2000 MME	0.15 M Potassium bromide
G11	0.1 M Bis-Tris	5,5		2 M Ammonium sulfate
G12	0.1 M Bis-Tris	5,5		3 M Sodium chloride
H1	0.1 M Bis-Tris	5,5		0.3 M Magnesium formate dihydrate
H2	0.1 M Bis-Tris	5,5	1 % w/v PEG 3350	1 M Ammonium sulfate
H3	0.1 M Bis-Tris	5,5	25 % w/v PEG 3350	
H4	0.1 M Bis-Tris	5,5	45 % v/v MPD	0.2 M Calcium chloride dihydrate
H5	0.1 M Bis-Tris	5,5	45 % v/v MPD	0.2 M Ammonium acetate
H6	0.1 M Bis-Tris	5,5	17 % w/v PEG 10.000	0.1 M Ammonium acetate
H7	0.1 M Bis-Tris	5,5	25 % w/v PEG 3350	0.2 M Ammonium sulfate
H8	0.1 M Bis-Tris	5,5	25 % w/v PEG 3350	0.2 M Sodium chloride
H9	0.1 M Bis-Tris	5,5	25 % w/v PEG 3350	0.2 M Lithium sulfate
H10	0.1 M Bis-Tris	5,5	25 % w/v PEG 3350	0.2 M Ammonium acetate
H11	0.1 M Bis-Tris	5,5	25 % w/v PEG 3350	0.2 M $MgCl_2$ hexahydrate
H12	0.1 M HEPES	7,5	45 % v/v MPD	0.2 M Ammonium acetate

Appendix E. 3. Pi-PEG screening plate

Pi-PEG screening plate was developed for efficient crystallisation screening of integral MPs. Its formulation was generated in order to create novel combinations of precipitants, buffers and additives across a standard 96-condition plate layout. Thus, the diversity amongst the crystallization conditions is ideal for initial screening. It includes various PEG mixtures, additives and buffers covering a pH range from 4,0 – 9,5 and hence is suitable for integral membrane proteins as well as for soluble proteins.

Well	Buffer	pH	Precipitants	Additives
A1	50 mM Sodium acetate	4.8	22.5 % v/v PEG 200	
A2	50 mM Sodium acetate	5.2	20.00 % v/v PEG 300	
A3	50 mM MES	5.6	20.00 % v/v PEG MME 350	
A4	50 mM MES	6.0	20.00 % v/v PEG 400	
A5	50 mM ADA	6.4	20.00 % v/v PEG MME 550	
A6	50 mM ADA	6.8	20.00 % v/v PEG 600	
A7	50 mM HEPES	7.1	17.5 % w/v PEG 1000	
A8	50 mM HEPES	7.3	17.5 % w/v PEG 1500	
A9	50 mM TRIS	7.6	15.00 % w/v PEG 2000	
A10	50 mM TRIS	8.0	15.00 % w/v PEG MME 2000	
A11	50 mM BICINE	8.4	15.00 % w/v PEG 3000	
A12	50 mM BICINE	8.8	15.00 % w/v PEG 4000	
B1	50 mM Sodium acetate	4.8	15.00 % w/v PEG 1500	3.6 % w/v PEG 4000
B2	50 mM Sodium acetate	5.2	12.9 % w/v PEG 2000	6.4 % v/v PEG 200
B3	50 mM MES	5.6	12.9 % w/v PEG MME 2000	5.7 % v/v PEG 300
B4	50 mM MES	6.0	12.9 % w/v PEG 3000	5.7 % v/v PEG MME 350
B5	50 mM ADA	6.4	12.9 % w/v PEG 4000	5.7 % v/v PEG 400
B6	50 mM ADA	6.8	19.3 % v/v PEG 200	5.7 % v/v PEG MME 550
B7	50 mM HEPES	7.1	17.1 % v/v PEG 300	5.7 % v/v PEG 600
B8	50 mM HEPES	7.3	17.1 % v/v PEG MME 350	5.00 % w/v PEG 1000
B9	50 mM TRIS	7.6	17.1 % v/v PEG 400	5.00 % w/v PEG 1500
B10	50 mM TRIS	8.0	17.1 % v/v PEG MME 550	4.3 % w/v PEG 2000
B11	50 mM BICINE	8.4	17.1 % v/v PEG 600	4.3 % w/v PEG MME 2000
B12	50 mM BICINE	8.8	15.00 % w/v PEG 1000	4.3 % w/v PEG 3000
C1	50 mM Sodium acetate	4.8	14.3 % v/v PEG MME 350	11.4 % v/v PEG 300
C2	50 mM Sodium acetate	5.2	14.3 % v/v PEG 400	11.4 % v/v PEG MME 350
C3	50 mM MES	5.6	14.3 % v/v PEG MME 550	11.4 % v/v PEG 400
C4	50 mM MES	6.0	14.3 % v/v PEG 600	11.4 % v/v PEG MME 550
C5	50 mM ADA	6.4	12.5 % w/v PEG 1000	11.4 % v/v PEG 600
C6	50 mM ADA	6.8	12.5 % w/v PEG 1500	10.00 % w/v PEG 1000
C7	50 mM HEPES	7.1	10.7 % w/v PEG 2000	10.00 % w/v PEG 1500
C8	50 mM HEPES	7.3	10.7 % w/v PEG MME 2000	8.6 % w/v PEG 2000
C9	50 mM TRIS	7.6	10.7 % w/v PEG 3000	8.6 % w/v PEG MME 2000
C10	50 mM TRIS	8.0	10.7 % w/v PEG 4000	8.6 % w/v PEG 3000
C11	50 mM BICINE	8.4	16.1 % v/v PEG 200	7.1 % w/v PEG 4000
C12	50 mM BICINE	8.8	14.3 % v/v PEG 300	12.9 % v/v PEG 200
D1	50 mM Sodium acetate	4.8	8.6 % w/v PEG MME 2000	17.1 % v/v PEG 400
D2	50 mM Sodium acetate	5.2	8.6 % w/v PEG 3000	17.1 % v/v PEG MME 550
D3	50 mM MES	5.6	8.6 % w/v PEG 4000	17.1 % v/v PEG 600
D4	50 mM MES	6.0	12.9 % v/v PEG 200	15.00 % w/v PEG 1000
D5	50 mM ADA	6.4	11.4 % v/v PEG 300	15.00 % w/v PEG 1500
D6	50 mM ADA	6.8	11.4 % v/v PEG MME 350	12.9 % w/v PEG 2000

D7	50 mM HEPES	7.1	11.4 % v/v PEG 400	12.9 % w/v PEG MME 2000
D8	50 mM HEPES	7.3	11.4 % v/v PEG MME 550	12.9 % w/v PEG 3000
D9	50 mM TRIS	7.6	11.4 % v/v PEG 600	10.7 % w/v PEG 4000
D10	50 mM TRIS	8.0	10.00 % w/v PEG 1000	19.3 % v/v PEG 200
D11	50 mM BICINE	8.4	10.00 % w/v PEG 1500	17.1 % v/v PEG 300
D12	50 mM BICINE	8.8	8.6 % w/v PEG 2000	17.1 % v/v PEG MME 350
E1	50 mM Sodium acetate	4.8	8.6 % v/v PEG MME 550	22.9 % v/v PEG 600
E2	50 mM Sodium acetate	5.2	8.6 % v/v PEG 600	20.00 % w/v PEG 1000
E3	50 mM MES	5.6	7.5 % w/v PEG 1000	20.00 % w/v PEG 1500
E4	50 mM MES	6.0	7.5 % w/v PEG 1500	17.1 % w/v PEG 2000
E5	50 mM ADA	6.4	6.4 % w/v PEG 2000	17.1 % w/v PEG MME 2000
E6	50 mM ADA	6.8	6.4 % w/v PEG MME 2000	17.1 % w/v PEG 3000
E7	50 mM HEPES	7.1	6.4 % w/v PEG 3000	14.3 % w/v PEG 4000
E8	50 mM HEPES	7.3	6.4 % w/v PEG 4000	25.7 % v/v PEG 200
E9	50 mM TRIS	7.6	9.6 % v/v PEG 200	22.9 % v/v PEG 300
E10	50 mM TRIS	8.0	8.6 % v/v PEG 300	22.9 % v/v PEG MME 350
E11	50 mM BICINE	8.4	8.6 % v/v PEG MME 350	22.9 % v/v PEG 400
E12	50 mM BICINE	8.8	8.6 % v/v PEG 400	22.9 % v/v PEG MME 550
F1	50 mM Sodium acetate	4.8	4.3 % w/v PEG 4000	25.00 % w/v PEG 1500
F2	50 mM Sodium acetate	5.2	6.4 % v/v PEG 200	21.4 % w/v PEG 2000
F3	50 mM MES	5.6	5.7 % v/v PEG 300	21.4 % w/v PEG MME 2000
F4	50 mM MES	6.0	5.7 % v/v PEG MME 350	21.4 % w/v PEG 3000
F5	50 mM ADA	6.4	5.7 % v/v PEG 400	17.9 % w/v PEG 4000
F6	50 mM ADA	6.8	5.7 % v/v PEG MME 550	32.1 % v/v PEG 200
F7	50 mM HEPES	7.1	5.7 % v/v PEG 600	28.6 % v/v PEG 300
F8	50 mM HEPES	7.3	5.00 % w/v PEG 1000	28.6 % v/v PEG MME 350
F9	50 mM TRIS	7.6	5.00 % w/v PEG 1500	28.6 % v/v PEG 400
F10	50 mM TRIS	8.0	4.3 % w/v PEG 2000	28.6 % v/v PEG MME 550
F11	50 mM BICINE	8.4	4.3 % w/v PEG MME 2000	28.6 % v/v PEG 600
F12	50 mM BICINE	8.8	4.3 % w/v PEG 3000	25.00 % w/v PEG 1000
G1	50 mM Sodium acetate	4.8	2.5 % w/v PEG 1000	25.7 % w/v PEG MME 2000
G2	50 mM Sodium acetate	5.2	2.5 % w/v PEG 1500	25.7 % w/v PEG 3000
G3	50 mM MES	5.6	2.1 % w/v PEG 2000	21.4 % w/v PEG 4000
G4	50 mM MES	6.0	2.1 % w/v PEG MME 2000	38.6 % v/v PEG 200
G5	50 mM ADA	6.4	2.1 % w/v PEG 3000	34.3 % v/v PEG 300
G6	50 mM ADA	6.8	2.1 % w/v PEG 4000	34.3 % v/v PEG MME 350
G7	50 mM HEPES	7.1	3.2 % v/v PEG 200	34.3 % v/v PEG 400
G8	50 mM HEPES	7.3	2.9 % v/v PEG 300	34.3 % v/v PEG MME 550
G9	50 mM TRIS	7.6	2.9 % v/v PEG MME 350	34.3 % v/v PEG 600
G10	50 mM TRIS	8.0	2.9 % v/v PEG 400	30.00 % w/v PEG 1000
G11	50 mM BICINE	8.4	2.9 % v/v PEG MME 550	30.00 % w/v PEG 1500
G12	50 mM BICINE	8.8	2.9 % v/v PEG 600	25.7 % w/v PEG 2000
H1	50 mM Sodium acetate	4.8		25.00 % w/v PEG 4000
H2	50 mM Sodium acetate	5.2		45.00 % v/v PEG 200
H3	50 mM MES	5.6		40.00 % v/v PEG 300
H4	50 mM MES	6.0		40.00 % v/v PEG MME 350
H5	50 mM ADA	6.4		40.00 % v/v PEG 400
H6	50 mM ADA	6.8		40.00 % v/v PEG MME 550
H7	50 mM HEPES	7.1		40.00 % v/v PEG 600
H8	50 mM HEPES	7.3		35.00 % w/v PEG 1000
H9	50 mM TRIS	7.6		35.00 % w/v PEG 1500
H10	50 mM TRIS	8.0		30.00 % w/v PEG 2000
H11	50 mM BICINE	8.4		30.00 % w/v PEG MME 2000
H12	50 mM BICINE	8.8		30.00 % w/v PEG 3000

Appendix E. 4. PAC13 screening plate

PAC13 screening is a custom plate designed by the PAC (IBMB-IRB) that mimics the commercial plate Memgold™.

Well	Buffer	pH	Precipitant	Additive
A1	0.08 M Tri-sodium citrate	5.2	2.2 M Ammonium Sulfate	
A2	0.01 M TRIS	8.0	1.2M Tri-sodium citrate	
A3	15 mM Tricine	8.5	24%w/v PEG 4000	
A4	15 mM Sodium phosphate	7.0	3.9%w/v PEG 4000	0.36 M Sodium Chloride 0.1 % w/v Sodium Azide
A5	0.01 M TRIS	8.0	27.5%w/v PEG 4000	0.3 M Sodium Chloride
A6	22.5 mM MES	6.6	6.6%w/v PEG 6000	
A7	0.1 M HEPES	7.5	12%w/v PEG 4000	0.1 M Ammonium Sulfate
A8	0.02 M MES	6.5	7.7%w/v PEG 1500	0.02 M Calcium chloride 0.01 M Magnesium Sulfate
A9	0.05 M HEPES	7.5	2.5M Ammonium Sulfate	
A10	66.5 mM HEPES	7.5	1.1M Tri-sodium citrate	
A11	0.15 M Potassium phosphate	6.5	3.3M Ammonium Sulfate	
A12	0.1 M Tri-sodium citrate	5.8	14%w/v PEG MME 5000	0.1 M Magnesium Acetate tetrahydrate
B1	0.02 M Tri-sodium citrate	5.6	11%w/v PEG 3350	0.1 M Sodium Chloride
B2	0.02 M Tri-sodium citrate	5.6	5.5%w/v PEG 3350	0.1 M Sodium Chloride
B3	0.1 M TRIS	8.2	32%v/v PEG 400	0.05 M Calcium chloride 0.05 M Barium chloride
B4	0.1 M Sodium phosphate	6.2	16%w/v PEG 4000	0.05 M Sodium Chloride
B5	0.1 M CHES	10.0	14%w/v PEG 4000	0.2 M Ammonium Sulfate
B6	25 mM HEPES	7.5	13%w/v PEG 4000	0.2 M Sodium Chloride
B7	0.1 M HEPES	7.5	11%w/v PEG 3350	
B8	0.02 M KMES	6.7	6.6%w/v PEG 4000	0.1 M Sodium Chloride
B9	0.02 M TRIS	7.0	20%w/v PEG 4000	0.1 M Potassium Chloride
B10	0.1 M Cacodilate	6.7	6.6%w/v PEG 3350	0.05 M Magnesium Chloride 0.1 % w/v Sodium Azide
B11	0.02 M TRIS	7.4	12.5%w/v PEG MME 2000	
B12	0.1 M TRIS	8.0	5.5%w/v PEG 4000	
C1	0.02 M TRIS	7.0	7.7%w/v PEG 4000	0.1 M Sodium Chloride
C2	0.1 M TRIS	7.5	22%v/v PEG 400	0.1 M Magnesium Chloride
C3	0.04 M TRIS	8.0	27%v/v PEG MME 350	0.04 M Sodium Chloride
C4	0.1 M Tri-sodium citrate	6.0	22%v/v PEG 400	0.05 M Sodium Chloride 0.02 M Magnesium Chloride
C5	0.1 M Sodium acetate	5.5	8.8%w/v PEG MME 2000	
C6	0.4 M Ammonium Acetate	8.0	13%w/v PEG MME 2000	
C7	0.02 M Bis-tris	7.0	15%w/v PEG 2000	
C8	0.02 M TRIS	7.5	11%w/v PEG 1500	0.1 M Sodium Chloride 0.1 M Magnesium Chloride
C9	0.1 M HEPES	8.0	11%w/v PEG 1500	0.1 M Sodium Chloride 0.1 M Magnesium Chloride
C10	0.1 M HEPES	7.0	22%w/v PEG 3000	0.2 M Sodium acetate 0.2 M Potassium Chloride
C11	0.01 M HEPES	7.0	33%v/v Jeffamine-M600	0.02 M Nickel Sulfate
C12	0.1 M TRIS	8.0	13%w/v PEG 6000	0.15 M Sodium Chloride
D1	0.1 M HEPES	7.5	53%v/v PEG 400	0.2 M Calcium chloride
D2	0.05 M Sodium acetate	5.0	28%v/v PEG 400	0.05 M Magnesium Acetate tetrahydrate

D3	0.05 M HEPES	7.5	22%w/v PEG 4000	
D4	0.1 M TRIS	8.0	44%v/v PEG 400	0.2 M Calcium chloride
D5	0.05 M Sodium acetate	5.4	24%v/v PEG 400	0.05 M Magnesium Acetate tetrahydrate
D6	0.1 M MES	6.5	26%v/v PEG MME 350	0.2 M Calcium chloride
D7	0.1 M TRIS	8.5	39%v/v PEG 400	0.1 M Potassium Chloride
D8	0.1 M Glycine	9.0	22%v/v PEG 400	0.05 M Magnesium Chloride
D9	0.1 M Glycine	3.8	28%w/v Triethylene Glycol	0.1 M Ammonium Sulfate
D10	0.1 M HEPES	7.2	18%w/v PEG 3350	0.15 M Sodium Formate
D11	0.2 M Sodium acetate	6.8	8.8%w/v PEG 6000	
D12	0.1 M MES	6.5	18%w/v PEG 6000	0.2 M Potassium Chloride
E1	0.1 M TRIS	8.0	35%v/v PEG 400	0.22 M Tri-sodium citrate
E2	0.1 M Sodium acetata	4.5	17%v/v PEG 400	
E3	0.02 M TRIS	8.5	1.8%w/v PEG 8000	
E4	0.02 M TRIS	7.5	22.5%v/v PEG MME 500	
E5	0.02 M Glycine	10.0	33%w/v PEG 1000	0.05 M Sodium Chloride
E6	0.1 M TRIS	8.5	25%w/v PEG 4000	0.2 M Magnesium Chloride
E7	0.1 M Cacodilate	6.5	31%w/v PEG 2000	0.2 M Magnesium Chloride
E8	0.64 M Sodium acetate	4.6	18%w/v PEG 3350	
E9	0.1 M TRIS	8.0	33%v/v PEG 400	0.1 M Sodium Chloride 0.1 M Cadmium Chloride
E10	0.1 M Bicine	8.9	31%w/v PEG 2000	
E11	0.05 M TRIS	8.5	35%v/v PEG 400	0.05 M Sodium Sulfate 0.05 M Lithium sulfate monohydrate
E12	0.05 M Glycine	9.5	33%v/v PEG 300	0.1 M Sodium Chloride
F1	0.1 M TRIS	8.0	23%w/v PEG 2000	0.3 M Magnesium Nitrate
F2	0.02 M TRIS	7.5	20%v/v PEG 300	0.12 M Lithium sulfate monohydrate
F3	0.12 M TRIS	9.4	20%v/v PEG 400	0.1 M Sodium Chloride
F4	0.1 M HEPES	7.0	22%v/v PEG MME 500	0.2 M Sodium Chloride
F5	0.1 M TRIS	8.0	21%v/v PEG 400	0.1 M Sodium Chloride 235 mM Sodium acetate
F6	0.08 M Sodium phosphate	6.2	18%w/v PEG 2000	0.02 M Tri-sodium citrate
F7	0.03 M Phosphate Citrate	6.5	7.7%w/v PEG 4000	0.02 M Potassium Nitrate
F8	0.1 M TRIS	8.5	30%w/v PEG MME 2000	0.1 M Sodium Chloride 5 mM Magnesium Chloride
F9	0.1 M HEPES	7.0	33%v/v PEG 400	0.2 M Calcium chloride
F10	0.1 M TRIS	6.5	13%w/v PEG MME 2000	0.1 M Calcium chloride
F11	0.02 M Sodium acetate	4.0	33%v/v PEG 200	0.2 M Ammonium Sulfate 0.02 M Sodium Chloride
F12	0.05 M Tri-sodium citrate	4.5	22%v/v PEG 400	0.07 M Sodium Chloride
G1	0.1 M Sodium acetate	4.6	28%v/v PEG MME 500	0.2 M Ammonium Sulfate
G2	0.05 M Glycine	9.0	55%v/v PEG 400	
G3	0.1 M TRIS	8.5	33%v/v PEG 400	0.1 M Magnesium Chloride 0.1 M Sodium Chloride
G4	0.05 M Citric Acid		19%w/v PEG 1000	0.1 M Lithium sulfate monohydrate 0.1 M Di-sodium phosphate
G5	25 mM Tri-sodium citrate	4.0	33%v/v PEG 400	0.2 M Magnesium Chloride 0.1 M Potassium Chloride
G6	0.05 M MES	6.1	11%w/v PEG 8000	0.05 M Zinc acetate
G7	0.1 M TRIS	8.0	22%w/v PEG 2000	0.3 M Magnesium Nitrate
G8	0.1 M MES	6.5	33%v/v PEG 400	0.1 M Sodium Chloride

				4 % v/v Ethylene Glycol
G9	0.1 M Tri-sodium citrate	5.5	26%v/v PEG 400	0.05 M Sodium Chloride
G10	0.1 M Glycine	9.3	30%v/v PEG 400	0.1 M Lithium sulfate monohydrate
G11	25 mM potassium phosphate	5.1	13%w/v PEG 8000	
G12	0.05 M HEPES	8.0	28%v/v PEG 600	1 mM Zinc sulfate heptahydrate
H1	0.1 M Sodium phosphate	7.0	33%v/v PEG 300	0.1 M Sodium Chloride
H2	0.05 M Bicine	9.0	33%v/v PEG 300	0.1 M Sodium Chloride
H3	0.1 M Cacodilate	6.0	6.6%w/v PEG 8000	0.05 M Zinc acetate 6 % v/v Ethylene Glycol
H4	0.1 M Tri-sodium citrate	3.5	28%v/v PEG 400	0.2 M Lithium sulfate monohydrate
H5	0.1 M TRIS	7.5	11%w/v PEG 4000	0.1 M Sodium Chloride
H6	0.02 M TRIS	7.5	33%w/v PEG 1500	
H7	0.1 M Cacodilate	6.4	12%w/v PEG 2000	
H8	0.1 M Tricine	8.0	31%w/v PEG 1000	0.35 M Sodium Chloride
H9	0.05 M Cacodilate	6.6	11%w/v PEG 3350	0.2 M Magnesium Acetate tetrahydrate
H10	0.05 M TRIS	7.5	13%w/v PEG 6000	0.15 M Zinc acetate 0.05 M Zinc Chloride
H11	0.1 M ADA	6.6	13%w/v PEG 3000	0.1 M Lithium sulfate monohydrate
H12	0.05 M Sodium acetate	4.3	33%v/v PEG MME 500	

Appendix E. 5. PAC 22 screening plate

PAC13 screening is a custom plate designed by the PAC (IBMB-IRB) that mimics the commercial plate Pi-PEG.

Well	Buffer	pH	Precipitant 1	Precipitant 2
A1	0,1M Sodium acetate	4,6	22,5%v/v PEG 200	
A2	0,1M Sodium acetate	5	20%v/v PEG 300	
A3	0,1M MES	5,6	20%v/v PEG MME 350	
A4	0,1M MES	6	20%v/v PEG 400	
A5	0,1M Cacodilate	6,4	20%v/v PEG MME 500	
A6	0,1M Cacodilate	6,7	20%v/v PEG 600	
A7	0,1M HEPES	7,2	17,5%w/v PEG 1000	
A8	0,1M HEPES	7,5	17,5%w/v PEG 1500	
A9	0,1M TRIS	8	15%w/v PEG 2000	
A10	0,1M TRIS	8,2	15%w/v PEG MME 2000	
A11	0,1M Glycine	8,5	15%w/v PEG 3000	
A12	0,1M Glycine	9	15%w/v PEG 4000	
B1	0,1M Sodium acetate	4,6	15%w/v PEG 1500	3,571%w/v PEG 4000
B2	0,1M Sodium acetate	5	12,857%w/v PEG 2000	6,429%v/v PEG 200
B3	0,1M MES	5,6	12,857%w/v PEG MME 2000	5,714%v/v PEG 300
B4	0,1M MES	6	12,857%w/v PEG 3000	5,714%v/v PEG MME 350
B5	0,1M Cacodilate	6,4	12,857%w/v PEG 4000	5,714%v/v PEG 400
B6	0,1M Cacodilate	6,7	19,286%v/v PEG 200	5,714%v/v PEG MME 500
B7	0,1M HEPES	7,2	17,143%v/v PEG 300	5,714%v/v PEG 600
B8	0,1M HEPES	7,5	17,143%v/v PEG MME 350	5%w/v PEG 1000

B9	0,1M TRIS	8	17,143%v/v PEG 400	5%w/v PEG 1500
B10	0,1M TRIS	8,2	17,143%v/v PEG MME 500	4,286%w/v PEG 2000
B11	0,1M Glycine	8,5	17,143%v/v PEG 600	4,286%w/v PEG MME 2000
B12	0,1M Glycine	9	15%w/v PEG 1000	4,286%w/v PEG 3000
C1	0,1M Sodium acetate	4,6	14,286%v/v PEG MME 350	11,429%v/v PEG 300
C2	0,1M Sodium acetate	5	14,286%v/v PEG 400	11,429%v/v PEG MME 350
C3	0,1M MES	5,6	14,286%v/v PEG MME 500	11,429%v/v PEG 400
C4	0,1M MES	6	14,286%v/v PEG 600	11,429%v/v PEG MME 500
C5	0,1M Cacodilate	6,4	12,5%w/v PEG 1000	11,429%v/v PEG 600
C6	0,1M Cacodilate	6,7	12,5%w/v PEG 1500	10%w/v PEG 1000
C7	0,1M HEPES	7,2	10,714%w/v PEG 2000	10%w/v PEG 1500
C8	0,1M HEPES	7,5	10,714%w/v PEG MME 2000	8,571%w/v PEG 2000
C9	0,1M TRIS	8	10,714%w/v PEG 3000	8,571%w/v PEG MME 2000
C10	0,1M TRIS	8,2	10,714%w/v PEG 4000	8,571%w/v PEG 3000
C11	0,1M Glycine	8,5	16,071%v/v PEG 200	7,143%w/v PEG 4000
C12	0,1M Glycine	9	14,286%v/v PEG 300	12,857%v/v PEG 200
D1	0,1M Sodium acetate	4,6	8,571%w/v PEG MME 2000	17,143%v/v PEG 400
D2	0,1M Sodium acetate	5	8,571%w/v PEG 3000	17,143%v/v PEG MME 500
D3	0,1M MES	5,6	8,571%w/v PEG 4000	17,143%v/v PEG 600
D4	0,1M MES	6	12,857%v/v PEG 200	15%w/v PEG 1000
D5	0,1M Cacodilate	6,4	11,429%v/v PEG 300	15%w/v PEG 1500
D6	0,1M Cacodilate	6,7	11,429%v/v PEG MME 350	12,857%w/v PEG 2000
D7	0,1M HEPES	7,2	11,429%v/v PEG 400	12,857%w/v PEG MME 2000
D8	0,1M HEPES	7,5	11,429%v/v PEG MME 500	12,857%w/v PEG 3000
D9	0,1M TRIS	8	11,429%v/v PEG 600	10,714%w/v PEG 4000
D10	0,1M TRIS	8,2	10%w/v PEG 1000	19,286%v/v PEG 200
D11	0,1M Glycine	8,5	10%w/v PEG 1500	17,143%v/v PEG 300
D12	0,1M Glycine	9	8,571%w/v PEG 2000	17,143%v/v PEG MME 350
E1	0,1M Sodium acetate	4,6	8,571%v/v PEG MME 500	22,857%v/v PEG 600
E2	0,1M Sodium acetate	5	8,571%v/v PEG 600	20%w/v PEG 1000
E3	0,1M MES	5,6	7,5%w/v PEG 1000	20%w/v PEG 1500
E4	0,1M MES	6	7,5%w/v PEG 1500	17,143%w/v PEG 2000
E5	0,1M Cacodilate	6,4	6,429%w/v PEG 2000	17,143%w/v PEG MME 2000
E6	0,1M Cacodilate	6,7	6,429%w/v PEG MME 2000	17,143%w/v PEG 3000
E7	0,1M HEPES	7,2	6,429%w/v PEG 3000	14,286%w/v PEG 4000
E8	0,1M HEPES	7,5	6,429%w/v PEG 4000	25,714%v/v PEG 200
E9	0,1M TRIS	8	9,643%v/v PEG 200	22,857%v/v PEG 300
E10	0,1M TRIS	8,2	8,571%v/v PEG 300	22,857%v/v PEG MME 350
E11	0,1M Glycine	8,5	8,571%v/v PEG MME 350	22,857%v/v PEG 400
E12	0,1M Glycine	9	8,571%v/v PEG 400	22,857%v/v PEG MME 500
F1	0,1M Sodium acetate	4,6	4,286%w/v PEG 4000	25%w/v PEG 1500
F2	0,1M Sodium acetate	5	6,429%v/v PEG 200	21,429%w/v PEG 2000
F3	0,1M MES	5,6	5,714%v/v PEG 300	21,429%w/v PEG MME 2000
F4	0,1M MES	6	5,714%v/v PEG MME 350	21,429%w/v PEG 3000
F5	0,1M Cacodilate	6,4	5,714%v/v PEG 400	17,857%w/v PEG 4000
F6	0,1M Cacodilate	6,7	5,714%v/v PEG MME 500	32,143%v/v PEG 200
F7	0,1M HEPES	7,2	5,714%v/v PEG 600	28,571%v/v PEG 300
F8	0,1M HEPES	7,5	5%w/v PEG 1000	28,571%v/v PEG MME 350
F9	0,1M TRIS	8	5%w/v PEG 1500	28,571%v/v PEG 400
F10	0,1M TRIS	8,2	4,286%w/v PEG 2000	28,571%v/v PEG MME 500
F11	0,1M Glycine	8,5	4,286%w/v PEG MME 2000	28,571%v/v PEG 600
F12	0,1M Glycine	9	4,286%w/v PEG 3000	25%w/v PEG 1000
G1	0,1M Sodium acetate	4,6	2,5%w/v PEG 1000	25,714%w/v PEG MME 2000
G2	0,1M Sodium acetate	5	2,5%w/v PEG 1500	25,714%w/v PEG 3000

G3	0,1M MES	5,6	2,143%w/v PEG 2000	21,429%w/v PEG 4000
G4	0,1M MES	6	2,143%w/v PEG MME 2000	38,571%v/v PEG 200
G5	0,1M Cacodilate	6,4	2,143%w/v PEG 3000	34,286%v/v PEG 300
G6	0,1M Cacodilate	6,7	2,143%w/v PEG 4000	34,286%v/v PEG MME 350
G7	0,1M HEPES	7,2	3,214%v/v PEG 200	34,286%v/v PEG 400
G8	0,1M HEPES	7,5	2,857%v/v PEG 300	34,286%v/v PEG MME 500
G9	0,1M TRIS	8	2,857%v/v PEG MME 350	34,286%v/v PEG 600
G10	0,1M TRIS	8,2	2,857%v/v PEG 400	30%w/v PEG 1000
G11	0,1M Glycine	8,5	2,857%v/v PEG MME 500	30%w/v PEG 1500
G12	0,1M Glycine	9	2,857%v/v PEG 600	25,714%w/v PEG 2000
H1	0,1M Sodium acetate	4,6		25%w/v PEG 4000
H2	0,1M Sodium acetate	5		45%v/v PEG 200
H3	0,1M MES	5,6		40%v/v PEG 300
H4	0,1M MES	6		40%v/v PEG MME 350
H5	0,1M Cacodilate	6,4		40%v/v PEG 400
H6	0,1M Cacodilate	6,7		40%v/v PEG MME 500
H7	0,1M HEPES	7,2		40%v/v PEG 600
H8	0,1M HEPES	7,5		35%w/v PEG 1000
H9	0,1M TRIS	8		35%w/v PEG 1500
H10	0,1M TRIS	8,2		30%w/v PEG 2000
H11	0,1M Glycine	8,5		30%w/v PEG MME 2000
H12	0,1M Glycine	9		30%w/v PEG 3000

Resum en català

Índex

Introducció

1. L'evolució de la vida

1.1. Membranes i proteïnes

Durant l'evolució de la vida, un dels passos més crucials va ser la compartimentalització finita de la sopa prebiòtica. Aquest tancament en compartiments de les substàncies va suposar un entorn altament favorable pel procés evolutiu.

Llavors, va emergir la necessitat d'una bona comunicació entre l'interior i l'exterior d'aquests nous compartiments, d'aquests nous prototips de cèl·lules. Aquesta comunicació, o trànsit de substàncies, havia d'estar molt ben regulat. En cas contrari, la compartimentalització hagués caigut en va.

És llavors quan sorgeixen els enzims acorats a membrana, coneguts com a proteïnes de membrana (PMs), les quals serveixen de vàlvules reguladores capaces de catalitzar el transport de substàncies a través de la membrana lipídica. Aquestes PMs són, doncs, les responsables de conferir a la bicapa lipídica de la seva característica més primordial, la permeabilitat selectiva.

Les PMs no només actuen com a transportadors, si no que actuen dins un ampli ventall de funcions (Almén et al., 2009). Com per exemple, receptors per induir senyals intracel·lulars, enzims capaços de catalitzar reaccions químiques, lligands per altres PMs... L'alta diversitat de PMs relacionades amb el transport exerceixen la seva funció d'acord amb la següent categorització (Lodish et al., 2000):

- **Difusió passiva:** la manera més simple per petites molècules de travessar la membrana a favor de gradient.
- **Transport facilitat**: els altres tipus de sistemes de transport que requereixen de PMs:
    - **Difusió facilitada:** involucren canals i transportadors que permeten el pas de substàncies a favor de gradient sense despesa energètica.
    - **Transport actiu**: involucren PMs directament acoblades a una font d'energia. Aquests poden ser, uniportadors (transporten una sola molècula), simportadors (transporten dues o més molècules en el mateix sentit) o antiportadors (transporten dues o més molècules en sentits oposats).

La proporció de PMs en relació a totes les proteïnes és d'entre un 15 i un 39 % depenent de l'espècie (Almén et al., 2009). Pel genoma humà, constitueixen un 23

% d'aquest (Figura 1 A) (Uhlén et al., 2015). La importància de les PMs guanya rellevància quan es té en compte que són el 60 % de les dianes terapèutiques dels fàrmacs actuals (Figura 1 B) (Overington et al., 2006). Malauradament, només una fracció molt petita de PMs ha estat resolta estructuralment (Almeida et al., 2017). Un total de 193,455 estructures de proteïnes es troben dipositades a l'RCSB PDB, però només 1,471 corresponen a PMs (Figura 1 C), un 0.75% (dades de l'RCSB PDB (rcsb.org) i l'mpstruc (blanco.biomol.uci.edu/mpstruc/) a 28 de juliol de 2022). Aquesta discrepància entre la poca disponibilitat d'estructures i la rellevància terapèutica de les PMs (Figura 1) es deu a les peculiaritats d'aquest tipus de proteïnes que en fa tan difícil el seu estudi, principalment l'hidrofobicitat.

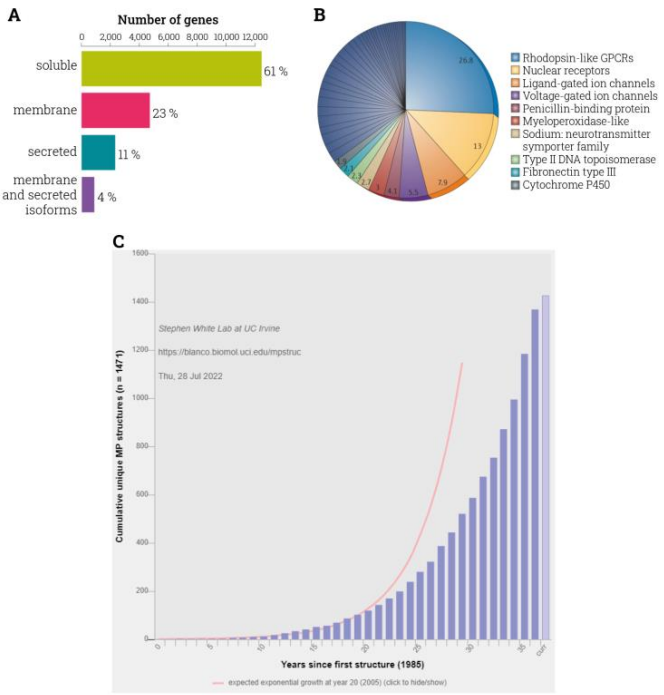

Figura 1. Discrepància entre la baixa disponibilitat d'estructures de PMs i la seva rellevància. A. Distribució dels gens humans classificats en categories (soluble, de membrana, secretades i les que pertanyen a varis dels anteriors) (Uhlén et al., 2015). **B.** Percentatges de distribució de les famílies gèniques de les dianes de fàrmacs aprovats per l'administració dels aliments i fàrmacs (FDA) (Overington et al., 2006) **C.** Progrés de la determinació d'estructures de PMs per any (blau) comparat amb el creixement esperat (vermell). Dades de l' RCSB-PDB (rcsb.org) i l'mpstruc (blanco.biomol.uci.edu/mpstruc/) a 28 de juliol de 2022.

1.2. La importància dels aminoàcids

Un altre dels passos més crucials en l'evolució de la vida va ser la síntesi de substàncies i molècules, entre ells les PMs. Els aminoàcids (AA) en són la base, els blocs de construcció de totes les proteïnes, essencials i amb una àmplia varietat de funcions (e.g., precursors de síntesi d'altres molècules, coenzims...)

Aquests AA són absorbits a l'intestí, el jejú majoritàriament (Silk et al., 1985; Mariotti et al., 2000). I també són reabsorbits amb alta eficàcia (95-99 %) als ronyons (Young and Freedman, 1971; Silbernagl et al., 1975; Silbernagl, 1979, 1988). Els responsables d'aquests dos processos, l'absorció i la reabsorció, són els transportadors d'AA. Diversos estudis (Milne, 1964; Young and Freedman, 1971; Bröer, 2008) n'han permès categoritzar les diverses activitats transportadores, o sistemes, compartits entre els transportadors, que són:

- **Sistema neutral:** transporta els AA neutrals (AA^0) que són: alanina, serina, treonina, valina, leucina, isoleucina, fenilalanina, tirosina, triptòfan, asparagina, glutamina, histidina, cisteïna, metionina and citrul·lina.
    a. **Sistema L**: transporta leucina i altres AA^0 voluminosos i hidrofòbics.
    b. **Sistema A**: transporta AA^0 polars.
    c. **Sistema ASC**: transporta alanina, serina i cisteïna.
- **Sistema bàsic** o **sistema y^+:** transporta els AA catiònics (AA^+) que són: lisina, arginina ornitina. I també transporta la cistina.
- **Sistema àcid** o **sistema XAG^-**: que transporta el glutamat i l'aspartat.
- **Sistema iminoglicina:** transporta prolina, hidroxiprolina i glicina.
- **Sistema β-aminoàcid:** transporta AA β i taurina.

El nostre laboratori ha dedicat més de 25 anys a la recerca dels transportadors d'aminoàcids tant amb estudis adreçats a descriure els processos fisiològics com amb estudis adreçats a la caracterització estructural i funcional dels transportadors (Palacín et al., 1998; Palacín and Kanai, 2004; Palacín et al., 2005; Bröer and Palacín, 2011; Fotiadis et al., 2013; Bartoccioni et al., 2019; Errasti-Murugarrzzen et al., 2019).

1.3. Classificació dels transportadors

Hi ha diverses nomenclatures per classificar els transportadors. El sistema de nomenclatura SLC va ser desenvolupada originalment entre el Comitè de Nomenclatura Gènica HUGO (HGNC) (http://www.genenames.org/) i les taules SLC (https://www.bioparadigms.org/slc/intro.htm). Segons aquest sistema, hi ha més de 450 SLCs (gens i pseudogens) agrupats en 71 famílies. El sistema SLC categoritza els transportadors segons la seva funció, homologia i fenotip.

Per altra banda, també existeix la Classificació de Transportadors (TC, www.tcdb.org) , sistema que va néixer amb una perspectiva de multiorganismes,

anàleg al sistema de la Comissió d'Enzims (EC). El sistema TC classifica els transportadors no només per la seva funció, també segons el seu origen filogenètic tot seguint cinc criteris: la classe (i.e, canal, portador, transportador actiu primari o grup translocador), la subclasse (segons la font d'energia que utilitzen, en el cas dels transportadors primaris actius), la família o subfamília i, finalment, segons els substrats que reconeixen. En el sistema TC també s'hi pot trobar les seqüències homòlogues de funció desconeguda.

1.3.1. La superfamília aminoàcid / poliamina / organocatió

La superfamília APC va ser descrita inicialment l'any 2000 contenint 10 famílies (Jack et al., 2000), aquell mateix any, es va concloure que 20 famílies diferents estaven relacionades amb el transport d'AAs (Saier, 2000), actualment és una de les superfamílies més extenses. En l'actualitat la superfamília APC comprèn les famílies SLC6, SLC7, SLC32, SLC36 i SLC38 (Kandasamy et al., 2018). La selectivitat de substrats va ser, més endavant, ampliada a no només AAs i els seus derivats sinó a un gran rang de diversos soluts.

Els anàlisis de seqüència dels membres d'aquesta família va revelar que estaven estructuralment formades per 12 segments transmembrana (TMs), malgrat alguns en presentessin 10, 11 o 14. L'origen de la seva estructura es relaciona amb la superfamília de facilitadors majors (MSF) ja que es creu que els membres d'ambdues superfamílies provenen d'un mateix ancestre comú de dos TMs (Figura 2. A). Wong et al., coincidint amb Reddy et al., van proposar dos processos evolutius, dirigits per processos de replicacions intragèniques, que haurien dut aquest ancestre comú de 2 TMs al que actualment és l'estructura dels APC i MSFs (Figura 2. B) (Reddy et al., 2012; Wong et al., 2012).

Tots els membres de la superfamília APC comparteixen, doncs, el mateix plegament, el que s'anomena plegament APC o plegament LeuT.

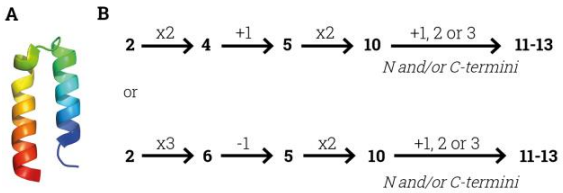

Figura 2. L'origen de la superfamília APC. A. Representació esquemàtica d'una proteïna de 2 TMs, com l'ancestre comú de les superfamílies APC i MSF (PDB ID 1EI0, *hairpin* d'hèlix alfa de P8MTCP1). **B.** Possibles processos evolutius de modificació intragènica dels TMs des de l'ancestre comú a l'actualitat dels APCs (adaptat de Wong et al., 2012).

1.3.2. La família aminoàcid / poliamina / organocatió

La família APC forma part de la superfamília APC i conté els simportadors de funció solut:catió i els antiportadors solut:solut (Jack et al., 2000). L'especificitat de substrats dels transportadors pot ser des d'un gran rang de soluts fins a tan sols un o varis AAs o derivats (Brechtel and King, 1998; Hu and King, 1998; Sato et al., 1999).

Tot i que la família APC inclou membres amb diferents mecanisme de transports (i.e., diferents estequiometries i acoblaments d'ions), els estudis filogenètics reforcen la seva relació comuna. Els membres d'aquesta família es troben en bacteris, arquees, llevats, fongs, protists eucariòtics unicel·lulars, molses, plantes i animals (Jack et al., 2000).

Els transportadors d'aminoàcids tipus L (LATs) humans (hLATs) que pertanyen a la subfamília LAT també pertanyen a la família de transportadors de soluts 7 (SLC7). La família SLC7 no només conté hLATs, sinó també els transportadors d'aminoàcids catiònics (CATs). Els CATs comprenen des de l'SLC7A1 fins l'SLC74 i els LATs des de l'SLC7A5 a l'SCL7A15. Els CATs tenen 14 TMs i transporten principalment aminoàcids catiònics (AA+) per difusió facilitada, mentre els LATs, amb 12 TMs, antiporten diferents tipus d'AA segons la seva especificitat de substrat. L'alineament de CATs i LATs resulta en un 25 % d'identitat de seqüència (SI). A més a més, els hLATs necessiten associar-se a una glicoproteïna de la família SLC3 per localitzar-se a la membrana lipídica.

1.3.3. La subfamília de transportadors d'aminoàcids tipus L

La subfamília LAT comprèn les subunitats lleugeres dels transportadors heteromèrics d'aminoàcids (HATs) humans i d'altres homòlegs de diverses espècies. Entre ells hi trobem l'intercanviador d'alanina-serina-cisteïna bacterià (BasC) expressat pel *Carnobacterium sp. AT7*. BasC va ser identificat com el candidat procariòtic per excel·lència per l'anàlisi d'estructura i funció dels hLATs després de l'anàlisi per BLAST mostrant que BasC comparteix entre un 25 i 30 % d'SI amb els hLATs (Bartoccioni et al., 2019). L'estudi filogenètic de la família APC indica que BasC estaria agrupat dins de la subfamília LAT (Figura 4). I no només això, BasC també té unes característiques funcionals molt similars als membres de la subfamília LAT, fet que el fa un molt bon candidat per l'estudi del mecanisme de transport dels LATs.

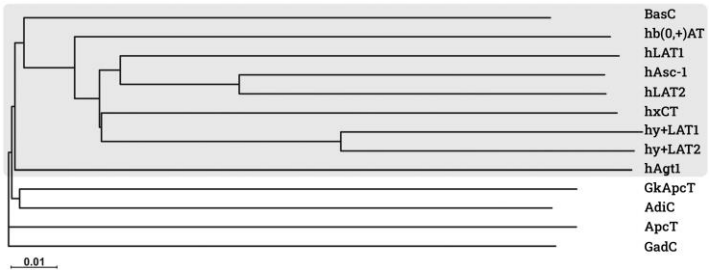

Figura 4. Relacions filogenètiques entre BasC i membres de la família APC. Arbre filogenètic de varis membres de la família APC, entre els quals també hi ha els LATs (àrea grisa) i els homòlegs procariòtics més rellevants. L'arbre va ser obtingut fent servir les seqüències accessibles del sistema TC (www.tcdb.org) (Bartoccioni et al., 2019).

2. Transportadors heteromèrics d'aminoàcids

Els transportadors heteromèrics d'aminoàcids (HATs) pertanyen a la superfamília coneguda com a transportadors de soluts heteromèrics (Saier et al., 2016), una de les tres superfamílies de transportadors humans més conegudes. Les característiques d'aquests transportadors es descriu a continuació (Verrey et al., 1999; Jack et al., 2000; Verrey et al., 2000, 2004; Palacín and Kanai, 2004; Scalise et al., 2018; Fairweather et al., 2020; Nicolàs-Aragó et al., 2021; Fort et al., 2021; Rullo-Tubau et al., 2022).

Els HATs estan formats per dues subunitats unides per un pont disulfur:

- **Subunitat lleugera**: PMs que tenen l'activitat translocadora d'AA. Les subunitats lleugeres són els LATs, pertanyents a la família SLC7. Existeixen 11 LS-HATs diferents, de l'SLC7A5 a l'SLC7A15.
- **Subunitat pesada**: PMs d'un únic TM sense activitat translocadora d'AA amb funció de localització de l'heterodímer a la membrana plasmàtica (Bartoccioni et al., 2008; Feliubadaló et al., 1999; Mastroberardino et al., 1998; Verrey et al., 2000). Hi ha dos HS-HATs: rBAT (SLC3A1) i 4F2hc (SLC3A2) (Ohgimoto et al., 1995). Ambdós comparteixen un 30 % d'SI i tenen pesos moleculars ~90 i ~80 kDa, respectivament.

Actualment es coneixen 10 LATs diferents i per la majoria se'n coneix la seva subunitat pesada. Sis d'ells s'aparellen amb 4F2hc (LAT1, LAT2, y^+LAT1, y^+LAT2, Asc-1, i xCT); dos amb rBAT ($b^{0,+}$AT i AGT-1); i n'hi ha dos que no s'expressen en humans, són pseudogens i, per tant, se'n desconeix la seva subunitat pesada (Asc-2 i arpAT) (Fernández et al., 2005). Els HATs en general estan estretament relacionats a la funció intercanviadora, amb l'excepció d'Asc-1 amb 4F2hc que també pot arribar a funcionar com a uniportador (Fukasawa et al., 2000; Pineda et al.,

2004). En general mostren un ampli ventall de substrats, AAs, i presenten afinitats de substrats diferents per cada cara (Napolitano et al., 2017; Scalise et al., 2018; Rodriguez et al., 2021).

2.1. Malaltia humana i els HATs

Diverses patologies humanes posen de relleu el rol fisiològic que els HATs tenen. Mutacions a rBAT o $b^{(0,+)}$AT es relacionen amb la cystinuria (Calonge et al., 1994; Feliubadaló et al., 1999), mentre que mutacions a y^+LAT1 es relacionen amb la intolerància proteica lisinúrica (LPI) (Borsani et al., 1999; Torrents et al., 1999). Altres mutacions a LAT1 estan associades a desordres de l'espectre autista i retard motor (Tărlungeanu et al., 2016), mentre que nivells baixos de LAT1 en els capil·lars cerebrals estan relacionats amb el parkinson(Ohtsuki et al., 2010). Mutacions a LAT2 es relacionen amb la pèrdua d'oïda associada a l'edat (Espino Guarch et al., 2018) i cataractes (Knöpfel et al., 2019). A més a més, xCT i LAT1 es troben sobreexpressats en molts tumor humans (del Amo et al., 2008; Lo et al., 2008; Savaskan and Eyüpoglu, 2010).

Els HATs també juguen papers importants en el tractament de certes malalties, com el de l'esquizofrènia, on Asc-1 és la diana pels (Sakimura et al., 2016).

2.1.1. Intolerància proteica lisinúrica

L'LPI va ser diagnosticada per primera vegada l'any 1965 a Finlàndia (Perheentupa and Visakorpi, 1965). La pèrdua de funció hereditària y^+LAT1 causa aquesta malaltia molt rara, recessiva i autosòmica (Borsani et al., 1999; Torrents et al., 1999). L'LPI es caracteritza per una deficiència en el transport d'AA^+, una mala absorció i reabsorció d'aquests que desencadena en hiperammonemia (nivells d'amoni alts en sang) que a la seva vegada provoca encefalopaties. Altres simptomatologies que s'han descrit en pacients d'LPI són: insuficiència renal, osteoporosis i complicacions gastrointestinals entre d'altres (Zhang and Cao, 2017).

S'han descrit 59 mutacions diferents a l'SLC7A7, y^+LAT1, en més de 180 pacients de 120 famílies independents (Fairweather et al., 2020). Una d'elles, objecte d'estudi d'aquesta tesi, és la K191E (Sperandeo et al., 2008), K154A en BasC, mutació que elimina una lisina completament conservada en tots els LATs.

2.2. Estructures dels transportadors amb plegament APC

L'estructura atòmica dels LATs és, al cap i a la fi, una eina poderosa per poder estudiar la selectivitat de substrat, el mecanisme de transport i, no menys important, com poden actuar i es poden dissenyar les teràpies (Morth et al., 2009).

El primer transportador de la superfamília APC a ser resolt estructuralment va ser LeuT (Yamashita et al., 2005). Aquest transportador de leucina és de la família NSS

o té tan sols un ~9 % SI amb els LATs. Tot i així, LeuT ha rebut una atenció no gens ignorable pel que fa al plegament que tenen els transportadors de la superfamília APC, plegament de 12 TMs (Figura 6. B), el plegament APC (Figura 6. A).

Aquest plegament comporta trets comuns a les proteïnes que l'adopten. Està basat en una repetició de 5 TMs a mode de pseudo-simetria (Bai et al., 2017; Navratna and Gouaux, 2019). La repetició comprèn del TM1 al 5 i del TM6 al 10. Els TMs restants queden fora d'aquest nucli de repetició. A més, s'han descrit dos subdominis (Shi et al., 2008; Fairweather et al., 2020) anomenats "*bundle*" (TM1, 2, 6 i 7) i "*hash*" (TM4, 4, 8 i 9) (Figura 6. C). El lloc d'unió a substrat es troba a una zona descargolada dels TMs 1 i 6 al centre de la molècula, separant aquest dos TMs en TM1a i 1b i TM6a i 6b. Els TM5 i 10 es consideren fora dels dominis com a sub-dominis conservats i es refereix a ells com a "braços" (Shimamura et al., 2010; Krishnamurthy and Gouaux, 2012; Penmatsa and Gouaux, 2014).

LeuT va permetre definir dos llocs d'unió a substrats, l'S1 i l'S2 (Yamashita et al., 2005). El primer és el que es troba a la regió descargolada dels TM1 i 6. El segon es troba a mig camí entre l'S1 i l'entrada extracel·lular (Singh et al., 2008, 2007; Quick et al., 2009; Coleman and Gouaux, 2018; Coleman et al., 2019).

Els transportadors de la superfamília APC que són simportadors acoblats a ions, presenten dos llocs d'unió al sodi, l'Na1 i l'Na2. El segon, està altament conservat entre tots els transportadors que presenten el plegament APC.

Les estructures amb plegament APC poden presentar varies conformacions, en aquesta tesi ens referirem a elles com a mirant cap a dins o cap a fora, indicant cap a on tenen accessible el lloc d'unió al substrat prenent com a referència la porta citoplasmàtica. Llavors, mirant cap a dins comporta que la porta citoplasmàtica estigui oberta i mirant cap a fora, closa.

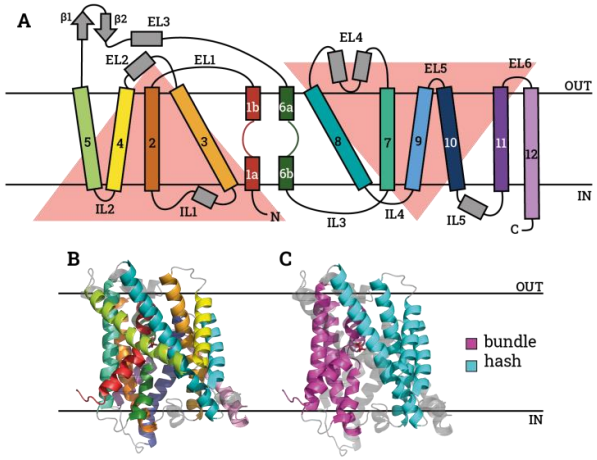

Figura 6. El plegament APC . (*Pàgina anterior*) Les línies horitzontals negres simbolitzen la membrana lipídica. **A.** Esquema del plegament APC, els triangles vermells representen les dues pseudo-simetries. Els TMs, així com els *loops* interns (IL) i els *loops* externs (EL) estan numerats i indicats. Dos fulls beta van ser descrits entre els TM5 i 6 (adaptat de Yamashita et al., 2005). **B-C.** Estructura de BasC (PDB ID: 6F2W). En l'apartat B, pintada com descrita a l'apartat A, i al C pintada segons els subdominis *hash* i *bundle* amb la resta de TMs en gris transparents.

Actualment es disposa de moltes estructures dels transportadors amb plegament APC, en una gran diversitat de conformacions. Ara bé, gairebé totes les estructures dels LATs s'han resolt en conformació mirant cap a dins (Nicolàs-Aragó et al., 2021) amb la única excepció de LAT1 unit a inhibidors que es va poder resoldre mirant cap a fora / totalment tancada (Yan et al., 2021).

2.3. Caracterització funcional i estructural de BasC

El nostre grup ha publicat dos articles de caracterització funcional (Bartoccioni et al., 2019) i estructural (Errasti-Murugarren et al., 2019) de BasC. És a partir d'aquests dos articles que se n'extreu tot el contingut d'aquest apartat de la introducció.

BasC presenta una activitat d'intercanviador d'AA obligatòria independent d'ions, necessita la presència de substrat a les dues bandes de la membrana per funcionar (Figura 7. A). També presenta una afinitat asimètrica pels substrats, amb diferents constants d'afinitat segons la cara per aquests. L'extracel·lular és la d'alta afinitat (µM rang) i la citoplasmàtica, la de baixa afinitat (mM rang) (Figura 7. B). La selectivitat de substrats d'aquest transportador és la d'AA^0 petits (com la Gly, L-Ala ó D-Ala, L-Ser o D-Ser...) i l'L-Asp (Figura 7. C).

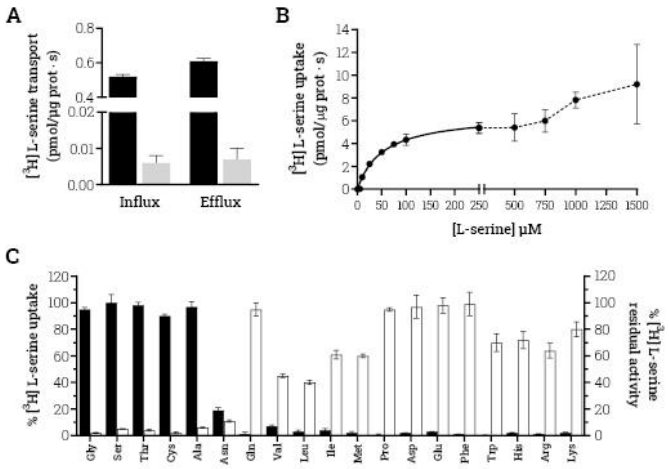

Figura 7. Caracterització funcional de BasC. (*Pàgina anterior*) **A.** Comparativa de l'influx i l'eflux de 10 µM [^{3}H]L-serina (1 µCi/punt) en PLs amb BasC-GFP reconstituït contra una solució que conté (negre) o no conté (gris) AA (L-Ala 4 mM). Només és capaç de transportar si hi ha AA a ambdós costats de la membrana lipídica. **B.** Determinació dels paràmetres cinètics extraliposomals. Gràfic de Michaelis-Menten del transport d'influx de [^{3}H]L-Ser (1 µCi/µl, 4 s pmol/$\mu g_{protein}$/s) en PLs amb BasC-GFP reconstituït contenint 4 mM L-Ala, incrementant la concentració extracel·lular d'L-Ser (0–1,500 µM). La K_m and V_{max} van ser de 45 ± 5 µM i 6.0 ± 0.2 pmol [^{3}H]L-Ser/$\mu g_{protein}$/s, respectivament. **C.** Influx de 10 µM [^{3}H]L-Ser (1 µCi/µl) en PLs amb BasC-GFP reconstituït contenint 4 mM de l'AA indicat (negre). Transport expressat segons el percentatge de l'influx contra 4 mM d'L-Ala. Les barres blanques indiquen l'influx de 10 µM [^{3}H]L-Ser (1 µCi/µl) en PLs amb BasC-GFP reconstituït contenint 4 mM d'L-Ala amb la presència extraliposomal de 5 mM de l'AA. Inhibició expressada com al percentatge del transport en PLs amb BasC-GFP reconstituït contenint 4 mM d'L-Ala sense cis-inhibidors (adaptat de Bartoccioni et al., 2019).

A l'hora de reconstituir BasC-GFP a PLs, aquest ho fa de manera aleatòria, tant cap per amunt com cap per avall (Bartoccioni et al., 2019). Per poder aconseguir les constants d'afinitat de cada cara, Km, es van fer servir uns compostos específics per inhibir selectivament les molècules d'una orientació o de l'altra (Bartoccioni et al., 2019). D'aquesta manera els resultats van ser: $K_{m,extracel·lular}$ = 45 ± 5 µM, $K_{m,citoplasmàtica}$ = 2.5 ± 0.4 mM).

L'estructura de BasC està resolta en conformació mirant cap a dins, en apo i unida a 2-AIB, un substrat pobre. Ambdues van ser resoltes en complex amb un nanocòs (Nb), el Nb74. Un Nb inhibidor de l'activitat de BasC. Finalment es va poder comprovar que BasC comparteix el plegament APC amb 12 TMs organitzats com la resta de membres de la superfamília APC i els LATs (Figura. 9).

També es va publicar la caracterització funcional dels mutants d'LPI relacionats amb la K191E de y+LAT1, les variants **K154A** i **K154E** de BasC (Errasti-Murugarren et al., 2019). Aquestes dues presentaven gairebé anul·lada l'influx d'L-Ala amb una reducció de 10 vegades l'afinitat externa (K_M = 474 ± 42 µM). Sorprenentment la interna no presentava canvis remarcables. A més, aquestes mutacions també presentaven una $V_{màx}$ reduïda 20 vegades (V_{max} = 0.32 ± 0.04 $pmols_{L-Ala}$ /μg_{prot} /s). Aquestes característiques posen de manifest el paper clau d'aquest residu en la subfamília de transportadors LATs.

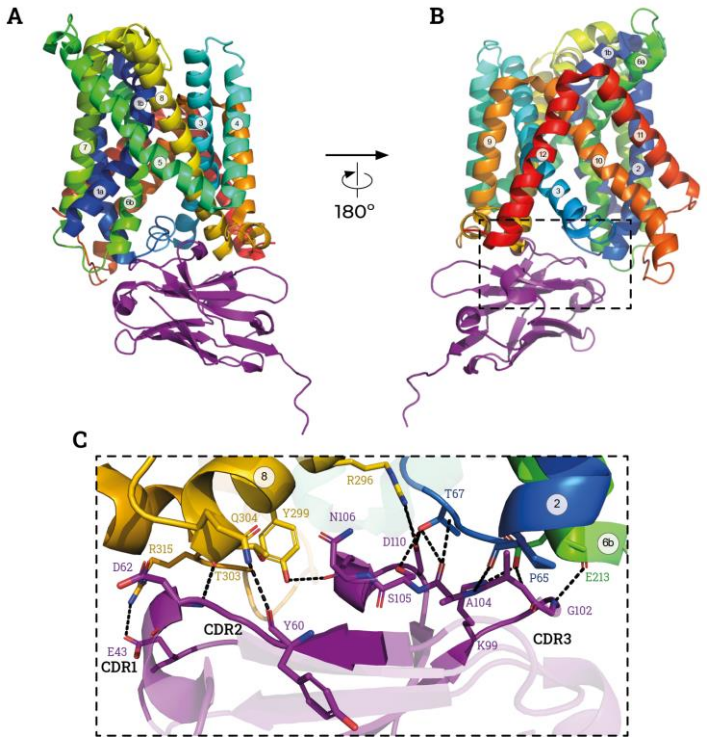

Figura 9. Estructura de BasC-Nb74. Els TMs estan pintats de blau a vermell des de l'N-terminal. El Nb74 es mostra en lila. **A-B.** Vista general i lateral de BasC-Nb74 (PDB ID 6F2G) , el primer en conformació mirant cap a dins. **C.** Visió detallada de les interaccions entre Nb74 i BasC. Les regions determinants de complementarietat interaccionen amb el TM2, 6b, 8 i l'IL4 (entre el TM8 i 9).

2.4. Mecanisme de transport

L'objectiu principal de la present tesi és poder descriure i desxifrar certs detalls del mecanisme de transport dels LATs amb BasC com a model. En aquest apartat es presentaran estudis anteriors al voltant de transportadors de la superfamília APC sobre els quals es basa la hipòtesi del que podria ser el mecanisme el mecanisme de transport dels LATs. El nexe d'unió, motiu pel qual s'extrapola el mecanisme de transport entre anomenats membres, és el plegament APC i certs motius que es repeteixen. Com és el cas del motiu GX_nP del TM5 descrit pels transportadors NSS (Billesbølle et al., 2015; Stolzenberg et al., 2017) i que ha demostrat

ser de gran importància pel mecanisme de transport al desenrotllar-se i permetre l'entrada de molècules d'aigua per desencadenar la sortida del sodi de l'N2 i, com a conseqüència, la translocació final del substrat com es detalla a continuació.,

L'N1 i N2 van ser descrits ja des d'un bon inici a tan sols 6 Å de distància del carboni α del substrat unit (Figura 10. A) (Loo et al., 2013). Per una banda, l'Na1 es relaciona amb el TM1, 6 i 7, mentre que l'Na2 s'associa amb el TM1 i 8 (Figura 10. B) (Yamashita et al., 2005). Aquest últim és el més conservat entre tots els membres amb plegament APC (del Alamo et al., 2022). Fins i tot pels transportadors que no co-importen amb ions, aquests presenten certes reminiscències de l'N2 creant una regió plena de residus carregats (Shaffer et al., 2009; Tang et al., 2010; Jungnickel et al., 2018; Errasti-Murugarren et al., 2019).

El mecanisme de transport es basa en un mecanisme d'accés alternat, la coordinació de tots els seus factors fa que els transportadors s'obrin cap a dins o cap a fora segons el moment, però mai alhora. Els TMs que orquestren aquests moviments són els TM1, 5, 6, 7 i 10 (Nicolàs-Aragó et al., 2021; del Alamo et al., 2022).

El TM5, juntament amb l'IL2, és un TM extremament mòbil de la part citosòlica, es pot veure comparant diferents estructures de conformacions diferents (Billesbølle et al., 2015; Stolzenberg et al., 2017) i la dificultat de poder-ne resoldre la seva estructura (Jungnickel et al., 2018). Aquest TM juntament amb el TM1a i TM6b forma la porta física de l'entrada citosòlica. Simètricament el TM10 té el mateix rol a la part extracel·lular dels transportadors (Bozzi et al., 2019). A la part citosòlica, també, el TM1a s'ha descrit com un dels que més es mou. En LeuT, TM1a es mou fins a 45 º (del Alamo et al., 2022) i també entre els membres de la família APC. Aquest moviment en LATs estaria coordinat directament amb el TM5 i 8 i ocorre simultàniament amb el moviment del TM6b. (Figura 11). A l'altre extrem dels TM1 i 6, el TM1b i 6a, funcionen de manera contraposada al que passa a la part citosòlica (Singh et al., 2008; Claxton et al., 2010). Aquests es mouen d'acord amb l'EL4 que es situa formant part del tancament la porta extracel·lular. Finalment, el TM7 també es doblega durant el transcurs del cicle de transport. De fet, és el canvi més gran observat, per exemple, per LAT1 (Yan et al., 2021).

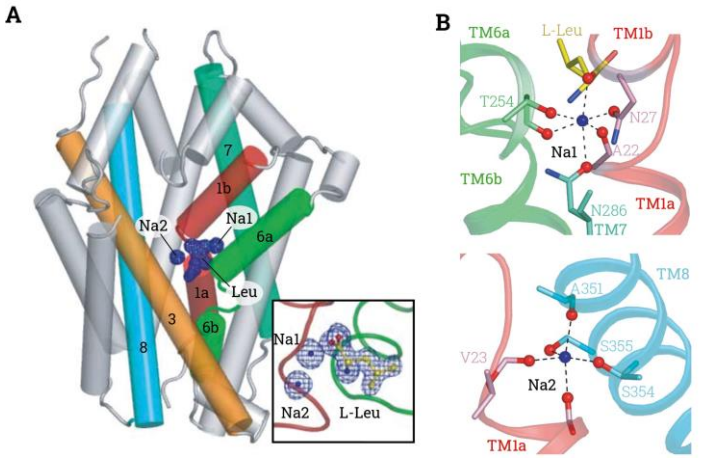

Figura 10. Llocs d'unió al sodi de LeuT. A. Visió general del transportador LeuT amb les densitats electròniques del substrat (L-Leu) i els sodis (Na1 i Na2) marcats en blau. Ambdós llocs d'unió al sodi estan adjacents al lloc d'unió al substrat. **B.** Detall estructural dels llocs d'unió al sodi Na1 (superior) i Na2 (inferior). Es mostren els ions de sodi (esferes blaves) i els residus amb els que interacciona (en barres) i el TM al que pertanyen. Les línies discontínues representen els ponts d'hidrogen (Yamashita et al., 2005).

La Lys 154 de BasC, conservada entre tots els LATs (Bartoccioni et al., 2019), està localitzarà a la posició equivalent de l'Na2 dels simportadors dependents de sodi (Loo et al., 2013; Tavoulari et al., 2016), És aquesta Lys que en els LATs es creu que té un rol essencial entre la coordinació del TM1a i 8 tal i com és per l'Na2 (Loo et al., 2013; Yamashita et al., 2005). La comparació d'estructures entre BasC i GkApcT així ho mostra (Figura 11) (Errasti-Murugarren et al., 2019). Aquesta evidència estructural reforça la hipòtesi del seu rol putatiu, tant important.

Estudis de dinàmica s'han dut a terme per LeuT, a través de smFRET intramolecular tot monitoritzant els moviments de la porta citosòlica. Aquests estudis van revelar dos estats coexistents en condicions basals en presència de 200 mM K^+ i absència de Na^+ (Zhao et al., 2011). Aquests estats, d'alt i baixa eficiència de FRET (E*), representen la conformació mirant cap a dins i la conformació mirant cap a fora, respectivament. La distribució d'aquests estat era modificada per la presència de Na+, arribant a situar-se en el 100 % de molècules a l'alt FRET; conformació mirant cap a fora. Ara bé, la presència de substrat no canviava la distribució dels estats, però sí la rapidesa d'intercanvi entre un i l'altre, en presència de Na+.

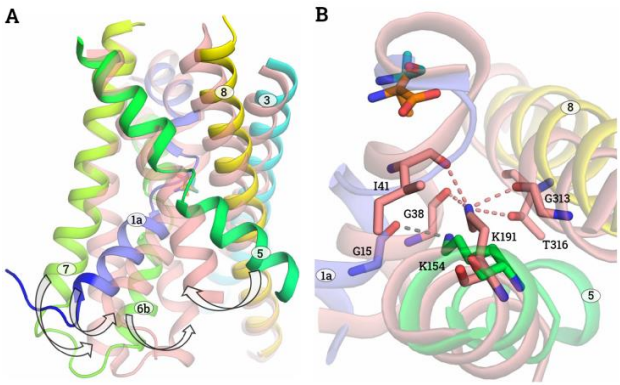

Figura 11. Oclusió dels transportadors SLC7. A. Comparativa de les estructures de BasC (arc iris) unit a 2-AIB (taronja) (PDB ID: 6F2W) en conformació mirant cap a dins i de GkApcT (salmó) unit a L-Ala (cian) (PDB ID: 5OQT) en conformació mirant cap a dins, closa. Els moviments del TM1a, 6b, 7 i 5 estan representats amb fletxes i suposen el tancament de la porta citosòlica. Només es mostren els TMs 1, 3, 5, 6, 7, i 8 per claredat. **B.** Detall de la interacció entre els TMs 1a, 5 i 8 a través de la Lys conservada dels LATs, la K191 i K154 per GkApcT i BasC, respectivament. En GkApcT s'hi veu la interacció completa mentre que en BasC tan sols s'hi detecta la interacció entre el TM1a i el TM5.

Un altre factor, és la presència descrita d'un segon lloc d'unió a substrat, anomenat S2. L'S2 ha estat descrit en ocasions com un lloc al·lostèric de baixa afinitat on s'hi ha trobat units inhibidors (Singh et al., 2007) i, fins i tot, molècules de detergent (Quick et al., 2009). No només se'n té constància estructural, també per estudis de dinàmica molecular (MD) fets en LeuT (Shi et al., 2008).

Considerant tots els estudis anteriors, es pot descriure el mecanisme de transport pels simportadors de sodi (Figura 14).

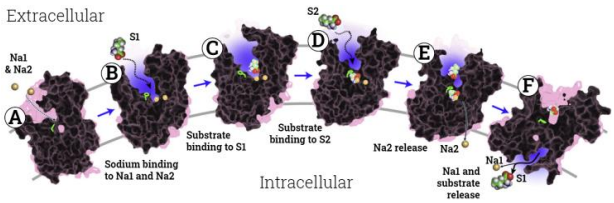

Figura 14. Model esquemàtic del mecanisme de transport per LeuT. Primer els ions de sodi s'uneixen als Na1 i Na2 des de l'exterior (**A**). Llavors una primera molècula de substrat s'uniria a l'S1 (**B**), també des de l'exterior, i un cop tancada la Phe entre l'S1 i l'S2 (**C**) una segona molècula de substrat s'uniria a l'S2 (**D**), des de l'exterior també. Aquesta segona molècula de substrat unida a l'S2 desencadenaria l'alliberament del sodi de l'Na2 cap a l'interior (**E**), finalment el substrat de l'S1 i el sodi de l'N1 serien co-transportats cap a l'interior de la membrana (**F**). Adaptat a partir de Shi et al., 2008.

Ara caldria poder esbrinar com es tradueix aquest mecanisme de transport dintre els membres de la subfamília LAT, sense la seva dependència al sodi, ja que actualment segueix sent poc clar (Nicolàs-Aragó et al., 2021). En els LATs, l'S2 s'ha especulat (Lee et al., 2019; Yan et al., 2021) al interpretar un espai obert a les estructures de LAT1 (PDB ID 6IRT and 6IRS) després d'anomenar-lo lloc distant d'unió al substrat (Yan et al., 2019), espai on la cua de certs inhibidors s'hi va trobar, posteriorment, unida (Yan et al., 2021). Altres autors han descrit que el lloc d'unió al substrat tindria dos espais, un on acomodar les cadenes primàries i l'altre que podria oferir un lloc promiscu d'unions secundàries i inhibitòries (Lee et al., 2019). Similarment, en LAT2 (PDB ID 7CMH and 7CMI), es va observar un possible lloc distant d'unió a substrat (Yan et al., 2020b), però anàlisis de MD no n'han predit aquesta funció encara (Rodriguez et al., 2021).

Objectius

i. Caracteritzar els nanobodies pel seu ús en l'obtenció de l'estructura de BasC en noves conformacions i pels estudis de dinàmica de la porta citosòlica.
ii. Revelar el rol de la Lys conservada en LATs del TM5, K154A en BasC, en la dinàmica de tancament de la porta citosòlica.

Resultats

1. Caracterització dels nanocossos

Els nanocossos (Nbs, de l'anglès nanobodies) contra BasC-GFP es van generar injectant a una llama PLs plens de L-Ala a 4 mM on s'hi havia reconstituït BasC-GFP. Després es va crear una llibreria de les cèl·lules B del sistema immunitari per extreure'n els gens codificants dels Nbs i se'n va fer una selecció per bacteriòfags que va resultar en 29 Nbs diferents.

2.5. Caracterització de la unió dels nanocossos

El cribratge de Nbs contra BasC es va fer per ressonància plasmàtica de superfície (SPR, de l'anglès surface plasmon resonance) contra BasC solubilitzat en DM (Experimental Procedures 1.1). Aquest cribratge dels 29 Nbs va permetre categoritzar-los segons la seva afinitat (K_D) i detallar-ne la seva constant d'unió (k_a), desunió (k_d) i la força de la unió (R_{max}) segons el màxim de la resposta detectada per SPR (Taula 7. A-B). No es van observar diferències entre condicions apo (i.e., sense substrat) i holo (i.e., amb substrat, L-Ala).

També se'n va fer un cribratge per cromatografia d'exclusió molecular (SEC, de l'anglès size exclusion chromatography) per tal d'esbrinar la factibilitat de purificar els complexes BasC-Nb en detergents i altes concentracions (Taula 7. C). La majoria de Nbs tenen afinitats altes, per sota de 150 nM, i són capaços de formar complexes amb Bas per SEC en alta concentració.

2.6. Cara d'unió dels nanocossos

Per saber la cara d'unió a BasC per part dels Nbs, es va utilitzar la metodologia provada pel Nb74 (Errasti-Murugarren et al., 2019) basada en la orientació aleatòria de BasC en la reconstitució en PLs (i.e., cap per amunt o cap per avall) i la seva afinitat de substrat asimètrica (Bartoccioni et al., 2019).

Omplint els PLs amb una concentració baixa de substrat radioactiu (10 µM d'AA) dins una solució d'alta concentració de substrat (4 mM d'AA), només en detectarem l'activitat d'eflux d'aquells transportadors que estan mirant amb la seva cara d'alta afinitat, la citosòlica, cap a l'interior (i.e., cap per amunt). Així doncs, si afegim el Nb a l'exterior dels PLs, només en detectarem la inhibició del transport d'aquells que s'uneixin per la cara de baixa afinitat (i.e., l'extracel·lular).

El cribratge de l'influx (PLs plens de 4 mM L-Ala en una solució de 10 µM d'L-Ser radioactiva) i l'eflux (PLs plens de 10 µM de L-Ser radioactiva en una solució de 4 mM d'L-Ala) es mostra complet a la Figura 18. D'aquests en podem extreure els potencials bloquejadors com es detalla a continuació. Bloquejadors extracel·lulars: Nb58 i 78, els quals mostren perfils d'inhibició clars per l'influx i no per l'eflux. Bloquejadors citoplasmàtics: Nb50-57, 60, 62-63, 65-67, 69-74 i 77, els quals mostren perfils d'inhibició clars per l'eflux i no per l'influx. Bloquejadors confusos: Nb59 i 64. Els quals no mostren perfils d'inhibició clars. No-bloquejadors: Nb61, 66, 68, 75 i 76. Els quals no mostren inhibicions en cap dels casos.

A

Nb	SPR K_D (nM)	R_{max}	k_a	k_d
50	5			
51	36			
52	34			
53	26			
54	72			
55	101			
56	26			
57	217			
58	28			
59	248			
60	19			
61	33			
62	indetectable			
63	indetectable			
64	indetectable			
65	11			
66	115			
67	97			
68	indetectable			
69	25			
70	57			
71	25			
72	85			
73	119			
74	4			
75	indetectable			
76	indetectable			
77	115			
78	55			

B

	R_{max} (R.U.)	k_a ($1/s^9$)	k_d ($1/s^3$)
	≥ 1000	≥ 1000	≥ 200
	[500 ; 1000)	[300 ; 1000)	[40 ; 200)
	[100 ; 500)	[200 ; 300)	[15 ; 40)
	[20 ; 100)	[75 ; 200)	[5 ; 15)
	< 20	< 75	< 5

C

Nb	SEC
50	✓
51	✓
52	
53	✓
54	✓
55	✓
56	✓
57	✓
58	✓
59	✗
60	✓
61	✗
62	
63	✗
64	✗
65	✓
66	✗
67	
68	
69	
70	✓
71	✓
72	
73	
74	✓
75	
76	
77	✓
78	✓

Taula 7. Caracterització de la unió a BasC dels nanocossos. A. Resultats del cribratge per SPR dels Nbs. La constant de dissociació (K_D) es va obtenir a partir de dues concentracions diferents de BasC (K_D en gris) o quatre (K_D en negre). Tant la resposta màxima (R_{max}), com la constant d'associació i dissociació (k_a and k_d) estan pintades segons les categories mostrades a l'apartat (B). **B.** Llegenda de colors de les categories de l'R_{max}, k_a i k_d de l'apartat (A). **C.** Factibilitat de purificar els diversos complexes BasC-Nb per SEC en detergents. Les cel·les buides corresponen als Nbs no assajats; les verdes, als que s'ha aconseguit purificar el complex; i les vermelles, als que no.

Figura 18. Cribratge de l'efecte dels Nb al transport de BasC. Transport relatiu d'influx i eflux per cadascun dels complexes BasC-Nb i BasC en PLs contenint BasC-GFP reconstituït i afegint els Nbs a l'espai extracel·lular a 15 or 5 µM per l'influx o l'eflux, respectivament. Es mostra la mitjana ± s.e.m. per cadascun dels complexes i BasC per un mínim de dos experiments independents. Tests múltiples de Dunett s'han fet entre els efectes de cada complex i el seu control de BasC, separadament influx i eflux (asteriscs). I entre l' influx i l'eflux de cada complex s'ha realitzat un T-test (coixinets). (* ó # p.valor < 0.0332, ** ó ## p.valor < 0.0021, *** ó ### p.valor < 0.0002 i **** ó #### p.valor < 0.0001).

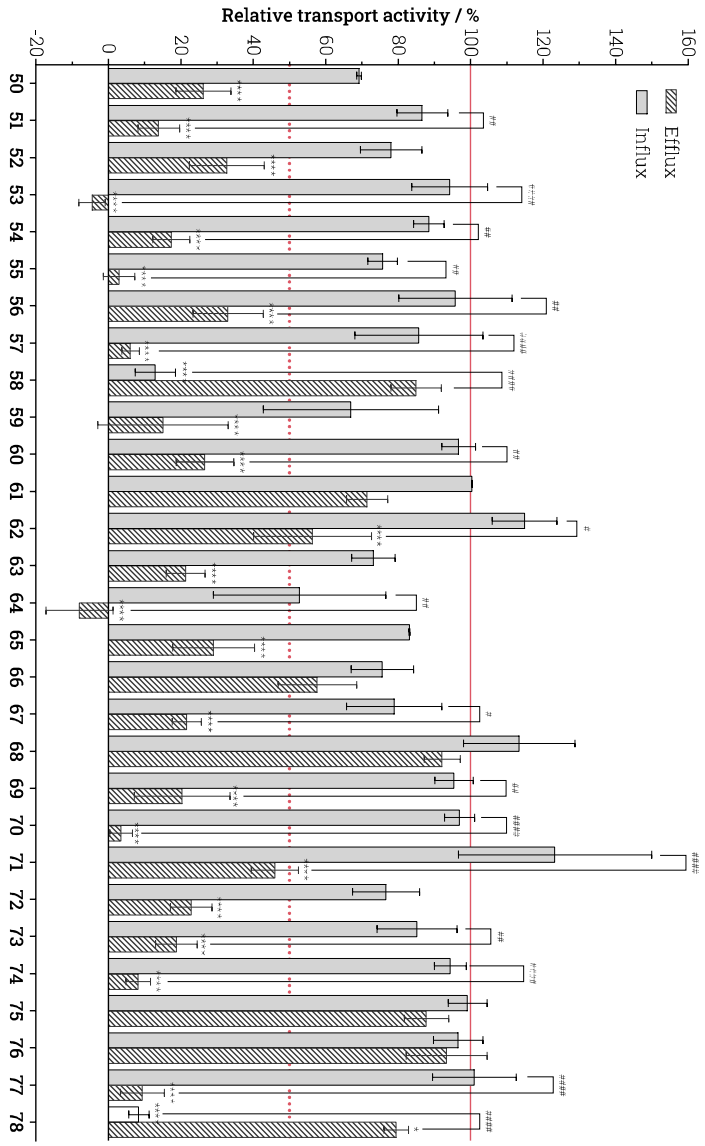
Relative transport activity / %
-20
0
20
40
60
80
100
120
140
160
Efflux
Influx
50 51 52 53 54 55 56 57 58 59 60 61 62 63 64 65 66 67 68 69 70 71 72 73 74 75 76 77 78

Pels Nbs inhibidors extracel·lulars i confusos es va estudiar el seu perfil d'inhibició per dosi resposta. Els resultats van ser de IC_{50}s de 9.44 ± 2.42 nM pel Nb58, 34.8 ± 8.01 nM pel Nb78, aquests dos assolint inhibicions del 100%, i de 518 ± 170 i 362 ± 153 nM, pels Nb59 i 64, respectivament. Aquests dos últims sense assolir inhibicions per sobre del 70 %. És inexplicable com els inhibidors confusos poden inhibir interaccionant per ambdues cares de BasC. Una de les dues unions ha de ser no específica i, per aquest motiu, els Nb59 i 64 van ser descartats per cristal·litzar BasC en noves conformacions. Així com el Nb58 i 78 van ser seleccionats com a prometedors, sent els únics dos, de 29, que s'uneixen clarament per l'exterior de BasC.

2.7. Compatibilitats entre nanocossos

Amb l'objectiu de saber si els Nbs inhibidors estan bloquejant BasC en una conformació diferent de la ja resolta estructuralment, es va assajar la factibilitat d'aparició de complexes terciaris aparellant nanocossos inhibidors per les diferents cares de BasC (Figura 20).

Els Nb58 i 78 van resultar ser complementaris amb el Nb74 (Figura 20. A-B) i que, a més, apareixien complexes de més pes molecular a la SEC. Per tant, les conformacions que aquests Nbs detecten de BasC són compatibles. A la seva vegada, i utilitzant com a control conformacional el Nb78, tots els Nbs citosòlics assajats (Nb51, 53, 54, 55, 57, 70 and 77) també van resultar ser compatibles amb aquest (Figura 20. F). Per tant, no es va poder seleccionar cap Nb prometedor en forçar BasC a adoptar una conformació diferent a la del Nb74, ja que totes les conformacions detectades pels Nbs assajats eren compatibles entre elles.

Tanmateix, també es va intentar l'assoliment de complexes terciaris entre Nbs que s'unissin per la mateixa cara, però el resultat va resultar negatiu en els casos provats, entre els Nb58 i 78 i entre els Nb74 i 71 (Figura 20. C-D i G).

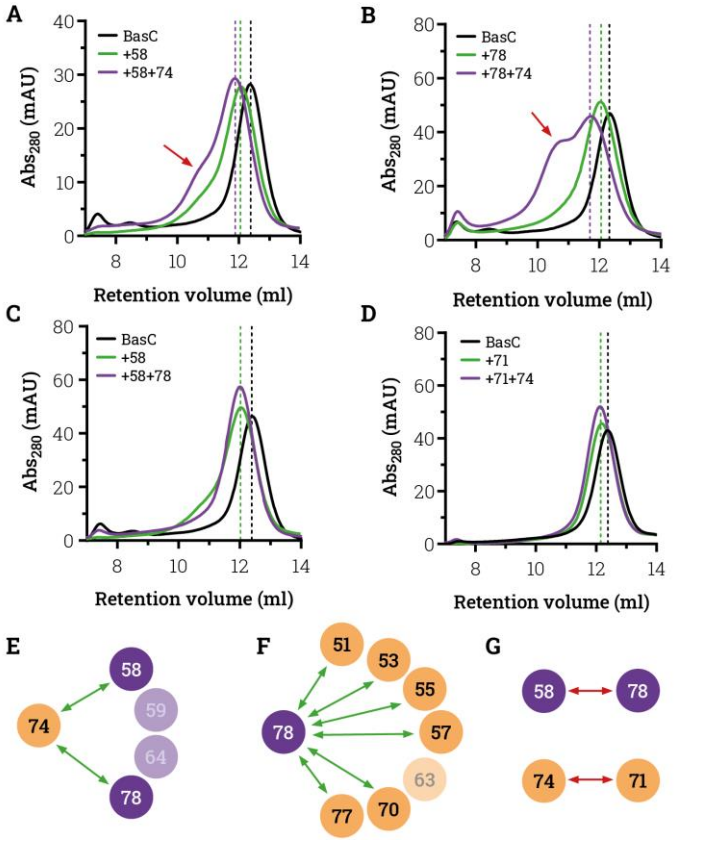

Figura 20. Compatibilitats entre nanocossos. Assaig de compatibilitats per SEC en una columna Superdex 200 10/300 GL amb BasC solubilitzat en DDM. **A-D.** Perfils de SEC tallats, normalitzats i superposats per BasC (negre), BasC+Nb1 (verd) i BasC-Nb+Nb_{ctrl} (lila). Volums de retenció marcats en línies verticals. **A-B.** Compatibilitats dels Nb58 i 78 amb el Nb74. Apareixen agregats de major pes molecular en ambdós casos (fletxes vermelles). **C-D.** Incompatibilitat entre els Nb58 i 78 i entre els Nb71 i 74. No es detecta la formació de complex terciari. **E-G.** Representació esquemàtica de les compatibilitats entre Nb citosòlics (taronja) i extracel·lulars (lila). Els Nb que no s'uneixen en basc estan representats semi-transparents. Les compatibilitats estan representades amb fletxes verdes i les incompatibilitats amb fletxes vermelles pels cribratges entre els Nbs extracel·lulars (**E**), citoplasmàtics (**F**) i parelles de la mateixa cara (**G**).

2.8. Cribratge dels nanocossos per dinàmica de la porta citoplasmàtica

Pels estudis de dinàmica i anàlisi de les conformacions de BasC es va utilitzar la tècnica transferència d'energia de ressonància fluorescent per molècules individuals (smFRET) combinada amb l'alternació d'excitació per làsers (ALEX) (Hohlbein et al., 2014) duta a terme en col·laboració amb el laboratori del Dr. Thorben Cordes a l'LMU, Múnic, Alemanya. La tècnica d'ALEX-smFRET es basa en l'excitació alternada amb els làsers apropiats de dos fluoròfors ancorats a residus concrets d'una mateixa molècula (intramolecular). Les poblacions d'eficiència de transferència van ser mesurades sobre diferents variants dobles de cisteïna de BasC analitzades en un rang pM solubilitzades en DDM. L'aplicació d'aquesta tècnica en BasC es basa en els estudis de Majumdar amb el transportador LacY (Majumdar et al., 2007) i el de Zhao amb LeuT (Zhao et al., 2011).

L'objectiu d'utilitzar aquesta tècnica en l'estudi de la dinàmica i conformacions de BasC és poder seleccionar aquells Nbs que confereixin estats diferents que els que ens pogués donar el Nb74 o l'estat apo, el que es creu que és el majoritari en solució. A més de poder estudiar les dinàmiques sense Nb i en la variant d'LPI (BasC K154A). En BasC es van crear diferents mutants de cisteïna en residus clau i prometedors per tal d'ancorar en ells els fluoròfors a través de reaccions de maleimida.

Primer es va dur un anàlisi conformacional de les estructures conegudes en aquell moment. Abans que les primeres estructures de LATs fossin publicades, es van comparar les conformacions d'AdiC oberta enfora (PDB ID 3OB6) i l'estructura oberta endins de BasC (PDB ID 6F2G). AdiC és un transportador homòleg que té un 18 % d'SI amb els LATs eucariòtics, la seva estructura ja coincidia amb les de baixa resolució dels LATs (Rosell et al., 2014). Amb aquest anàlisi i segons les teories del mecanisme de transport pels simportadors d'ions es va concloure estimar les dinàmiques i conformacions de BasC a partir de l'extrem citosòlic del TM1a i l'extracel·lular del TM6a.

Posteriorment, quan es va publicar la primera, i única, estructura d'un LAT tancat per dins, es va repetir l'anàlisi entre les estructures de BasC obert endins (PDB ID 6F2G) i un model de BasC segons la conformació de LAT1 tancat per dins (PDB ID 7DSK) (Figura 22. A). Aquesta nova comparació va permetre corroborar que, en LATs, també s'espera un moviment del TM1a (Figura 22. B), però no del TM6a (Figura 22. C). Els residus de referència per aquestes posicions, en regions que havien de ser immòbils, es van escollir a l'extrem extracel·lular del TM4 (Figura 22. D) i l'extrem citoplasmàtic del TM12 (Figura 22: A), utilitzant avantatjosament la única cisteïna de la seqüència WT de BasC (C427).

Com que es va veure que el TM6a no semblava ser mòbil, es va decidir centrar l'estudi en el moviment del TM1a a la porta citoplasmàtica del transportador cercant l'interès en les parelles dobles de cisteïna entre TM1a-4, TM1a-6 i TM1a-12.

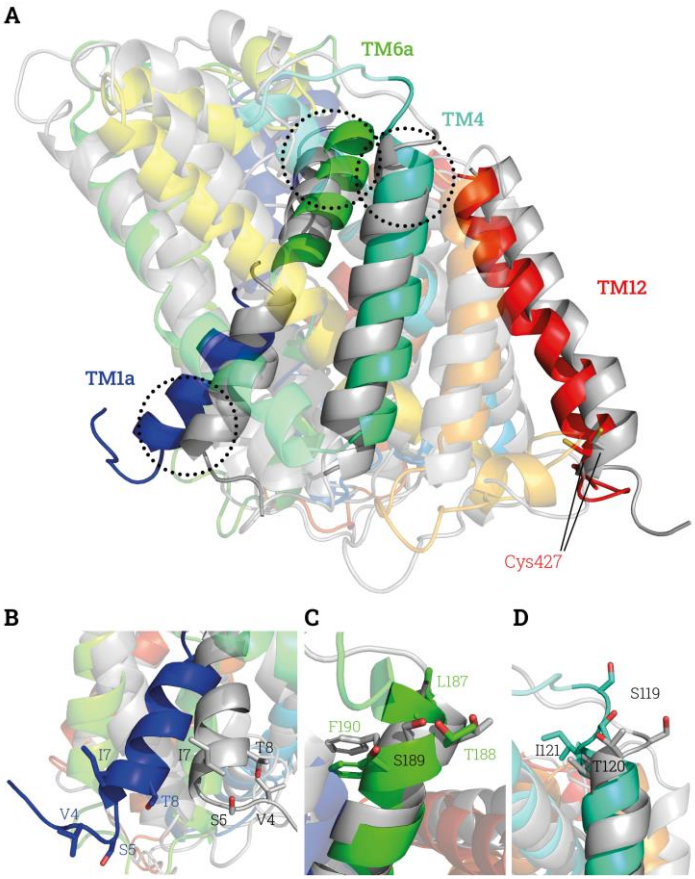

Figura 22. Model de dinàmica en LATs. L'estructura de BasC mirant endins (PDB ID: 6F2G) està representada en arc-iris I el model de BasC segons LAT1 clos per dins (PDB ID 7DSK), en gris. **A.** Visió lateral i general de la superposició d'ambdues representacions. Els TMs seleccionats per l'estudi d'ALEX-smFRET estan ressaltats sent opacs (TM1a en blau, TM6a en verd clar, TM4 en turquesa i TM12 en vermell). La C427 està representada en pals. Els residus seleccionats per mutar a cisteïna estan representats en pals a les ampliacions pel TM1a (**B**), TM4 (**C**) i TM6a (**D**) de les àrees encerclades a l'apartat (A).

2.8.1. Variants de cisteïna

Els diferents mutants simples de cisteïna es van crear per a cada TM i es va mesurar la seva activitat transportadora en PLs (Figura 23) per seleccionar els que permetien a BasC seguir sent funcional. Totes les variants van ser creats sobre la versió lliure de cysteines (C427A). La variant S189C va ser exclosa de l'anàlisi funcional per la seva baixa expressió. El mutant que mantenia més activitat dins de cada TM (I7C pel TM1a, T120C pel TM4, L187C pel TM6a) va ser el seleccionat per crear les variants dobles de cisteïna conjuntament amb la C427 del TM12 i repetir l'anàlisi de transport en PLs per aquestes (Figura 24).

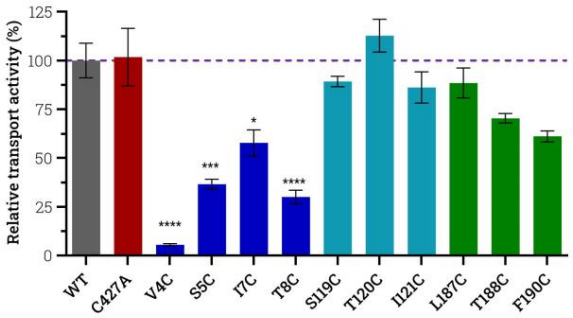

Figura 23. Activitat de transport relativa dels mutants de cisteïna simples. Activitat d'influx relativa de 10 µM L-[^{3}H]-Ser (1 µCi/µl) a dins de PLs plens de 4 mM L-Ala contenint les variants de cisteïna simples de BasC-GFP. Es mostren BasC WT (gris), lliure de cysteines (C427A en vermell) i els mutants simples per TM: TM1a (V4C, S5C, I7C i T8C en blau fosc), TM4 (S119C, T120C i I121C en turquesa) i TM6a (L187C, T188C i F190C en verd fosc). Les dades mostrades (mitjana ± s.e.m.) provenen dels triplicats d'un experiment. T-test * $p < 0.05$, *** $p < 0.005$, **** $p < 0.001$.

Aquestes variants dobles de cisteïna seran anomenades d'ara en endavant com es mostra a continuació: TM1a-12 (I7C-C427), TM1a-4 (I7C-T120C-C427A), TM1a-6a (I7C-L187C-C427A), TM4-12 (T120C-C427), TM4-6a (T120C-L187C-C427A) and TM6a-12 (L187C-C427). En quant a la selecció de mutants, només el mutant de cisteïnes entre el TM1a i TM6a va ser el que perdia més del 50 % de l'activitat, i va ser descartat. Com que s'havia decidit analitzar el moviment de la porta interna prenent el TM1a com a referència, les variants dobles de cisteïna per Bas finalment utilitzades van ser la TM1a-4 i la TM1a-12.

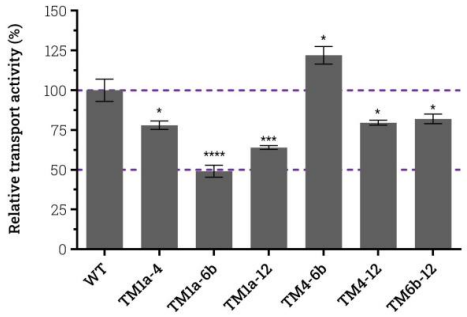

Figura 24. Activitat de transport relativa de les variants dobles de cisteïna. Activitat d'influx relativa de 10 µM L-[^{3}H]-Ser (1 µCi/µl) a dins de PLs plens de 4 mM L-Ala contenint les variants dobles de cisteïna de BasC-GFP. Les dades mostrades (mitjana ± s.e.m.) provenen dels triplicats d'un experiment. T-test * $p < 0.05$, *** $p < 0.005$, **** $p < 0.001$.

2.8.2. Efecte dels nanocossos sobre la porta citosòlica de BasC

Els efectes dels Nbs sobre la conformació de BasC es poden veure per cadascuna de les variants de cisteïna dobles de BasC utilitzades segons el seu marcatge amb les diferents parelles de fluoròfors (sCy3-sCy5 o Alexa 546-Alexa 647) (Figures 27-28).

Primerament, per la variant doble de cisteïnes TM1a-4 marcada amb sCy3-sCy5 (Figura 27), podem detectar una sola població en condicions apo (Figura 27. A-B) que s'obre (disminueix la seva *E**) quan s'afegeix Nb71 i 51. Tot i que el Nb59 no mostra resultats estadísticament significatius, presenta la tendència d'obrir-lo també. En el sentit contrari, podem veure com el Nb74 tanca el transportador mentre que també ho fan el Nb53 i 58 en la seva mesura (Figura 27. B-C). El Nb78 també va mostrar la tendència d'incrementar la *E**. El resum de tots els efectes dels Nbs en aquesta variant doble de cisteïna es troba a la Figura 27. C.

Els mateixos Nbs van ser assajats sobre la variant doble de cisteïnes TM1a-12 marcada amb sCy3-sCy5 (Figura 28). Es van obtenir resultats similars. Es mostrava una sola població per les condicions apo (Figura 28. A-B) i els diferents desplaçaments de tancament o obertura de la porta citosòlica segueixen la mateixa direcció per cadascun dels Nbs (Figura 28. B-C).

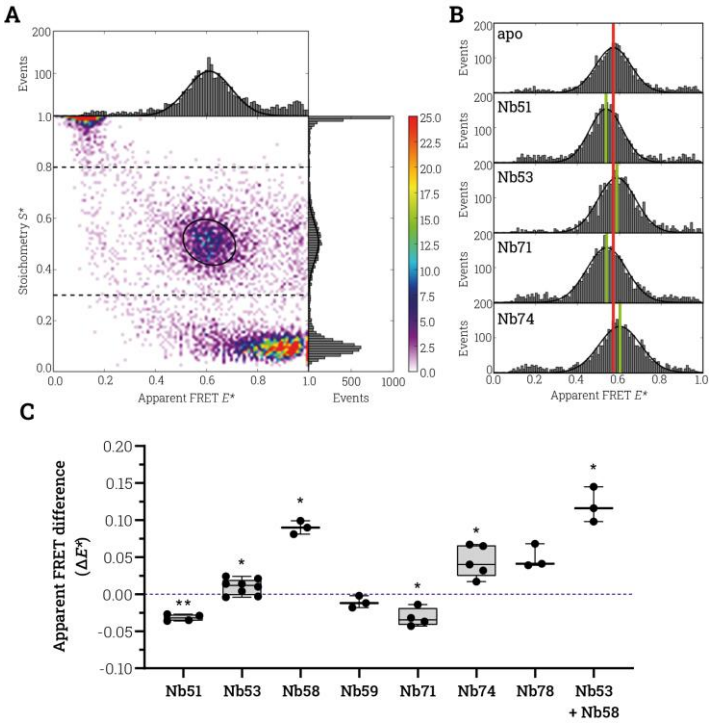

Figura 27. Efecte dels Nb sobre la variant doble de cisteïna TM1a-4 marcada amb sCy3-sCy5. Anàlisi per ALEX-smFRET en difusió sobre BasC solubilitzat en DDM. **A.** Histogrames complets E^* vs. S^* per apo en mode APBS. Una sola població és detectada amb E^* = 0.612 i S^* = 0.505. **B.** Histogrames representatius d'esdeveniments vs. E^* del mateix dia per l'apo, Nb51, 53, 71 i 74 en mode DCBS. Els Nbs es van afegir a una concentració mínima d'1 µM. Les línies verticals vermelles marquen la població d'apo i les verdes les de cadascun dels Nbs. **C.** Mitjana ± s.e.m de totes les mesures preses per cada Nb (a 1 µM mínim). Valors expressats en ΔE^* respecte l'apo del mateix dia. T-tests aparellats fets amb els valors absoluts entre el valor de la població del Nb i l'apo del mateix dia (* p.valor < 0.05, ** p.valor < 0.01).

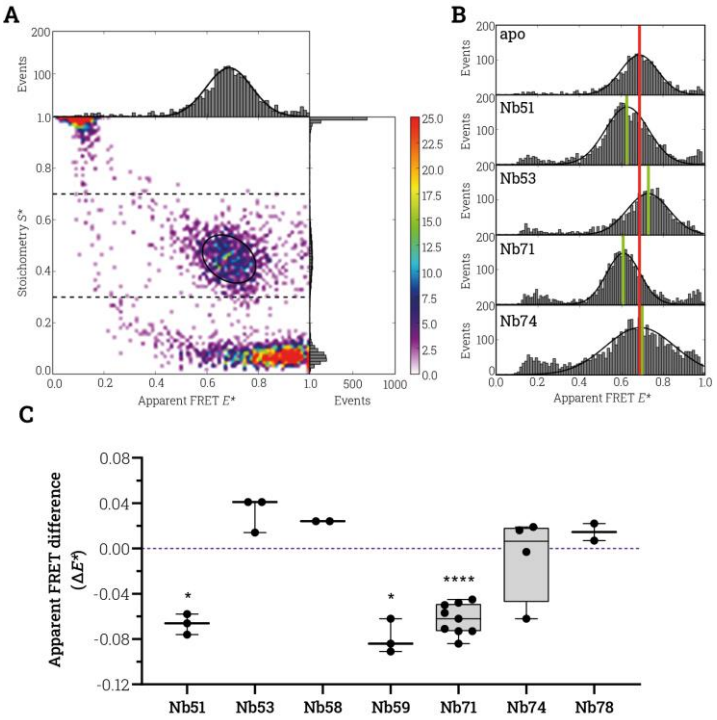

Figura 28. Efecte dels Nb sobre la variant doble de cisteïna TM1a-12 marcada amb sCy3-sCy5. Anàlisi per ALEX-smFRET en difusió sobre BasC solubilitzat en DDM. **A.** Histogrames complets E^* vs. S^* per apo en mode APBS. Una sola població és detectada amb E^* = 0.687 i S^* = 0.447. **B.** Histogrames representatius d'esdeveniments vs. E^* del mateix dia per l'apo, Nb51, 53, 71 i 74 en mode APBS. Els Nbs es van afegir a una concentració mínima d'1 µM. Les línies verticals vermelles marquen la població d'apo i les verdes les de cadascun dels Nbs. **C.** Mitjana ± s.e.m de totes les mesures preses per cada Nb (a 1 µM mínim). Valors expressats en ΔE^* respecte l'apo del mateix dia. T-tests aparellats fets amb els valors absoluts entre el valor de la població del Nb i l'apo del mateix dia (* p.valor < 0.05, **** p.valor < 0.0001).

2.8.3. Estructura de BasC en nova conformació

L'estructura de BasC s'ha resolt a baixa resolució en complex amb els Nb53 i 58 per cristal·lografia de raigs X (Figura 33) i amb el Nb71 per cryo-EM (Figura 35).

Cap de les dues estructures mostra una conformació diferent, malgrat els resultats d'ALEX-smFRET semblaven indicar-ho. Malgrat aquest resultat inesperat i la baixa resolució de les estructures, es poden definir les regions d'interacció de cada Nb amb BasC per la proximitat de les densitats electròniques, tant per l'obtinguda per cristal·lografia de raigs X (BasC-Nb53-58) com per l'obtinguda per cryo-EM (BasC-Nb71).

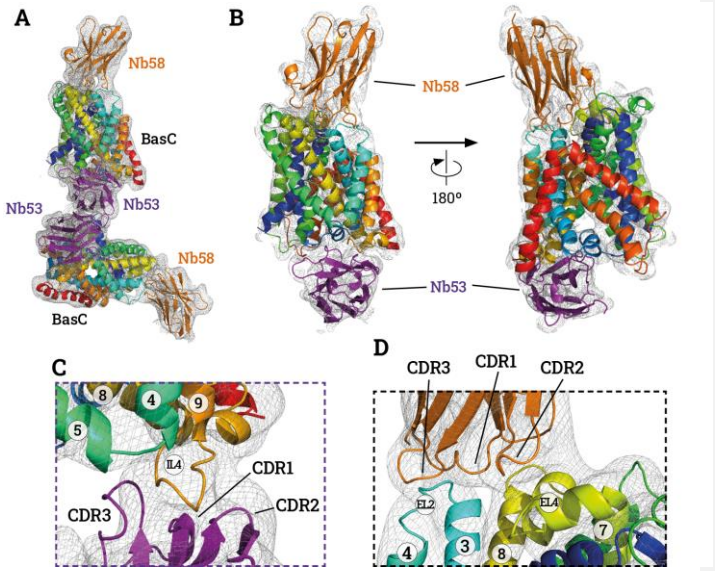

Figura 33. Estructura del complex BasC-Nb53-58. Densitat electrònica del complex BasC-Nb53-58 (xarxa gris) on es mostra BasC (arc iris) modelat a partir del BasC de l'estructura del complex BasC-Nb74 (PDB ID 6F2W) (Errasti-Murugarren et al., 2019). Els Nb53 I 58 també es mostren en lila i taronja, respectivament. **A.** Visió general dels contactes entre complexes a través dels respectius Nb53. B. Perpsectiva lateral d'un únic complex. La conformació és mirant cap a dins, oberta. El Nb53 (lila) s'uneix a la part citosòlica i el Nb58 (taronja) a l'extracel·lular. La cavitat citosòlica roman oberta i accessible deixant accessible el lloc d'unió al substrat per part d'aquest des del citosol. **C.** Detall de la interacció del Nb53 amb BasC a través de l'IL4. **D.** Detall de la interacció del Nb58 amb BasC a través de l'EL2 i 4.

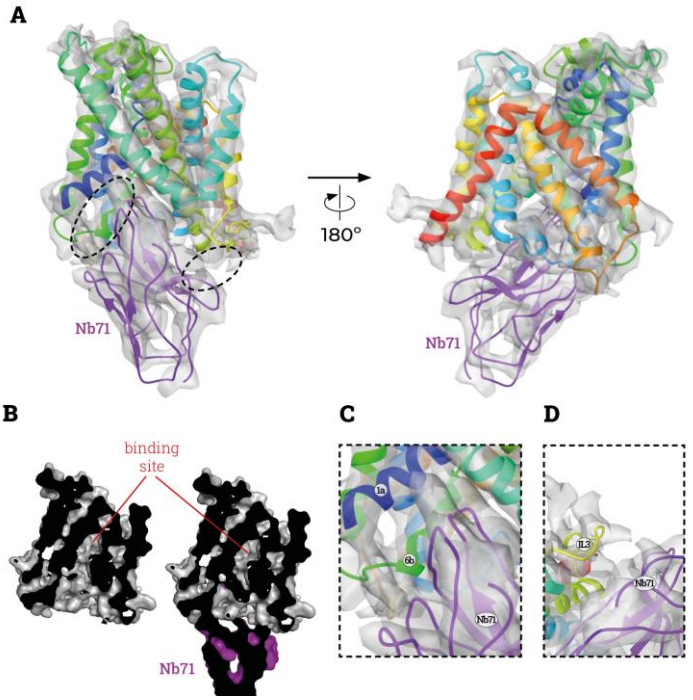

Figura 35. Estructura del complex BasC-Nb71. Estructura modelada de BasC (arc iris) a partir de BasC de l'estructura del complex BasC-Nb74 (PDB ID: 6F2W) (Errasti-Murugarren et al., 2019). També s'hi representa el modelatge de Nb71 (lila) **A.** Visió lateral del complex en conformació mirant cap a dins i apo. El Nb71 interacciona amb BasC des de la cara citosòlica ocupant la cavitat que dóna accés al lloc d'unió al substrat des del citosol (**B**) i interaccionant amb dues parts, oposades, d'aquesta cavitat: els TM1a i 6b (**C**) i l'IL4 (TM8-9) (**D**). **B.** Representacions tallades de l'estructura amb (dreta) i sense (esquerra) el Nb71. El camí obert de la cavitat citosòlica que s'observa a l'esquerra, per la qual es dona accés al lloc d'unió al substrat des del citosol, queda obstruït i truncat per la unió del Nb71, a la dreta. **C-D.** Detall de la interacció entre el Nb71 i els TM1a i 6b (**C**) i entre el Nb71 i l'IL4 (**D**). Els possibles residus responsables d'aquesta es mostren marcats a la figura, mostrant-ne les seves cadenes laterals.

2.8.4. Efecte dels nanocossos a la mobilitat dels fluoròfors

Després de veure que les conformacions no eren diferents a la ja resolta amb anterioritat (Errasti-Murugarren et al., 2019) es va analitzar el possible efecte

estèric dels Nbs als AV dels fluoròfors en BasC. Es va comprovar que la presència de Nb71 desplaçava el centre dels AV dels fluoròfors a la posició del TM1a, I7C (Figura 36). Aquesta diferència de desplaçaments eixamplaria la distància entre fluoròfors de la variant doble de cisteïna marcada amb sCy3 i sCy5 de 55.47 a 57.33 Å. Aquest desplaçament podria ben ser el detectat per ALEX-smFRET en les mesures del Nb71. Pel Nb53, l'altre Nb citosòlic amb estructura coneguda, també es va estudiar però no s'hi va veure efecte (dades no mostrades).

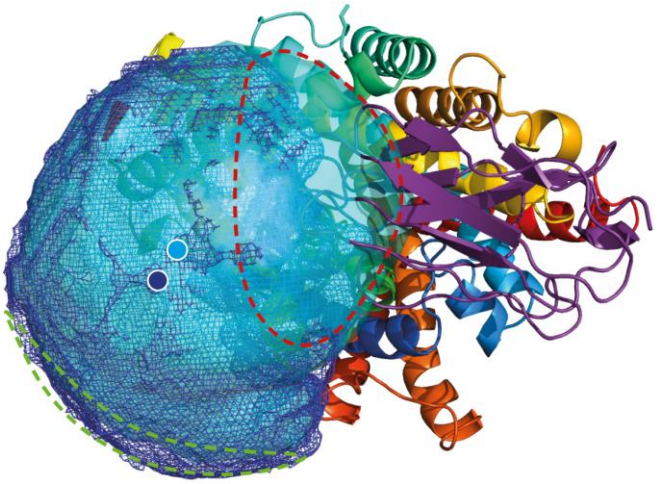

Figura 36. Efecte del Nb71 sobre els volums accessibles dels fluoròfors en TM1a. Visió citoplasmàtica del complex BasC-Nb71 amb els AV de sCy3 en posició TM1a, I7C per l'estructura de BasC oberta cap a dins ja publicada (PDB ID: 6F2W) i l'estructura del complex BasC-Nb71 en blau fosc i cian, respectivament. El Nb71 desplaça els centres dels AV (circumferències pintades com els seus AV) mossegant una part del volum (àrea encerclada en vermell) i empenyent l'AV cap a l'exterior (àrea encerclada en verd).

3. Dinàmica i disfuncions de la porta citoplasmàtica

Paral·lelament al cribratge dels Nbs per la conformació que obliguen a BasC es va estudiar l'efecte dels substrats i les disfuncions associades a la variant relacionada amb LPI d'aquest moviment citoplasmàtic.

3.1. Efecte dels aminoàcids sobre la porta citosòlica de BasC

L'efecte dels substrats també va ser analitzat per ALEX-smFRET. L'L-Ala es va assajar sobre tres diferents mostres: TM1a-4 i TM1a-12 marcats amb sCy3 i

sCy5 i també sobre TM1a-12 marcat amb Alexa 546-Alexa 647 (Figura 38). En tots els casos l'L-Ala augmentava l'*E**, tancava el transportador, cadascuna en diferents mesures. També feia el mateix efecte l'L-Ser, però no l'L-Gln (Figura 38. A).

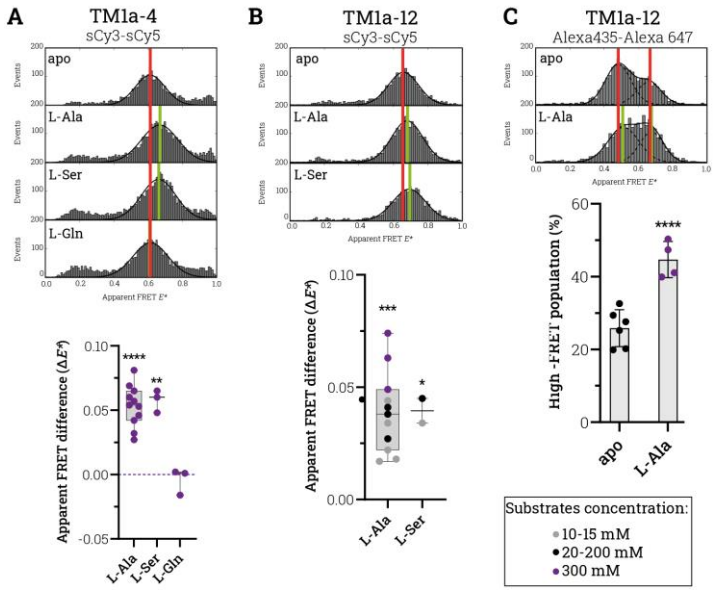

Figura 38. Efecte dels aminoàcids a la dinàmica del TM1a. Efectes de l'L-Ala, L-Ser i L-Gln en les variants dobles de cisteïna de BasC TM1a-4 marcat amb sCy3-sCy5 (**A**), TM1a-12 marcat amb sCy3-sCy5 (**B**) i TM1a-12 marcat amb Alexa 546-Alexa 647 (**C**). **A-C (superior).** Histogrames d'esdeveniments vs. *E** de les condicions apo i holo per cada variant de BasC. Les línies verticals vermelles marquen les poblacions de les condicions apo, mentre que les verdes marquen les de les condicions holo. **A-C (inferior).** Mitjana ± s.e.m. d'experiments independents (punts). La concentració de l'AA utilitzat es mostra segons la llegenda: per les baixes concentracions (de 10 a 15 mM) en gris, les mitjanes (de 20 a 200 mM) en negre i les altes (300 mM) en lila. Un increment d'*E** s'aprecia per l'L-Ala i l'L-Ser (A-B) i no per l'L-Gln (A). L'Ala augmenta la quantitat d'esdeveniments de la població d'alt FRET. Anàlisi estadístic per T-test aparellat entre els valors absoluts d'apo i holo del mateix dia (A-B) o entre els percentatges de les poblacions d'alt FRET d'apo i holo del mateix dia (C). (* p.value < 0.05, ** p.value < 0.01, *** p.value < 0.005 and **** p.value < 0.001).

3.2. Disfuncions de la dinàmica del TM1a associades a la variant relacionada a la LPI

Un cop analitzats els efectes dels substrats sobre la dinàmica del TM1a de la porta citosòlica de la variant salvatge de BasC es va prosseguir amb l'anàlisi del mateix moviment en la variant malalta d'LPI, BasC K154A. Les variants dobles de cisteïna TM1a-4 i TM1a-12 es van generar sobre la variant de K154A i marcar amb sCy3-sCy5 i Alexa 546-Alexa 647, respectivament.

En les mesures d'ALEX-smFRET es va poder comprovar com el comportament d'aquesta variant d'LPI és diferent al de la variant salvatge quan s'administrava substrat (300 mM d'L-Ala) (Figura 41). En el cas de la variant doble de cisteïna TM1a-4 la població apo de la variant malalta no responia a un augment d'E* quan s'administrava substrat (Figura 41. A). I en el cas de la variant doble de cisteïna TM1a-12, no només no respon a substrat, si no que les poblacions en apo són totalment diferents. En aquesta última variant doble de cisteïnes, la variant malalta d'LPI en apo presenta sols una població, a diferència de les dues que mostra la variant salvatge. I aquesta població tan sols es mou 0.014 punts d'E* tancant-se, sense resultar estadísticament significatiu i, ni de bon tros, similar al comportament de la salvatge (Figura 41. B)

Amb aquests resultats, s'assumeix que la variant d'LPI no pot tancar la porta citosòlica tal i com ho fa la varietat salvatge responent a l'addició de substrat. Aquest fet constitueix la primera evidència experimental del mal funcionament en transport d'aquesta variant i, per tant, posa de relleu la importància del residu de Lys, K154 en BasC, tan conservat entre tots els membres de la subfamília LAT.

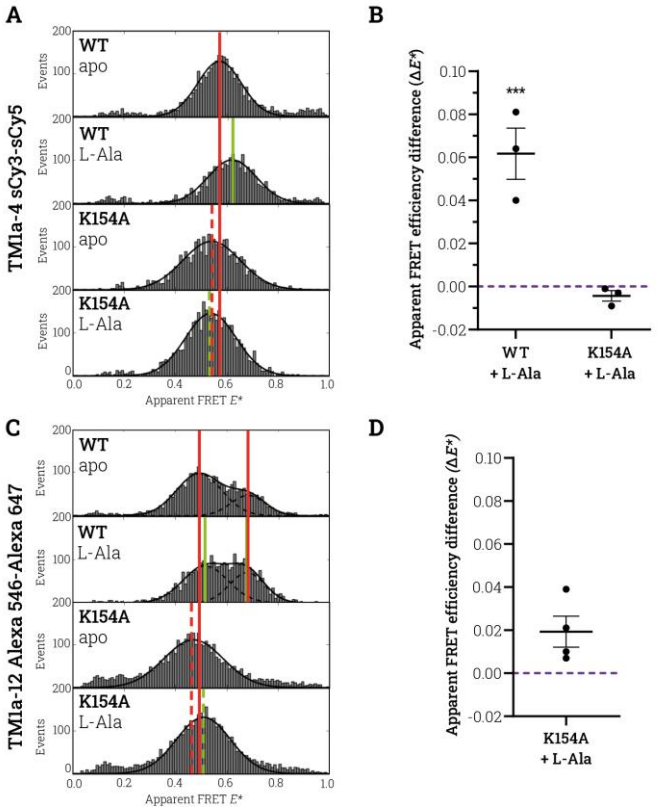

Figura 41. Dinàmica de la variant K154A de BasC. Experiments d'ALEX-smFRET sobre la variant K15A de BasC sobre les variants dobles de cisteïna TM1a-4 (A-B) i TM1a-12 (B-C) marcades amb sCy3-sCy5 i Alexa 546-Alexa 64, respectivament. **A i C.** Histogrames representatius d'esdeveniments vs. *E** per les dues variants, salvatge i K154A, de BasC en apo i holo (300 mM L-Ala). Les línies vermelles verticals marquen les poblacions apo de la variant salvatge (continua) i de la K154A (puntejada). Les línies verdes marquen les poblacions holo de les variants salvatges (continua) i de la K154A (puntejada). **B i D.** Comparació de les l'efecte del substrat (300 mM d'L-Ala) en les poblacions salvatges i/o K154A. Es mostra la mitjana +- s.e.m. de les dades obtingudes de tres experiments de dies diferents. T-tests fets sobre els valors absoluts dels valors d'apo i holo del mateix dia dins de les mateixes variants. Només es detecta significança estadística per la variant salvatge com ja s'ha mostrat anteriorment (Figura 37).

3.3. Efecte dels nanocossos en bloquejar l'efecte induït pels substrats en tancar la porta citoplasmàtica

És clar que els substrats, doncs, són responsables del tancament del TM1a de la porta citosòlica de BasC. En aquest punt, es va provar de bloquejar aquest efecte dels substrats amb la unió de Nbs (Nb53, 71 i 74) (Figura 42) utilitzant la variant doble de cisteïna TM1a-4 de BasC marcada amb sCy3-sCy5. Es va comprovar com el Nb53 no era capaç de bloquejar aquest efecte (Figura 42. A), mentre que el Nb71 sí el bloquejava (Figura 42. C). A mig camí entre un i l'altre, el Nb74 bloqueja parcialment aquest moviment, permetent, tot i així, que el TM1a es mogui en gran part (Figura 42. B). A part, l'efecte bloquejador del Nb71 també es va assajar amb la variant doble de cisteïna TM1a-12 de BasC marcada amb Alexa 546-Alexa 647. En aquesta mostra també es va veure com el Nb71 mantenia una sola població de FRET encara que s'afegís L-Ala (Figura 42. D).

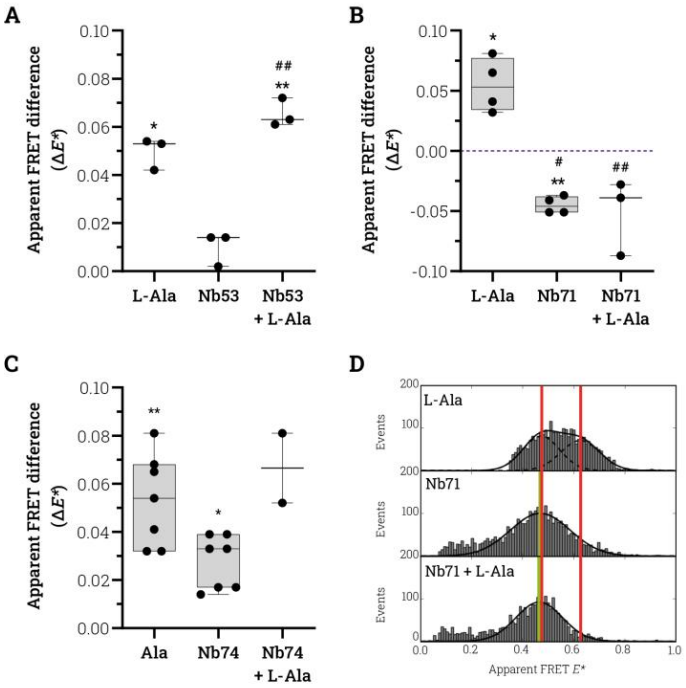

Figura 42. Efecte dels Nb contra l'efecte dels substrats. (*a la pàgina anterior*) Experiments d'ALEX-smFRET sobre les variants dobles de cisteïna TM1a-4 de BasC marcada amb sCy3-sCy5 (**A-C**) i TM1a-12 marcada amb Alexa 546-Alexa 647 (**D**). Els Nbs van ser afegits al menys a 1 µM i l'L-Ala a 300 mM. **A-C.** Mitjana ± s.e.m. de diferents experiments (punts). Anàlisi estadístic fet a partir de T-tests aparellats entre cadascun dels punts i l'apo del mateix dia en valors absoluts. * p.value < 0.05 and ** or ## p.value < 0.01. **A.** Nb53 no bloqueja el moviment del TM1a induït per substrat. L'amplitud d'aquest increment induït per substrat és de 0.055 o 0.049 amb i sense Nb53, respectivament. **B.** Nb71 bloqueja el moviment del TM1a induït per substrat. No s'observa cap increment d'*E**amb el Nb71. **C.** Nb74 permet el moviment del TM1a induït per substrat en una amplitud de 0.039 en comparació l'amplitud de 0.053 en la seva absència. **D.** Experiment de l'efecte bloquejant per part del Nb71 vers el moviment del TM1a induït per substrat. Nb71 manté una sola població de FRET amb i sense L-Ala.

4. Perspectives de futur: nanodiscs

Es va aconseguir la reconstitució de BasC en nanodiscs (ND) amb l'objectiu d'estudiar-ne la seva estructura per cryo-EM i la seva dinàmica per ALEX-smFRET en un entorn amfipàtic més fidel al fisiològic.

La reconstitució es va dur a terme sobre la proteïna de bastida 1D1 (MSP1D1) i POPC com a lípid amb la ràtio molar de 0.1:1:50 (BasC-GFP:MSP1D1:POPC). La deslipidació de les mostres després d'ajuntar-les es va dur a terme mitjançant BioBeads. I la mostra es va córrer per SEC en una columna Superosa 6 10/300 GL abans i després de la purificació dels ND plens a través de l'etiqueta d'histidines i tallant amb la proteasa 3C entre BasC i GFP (Figura 43. A) i la presència de BasC en els NDs de MSP1D1 es va comprovar per electroforesi en gels de poliacrilamida (Figura 43. B). Les imatges de cryo-EM obtingudes amb un microscopi de 100 kV mostren una homogeneïtat de les mostres d'entre 85 i 112 A (Figura 43. C).

Paral·lelament la variant salvatge de BasC i doble cisteïna TM1a-4 marcada amb sCy3-sCy5 (Figura 46. A) va ser reconstituïda en ND. En aquest cas no es van poder seleccionar els ND plens dels buits, per l'ús previ de l'etiqueta d'His durant el procés de marcatge. Malgrat això, els ND plens de BasC marcat es separaven dels buits per SEC en una columna Superdex 200 increase 3.2/300 (Figura 46. A) i es van recollir les fraccions que contenien marcatge, es van congelar en nitrogen líquid i preservar a -80 ºC fins el seu assaig per ALEX-smFRET. La baixa concentració dels ND amb BasC marcat només van permetre poder mesurar en condicions apo i holo (Figura 46. B-C) i, sorprenentment, BasC es mostrava més tancat que solubilitzat en detergent (Figura 27 i 37. A). En ND aquesta mostra va resultar tenir una població d'E* = 0.665, (Figura 46. B), mentre que en DDM era menor, 0.598. A més a més, aquesta mostra no va respondre a l'addició de substrat tancant-se (Figura 46. C). El fet que en ND BasC sembli estar tancat en apo i sense respondre quan s'afegeix substrat, podria venir donat per com la membrana lipídica podria estar forçant els AV dels fluoròfors a adoptar posicions més properes, al quedar les posicions a ser marcades dins d'aquesta (Figura 47).

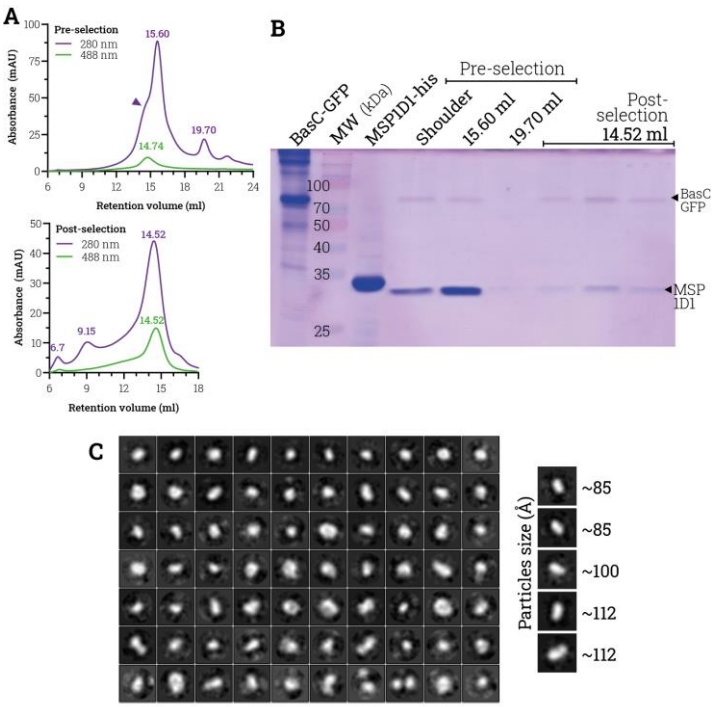

Figura 43. Cryo-EM de BasC en ND. A. BasC-GFP-his reconstituït en ND en relació molar 0.1:1:50 (BasC:MSP1D1:POPC), les mostres es van injectar abans (superior) i després (inferior) de ser seleccionades per l'etiqueta d'His. Els perfils de SEC mostren la lectura d'absorbància a 280 (proteïna) i 488 nm (GFP). A la part superior es pot veure la diferència entre els ND plens (elueixen a 14.74 ml) i buits (elueixen a 15.60 ml). **B.** Electroforesi en gel de poliacrilamida tenyit en blau de coomassie amb els diferents pics carregats de les dues SECs de l'apartat (**A**). BasC es detecta en totes les fraccions excepte al pic de 19.70, que segurament siguin molècules no dimeritzades de MSP1D1. La relació de marca entre BasC i MSP1D1 de les mostres de la post-selecció mostren que una sola molècula de BasC estaria reconstituïda per cada ND. **C**. BasC en ND classes mitges de 2D classificades per CryoSPARC. La mida de les partícules des d'una perspectiva lateral es mostren en Å.

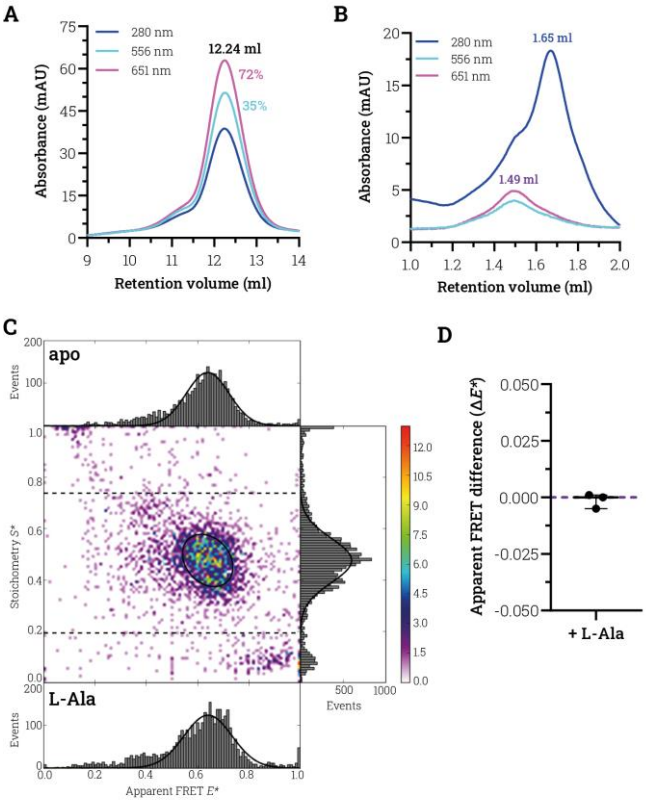

Figura 46. Dinàmica del TM1a en BasC reconstituït en ND. Variant salvatge de BasC i doble cisteïna TM1a-4 marcat amb sCy3-sCy5 i reconstituït en MSP1D1ND estudiat per ALEX-smFRET. **A.** SEC en columna Superdex 200 10/300 GL de la mostra de BasC marcada solubilitzada en DDM abans de reconstituir-la en NDs. **B.** SEC en columna Superdex 200 increase 3.2/300 GL de la mostra de BasC marcada reconstituïda en ND. Els ND buits elueixen a 1.65 ml i els plens a 1.49 ml. **C.** Histogrames complets d'E^* vs. S^* representatius en mode APBS en apo (superior). Histograma representatiu d'esdeveniments vs. E^* de l'holo (300 mM L-Ala). Una única població és detectada en ambdós casos, a E^* = 0.640 i 0.641 per l'apo i l'holo, respectivament. **D.** Mitjana ± s.e.m. de mesures triplicades de dies diferents de la diferència d'E* entre l'holo i l'apo de cada dia. No s'observa significança estadística al fer T-tests aparellats entre els valors absoluts d'apo i holo aparellats per cada dia.

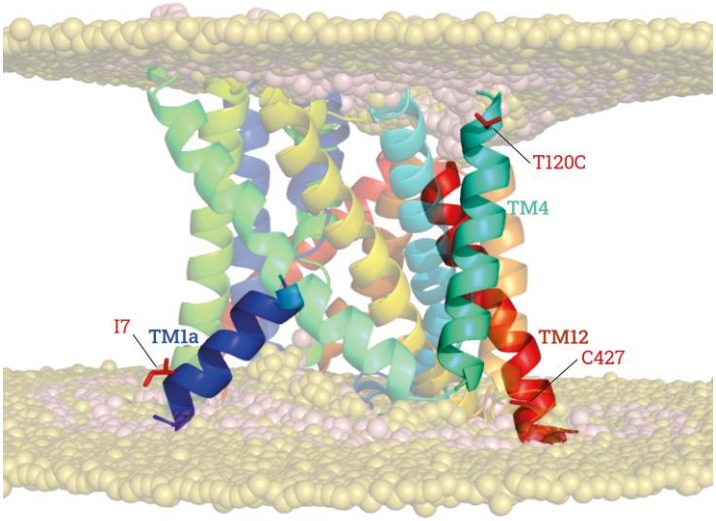

Figura 47. Simulació de la membrana lipídica per BasC. Simulació d'una membrana lipídica de DPPC (esferes) on s'hi reconstituiria BasC (arc iris). Les posicions de cisteïna marcades i analitzades per ALEX-smFRET en aquesta tesi, I7 (TM1a), T120 (TM4) i C427 (TM12), es mostren en barres i totes queden dins de la membrana.

Discussió

En la cerca de noves conformacions dels LATs

Ja hem vist com malgrat tots els esforços de la comunitat científica per resoldre les estructures de PMs des de l'inici de la XRC ha sigut molt difícil obtenir-ne. Actualment l'ús dels detergents és clau, però s'està començant ja a emprar altres entorns amfipàtics més similars als fisiològics, com els ND, i a utilitzar la cryo-EM per resoldre estructures en altres conformacions i en aquest nou entorn. Serà aquest el nou enfoc que permetrà obtenir més estructures i en conformacions diferents?

Fins el moment les estructures dels LATs s'han resolt en una conformació majoritària, la mirant cap endins. Aquest fet destaca el que seria la conformació predominant i més estable dels LATs. Les úniques estructures que s'han resolt en conformacions mirant cap enfora han estat gràcies a la unió d'inhibidors, el que sembla ser l'únic mode d'aconseguir que els LATs adoptin aquests estats.

Al llarg de la tesi s'han utilitzat els Nbs amb l'esperança de forçar a BasC a adoptar conformacions obertes cap a fora, essent insuficient per aquest objectiu. S'ha pogut observar com la gran majoria dels Nbs s'uneixen per la cara interior del transportador, això significaria que o bé BasC exposa una major superfície per la cara citosòlica o bé que la cara citosòlica és menys mòbil que l'extracel·lular, i com a conseqüència, més accessible pels Nbs. A més a més, pel cribratge de Nbs fet en quant a dinàmica del TM1a, no s'ha pogut detectar cap Nb que destaqués en tancar la proteïna en una mesura similar a la que ho induïen els substrats. En aquest sentit, s'ha pogut constatar com l'enfoc de la tècnica ALEX-smFRET en BasC i Nb no ha estat del tot apropiada i hi ha hagut factors importants que no havien estat contemplats.

El primer d'aquests factors és l'efecte estèric que els Nbs poden efectuar sobre els AV dels fluoròfors. Que poden afectar la lectura del FRET i emmascarar l'efecte conformacional que poden efectuar a BasC. L'altre factor seria l'efecte que les micel·les de detergent poden efectuar sobre els AV dels fluoròfors, fins ara no descrit a la literatura. Un efecte que es desconeix si seria de repulsió o afinitat, però que per la proximitat dels residus d'unió als fluoròfors i la micel·la de detergent haurien de ser contemplats. Aquest efecte de les micel·les dels detergents també es pot traduir a l'efecte que pot efectuar la bicapa de lípids dels NDs que hem vist en les lectures de FRET quan BasC estava reconstituït en ND.

En aquest sentit nous residus es podrien seleccionar a l'hora de dissenyar propers experiments de dinàmica per FRET (ALEX-smFRET; TIRF-smFRET). Residus situats a les regions més allunyades de les cares hidrofòbiques de la proteïna on es situen les micel·les de detergents i els lípids de les membranes. Així com estudiar i canviar, si s'escau, el tipus de detergent emprat per la solubilització en els experiments d'ALEX-smFRET així com els lípids que s'utilitzen per construir els NDs amb BasC reconstituït.

Desxifrant el mecanisme de transport dels LATs

Hem vist com els simportadors de sodi en condicions apo tendeixen a adoptar una conformació mirant cap a fora, així ho constaten els estudis de TIRF fets amb LeuT (Zhao et al., 2011). Mentre que per estudis d'ALEX-smFRET en BasC, en condicions apo aquest adopta una conformació mirant cap a dins.

En els nostres estudis de BasC l'adició de substrat ha suposat en totes les mesures preses un tancament del TM1a per la porta citosòlica. El fet que veiem diferents poblacions, malgrat el mateix comportament de tancament citosòlic, pot ser degut a la naturalesa dels fluoròfors emprats fent que l'ús de la parella sCy3-sCy5 no permeti distingir entre les dues poblacions existents que sí s'han pogut discernir emprant la parella de fluoròfors Alexa 546-Alexa 647. A més, l'adició de substrats no ha abolit per complet l'existència de la conformació oberta per dins, deixant entreveure el possible augment de la velocitat d'intercanvi entre conformacions o l'estabilització de la conformació tancada respecte aquest estat en les condicions apo.

Tenint en compte tots els efectes i conformacions detectades en les condicions apo i holo, podem dir que els LATs tendeixen a estar oberts cap a dins. I tan sols el transport de substrat de dins cap a fora pot fer tancar-lo per dins. Un cop oberts cap a fora, els transportadors tornarien ràpidament a la conformació oberta cap a per l'alta afinitat de substrat que aquests presenten per la cara extracel·lular.

En quant l'efecte inhibidor o no-inhibidor dels Nb53, 71 i 74 de l'efecte del substrat en la dinàmica del TM1a, poden inferir amb les estructures resoltes el seu paper segons les interaccions establertes entre aquests Nbs i les regions de BasC.

En primer lloc, hem pogut veure com el Nb71 bloquejava el moviment del TM1a induït pel substrat. I l'estructura ens mostra com aquest Nb interacciona amb BasC directament amb BasC per la cara citosòlica amb el TM1a, també amb el TM6b i, a l'altra cara d'aquesta cavitat citosòlica, amb l'IL3. AL mateix temps, el Nb71 bloqueja l'accés del substrat al lloc d'unió al substrat ocupant l'espai de la cavitat citosòlica. Aquests dos factors són els responsables del bloqueig del Nb71 sobre l'efecte del substrat i els que permeten validar totes les mesures tretes per ALEX-smFRET al constatar i evidenciar la interacció amb el TM1a i la inhibició del moviment induït per substrat.

De manera oposada, el Nb53 no bloqueja el moviment del TM1a induït per substrat. I l'estructura de BasC-Nb53-58 ha permès veure com aquest Nb tan sols interacciona amb basc per l'IL3, deixant lliure el TM1a i l'accés del substrat al lloc d'unió al substrat. Permetent doncs que el TM1a es pugui seguir movent malgrat el transport de substrat quedi inhibit. Bé perquè el moviment del TM1a no és complet o el tancament del TM5 queda compromès per la interacció del Nb53 amb l'IL3.

A mig camí entre el Nb71 i el Nb53 trobem el Nb74 el qual per dinàmica del TM1a hem pogut veure com la unió del Nb74 seguia permetent un moviment incomplet

del TM1a. A l'estructura de BasC-Nb74 publicada podem veure com el Nb71 interacciona amb el TM2, 6b, 8 i l'IL4 i no obstrueix l'accés del substrat al lloc d'unió al substrat. De tal manera que el substrat podria induir el tancament del TM1a, però aquest no es podria dur a terme en la seva totalitat ja que el Nb74 ocupa part de la cavitat citosòlica i interacciona amb altres TMs que acompanyen el TM1a en el tancament de la porta citosòlica.

A més a més, hem pogut constatar com la variant d'LPI, BasC-K154A, és incapaç de tancar la porta citosòlica de la mateixa manera que ho fa el transportador de varietat salvatge, BasC-WT. Aquest fet comporta la primera evidència experimental del funcionament erroni d'aquesta varietat de malaltia, posant de manifest el rol clau que la Lys conservada del TM5 en LATs té pel tancament de la porta citosòlica.

En aquest punt es pot relacionar el mecanisme de transport descrit pels simportadors de sodi amb plegament APC amb el mecanisme de transport dels LATs. Ja que la Lys conservada dels LATs es troba dins el motiu conservat dels transportadors NSS GX_nP (Figura 48. A-B), el responsable de la solvatació de l'Na2 i el conseqüent desencadenament de la translocació de substrat cap al citosol. En LATs, aquest paper el faria aquesta Lys, permetent l'obertura i tancament idoni de la porta citosòlica segons la interacció d'aquesta amb els TM1a i 8. En els LATs humans, el motiu GX_nP no és present i només contenen la Lys conservada (K204 en LAT1) (Figura 48. C) i BasC podria ser el model perfecte per la traducció del mecanisme de transport dels NSS als LATs tot analitzant les interaccions amb el TM1a per part del substrat i la Lys del TM5. Aquesta Lys conservada de LATs es podria confondre amb la Lys o Arg que també està conservada dins el motiu GX_nP dels NSS, malgrat aquesta no tingui la mateixa funció al estar situada més avall del TM5 i no s'involucri en les interaccions de l'Na2 (Figura 48. A).

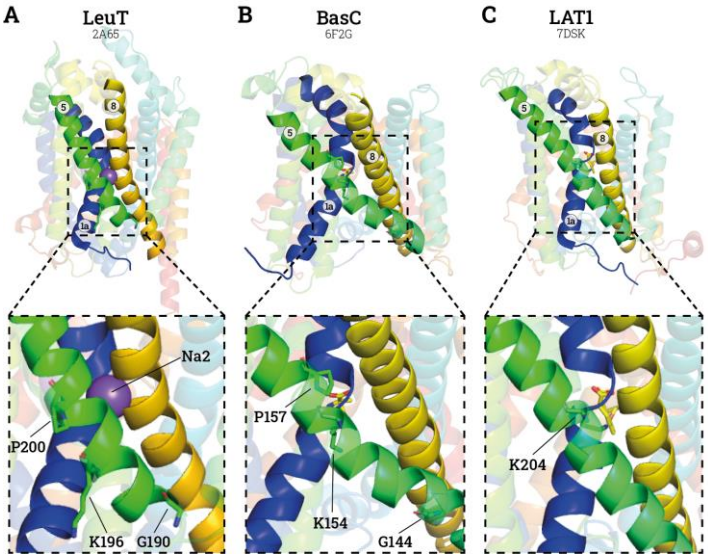

Figura 48. Interaccions entre els residus del TM5 dels transportadors amb plegament APC. Estructures de LeuT mirant a fora (PDB ID 2A65) (Yamashita et al., 2005) (**A**), BasC mirant a dins (PDB ID 6F2G) (Errasti-Murugarren et al., 2019) (**B**) i LAT1 mirant a fora (PDB ID 7DSK) (Yan et al., 2021) (**C**). Només els TMs involucrats amb la interacció del TM5 (verd) i l'Na2 es mostren (TM1a en blau i TM8 en groc). Els substrats i inhibidors també es mostren en barres grogues, això com l'Na2, com a esfera lila. Les representacions ampliades mostren els residus rellevants del TM5, les Lys conservades dels LATs (K154 en BasC i K294 en LAT1) així com els motius GX_nP de LeuT i BasC (G190-P200 en LeuT i G144 i P157 en BasC). La Lys de LeuT també s'hi mostra (K196) i es pot veure com projecta la seva cadena lateral cap a l'exterior i no cap a l'Na2.

La interacció entre el TM1a, 5 i 8 és crucial pel tancament de la porta interna, TM1a, 6b, 5 i 7. Sent imprescindible i coordinadora d'aquesta part del mecanisme la K154 en BasC. Així, la inviabilitat de la variant BasC-K154A de tancar la porta citosòlica afecta indirectament l'afinitat de la cara extracel·lular, tenint en compte el mecanisme d'accés alternat que adopten els transportadors amb plegament APC. Els estudis funcionals així van demostrar com l'afinitat exterior decreixia passant de presentar una K_M de 45 ± 5 µM a 474 ± 42 µM per l'L-Ala, mentre que l'afinitat interna romania pràcticament inamovible (Errasti-Murugarren et al., 2019).

Els estudis de MD (Errasti-Murugarren et al., 2019) també descrivien com la interacció del substrat amb la K154A desestabilitzaria la interacció d'aquesta amb el TM1a i 8, desencadenant l'obertura interna del transportador i la conseqüent translocació del substrat. Si invertim els passos, partint de la conformació oberta

cap a dins, el substrat, prèviament a la unió al lloc d'unió al substrat, interaccionaria amb la K154, i després es translocaria a aquest lloc d'unió al substrat. Permetent a la K154 interaccionar amb el TM1a i 8, desencadenant el tancament de la porta interna. Així doncs les interaccions del TM1a amb el substrat o K154, serien les responsables d'aquesta dicotomia entre la porta interna tancada i oberta. Les interaccions entre els residus del TM1a, 5 i 8 en BasC encara no són clars, ja que l'estructura tancada per dins no s'ha resolt. Malgrat això, la comparació entre l'estructura de LAT1 mirant a fora i BasC poden encaminar aquesta predicció (Figura 49). Així doncs, BasC passaria de la conformació oberta cap a dins, on K154 (TM5) interacciona amb la G15 (TM1a), a també interaccionar amb la cadena principal de l'S280 (TM8) tal i com LAT1 ho mostra entre la seva K204 (TM5) i l'S334 (TM8) (Figura 49). Aquest equilibri entre interaccions de la K154 en les conformacions obert cap a dins i cap a fora dependria de l'estat de protonació i desprotonació d'aquest residu tal i com ha estat hipotetitzat per la Lys158 d'ApCT, predita també com la substituta de l'Na2 (Stolzenberg et al., 2017).

La translocació del substrat cap a l'espai extracel·lular roman incert encara. Però l'enfoc d'ALEX-smFRET presentat en aquesta tesi en combinació amb estudis estructurals de baixa resolució amb Nbs per XRC i/o cryo-EM ha resultat ser prometedor. Aquesta combinació de tècniques permetria l'estudi d'altres TMs involucrats en el mecanisme de transport per poder revelar nous moviments i detalls del mecanisme de transport dels LATs. Tanmateix, la implementació d'altres factors com la reconstitució de LATs en ND per l'estudi per ALEX-smFRET o la implementació e TIRF, permetrien mesurar la ràtio d'intercanvi entre conformacions, així com l'efecte dels substrats o variants de malaltia, a més de revelar possibles efectes d'un entorn lipídic vers l'emprat fins ara, la solubilització en micel·les de detergent.

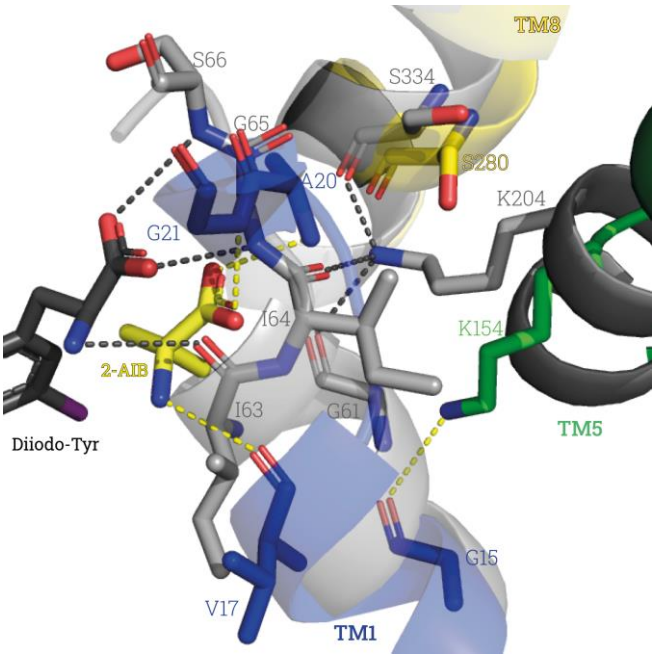

Figura 49. Interaccions del TM1a amb el substrat i el TM5 en LATs. Estructura de BasC (colors) mirant cap a dins unit al substrat pobre 2-AIB (groc) (PDB ID 6F2G) (Errasti-Murugarren et al., 2019) superposada a l'estructura de LAT1 (gris) mirant cap a fora unit a l'inhibidor DiiodoTyr (negre) (PDB ID 7DSQ) (Yan et al., 2021). Només es mostren els TMs involucrats (TM1a en blau, TM5 en verd i TM8 en groc) per facilitar la interpretació. Els residus involucrats en la interacció entre el TM1a i el substrat, així com entre els TM1a 5 i 8 es mostren en barres i les seves interaccions amb línies discontinues (color groc per BasC i negre per LAT1).

Conclusions

i. Els estats mirant cap a dins tancat i obert coexisteixen en BasC en condicions apo quan aquest està reconstituït en n-dodecil-β-maltòsid (DDM).

ii. L'estat conformacional de més baixa energia i més estable per BasC és mirant cap a dins obert en condicions apo quan està reconstituït en n-dodecil-β-maltòsid (DDM).

iii. Els substrats L-alanina i L-serina comporten el tancament de la porta citosòlica mentre l'inhibidor L-glutamina no comporta cap canvi respecte les condicions apo en BasC solubilitat en n-dodecil-β-maltòsid (DDM).

iv. La variant relacionada amb la LPI BasC-K154A no és capaç de tancar la porta citosòlica de la mateixa manera que ho fa la variant salvatge.

v. La combinació de la metodologia ALEX-smFRET I els nanocossos, substrats I variants relacionades amb malalties ha esdevingut una eina útil per desxifrar detalls del mecanisme de transport dels LATs.

vi. Existeix un efecte estèric dels nanocossos vers els volums d'accessibilitat dels fluoròfors, així com els que poden estar efectuant les micel·les de detergents i els lípids de membrana.

vii. S'ha aconseguit la reconstitució d'una sola molècula de BasC en nanodiscs formats per MSP1D1.